

**DESIGN AND DEVELOPMENT OF  
MAGNETORHEOLOGICAL FLUID DAMPER TO  
SUPPRESS THE TOOL VIBRATION IN HARD  
TURNING OPERATION**

Thesis

Submitted in partial fulfillment of the requirements for the degree of

**DOCTOR OF PHILOSOPHY**

by

**SUHAS S. ARALIKATTI**



DEPARTMENT OF MECHANICAL ENGINEERING  
NATIONAL INSTITUTE OF TECHNOLOGY KARNATAKA,  
SURATHKAL, MANGALORE – 575025

MAY 2023



**DESIGN AND DEVELOPMENT OF  
MAGNETORHEOLOGICAL FLUID DAMPER TO  
SUPPRESS THE TOOL VIBRATION IN HARD  
TURNING OPERATION**

Thesis

Submitted in partial fulfillment of the requirements for the degree of

**DOCTOR OF PHILOSOPHY**

by

**SUHAS S. ARALIKATTI**

Under the guidance of

**Dr. HEMANTHA KUMAR**

Associate Professor



DEPARTMENT OF MECHANICAL ENGINEERING  
NATIONAL INSTITUTE OF TECHNOLOGY KARNATAKA,  
SURATHKAL, MANGALORE – 575025

MAY 2023



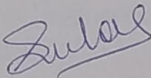


## DECLARATION

I hereby *declare* that the Research Thesis entitled “**DESIGN AND DEVELOPMENT OF MAGNETORHEOLOGICAL FLUID DAMPER TO SUPPRESS THE TOOL VIBRATION IN HARD TURNING OPERATION**” which is being submitted to the **National Institute of Technology Karnataka, Surathkal** in partial fulfillment of the requirements for the award of the Degree of **Doctor of Philosophy in Department of Mechanical Engineering** is a *bonafide report of the research work carried out by me*. The material contained in this Research Thesis has not been submitted to any University or Institution for the award of any degree.

Register Number : 177011ME020

Name of the Research Scholar : SUHAS S. ARALIKATTI

Signature of the Research Scholar : 

Department of Mechanical Engineering

Place : NITK, Surathkal

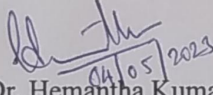
Date : 04/05/2023



## C E R T I F I C A T E

This is to *certify* that the Research Thesis entitled “**DESIGN AND DEVELOPMENT OF MAGNETORHEOLOGICAL FLUID DAMPER TO SUPPRESS THE TOOL VIBRATION IN HARD TURNING OPERATION**” submitted by **Mr. SUHAS S. ARALIKATTI (Register Number: 177011ME020)** as the record of the research work carried out by him, is *accepted as the Research Thesis submission* in partial fulfillment of the requirements for the award of degree of **Doctor of Philosophy**.

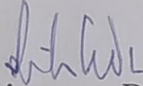
### Research Guide



Dr. Hemantha Kumar

Associate Professor,

Department of Mechanical Engineering  
NITK Surathkal



Chairman - DRPC

Department of Mechanical Engineering

NITK Surathkal

Place: NITK, Surathkal

Date: 4.5.2023





*Dedicated to my beloved mother.*



## ACKNOWLEDGEMENTS

It is my great pleasure to express my heartfelt gratitude to my research supervisor **Dr. Hemantha Kumar**, Associate Professor, Department of Mechanical Engineering, National Institute of Technology Karnataka, Surathkal, Mangalore, for their exemplary guidance and encouragement throughout my research work. Their encouragement and the valuable suggestions have increased my knowledge level which led to the completion of my research work and is demonstrated through this thesis.

I sincerely thank the RPAC members, **Dr. P. Jeyaraj**, Associate Professor, Department of Mechanical Engineering and **Dr. Nazar T.**, Associate Professor, Department of Water Resources and Ocean Engineering for providing valuable suggestion and support extended to me on all occasion.

I thank the reviewers and editors of journal articles who pushed me to challenges of research work to arrive at the final outcome of present form.

I wish to express my sincere thanks to **Prof. Ravikiran Kadoli**, Head of the Department, Department of Mechanical Engineering, National Institute of Technology Karnataka, Surathkal, Mangalore and **Prof. S. M Kulkarni**, **Prof. S. N. Narendranath**, & **Prof. Srikantha S Rao**, former HOD's for their kind help and continuous support in providing the facilities.

I acknowledge the support from Machine shop-II @ NITK and experimental facility provided by **Dr. Shivananda Nayaka**, Associate Professor, NITK Surathkal

I also sincerely acknowledge the help rendered by **Mr. C. A. Varghese**, Foreman and Mr. Pradeep, Mr. Guruprasad, Mr. Nishan, Technicians, Machine shop, NITK Surathkal in my entire experimental work.

I also acknowledge help rendered by **Dr. V. Sugumaran**, Professor, Department of Mechanical Engineering, VIT University.

The unfailing support of my colleagues had provided brilliant ideas, everlasting optimism and assistance. I would like to thank my seniors and friends Dr. Vipin Allien.,

Mr.Subhash Acharya., Dr. Rangaraj M Desai., Mr. Ravikumar K. N, Mr. Puneeth N.P., Mr. Radhe Shyam Saini., Mr. Hussain Jamadar, Mr. Ashok Kumar, Mr. Devikiran, Mr. Surya Rao for their selfless advice, assistance and contribution in completing this work.

I thank the financial and instrumentation support from Impacting Research Innovation and Technology (IMPRINT) Project No. IMPRINT/2016/7330 titled ‘Development of cost-effective magneto-rheological (MR) fluid damper in two-wheeler and four-wheeler automobile to improve ride comfort and stability’.

I whole heartedly thank my fellow friends and roommates Mr. Vishwanath F. B. and Mr. Umesh Shinde who have been there for me in my odd times to guide, support and encourage.

Lastly, I would like to immensely thank **my parents** Mr. Suresh & Mrs. Sarojini. my brother Mr. Prashant., for their undying love, encouragement and moral support throughout my life and education. Without them and their blessings, achieving this goal would not have been possible.

I wish to thank all other individuals who have directly or indirectly helped me to complete my research work.

*(Suhas S. Aralikatti)*



## ABSTRACT

The state of the cutting tool determines the quality of the surface finish produced on the machined parts. A faulty tool produces poor surface and inaccurate geometry leading to the rejection of parts. It is necessary to monitor tool conditions to have consistent quality and economic production. Condition monitoring is ineffective without the implementation of a real-time corrective strategy. In the present study, fault classification of single-point cutting tools for hard turning has been carried out by employing signal processing and machine learning technique using cutting force signals and vibration signals. A comparison of the performance of classifiers was made between cutting force and vibration signal to choose the best signal acquisition method in classifying the tool fault conditions using the machine learning technique. A set of four tool conditions, namely healthy, worn flank, broken insert and extended tool overhang, have been considered for the study. These faulty tools produce undesired vibration that reduces machine quality and production rate.

The adverse effect of tool vibration leads to loss of geometric tolerance, accelerated tool wear, poor surface finish and machine instability. The author designed a current-controlled compact magnetorheological fluid (MRF) damper consisting of an electromagnetic coil in the piston as a corrective measure. The damper is fitted onto the lathe machine with the optimal fluid composition to evaluate its performance in controlling the tool vibration. The optimal composition of MRF is identified by a genetic algorithm through the central composite design of the experiment. To cross-verify the algorithm's output values, a validation study is done. A comparison between optimal in-house MR fluid and commercial MR fluid is conducted. The comparison demonstrates that in-house prepared MR fluid performs equally well compared to commercial fluid. The MR damper effectively damps high-amplitude vibration at aggressive cutting conditions. The L9 Taguchi design of the experiment opted to arrive at minimal machining parameters to evaluate the performance of the damper in machining two workpiece materials, namely oil-hardened nickel steel (OHNS) and high carbon high chromium (HCHCR) die steel. The surface roughness and tool vibration

are reduced with the damper. It is noted that in-house MR fluid performed equally well as commercial MR fluid. The tool wear study is also carried out to monitor the influence of external damping over tool life. The stability lobe diagram is obtained analytically with experimental validation to mark the stability limit of the machining condition. The stability boundary increases with the damper enabling aggressive cutting conditions. The designed MR damper is controlled by a real-time controller considering the vibration-limiting feedback approach. The Bouc-Wen model is used to estimate the damping force based on the vibration feedback of the tool. The tool wear, surface roughness, and amplitude of tool vibration are evaluated with and without a semi-active MR damper.

The above-developed MR damper forms an external adaptor to control the tool vibration that can be installed on the lathe. To improve the design configuration of the MR damper, an internally damped novel tool holder is designed that houses MR fluid in its axial hollow section. The MR fluid is activated by the internal electromagnet coil wound around the inverse beam supported at the inner wall of the hollow portion. The developed MR tool damper reduces the tool vibration with the electric current supply.

**Keywords:** *Fault diagnosis, Machine learning, Hard turning, Tool life, Magnetorheological fluid, MR Damper, Optimization, Stability lobe diagram*

# CONTENTS

<b>ABSTRACT.....</b>	<b>iii</b>
<b>CONTENTS.....</b>	<b>v</b>
<b>LIST OF FIGURES .....</b>	<b>xiii</b>
<b>LIST OF TABLES .....</b>	<b>xx</b>
<b>ABBREVIATION .....</b>	<b>xxii</b>
<b>1 INTRODUCTION.....</b>	<b>1</b>
1.1 BACKGROUND .....	1
1.2 OVERVIEW OF METAL CUTTING.....	2
1.3 HARD TURNING .....	3
1.3.1 Forces and vibrations in hard turning operation .....	3
1.4 STABILITY LOBE DIAGRAM (SLD) .....	5
1.5 TOOL LIFE: WEAR AND FAILURE.....	6
1.6 TOOL FAULT DIAGNOSIS BY SIGNAL PROCESSING.....	7
1.6.1 Time domain analysis .....	7
1.6.2 The spectrum analysis.....	7
1.6.3 The cepstrum analysis.....	8
1.6.4 Short-time Fourier transform .....	8
1.6.5 Wavelet analysis .....	8
1.6.6 EMD.....	8
1.7 Tool fault diagnosis by machine learning.....	9
1.7.1 Feature extraction.....	10
1.7.2 Feature selection by using a decision tree.....	11
1.7.3 Classification.....	11

1.8 CHATTER VIBRATION DUE TO TOOL WEAR .....	11
1.9 TOOL VIBRATION MODEL.....	12
1.10 VIBRATION SUPPRESSION TECHNIQUE .....	12
1.10.1 Passive damping techniques .....	13
1.10.2 Active damping techniques.....	14
1.10.3 Semi-active damping techniques .....	15
1.11 MAGNETORHEOLOGICAL FLUID .....	15
1.11.1 Squeeze mode .....	16
1.11.2 Shear mode.....	17
1.11.3 Flow mode .....	17
1.12 MAGNETORHEOLOGICAL DAMPER .....	18
1.12.1 Mono tube MR Damper .....	19
1.12.2 Twin tube MR damper .....	19
1.12.3 Double rod end MR damper .....	20
1.13 MODELLING MR DAMPER.....	20
1.14 CONTROL STRATEGIES.....	21
1.14.1 Semi-active control .....	21
1.15 ORGANIZATION OF THE THESIS.....	23
<b>2 LITERATURE SURVEY.....</b>	<b>25</b>
2.1 INTRODUCTION .....	25
2.2 VIBRATION IN MACHINING OPERATION .....	25
2.3 A VIBRATION LIMITING CHART - SLD .....	26
2.4 VIBRATION INDUCED DUE TO FAULTY TOOL.....	27
2.5 SENSORS AND TRANSDUCERS FOR FAULT DIAGNOSIS .....	27
2.5.1 Milling.....	28
2.5.2 Turning.....	29

2.6 FAULT DIAGNOSIS USING SIGNAL PROCESSING.....	30
2.6.1 Time domain .....	31
2.6.2 Frequency domain.....	31
2.6.3 Cepstrum analysis .....	32
2.6.4 Wavelet analysis .....	33
2.7 FAULT DIAGNOSIS BY MACHINE LEARNING .....	34
2.7.1 Feature extraction.....	34
2.7.2 Empirical mode decomposition features.....	35
2.7.3 Feature selection .....	36
2.7.4 Classification of features.....	37
2.8 CONTROLLING VIBRATION IN MACHINING .....	39
2.8.1 Passive damping techniques .....	40
2.8.2 Active damping techniques.....	41
2.8.3 Semi-active techniques .....	42
2.9 DESIGN OPTIMIZATION AND APPLICATION OF mr DAMPER.....	43
2.10 MAGNETORHEOLOGICAL FLUID .....	45
2.10.1 Preparation and characterisation .....	45
2.10.2 Rheological study.....	47
2.10.3 Optimization of composition of MRF.....	47
2.11 DYNAMIC MODELLING OF MRD .....	48
2.12 MATHEMATICAL MODELLING OF CUTTING TOOL.....	48
2.13 CONTROL STRATEGIES.....	48
2.13.1 PID control.....	49
2.13.2 Fuzzy control .....	49
2.13.3 ANN.....	49
2.14 RESEARCH GAP.....	50

2.15 MOTIVATION FROM THE LITERATURE SURVEY .....	50
2.16 OBJECTIVES OF RESEARCH WORK.....	51
2.17 SCOPE OF CURRENT RESEARCH .....	51
2.18 SUMMARY .....	52
<b>3 METHODOLOGY .....</b>	<b>53</b>
3.1 INTRODUCTION .....	53
3.2 METHODOLOGY .....	55
3.2.1 Fault detection based on signal processing.....	55
3.2.2 Fault diagnosis based on machine learning .....	55
3.2.3 Design, development and characterisation of MR damper.....	56
3.2.4 Synthesis and characterisation of MR fluid .....	57
3.2.5 Implementation of MR damper to evaluate machining performance .....	58
3.2.6 Implementation of current control .....	58
3.2.7 Design of a novel anti-vibration tool holder .....	59
3.3 SUMMARY .....	60
<b>4 FAULT DIAGNOSIS OF SINGLE POINT CUTTING TOOL BY SIGNAL PROCESSING AND MACHINE LEARNING.....</b>	<b>61</b>
4.1 INTRODUCTION .....	61
4.2 SIGNAL PROCESSING TECHNIQUE .....	61
4.2.1 Time domain analysis .....	61
4.2.2 Frequency domain analysis .....	62
4.2.3 Wavelet analysis .....	62
4.3 Experimental work.....	63
4.4 Experimental procedure .....	65
4.5 RESULTS AND DISCUSSION ON VIBRATION SIGNAL.....	67
4.5.1 Time domain analysis .....	67

4.5.2 Frequency analysis .....	68
4.5.3 Time-frequency analysis/ wavelet analysis .....	69
4.6 RESULT AND DISCUSSION ON CUTTING FORCE SIGNAL .....	71
4.6.1 Time domain cutting force signals.....	71
4.6.2 Frequency domain analysis .....	73
4.6.3 Wavelet analysis of cutting force.....	74
4.7 TOOL FAULT DIAGNOSIS BY MACHINE LEARNING.....	76
4.7.1 Wavelet Transform Analysis .....	77
4.7.2 Feature extraction using discrete wavelet transform .....	79
4.7.3 Selection of features using a decision tree .....	81
4.7.4 Classification using Naïve Bayes classifier .....	82
4.7.5 Classification using rotation forest algorithm.....	83
4.8 RESULTS AND DISCUSSION .....	83
4.8.1 Feature extraction for cutting force using DWT.....	83
4.8.2 Feature extraction for vibration signal using DWT .....	84
4.8.3 Decision tree for feature selection .....	86
4.8.4 Classification using the Naïve Bayes algorithm for vibration signal .....	87
4.8.5 Classification using Naive Bayes for cutting force.....	88
4.8.6 Classification using Rotation forest algorithm for cutting force .....	88
4.8.7 Classification using Rotation forest algorithm for Vibration signal.....	89
4.8.8 Classification using Random tree algorithm for cutting force.....	89
4.8.9 Classification using Random tree algorithm for vibration signal .....	90
4.8.10 Comparison of various classifiers for their classification accuracy.....	90
4.9 TOOL FAULT DIAGNOSIS BY MACHINE LEARNING USING STATISTICAL FEATURES .....	91
4.9.1 Statistical feature extraction.....	91

4.10 RESULTS AND DISCUSSION .....	93
4.10.1 Statistical feature extraction for the experimental dataset .....	93
4.10.2 Feature selection using the J48 decision tree .....	96
4.10.3 Classification using various classifiers .....	97
4.10.4 Comparison of classifiers.....	100
4.10.5 SUMMARY .....	101
<b>5 DEVELOPMENT AND CHARACTERISATION OF MR DAMPER WITH OPTIMAL COMPOSITION OF MR FLUID .....</b>	<b>103</b>
5.1 INTRODUCTION .....	103
5.2 DETERMINING THE OPTIMAL COMPOSITION OF MRF FOR THE MR DAMPER.....	103
5.3 CHARACTERIZATION OF CARBONYL IRON PARTICLE (CIP) .....	105
5.4 SYNTHESIS AND CHARACTERISATION OF MR FLUID .....	106
5.5 DESIGN OF MR DAMPER.....	112
5.5.1 Design of Magnetic Circuit.....	113
5.5.2 Designing finite element models of MR damper .....	114
5.5.3 Comparison of finite element models .....	116
5.5.4 Estimation of damping force.....	119
5.6 OPTIMIZING THE GEOMETRIC DIMENSIONS OF MR DAMPER .....	121
5.7 CHARACTERISATION OF MR DAMPER .....	126
5.8 ANALYSIS OF VARIANCE (ANOVA) AND MULTI-OBJECTIVE OPTIMIZATION.....	128
5.9 SUMMARY .....	133
<b>6 EVALUATION OF MACHINING PERFORMANCE WITH MR DAMPER .....</b>	<b>135</b>
6.1 INTRODUCTION .....	135



6.2 MACHINING STUDY WITH MR DAMPER .....	135
6.3 EVALUATION OF TOOL VIBRATION.....	138
6.4 EVALUATION OF SURFACE ROUGHNESS .....	141
6.5 TOOL WEAR RATE.....	144
6.6 CHIP MORPHOLOGY .....	145
6.7 STABILITY LOBE DIAGRAM .....	146
6.8 EVALUATION OF MACHINING PERFORMANCE WITH MR DAMPER BY REAL-TIME CONTROL .....	148
6.8.1 Methodology .....	149
6.8.2 Control logic for the damper.....	149
6.9 MACHINING STUDY: IMPLEMENTATION OF MR DAMPER ON LATHE WITH CONTROLLER.....	150
6.10 RESULTS AND DISCUSSION .....	150
6.10.1 Vibration analysis of cutting tool with MR damper .....	152
6.10.2 Comparison of surface roughness.....	155
6.10.3 Comparison of tool wear of the cutting tool .....	155
6.11 SUMMARY .....	156
<b>7 DEVELOPMENT OF AN NOVEL ANTI-VIBRATION TOOL HOLDER FEATURING MR FLUID .....</b>	<b>159</b>
7.1 INTRODUCTION .....	159
7.2 DESIGN OF TOOL HOLDER.....	160
7.3 NUMERICAL CALCULATION FOR DESIGNING THE Tool mass DAMPER FOR UN-DAMPED STRUCTURE .....	161
7.4 DEVELOPMENT OF mr TOOL HOLDER.....	163
7.4.1 Magnetostatic analysis .....	163
7.4.2 Structural analysis of the MR tool holder.....	164

7.4.3 Fabrication of the tool holder.....	166
7.5 FORCED VIBRATION STUDY .....	170
7.6 MACHINING WITH MR TOOL HOLDER.....	172
7.7 SUMMARY .....	174
<b>8 SUMMARY AND CONCLUSION .....</b>	<b>175</b>
8.1 SUMMARY .....	175
8.2 CONCLUSIONS.....	177
8.2.1 Signal processing technique.....	177
8.2.2 Fault diagnosis by machine learning.....	178
8.2.3 MR fluid preparation and characterisation .....	178
8.2.4 Development of MR damper .....	178
8.3 SCOPE FOR FUTURE WORK.....	179
<b>REFERENCES.....</b>	<b>181</b>
<b>APPENDIX.....</b>	<b>195</b>
<b>LIST OF PUBLICATIONS .....</b>	<b>211</b>
<b>BIO-DATA.....</b>	<b>213</b>

## LIST OF FIGURES

Figure 1.1	Schematic of Chip formation in turning operation.....	2
Figure 1.2	Typical force and vibration measurement system for turning operation as illustrated by Zhang et al. (2021).....	4
Figure 1.3	Tool deflection at the tip due to cutting force.....	5
Figure 1.4	Classical stability lobe diagram (Vnukov et al. 2017).....	5
Figure 1.5	Flowchart of the Machine learning for fault classification....	10
Figure 1.6	Tool vibration model in tangential direction.....	12
Figure 1.7	Undamped single degree of freedom model.....	13
Figure 1.8	Tuned mass damper as a passive damping technique.....	13
Figure 1.9	Active damped tool model.....	14
Figure 1.10	Semi-active damped tool model.....	15
Figure 1.11	Behaviour of MR fluid a) In the absence of magnetic field b) In the presence of magnetic field.....	16
Figure 1.12	Squeeze mode.....	17
Figure 1.13	Shear mode.....	17
Figure 1.14	Flow mode.....	18
Figure 1.15	Monotube MR damper with accumulator.....	19
Figure 1.16	Twin tube MR damper.....	19
Figure 1.17	Double rod end MR damper.....	20
Figure 2.1	Vibration in tangential direction during longitudinal turning (Urbikain et al. 2013).....	26
Figure 2.2	A typical stability lobe diagram. Merritt (1965).....	26
Figure 2.3	Fault diagnosis using thermal imaging (Ramirez-Nunez et al. 2018).....	28
Figure 2.4	Geometric image of milling cutter in different condition (Ryabov et al. 1996).....	29
Figure 2.5	Experimental setup established for fault diagnosis using acoustic sensor and accelerometer (Bhuiyan et al. 2014).....	30
Figure 2.6	FFT plot of three vibration component (Plaza and López 2018).....	31

Figure 2.7	Vibration cepstrum of induction motor (a) healthy and (b) broken rotor (Liang et al. 2013).....	32
Figure 2.8	Fault diagnosis of ball bearing of IC engine gearbox using wavelet analysis (a) Healthy bearing (b) Inner race defect (c) Outer race defect (Ravikumar et al. 2020).....	33
Figure 2.9	Fault diagnosis procedure using machine learning (Lei et al. 2020).....	34
Figure 2.10	Decision tree used for milling tool insert fault diagnosis using histogram features (Madhusudana et al. 2016b).....	37
Figure 2.11	Damping methods employed for tool vibration.....	40
Figure 2.12	Milling tool embedded with passive damping unit. 1—end cover; 2—damping element; 3 and 8—gasket; 4—shell; 5—mass block; 6—steel rod; 7—support block (Ma et al. 2021).	41
Figure 2.13	Active spindle (Monnin et al. 2014).....	41
Figure 2.14	MR sponge used for vibration control in boring operation (Saleh et al. 2021).....	42
Figure 2.15	Magnetic flux density for various design configuration (Parlak et al. 2013).....	45
Figure 2.16	Iron Particle characterisation and preparation of MR fluid (Kumar Kariganaur et al. 2022).....	46
Figure 3.1	Flowchart of overall research methodology.....	54
Figure 3.2	Flowchart of fault diagnosis using machine learning.....	56
Figure 3.3	Flowchart of damper design and fluid synthesis.....	57
Figure 3.4	Block diagram of effective control of tool vibration with NI DAQ and accelerometer.....	59
Figure 4.1	Schematic representation of experimental setup.....	64
Figure 4.2	Experimental setup containing lathe machine with force measuring and analysing system.....	66
Figure 4.3	Photographic image of various tool wear (a) Healthy tool (b) Extended overhang (c) Worn flank (d) Broken tool.....	67
Figure 4.4	Time domain signals of various tool conditions.....	68

Figure 4.5	Spectrum plot of different tool conditions.....	69
Figure 4.6	CWT plot of Healthy tool.....	70
Figure 4.7	CWT plot for extended overhanging tool.....	70
Figure 4.8	CWT plot for worn flank.....	70
Figure 4.9	CWT plot for broken tool.....	71
Figure 4.10	Time domain plot of cutting force signal of healthy tool mounted properly.....	71
Figure 4.11	Time domain plot of cutting force signal of healthy tool mounted with extended overhang.....	72
Figure 4.12	Time domain plot of cutting force signal of worn flank.....	72
Figure 4.13	Time domain plot of cutting force signal of broken tool.....	73
Figure 4.14	Spectrum plots of cutting force signal for various tool conditions.....	74
Figure 4.15	Wavelet plot of healthy tool – cutting force.....	75
Figure 4.16	Wavelet plot of overhanging tool – cutting force.....	75
Figure 4.17	Wavelet plot of worn flank – cutting force.....	75
Figure 4.18	Wavelet plot of broken tool - cutting force.....	75
Figure 4.19	Methodology followed to classify tool faults using machine learning technique.....	76
Figure 4.20	Signal decomposition to obtain approximation coefficient and detailed coefficient.....	78
Figure 4.21	Decomposition level of signal using DWT (Saravanan and Ramachandran 2010).....	80
Figure 4.22	J48 decision tree for cutting force.....	86
Figure 4.23	J-48 Decision tree based on statistical features of vibration data.....	87
Figure 4.24	Decision tree (J-48) based on statistical features of vibration data.....	96
Figure 4.25	Decision tree based on statistical features of cutting force signal.....	97

Figure 5.1	Methodology of fluid synthesis and evaluation of its performance.....	104
Figure 5.2	Particle size distribution of CIP.....	105
Figure 5.3	SEM image of CIP.....	105
Figure 5.4	Magnetization curve of CIP.....	106
Figure 5.5	XRD image of the CIP.....	107
Figure 5.6	Rheometer to characterise MRF samples.....	109
Figure 5.7	Flow curves of MRF samples.....	110
Figure 5.8	Plot of dynamic yield stress for fluid samples under magnetic field (for input current).....	111
Figure 5.9	Viscosity curves of MRF under no magnetic field.....	112
Figure 5.10	Schematic representation of MR damper in shear mode.....	113
Figure 5.11	Electric boundary condition applied to magnetic circuit.....	114
Figure 5.12	Flux lines around the MR flow valve.....	115
Figure 5.13	Magnetic flux density distribution in MR fluid element between piston and cylinder of material AISI 1008.....	116
Figure 5.14	Magnetic flux density distribution in MR fluid element between piston and cylinder of material AISI 1010.....	117
Figure 5.15	Magnetic flux density distribution in MR fluid element between piston and cylinder of material AISI 1018.....	117
Figure 5.16	Magnetic flux density distribution for various current input (a) AISI 1008 (b) AISI 1010 (c) AISI 1018 (d) AISI 1020...	118
Figure 5.17	Magnetic flux density distribution in MR fluid element between piston and cylinder of material AISI 1020.....	118
Figure 5.18	Nomenclature and dimensions of the magnetic circuit.....	115
Figure 5.19	Force –Velocity plot of MR damper for various input current (a) AISI 1008 (b) AISI 1010 (c) AISI 1018 (d) AISI 1020.....	121
Figure 5.20	Computational domain of annular fluid flow gap.....	122
Figure 5.21	Response surface of coil width vs fluid gap.....	124
Figure 5.22	Response surface of coil width vs flange length.....	124

Figure 5.23	Response surface of fluid gap vs flange length.....	125
Figure 5.24	The damper fabricated to optimal design dimensions with its parts labelled.....	125
Figure 5.25	Damper testing machine with all its supporting elements.....	126
Figure 5.26	Force-displacement curves of MRD with various fluid samples.....	127
Figure 5.27	Pareto front plot generated by multi objective optimization...	131
Figure 5.28	Shear curve of S16 MRF sample.....	132
Figure 5.29	Damper characterised with S16 MRF sample.....	132
Figure 6.1	Experimental setup to evaluate the performance of the MR fluid damper.....	136
Figure 6.2	Vibration produced on OHNS workpiece with damper at various current for (a)-(c) in-house MR fluid, (d)-(f) commercial MR fluid.....	138
Figure 6.3	Comparison of vibration levels at various cutting conditions when in-house MR fluid and lord fluids are used in the damper while machining OHNS.....	139
Figure 6.4	Comparison of vibration level at various cutting conditions when in-house MR fluid and lord fluids are used in the damper while machining HCHCR D2 steel.....	139
Figure 6.5	Comparison of vibration level between OHNS and HCHCR D2 steel when in-house fluid is used in the damper.....	140
Figure 6.6	Comparison of vibration level between OHNS and HCHCR D2 steel when commercial fluid [Lord 132 DG] MR fluid is used in the damper.....	140
Figure 6.7	Direction of measurement of surface roughness.....	136
Figure 6.8	Direction of measurement of vibration.....	136
Figure 6.9	Comparison of surface roughness between in-house MR fluid and lord fluid while machining OHNS.....	142
Figure 6.10	Comparison of surface roughness between in- house MR fluid and lord fluid while machining HCHCR D2 steel.....	142

Figure 6.11	Comparison of surface roughness between OHNS and HCHCR D2 steel when LORD fluid is used in the damper...	143
Figure 6.12	Comparison of surface roughness between OHNS and HCHCR D2 steel when in-house fluid is used in the damper.	143
Figure 6.13	Comparison of tool life of OHNS material.....	144
Figure 6.14	Comparison of tool life of HCHCR D2 steel material.....	145
Figure 6.15	Stability lobe diagram for OHNS workpiece (a) Without damper (b) With damper.....	147
Figure 6.16	Stability lobe diagram for HCHCR D2 workpiece (a) Without damper (b) With damper.....	147
Figure 6.17	Flowchart of implementing control to MR damper.....	149
Figure 6.18	Block diagram of the experimental setup.....	149
Figure 6.19	Experimental setup showing data acquisition, controller and MR damper.....	152
Figure 6.20	(a) vibration signal of OHNS (b) Control pulse signal OHNS (c) Spectrum plot of OHNS.....	153
Figure 6.21	(a) Vibration signal of HCHCR D2 steel (b) Control pulse signal for HCHCR D2 (c) Spectrum plot of HCHCR D2.....	154
Figure 6.22	Roughness profile produced on workpiece with control ON and control OFF (a) 384 RPM, 0.043 mm/rev (b) 572 RPM, 0.093 mm/rev.....	155
Figure 6.23	(a) Healthy tool and (b) Worn flank.....	156
Figure 7.1	Parts label of the tool holder (1) outer tool body (2) slender bar (3) end cap (4) copper coil (5) fluid volume inside tool body (6) suspended mass (7) Insert.....	160
Figure 7.2	(a) Schematic of cross sectional view of MR tool holder 1-insert, 2-outer structure,3-MR fluid, 4-suspended mass, 5-copper coil, 6-inverse beam (b) 3D cross sectional view of MR tool holder (c) Magnetostatic analysis of active region in tool holder.....	163



Figure 7.3	ANSYS model of the tool holder showing hidden parts and outer structure .....	164
Figure 7.4	Harmonic response of the tool holder modelled in ANSYS for different damping ratio .....	165
Figure 7.5	Solid model of (a) Solid shank tool holder and (b) MR tool holder .....	165
Figure 7.6	Dismantled components of MR tool holder fabricated .....	166
Figure 7.7	Assembled image of the fabricated tool holder .....	167
Figure 7.8	Experimental setup showing the free vibration study .....	168
Figure 7.9	Frequency response of Solid tool holder for impulse excitation.....	168
Figure 7.10	Estimating damping ratio for solid tool with external damping .....	169
Figure 7.11	Frequency response of MR tool holder.....	170
Figure 7.12	Experimental setup of the forced excitation study .....	171
Figure 7.13	Acceleration response to forced excitation frequency of 968 Hz .....	171
Figure 7.14	Experimental setup showing the vibration acquisition setup and DC power source to supply current to the tool holder.....	172
Figure 7.15	Close-up view of the tool holder secured on the lathe, accelerometer mounted under tooltip to acquire tool vibration.....	173
Figure 7.16	Vibration during machining with solid shank tool and new MR tool holder at varies current.....	173

## LIST OF TABLES

Table 4.1	Chemical composition of Oil hardened nickel steel.....	63
Table 4.2.	Details of cutting conditions.....	64
Table 4.3.	Specification of Kistler 9257B Dynamometer.....	65
Table 4.4	Specification of the accelerometer used in the experiment.....	65
Table 4.5.	Discrete wavelet features extracted from the cutting force signal	84
Table 4.6	Discrete wavelet features extracted from the vibration signal.....	85
Table 4.7	Confusion matrix for Naive Bayes classifier – vibration signa...	88
Table 4.8	Confusion matrix for Naive Bayes classifier for cutting force....	88
Table 4.9	Confusion matrix of rotation forest algorithm for cutting force signal.....	89
Table 4.10	Confusion matrix of rotation forest algorithm for vibration signal using DWT features.....	89
Table 4.11	Confusion matrix of the random tree for cutting force signal using DWT features.....	90
Table 4.12	Confusion matrix of the random tree for vibration signal using DWT features.....	90
Table 4.13	Comparison of classification accuracy of various classifiers.....	91
Table 4.14	Statistical features and their definition.....	91
Table 4.15	statistical features extracted from the vibrational signal.....	94
Table 4.16	Statistical features extracted for cutting force signals.....	95
Table 4.17	Confusion matrix of Random tree – vibration signal.....	97
Table 4.18	Confusion matrix of Random tree-cutting force.....	98
Table 4.19	Confusion matrix of Naïve Bayes classifier – vibration signal.....	98
Table 4.20	Confusion matrix of Naïve Bayes classifier – cutting force.....	98
Table 4.21	Rotation forest` confusion matrix – vibration signal.....	99
Table 4.22	Rotation forest` confusion matrix – cutting force.....	99

Table 4.23	Classification accuracy comparison using statistical features....	100
Table 4.24	Classification accuracy of various classifiers for vibration and cutting force signal.....	100
Table 5.1	Nomenclature of MRF samples prepared for the experiment....	108
Table 5.2	Various levels of the parameters for DOE.....	108
Table 5.3	Estimating the saturation limit of particle loading.....	111
Table 5.4	Parametric boundaries and optimal dimensions.....	123
Table 5.5	DOE result obtained by CCD and its responses.....	128
Table 5.6	ANOVA for yield stress.....	129
Table 5.7	ANOVA for effective damping range.....	130
Table 5.8	The optimal parameters and their response obtained by MOGA.	131
Table 5.9	Comparison of MOGA output and validation experiment.....	133
Table 6.1	Levels and factors of DOE for machining trials.....	137
Table 6.2	Cutting conditions derived from DOE.....	137
Table 6.3	Chip morphology without damper and with damper while machining OHNS and HCHCR D2 steel.....	146
Table 6.4	Tool acceleration, surface roughness and tool wear measurement with damper and without damper.....	151
Table 7.1	Estimation of damping ratio with damper.....	169

## ABBREVIATION

<i>MR</i>	Magnetorheological
<i>AISI</i>	American Iron and Steel Institute
<i>DTM</i>	Dynamic Testing Machine
<i>DC</i>	Direct Current
<i>CBN</i>	Cubic boron nitride
<i>HRC</i>	Rockwell Harness type C
<i>TCM</i>	Tool condition monitoring
<i>SLD</i>	Stability lobe diagram
<i>MRR</i>	Material removal rate
<i>DOC</i>	Depth of cut
<i>SVM</i>	Support vector machine
<i>AUC</i>	Area under the curve
<i>ROC</i>	Receiver Operating Characteristics Curve
<i>TVA</i>	Tunable vibration absorber
<i>WT</i>	Wavelet transform
<i>OTF</i>	Orient transfer function
<i>EMD</i>	Empirical mode decomposition
<i>VMD</i>	Variable mode decomposition
<i>STDSA</i>	Short time difference spectrum analysis
<i>ASME</i>	American society for Mechanical Engineers
<i>Std. Dev.</i>	Standard deviation
<i>FRF</i>	Frequency response function
<i>NI DAQ</i>	National instruments data acquisition
<i>DSUB</i>	D-shaped sub miniature
<i>FFT</i>	Fast Fourier transform
<i>RF</i>	Rotation forest
<i>CM</i>	Condition monitoring
<i>ANN</i>	Artificial neural network
<i>SPCT</i>	Single point cutting tool

# CHAPTER 1

## INTRODUCTION

### 1.1 BACKGROUND

Surface machining removes the external layer of a workpiece to obtain the desired shape, form and geometry. It requires a relatively hard tool to machine the workpiece mounted over a rigid machine tool which provides sufficient power to shear the layer of the workpiece. Machining in a conventional lathe is still a practice in low and medium-scale shop floors where sophisticated CNC are costly to afford and maintain. The conventional lathe can effectively produce desired components without much compromise in quality. One major problem associated with machining with such old machine tools is backlash and lack of rigidity, leading to chatter during machining. Chatter occurs more frequently during roughing operations and hard turning with greater chip load and deeper cuts. Chatter is a relative movement of tool or workpiece during machining operation due to difference in stiffness or damping in them. This self-excited vibration lead to poor surface finish and lower productivity. Chatter could be suppressed by adjusting the system's structural dynamics or selecting optimal cutting conditions. The machining process has to be halted to change the cutting parameters; however, adjusting structural dynamics by incorporating vibration damping devices increases the system's dynamic stiffness. Machining is a complex, unstable phenomenon that requires continuous monitoring to achieve consistent performance. The tool is subjected to dynamic force and vibration that may lead to tool failure and poor surface finish over the machined component. Many factors contribute to tool wear, the major being flow of chips over the rake face and unstable machining with violent vibration. A stable contact between the tool and workpiece ensures a uniform surface finish. Unsteady vibration poses frequent contact loss, leading to wavy surface and accelerated tool wear. Hard turning poses challenges in machining with violent vibration and accelerated tool wear as it is performed without any coolant to avoid

forming an oxide layer over the workpiece. The most common tool failures are flank and crater wear in hard turning.

## 1.2 OVERVIEW OF METAL CUTTING

Machining has been done for decades and evolved to many sophisticated machine tools and process capabilities; however, the basic principle remains the same for the conventional metal removal process. The metal removal process shears the layer of the workpiece from a relatively hard tool by holding the tool and workpiece rigidly. Machining is often referred to as the secondary or finishing operations, as the material is removed from the parts manufactured using different methods. Various metal cutting operations are performed to generate features such as cylindrical parts on a lathe, rectangular slabs on a milling machine, holes in a drilling machine, groves in a shaper or planer, and ribs cut on form milling. Conventional machining involves using single-point or multi-point cutting tools with specific shapes and geometry. The schematic of chip formation is explained in Figure. 1.1 by considering a rotating workpiece (RPM) held rigidly in a chuck, machined by a single point cutting tool with the indented depth of cut (mm), traverses left at a velocity,  $V$  (mm/rev) to produce the chips which flow over the rake face of the cutting tool.

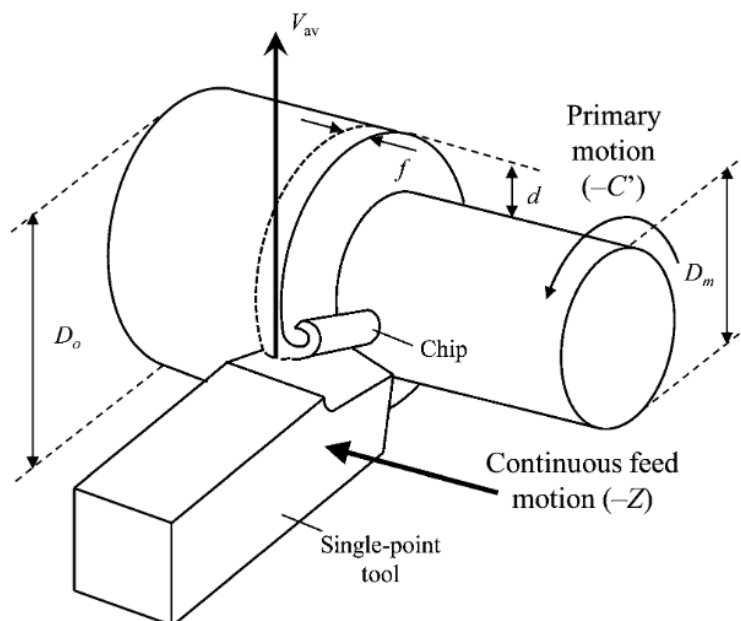


Figure 1.1 Schematic of Chip formation in turning operation (Girsang and Dhupia 2015)

The tool moves with constant velocity,  $V$ , relative to the workpiece to cut the material of depth,  $t_0$ , which produces the chip thickness,  $f$ , by continuously deforming and shearing the material along the shear plane. The independent factors that influence the machining are tool material; workpiece material; the shape of the tool; cutting speed, feed, depth of cut; fixtures; machine tool and cutting fluid. The responses affected by these factors are force, temperature rise; tool wear; surface finish and type of chip produced. A comprehensive examination is required for standard diagnostics when machining operations produce unacceptable results, such as the tool vibrating and chattering, the tool wearing rapidly and failing; the unacceptable surface finish is produced. The chatter vibration in machining is predominantly observed in machining hard steels, and unique materials such as Inconel and Titanium, machining of such materials are referred to as hard machining.

### **1.3 HARD TURNING**

Hard turning is machining workpieces of hardness values over 55 Rockwell hardness-C (HRC). Hard turning can create an equally good or superior surface quality at significantly greater material removal rates, eliminating grinding operation as a finishing operation. Hard turning can give a surface polish superior to grinding when using the proper combination of insert nose radii, feed rate, or the latest insert technology with process stability.

#### **1.3.1 Forces and vibrations in hard turning operation**

Knowledge of the cutting forces and power involved in machining operations is essential so that the workpiece can withstand these forces without excessive deformation; also, machine tools can be designed to minimise component distortion. Cutting force is typically measured using a force transducer, dynamometer or load cell. Cutting force can also be determined from the power consumption; however, the mechanical efficiency of the machine tool should be known. The contact stresses at the tool-chip and tool-workpiece interfaces are determined by the cutting force (Astakhov, 2004)

The vibration level in machining depicts the health of machine tool and the state of the machining operation. Various rotating parts such as spindle, tailstock, and gears; linear translation parts such as feed carriage, and compound rest produce vibration. Shearing of chips, the flow of chips over the tool, and rubbing of the flank face with the workpiece also generate vibration. Vibration measurement in machining can identify tool faults and monitor the machining quality. Fault diagnosis of the cutting tool and

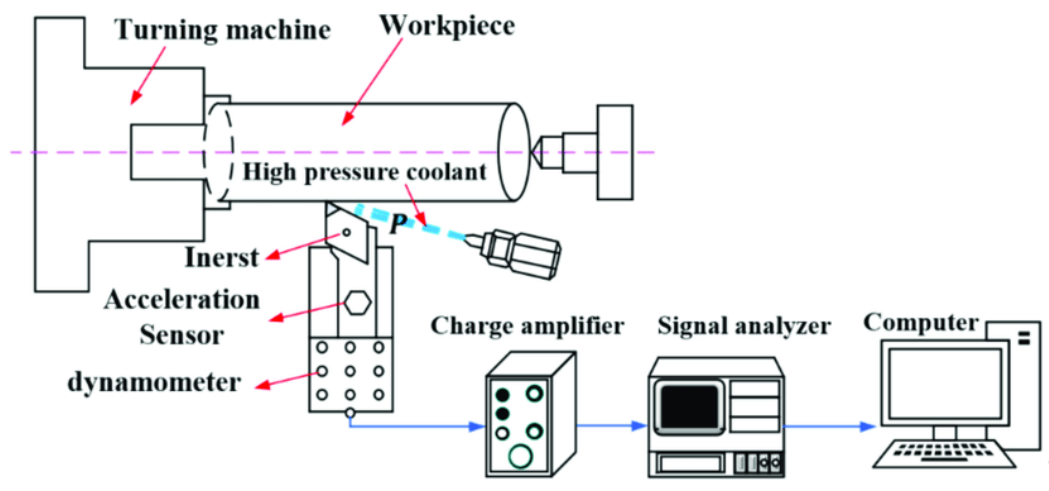


Figure 1.2 Typical force and vibration measurement system for turning operation as illustrated by Zhang et al. (2021).

surface finish produced on the workpiece can be monitored using the vibration signal. Accelerometer is employed to monitor the vibration. Digital signal processing and analysis are required to diagnose the tool faults and surface finish. Figure 1.2 shows a schematic of force and vibration measurement in turning operation using a dynamometer and accelerometer illustrated by Zhang et al. (2021).

Self-excited chatter vibrations usually result from a dynamic instability of the cutting process (such as cutting with large tool-work engagements. They are most harmful to any machining process. Free and forced vibrations can be easily identified, and vibration sources can be eliminated, but chatter vibrations are difficult to control. It is crucial to suppress vibrations of the machine tool structure as their presence results in poor surface quality, unacceptable inaccuracy, tool wear and machine tool damage (Siddhpura and Paurobally 2012). Indeed, the most common cases in the literature



usually involve facing operations where the tool vibrates in the feed direction (called type A chatter by Tobias et al.). However, there is another type of chatter (type B chatter) where the cutting edge vibrates parallel to the cutting speed direction or a component in this direction. Type A chatter arises for short overhangs, generally in the radial direction, whereas type B chatter occurs for large tool overhangs, as shown in Figure 1.3.

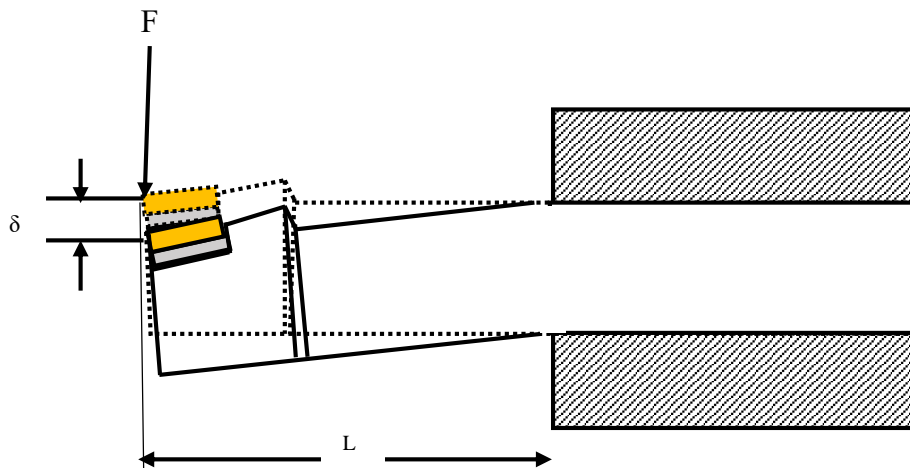


Figure 1.3 Tool deflection at the tip due to cutting force (Quintana and Ciurana 2011)

#### 1.4 STABILITY LOBE DIAGRAM (SLD)

The stability lobe diagram is a chart plotted between depth of cut (DOC) and spindle speed showing the stability boundary lines (shown in Figure 1.4) (Vnukov et al. 2017). The area inside the lobe is unstable, the area outside is stable, and points on the

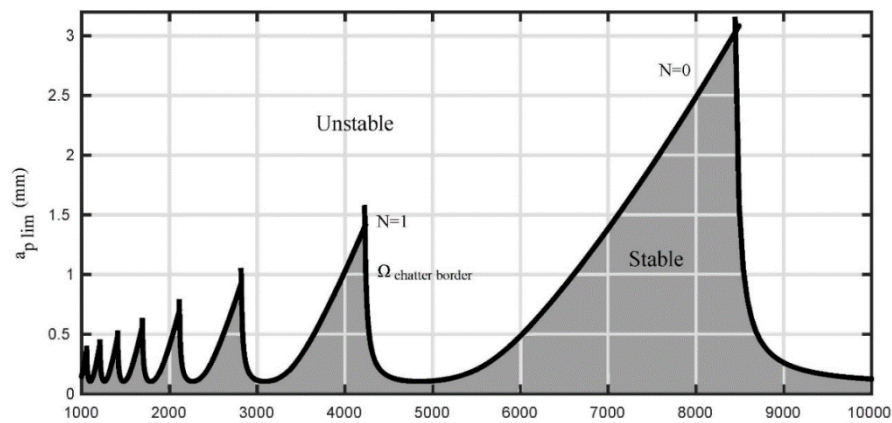


Figure 1.4 Classical stability lobe diagram (Vnukov et al. 2017)

boundary are conditionally stable which marks the chatter boundary. SLD is useful in improving the material removal rate (MRR) without chatter and knowing the limiting depth of cut for a particular spindle speed. This thesis addresses the improvement of the stability regime with an external damper, which increases the limiting DOC.

## **1.5 TOOL LIFE: WEAR AND FAILURE**

Tool geometry is an important parameter that influences chip flow, machining productivity, tool life and surface quality of machining. Hard turning is best accomplished with cutting inserts made from either coated tungsten carbide, CBN (Cubic Boron Nitride), Cermet or Ceramic (Shihab et al. 2014). Coated carbide inserts are the best option, provided the workpiece material is uniformly hard. Indexable inserts have proven effective compared to brazed tool holders or high-speed steel because of their replicability, additional hard coating, and chip-breaking geometry (Alok et al. 2021).

Tool wear is inevitable during machining; however, it should not obstruct machining. Tool life prediction by conventional methods, like using Taylor's tool life equation and modified Taylors tool life equation, fails to predict the tool life accurately due to assumptions that are not so practically feasible (Salonitis and Kolios 2014). Various types of tool wear observed in machining are (a) Crater wear (b) Flank wear (c) Built up edge (d) Chipping (e) Breakage.

These could be categorised as progressive wear or irregular wear. Irregular wear leads to catastrophic failure. Tool wear affects (a) Machine vibration and chatter (b) Surface finish (c) Tool life (d) Power consumption (e) Dimensional accuracy. Most tool wear tests are done under stable cutting conditions, which can't explain how the tool wears when the cutting is vibrating. In the current study, the author tries to figure out how a turning tool will wear and how long it will last when there are chatter and damped vibrations.

Condition monitoring ensures a 100% guarantee of quality and productivity. Tool condition monitoring is achieved by employing a sensor or sensors system, which

acquires real-time information about the tool condition. The sensor signals are post-processed to diagnose the condition of the tool.

## **1.6 TOOL FAULT DIAGNOSIS BY SIGNAL PROCESSING**

One of the significant tool failures is due to chattering. It reduces tool life and leads to early tool failure. A healthy or faulty tool produces a characteristic frequency, which could be harmonic or non-harmonic frequency. Chatter frequency helps to monitor the stability of the machining process. Locating the tool fault by its frequency component at the time it has occurred is recognised using wavelet analysis. With this, one can identify the origin of a fault at a time with its magnitude.

### **1.6.1 Time domain analysis**

The signals are recorded in the time domain and analysed in how a signal changes with time. An oscilloscope may be used to visualize the time series data. Statistical parameters such as RMS, mean, median, kurtosis, skewness, and many more could be used to monitor the signal in the time domain. A faulty tool would produce more peaks than a healthy tool. Similarly, each fault produces distinctive time-domain signatures. Keeping track of these parameters is known as signal processing through time domain analysis. Although the statistical measures indicate the presence of a fault, they do not provide any information about the type of that fault. Although the statistical measurements point to the existence of a fault, they do not offer any information regarding the nature of that fault.

### **1.6.2 The spectrum analysis**

In signal processing, analysing a signal in frequency component rather than time domain is called frequency domain analysis. A given time domain signal is converted to a frequency domain by applying a mathematical operator known as Fourier transform. The signal after the transform is called the spectrum of frequency components (Akan and Karabiber Cura 2021).

### **1.6.3 The cepstrum analysis**

Cepstrum is a tool that can be used to look at periodic patterns in frequency spectra (Norton and Karczub 2003). These effects are caused by echoes or reflections seen in the signal or by harmonic frequencies. It deals with the mathematical problem of deconvolution of signals in frequency space. A cepstrum is a forward Fourier transform of the logarithm of a spectrum. Given an actual signal, various cepstrum forms can be evaluated, namely real cepstrum analysis, the complex cepstrum analysis, and the power cepstrum of a signal to reveal the periodicity in the frequency domain.

### **1.6.4 Short-time Fourier transform**

In signal processing, time–frequency analysis studies a transient signal in both the time and frequency domains simultaneously. Classical Fourier analysis assumes signals are infinite in time or periodic, although many signals are short-lived and vary in intensity. Short-time Fourier transform (STFT) is a refinement of Fourier analysis, while wavelets are more advanced for unevenly spaced data.

### **1.6.5 Wavelet analysis**

Wavelets, which mean "little waves," are small oscillating waveforms that start at zero, develop to their highest point, and then quickly return to zero. Wavelet analysis provides the frequency component and its location on the time strap with a magnitude of frequency. Wavelet transform is an effective tool for damage localisation. This technique has been used to diagnose faults in bearing, gears and cutting tools.

### **1.6.6 EMD**

A complex and multiscale signal can be adaptively decomposed into a sum of a limited number of zero mean oscillating components known as Intrinsic Mode Functions (IMF) using the effective analytical technique of empirical mode decomposition. IMF records the signal's repetitive behaviour at a specific time frame. The EMD breaks down a time signal into a collection of basis signals similar to the Fourier or wavelet transforms; however, unlike those transformations, the basis functions are obtained directly from the data.

## **1.7 TOOL FAULT DIAGNOSIS BY MACHINE LEARNING**

Machine learning is programming computers to optimize a performance criterion using example data or past experience. The model is defined up to some parameters and learning is the experience execution of a computer program to optimize the model's parameters using the training data or past experience. The model may be *predictive* to make predictions in the future or *descriptive* to gain knowledge from data or both (Roy et al. 2022).

Machine learning uses the theory of statistics in building mathematical models because the core task is making inferences from a sample. Diagnostic tools play the important role of classifying the previously acquired and processed signals in a tool vibration control system and taking quick and precise decisions. Machine learning employs three basic steps for implementation: feature extraction, feature selection and classification, which is briefly explained using Figure 1.5.

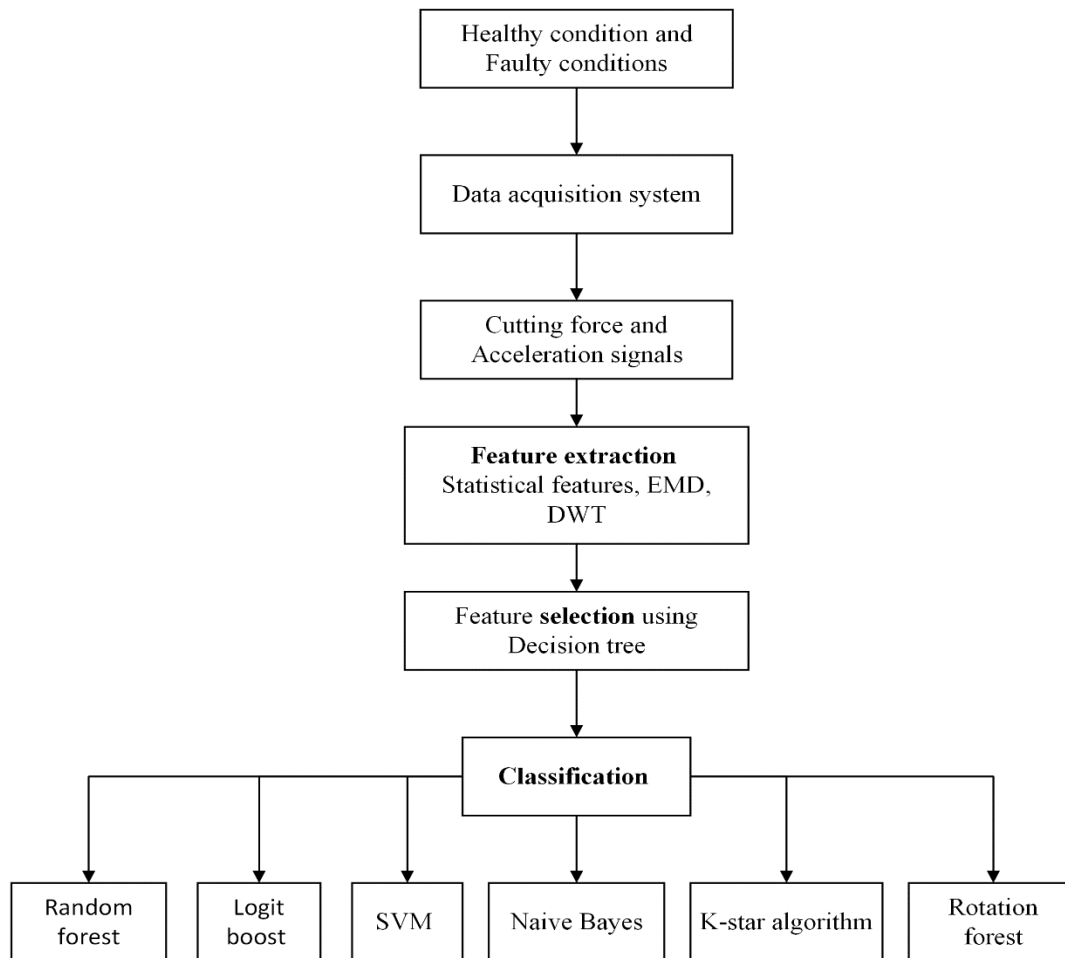


Figure 1.5 Flowchart of the Machine learning for fault classification (Ravikumar et al. 2019)

### 1.7.1 Feature extraction

The technique of converting raw data into numerical features that can be handled while keeping the information in the original data set is known as feature extraction. It produces accurate outcomes compared to using machine learning on the raw data directly. Identification and depiction of the characteristics pertinent to a particular condition are necessary for manual feature extraction. Knowing the domain can often aid in deciding which characteristics might be helpful. Engineers and scientists have created feature extraction techniques for images, signals, and text through many years of research. Signals are analysed to determine a signal's unique properties in the time, frequency, and time-frequency domains.

### **1.7.2 Feature selection by using a decision tree**

Using only a portion of the measured characteristics, feature selection minimizes the data dimensionality. Feature selection enables improved prediction performance, quicker and more affordable predictors, and a better understanding of the data (Guyon and Elisseeff 2003). Even when all features are significant, too many features can reduce prediction performance.

A decision tree consists of several branches, one root, several nodes and many leaves. One branch is a chain of nodes from the root to a leaf, and each node involves on an attribute (Peng et al. 2009). In real-world applications, decision trees provide a set of valuable features that can significantly improve a model's forecast accuracy.

### **1.7.3 Classification**

A classification algorithm is a supervised machine learning which "learns" to categorise new observations using previously trained data. The training data set is labelled data through which the algorithm learns to classify the observations into a number of classes such as 'yes or no', and 'spam or not spam'. The output of the classification is a category, not a value. Labelled dataset refers to input data set with corresponding known output, i.e. output (y) function is mapped to input variable (x).

The Classification algorithm's primary purpose is to determine the category of a given dataset, and these algorithms are primarily used to anticipate the output for categorical data.

## **1.8 CHATTER VIBRATION DUE TO TOOL WEAR**

During chatter vibration, the frictional force acting when the flank surface of a tool contacts the workpiece is critical in the supply of vibratory energy. Chatter stability decreases as tool wear flat of the cutting tool increases. However, some other aspects of damping of cutting tool chatter vibration due to tool wear must be investigated.

## 1.9 TOOL VIBRATION MODEL

The cutting tool in turning is modelled as an Euler Bernoulli's cantilever beam of a single degree of freedom system with stiffness  $k$  and internal damping coefficient  $c$  excited by a harmonic force  $F(t)$  at the free end. The response of the beam in the form of displacement or acceleration is analysed for varying input excitation, damping and stiffness. The chatter marks of  $\delta x$  are produced on the machined surface with  $\delta y$  deflection in a tangential direction, as depicted in Figure 1.6.

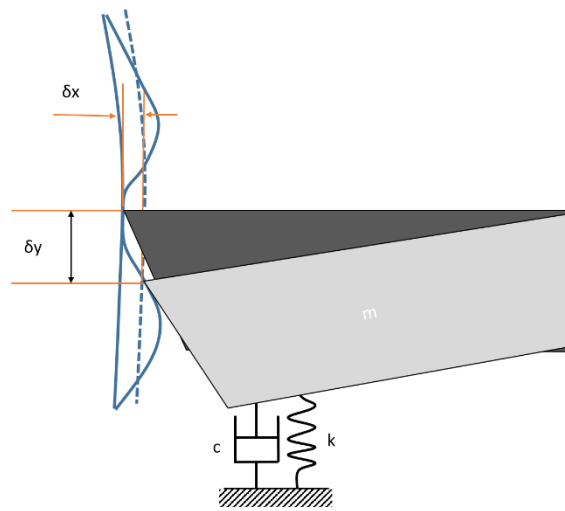


Figure 1.6 Tool vibration model in tangential direction (Urbikain et al. 2013)

## 1.10 VIBRATION SUPPRESSION TECHNIQUE

The chatter in machining is a well-known issue that reduces productivity. (Taylor 1906) noted that "chatter is the most mysterious and sensitive of all issues confronting the machinist." (Tobias and Fishwick 1958), and (Tlusty and Polacek 1963) identified the regeneration effect as the primary cause of chatter. Since then, one of the key problems has been the suppression of these self-excited vibrations, and the current situation implies that the prediction and suppression of chatter will continue to be an important issue in the future. Some techniques followed to suppress the chatter are development of special tools (Stone 2014) such as variable pitch tools (Shaw, M. C., et al. 1952), helical tools (Stone 1970; Vanherck 1967) and serrated tools (Stone 2014) that perturb the regenerative effect and process damping.



An un-damped tool vibration can be modelled as a single degree of freedom model, as shown in Figure 1.7 (Rao 2010).

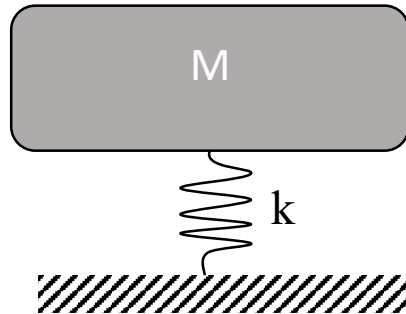


Figure 1.7 Undamped single degree of freedom model (Rao 2010)

Chatter can be avoided effectively by making the structure, tool, and/or part of the machine tool stiffer. If only one dominant mode is considered, the static stiffness and modal stiffness are the same, and increasing it makes the process more stable. When the static stiffness increases, the damping might decrease (Koenigsberger and Tlustý 1970). Hence increasing only stiffness by adding additional mass makes the machine tool bulky, requiring increased drive power to move the carriage or cross slide. At the same time, incorporating a damping mechanism ensures stable operation. There are three methods vibration suppression by external damping methods: passive, active, and semi-active.

### 1.10.1 Passive damping techniques

Increase the damping of the critical mode with passive solutions that don't need an outside power source to get rid of vibration energy. One can use passive damping techniques such as tuned mass dampers (Hahn 1951), impact dampers (Edhi and Hoshi

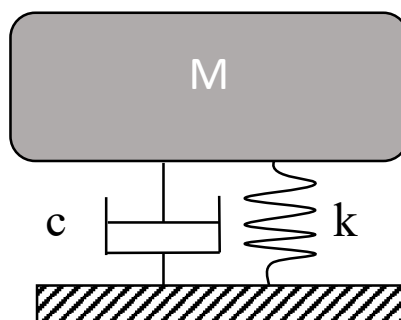


Figure 1.8 Tuned mass damper as a passive damping technique (Rao 2010)

2001), and installing internal damping materials (Kolluru et al. 2013). Figure 1.8 shows the passive damped tool model (Rao 2010).

Using a linear spring with stiffness and damping, passive damping adds inertial mass to the system to dampen chatter. These parameters' values are adjusted to reduce chatter by the original system's critical mode. The original mode is consequently split into two modes with dynamic rigidity. The passive damping reliability and ease of use are two of their most remarkable features. However, the passive damping benefits are restricted to a specific frequency range and need precise tuning to the intended frequency.

### 1.10.2 Active damping techniques

Active approaches measure a vibration-related parameter, process it, and then introduce a regulated force signal via an actuator in response to the measured signal. In this manner, the vibratory component receives extra force,  $F$ , that is dynamically connected

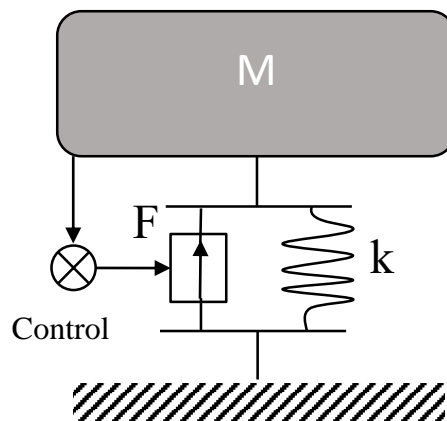


Figure 1.9 Active damped tool model  
(Preumont 1997)

through a control and a sensor (Preumont 1997), as shown in Figure 1.9. Piezoelectric and electromagnetic actuators, which have proven to be reliable, are the most commonly utilised technologies in active systems (Neugebauer et al. 2007) (Sims et al. 2005). There have also been other smart materials and fluids (electrorheological & Magnetorheological) primarily utilised in semi-active devices, which are essentially passive devices with real-time property tuning but cannot directly supply a mechanical force.

### 1.10.3 Semi-active damping techniques

Semi-active damping techniques are similar to passive damping techniques with provision to change the damper's properties such as the damping medium's viscosity as in magnetorheological and electrorheological fluids. The tool model attached with the variable damping coefficient is shown in Figure 1.10 (Pour and Behbahani 2016). This semi-active system performs with minimal power requirement and simple control. The semi-active system works as a passive system in case of power failure, unlike stalling of the active system during operation.

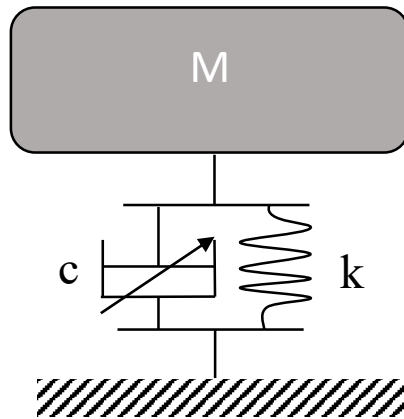


Figure 1.10 Semi-active damped tool model  
(Pour and Behbahani 2016)

## 1.11 MAGNETORHEOLOGICAL FLUID

Magnetorheological (MR) fluid and Electrorheological (ER) are smart materials whose rheological properties are very responsive to magnetic and electric fields, respectively. MR fluid consists of ferromagnetic particles suspended in a carrier fluid. MR fluid can produce maximum yield strength of 50-100 kPa in magnetic fields strength of 150-250 kA/m (Kciuk and Turczyn, 2006). Further, since the magnetic polarization mechanism is unaffected by temperature, the performance of MR-based devices is relatively insensitive to temperature over a broad temperature range. Figure 1.10 show changes in rheological properties in the absence and presence of a magnetic field. When fluid is exposed to the magnetic field, ferrous particles in the fluid form chain-like structure in the direction of the applied field, and the fluid tends to form a semisolid material in a

few milliseconds, which creates resistance against the fluid flow. This effect is completely reversible when the magnetic field is removed.

A typical MR fluid consists of 40-90 % by weight of relatively pure (1-10 micron diameter size) magnetisable particles suspended in a carrier liquid such as mineral oil, synthetic oil, water or glycol. Varieties of proprietary additives, similar to those found in commercial lubricants, are commonly added to MR fluids to enhance lubricity, modify viscosity, inhibit particle wear, delay gravitational settling, and promote particle suspension. MR fluid is used in various applications such as dampers, brakes, clutches, hydraulic valves, seals, flexible fixtures, pneumatic actuators and polishing devices (Wang and Meng, 2001). The MR fluids can be used in three different operating modes based on the different engineering applications. They are Squeeze mode, Shear mode and Valve mode.

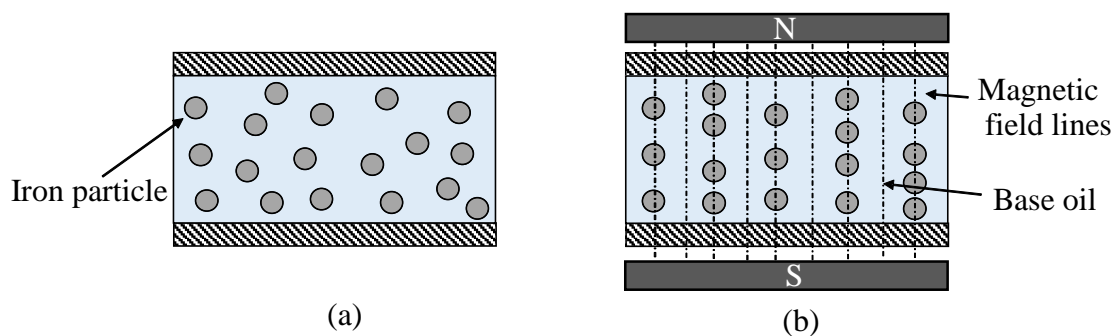


Figure 1.11 Behaviour of MR fluid a) In the absence of magnetic field b) In the presence of magnetic field (Kciuk and Turczyn, 2006)

### 1.11.1 Squeeze mode

In squeeze mode, the fluid is between two moving poles. Relative displacement is perpendicular to the direction of the fluid flow (Figure 1.12). The compression force applied to the fluid periodically varies. Displacements are small compared to the other modes, but resistive forces are high. This mode is used mainly in bearing applications (rong et al. 2013).

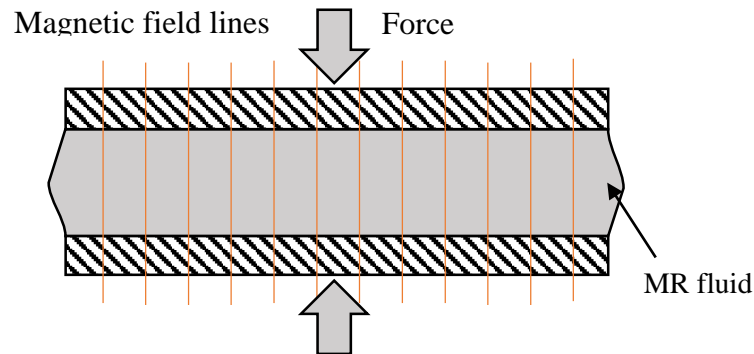


Figure 1.12 Squeeze mode (rong et al. 2013)

### 1.11.2 Shear mode

In shear mode, the fluid is located between a pair of poles in which one is stationary and the other slides with the first pole. The magnetic field is applied perpendicular to the direction of the shear poles (Figure 1.12). This mode of operation is suitable for clutches, brakes, and locking device applications.

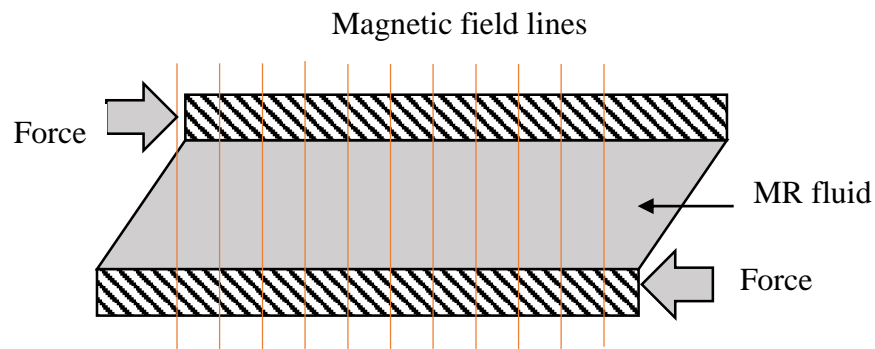


Figure 1.13 Shear mode (Spaggiari 2012)

### 1.11.3 Flow mode

In flow mode, the fluid is located between stationary poles. Flow between the plates occurs due to pressure drop. Resistance to the fluid flow is controlled by modifying the magnetic field between the poles in a direction perpendicular to the flow (Figure 1.13). Devices using this mode of operation include servo-valves, dampers, shock absorbers and actuator applications (Spaggiari 2012).

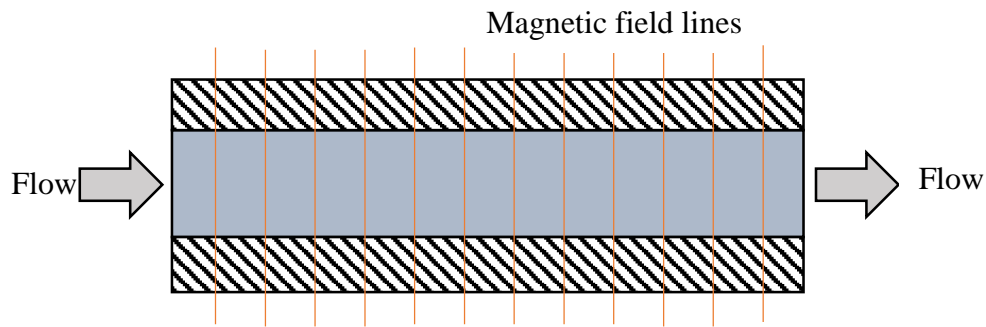


Figure 1.14 Flow mode (Spaggiari 2012)

MR fluid has been used for many applications, such as MR brakes, MR clutches, MR flow valves, and linear and rotary dampers. The rotary damper finds application in prosthetic knee, whereas linear damper finds application in vehicular suspension and civil structural damping subjected to seismic excitation. The variable coefficient of the MR damper makes it suitable to adapt to road conditions and ride comfort in the vehicular applications.

Servo-valves, dampers, and shock absorbers are a few examples of devices that operate in the pressure driven flow mode. Devices that operate in the direct-shear mode include clutches, brakes, chucking, and locking mechanisms. Squeeze-film mode, a third mode of operation, has also been applied in low motion, high force application (Spaggiari 2012).

### 1.12 MAGNETORHEOLOGICAL DAMPER

A magnetorheological damper is a semi-active device filled with magneto rheological fluid. In MR dampers, the magnetic field's action on the MR fluid controls the damping force. This allows the damping characteristics of the damper to be continuously controlled by varying the magnetic field. The construction of an MR damper is quite similar to the conventional hydraulic damper. Along with the typical configuration of the viscous dampers, MR dampers have an iron core with copper windings fitted to the piston. Leads of the windings are connected to a direct power (D.C) source. Because of road undulations, the hollow piston head moves inside the cylinder, a supply of electric current will magnetize the iron core and ferromagnetic particles dispersed in the fluid will align along the lines of magnetic flux, increasing the apparent viscosity of the fluid.

The MR dampers can be classified as monotube, twin tube and double rod end MR dampers.

### 1.12.1 Mono tube MR Damper

Mono tube MR damper consists of a single reservoir for MR fluid. Accumulator to accommodate the volume displaced by piston rod movement. The accumulator piston provides a barrier between MR fluid and compressed gas/compressed spring, as shown in Figure 1.14 (Gurubasavaraju et al. 2017).

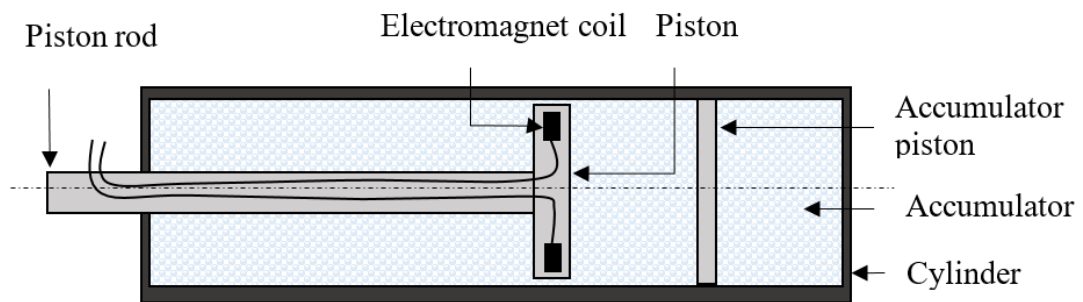


Figure 1.15 Monotube MR Damper with an accumulator (Gurubasavaraju et al. 2017)

### 1.12.2 Twin tube MR damper

The Twin tube MR damper (Figure 1.15) consists of two cylinders, namely the inner cylinder and the outer cylinder. The inner housing guides the piston rod during extension and compression, similar to the mono-tube damper. During piston compression, MR fluid is displaced from the inner cylinder to the outer cylinder through the base valve provided at the bottom of the inner cylinder (Desai et al. 2021).

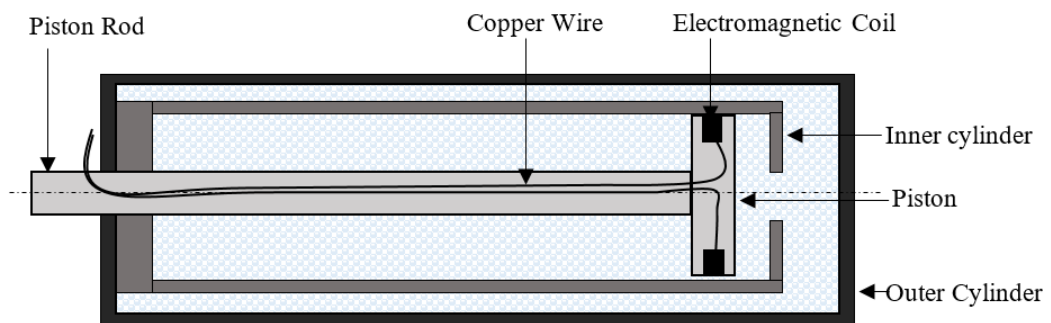


Figure 1.16 Twin tube MR damper (Desai et al. 2021)

### 1.12.3 Double rod end MR damper

Double-ended type MR damper consists of a piston rod of equal diameter that extends from both the ends of the damper housing, and in this damper, there is no change in volume as the piston moves and it does not require an accumulator mechanism as shown in Figure 1.16 (Poynor and Reinholtz 2001).

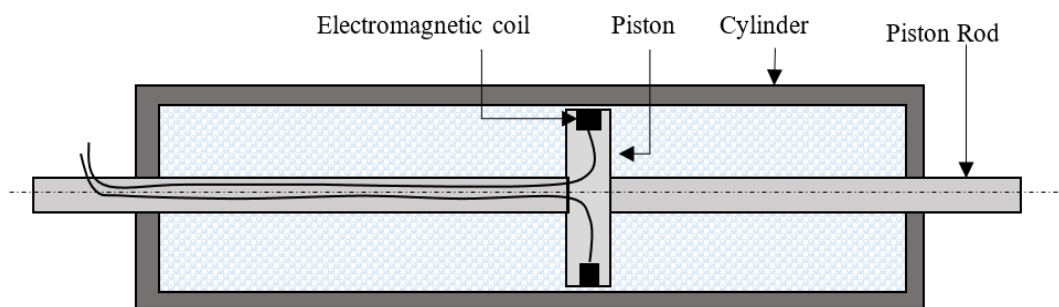


Figure 1.17 Double rod end MR damper (Poynor and Reinholtz 2001)

### 1.13 MODELLING MR DAMPER

Variable damper plays a key role in the control of semi-active suspension system. Designing and analysis of the suspension system controller requires an accurate model of the damper. A practical damper exhibits non-linearity and hysteresis, which must be taken into account in simulation studies in order to investigate the real-time system performance. Modelling of the dampers can be broadly classified into two categories: (a) Parametric modelling (b) Non-parametric modelling

In the parametric modelling approach, the damper is represented as an interconnection of mechanical elements like springs and dash pots. Parameters of the model are obtained through experimental results and mathematical methods. A number of parametric models have been proposed in the literature to describe the dynamic behaviour of MR damper. Some of the widely used models are: (a) Bingham model (b) Bouc-Wen model (c) Modified Bouc-Wen model (d) Kwok model

Non-parametric modelling describes the behaviour of the damper by analytic expressions that give the result close to experimental results. Non-parametric models



need a large amount of data to model the system. Non-parametric modelling methods are robust and can be applicable to linear, non-linear and systems with hysteresis. Non-parametric models can be classified as follows: (a) Polynomial-based techniques (b) Neural network-based methods

## 1.14 CONTROL STRATEGIES

An automatic controller, in general, compares the actual output of a plant with that of the reference input and produces a control signal that will reduce the deviation between the actual and desired values to zero or a small value. The controller detects the actuating error signal, which is usually a very low power level and amplifies it to a sufficiently high level via the current amplifier for MR devices. In this section, some effective control methodologies for tool vibration application featuring MR damper is proposed.

### 1.14.1 Semi-active control

Using MR devices, the damping of the system can be continuously controlled by controlling the intensity of the applied field. The desired damping force can be achieved in the controllable domain regardless of the velocity. This is a salient feature of the semi-active control system activated by MR devices. To achieve the desired damping force in the controllable domain, one can use three semi-active control methods: skyhook, ground hook, neuro-fuzzy and PID controllers. The logic of the skyhook controller (Wang et al. 2010) is simple and easy to implement in an actual field. The desired damping force,  $F_d$ , can be set by

$$F_d = C_{sky}(E)x' \quad (1.1)$$

Where  $C_{sky}$  is a control gain that physically indicates the damping. The magnetic field can judiciously tune the control gain to meet the desired damping force. In practice, the control gain can be chosen by on-off logic as:

$$C_{sky} \text{ is maximum, } x' > 0 \quad (1.2)$$

$$C_{sky} \text{ is minimum, } x' \leq 0 \quad (1.3)$$

The above logic of the controller is typically adopted for the vehicle suspension systems (Seung-Bok and Young-Min 2013). High and small damping can be controlled by just controlling the magnetic field without using the directional check valve. The skyhook control method is typically used to isolate the vibration of the sprung mass directly connected to the ground. Ground hook controller can isolate the vibration of unsprung mass, which is directly connected to the ground (Seung-Bok and Young-Min 2013).

Semi active dampers can also be controlled via proportional-integral-derivative (PID) control. The transfer function in the frequency domain serves as the basis for the linearized mathematical model of the semi-active suspension system. The performance of the PID-controlled system is determined by how accurately the linear model predicts the system's actual behaviour. A PID controller can be created by choosing appropriate gains for the proportional, integral, and derivative terms. Several tuning techniques are available to construct a PID controller and get the desired performance from the semi-active system (Talib and Darus 2013).

The fuzzy control algorithm is effective for uncertain systems. It should be noted that certain vehicles have displacement sensors built right into the suspension system. In this case, the fuzzy controller might operate successfully without additional sensors. In other words, the MRF-based suspension could be efficiently controlled by the suggested control algorithm with fuzzy steps utilising just one sensor, not increase hardware costs or system complexity (Phu et al. 2015).

The on-off control theory refers to the control system used to control such elements where the control element has only two positions: fully closed or fully open. This control element does not function in any intermediate position. When a tool vibration changes and crosses a certain pre-set level in this control system, the output value of the system is suddenly fully opened and gives total current or fully closed to 0 A. In theory, we assume there is no time delay for control equipment to be turned on and off. However, in practise, there is always a non-zero time delay for controller elements' closing and opening action.

## 1.15 ORGANIZATION OF THE THESIS

**Chapter 1** introduces various signal processing and machine learning techniques used in this thesis—a brief introduction on chatter vibration induced in hard turning process and various ways to control them.

**Chapter 2** reviews the literature on recent developments in controlling tool vibration, the advantages of signal processing and its application in various engineering applications. The machine learning algorithm is applied to various engineering applications such as machining and machinery fault diagnosis. Various developments are discussed in controlling the tool vibration by passive and semi-active methods.

**Chapter 3** illustrates the methodology followed to achieve the overall research objectives. The method to accomplish each objective is also shown as a flowchart with a brief explanation.

**Chapter 4** identifies and diagnoses the tool faults using signal processing and machine learning techniques. Time domain, frequency domain and wavelet transform are the various signal processing used to identify tool faults using vibration and cutting force signals. Machine learning techniques, such as the rotation forest algorithm, random tree and the Naïve Bayes algorithm with statistical and discrete wavelet features, are used for tool fault diagnosis.

**Chapter 5** deals with the design configuration and development of a mono-tube shear mode external mounted magnetorheological fluid damper to suppress the tool vibration. The preliminary study on fault diagnosis helps identifying the design input parameters and materials for the development of the MR damper. The optimal composition of in-house magnetorheological fluid for the developed MR damper is synthesised and characterised.

**Chapter 6** describes the implementation of the developed MR damper on the lathe machine to evaluate its ability to suppress the tool vibration using optimal MR fluid prepared in-house and commercial fluid. Online tool vibration control is ensured by implementing a current controller while monitoring the real-time vibration signal. The

amplitude of the tool vibration, surface finish, tool wear and stability boundary of the machining are evaluated with and without MR damper

**Chapter 7** establishes the development of an internally damped MR tool holder. A free vibration test, force vibration test and actual machining test was performed to evaluate the tool holder's vibration-damping ability.

**Chapter 8** concludes the research findings on tool fault diagnosis, MR damper and its machining performance in controlling the tool vibration with constant current and controller current.

## **CHAPTER 2**

### **LITERATURE SURVEY**

#### **2.1 INTRODUCTION**

Modern machining processes depend heavily on tool defect diagnosis to provide automation and precision manufacture with little human involvement. Automation promotes productivity and efficient job-handling ability. Cutting tool malfunction diagnosis is made possible via online tool condition monitoring. A sensor is employed to acquire information on the tool's condition. The sensor data will be in raw form, which must be processed using a signal processing technique to derive useful information about the tool fault.

Tool wear influences vibration during machining, which directly impacts tool life, productivity and accuracy of the machined component in any machining process. In the past few decades, many researchers have investigated the origin of chatter and developed various mathematical models to clearly understand the factors more influential on machining vibration. The literature survey in this chapter covers work by various researchers on tool fault diagnosis, tool vibration, magneto rheological fluid, use of MR damper in reducing the tool vibration, optimization of MR damper, controller and control strategy employed to control the damping force of MR damper of various application.

#### **2.2 VIBRATION IN MACHINING OPERATION**

Vibration in machining can be categorised as forced vibration and self-excited vibration, or chatter vibration. The causes of this vibration are improper cutting conditions, higher MRR, faulty tool conditions and hard-to-machine workpiece materials. The characteristics of these vibrations are the generation of poor surface finish, shrill noise, increased tool wear, and reduced tool life. Taylor (1906), who conducted a profound study on the cutting process, developed the cutting force model and stated that chatter is a delicate and catastrophic phenomenon in turning. Urbikain

et al. (2013) demonstrated the generation of surface roughness on the machined parts due to the cutting tool's tangential movement due to the tool holder's low flexion. The depiction of the surface roughness due to a slender tool is shown in Figure 2.1.

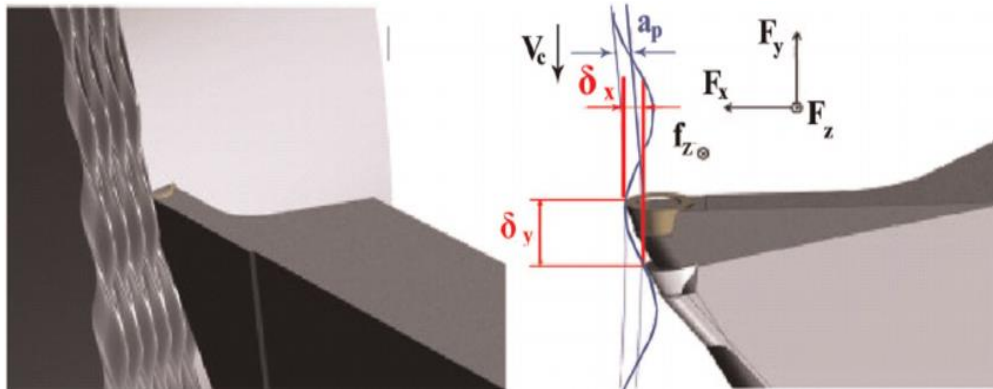


Figure 2.1 Vibration in tangential direction during longitudinal turning (Urbikain et al. 2013)

### 2.3 A VIBRATION LIMITING CHART - SLD

Merritt (1965) introduced the stability lobe diagram (SLD). It is a graph of spindle speed on abscissa and depth of cut on the ordinates. SLD represents the region of the stable and unstable regions to mark chatter-free and chatter conditions, respectively. Figure 2.2 shows typical SLD for turning operation as demonstrated by Merritt in 1965 in their article. Díaz-Tena et al. (2013) investigated the milling of thin floor parts with the aid of an MR damper, where the effect of tool trajectory on damping coefficient, rigidity,

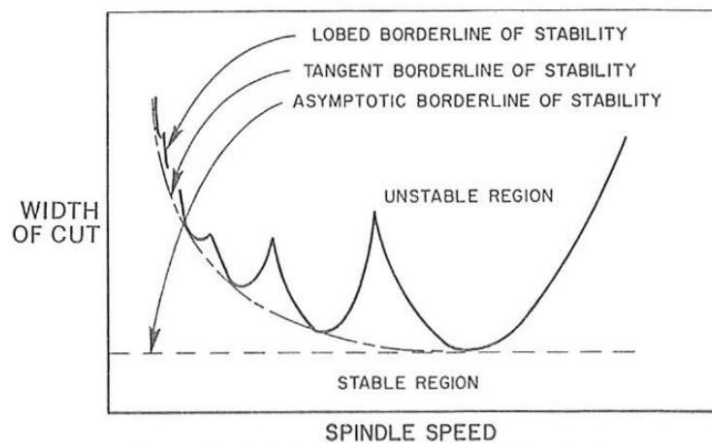


Figure 2.2 A typical stability lobe diagram. Merritt (1965)

the frequency was studied. A three-dimensional stability lobe diagram (SLD) showed that a machining speed of up to 24,000 rpm could be used to machine thin plates. A stability lobe diagram has been obtained in the current study through analytical calculation and validated by experimental study.

## **2.4 VIBRATION INDUCED DUE TO FAULTY TOOL**

A faulty tool induces undesired vibration that leads to poor surface finish and instability in machining. Each fault produces unique vibration characteristics; however, when multiple faults are induced, it is difficult to identify them through basic signal processing. Arizmendi et al. (2009) showed that tool vibrations during the cutting process are one of the elements that significantly impact the machined surface and can degrade its quality. Thomas et al. (1996) collected and evaluated surface roughness and tool vibration data from dry-turning mild carbon steel. According to vibration analysis, the dynamic force caused by a change in chip thickness acting on the tool is related to the amount of vibration the tool makes while cutting at its natural frequency.

## **2.5 SENSORS AND TRANSDUCERS FOR FAULT DIAGNOSIS**

Most down time in machining is caused due to tool breakage and tool handling. The only technique that is viable in reducing the down time during machining is Tool Condition Monitoring (TCM). TCM involves monitoring tool health status by acquiring real-time tool condition information using sensors and transducers such as an accelerometer (Ghule et al. 2017), dynamometer (Lyu et al. 2021), acoustic emission (AE) sensor (Kishawy et al. 2018) current sensor (Song et al. 2020), surface profiler (Muhammad et al. 2021), pyrometer (Kus et al. 2015) and charge-coupled device (CCD) camera (Wu et al. 2019). The cutting tool's condition monitoring (CM) is necessary to ensure efficient machining operation with minimal tooling costs and downtime. Tool fault diagnosis is one method of CM. Cuka and Kim (2017) performed embedded tool condition monitoring of the end milling tool with the signals acquired from the dynamometer, microphone, accelerometer and current sensor using a machine learning technique. The signal-to-noise ratio of a microphone is the least as monitoring the sound signal is influenced by external disturbances, and the bandwidth of that disturbance may lie in the same bandwidth of interest. Current sensors are the least

sensitive to minimal changes in the machining process. The current change is observed only when there is a difference in load than process changes.

### 2.5.1 Milling

Milling is also the most widely used machining process which requires condition monitoring for efficient machining. Hesser and Markert (2019) retrofitted an old CNC milling machine to monitor tool wear by embedding a programmable sensor (Bosch XRD sensor platform) that sends the machining process's vibration information through a wireless communication mode. Two tool conditions, healthy and worn tools, were considered for the study. Ramirez-Nunez et al. (2018) used infrared thermography to monitor tool breakage during the milling process under dry and wet conditions. A tool's healthy state or broken state is determined by analysing temperature gradients in the cutting zone. The flow process of the CM is shown in Figure 2.3. Cutting fluid surrounding the tool forms the barrier for direct measurement. Ryabov et al. (1996) used a laser sensor which reconstructs 3D image of milling tool profile with laser displacement and intensity technique to evaluate geometric failures of tool. The

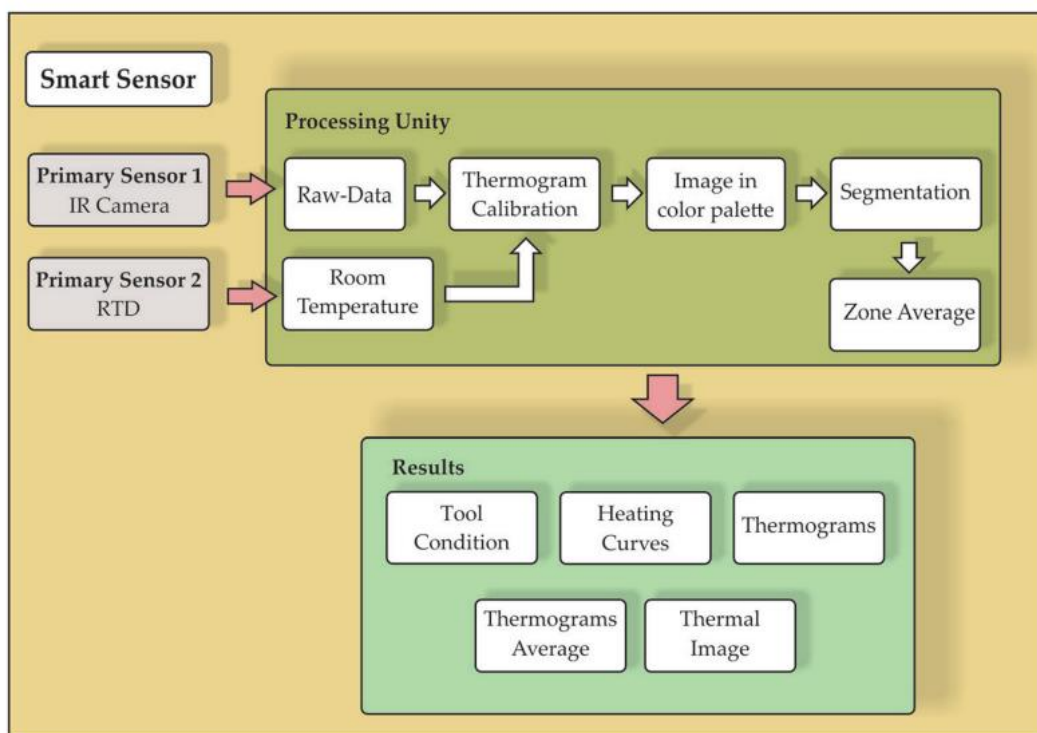


Figure 2.3 Fault diagnosis using thermal imaging (Ramirez-Nunez et al. 2018)



technique was able to detect the location of tool chipping and length of flank wear at an accuracy of 40 micron. Figure 2.4 shows healthy tool and worn tool through image

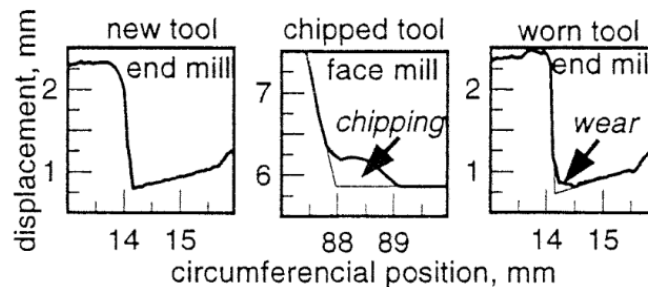


Figure 2.4 Geometric image of milling cutter in different condition (Ryabov et al. 1996)

processing. The image shows the scale to measure the area of wear land. These days, indirect method of tool wear monitoring is found to be more effective for online monitoring of machining operation with advancement of signal processing, image processing and artificial intelligence.

### 2.5.2 Turning

This section deals with sensors and transducers employed to turn operations for fault diagnosis. Jurkovic et al. (2005) used a CCD camera to create a 3D image of the relief surface to measure the tool wear of carbide inserts in turning operation. The technique had the characteristic of measuring the profile depth with the help of projected laser light using a diode and linear projector. Dimla (2002) followed experimental and analytical methods to independently correlate tool wear with measured vibration signal and cutting force signal for turning operation. The z-direction of the cutting force and vibration signal was found to be sensitive to tool wear. Bhuiyan et al. (2014) conducted an experimental investigation to monitor tool abrasion, surface finish and chip formation using an accelerometer and acoustic emission sensors in turning operation. Figure 2.5 shows the schematic of the experimental setup established for the CM of turning operation by Bhuyian et al.(2014). Schmitt et al. (2012) employed a machine vision system to measure tool wear and classify them by neural network based on an active contour algorithm. Tools were held in the special fixture for image acquisition of tool wear. Image processing chain comprised feature extraction, classification and tool wear measurement.

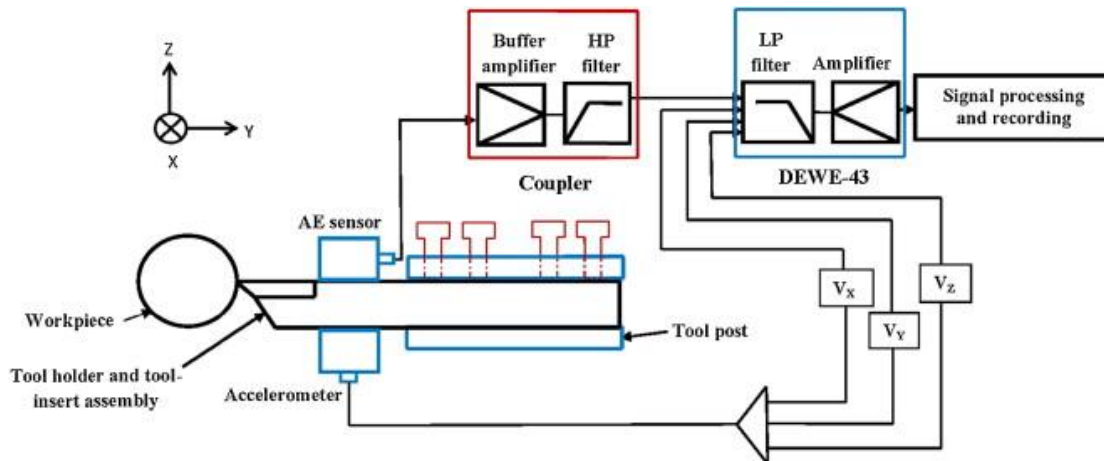


Figure 2.5 Experimental setup established for fault diagnosis using acoustic sensor and accelerometer (Bhuiyan et al. 2014)

Tool condition monitoring can be carried out either by direct measurement or indirect measurement. Non-contact, direct measurement of cutting tool edges with sophisticated systems give accurate information about tool wear. Dynamometers and accelerometers are preferred the most due to their short transfer path and better signal-to-noise ratio (Ingle, R., & Awale, R. 2018).

## 2.6 FAULT DIAGNOSIS USING SIGNAL PROCESSING

Tool wear estimation by conventional Taylor's tool life equation is prone to either underestimation or overestimation (Johansson et al. 2017). Excessive replacement of tools leads to a huge tooling cost. Consequently, valuable resources and precious time are at stake (Masood et al. 2016). The sensor data are in raw or time-domain, which is not in information-revealing form. These sensor data must be processed to improve subjective quality and detect components of interest in a measured signal. Researchers use various signal processing techniques: Fourier transform, short-time Fourier transform, and wavelet transform. Liu et al. (2018) applied signal-processing techniques such as time domain analysis, Fast Fourier Transform (FFT) analysis and wavelet decomposition method for both vibration signal and cutting force signal corresponding to the milling of thin wall feature to recognise the complex machining condition.

### 2.6.1 Time domain

Every signal acquired in CM and fault diagnosis is time series data. An oscilloscope may be used to visualise the time domain data; however, statistical features of the same signal can be evaluated to identify faults and features of the signal acquired. Time domain signal forms the basis for all signal processing and machine learning techniques. Gangsar and Tiwari (2014) classified five bearing fault conditions by considering three statistical features: standard deviation, kurtosis and skewness of a vibration signal. A frequency plot opts best whenever a rotating element is involved in any machinery system. Gangsar and Tiwari (2016) diagnosed the faults of the induction motor based on the analysis of the time-domain signal through a support vector machine. They had selected optimum statistical features from higher statistical moments to the faults.

### 2.6.2 Frequency domain

Frequency domain analysis reveals the periodicity of time domain measurement. The Fourier transform best identifies the frequency of rotation or oscillation. The amplitude variation indicates the degree or extent of the fault. Harmonics and non-harmonics of fundamental frequency can be used to monitor the system's health. Plaza and López (2018) monitored the online surface roughness of the finish turning operation on a CNC lathe by applying singular spectrum analysis to the vibration signal acquired during machining.

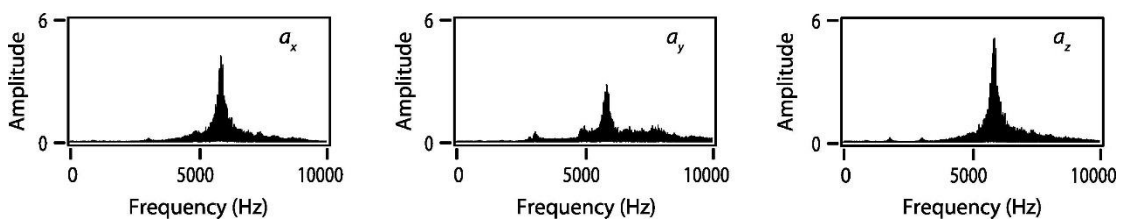


Figure 2.6 FFT plot of three vibration component (Plaza and López 2018)

A signal is divided into a collection of independent additive time series known as principal components using the non-parametric time series analysis technique known as singular spectrum analysis. The FFT plot of the three components of the vibration signal is shown in Figure 2.6. Plaza et al. (2017) evaluated the performance of an individual and grouped analysis of singular spectrum analysis in a series of trials under

various cutting settings in CNC. The findings demonstrate that vibration signal processing using singular spectrum analysis distinguished the frequency ranges useful for forecasting surface roughness. The findings demonstrate that singular spectrum analysis is perfect for examining vibration signals for online surface roughness monitoring.

### 2.6.3 Cepstrum analysis

Cepstrum identifies the periodicity in a frequency plot and is also helpful in identifying the side bands of a fundamental frequency that is otherwise not revealed in the spectrum plot. Liang et al. (2013) compared the application of power spectrum, cepstrum and neural network to identify and classify faults in an induction motor. The cepstrum analysis could reveal the sidebands related slip frequency dependent on motor load. The cepstrum plot for the healthy and broken rotor is shown in Figure 2.7. The sidebands shifted wider, and increased amplitude as the load on the broken rotor bar increased. A similar observation was noted on stator current power spectra. Kim et al. (2021) decomposed vibration signals using empirical wavelet filters based on cepstrum analysis. The suggested method averages the envelopes of decomposed signals for demodulation analysis to improve fault-related signals. Simulation and experiment validated the method. The proposed method increased the fault diagnostic performance over previous methods.

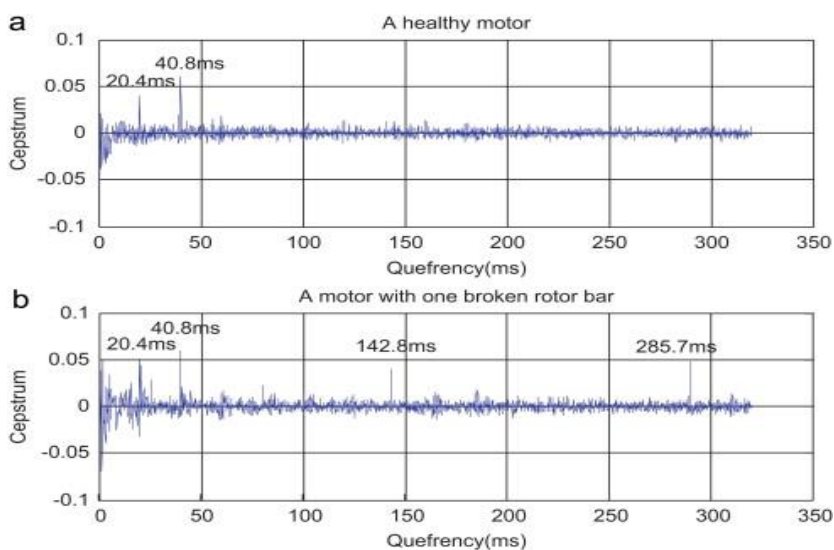


Figure 2.7 Vibration cepstrum of induction motor (a) healthy and (b) broken rotor (Liang et al. 2013)

### 2.6.4 Wavelet analysis

Wavelet analysis is a time-frequency analysis that reveals the time and frequency resolution of the signal under consideration. Some of the applications where wavelet signal processing is applied are reviewed in this section. Using continuous wavelet transform analysis, Ravikumar et al.(2020) diagnosed ball bearing in a two-stroke IC engine. The author had considered healthy, 50 % defect and 100 % defect in the gear tooth at three different loading conditions. The bearing faults identified through the wavelet plot are shown in Figure 2.8. Barbieri et al. (2019) developed a technique to identify the presence of damage in gearboxes using vibration signals. Signal processing techniques, wavelet transform, and mathematical morphology were used to check the presence of a fault in the gearbox. Pattern spectrum and selective filtering were used to identify gearbox damage.

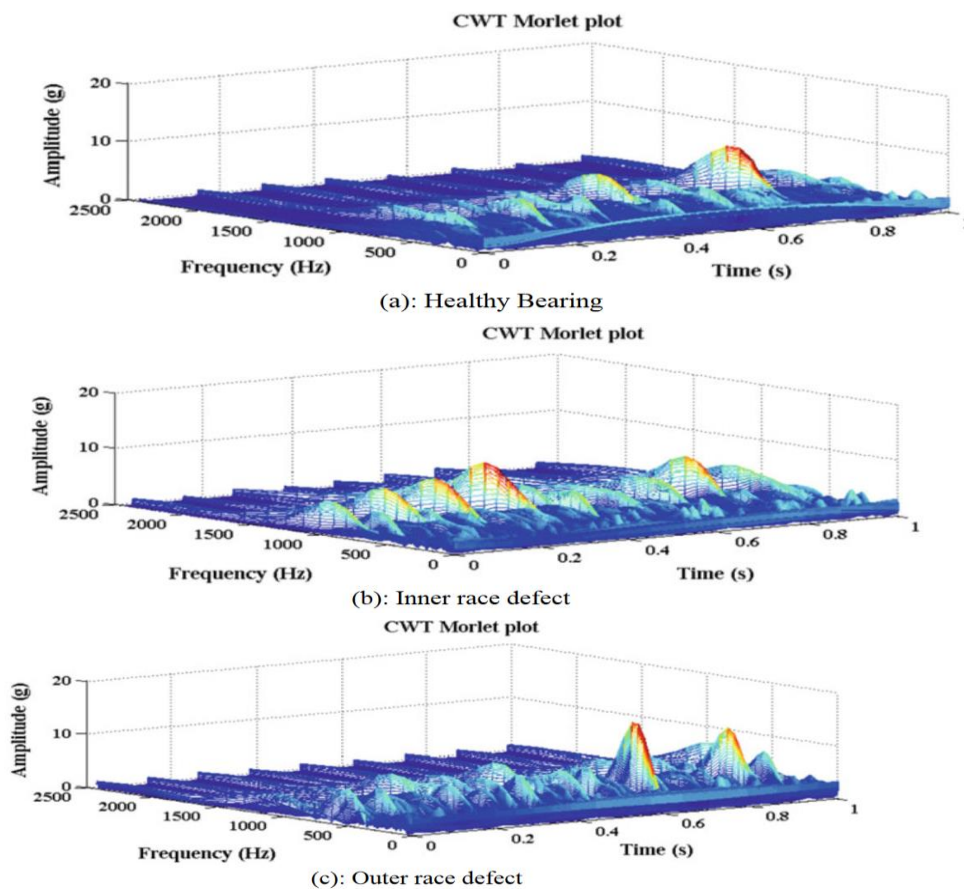


Figure 2.8 Fault diagnosis of ball bearing of IC engine gearbox using wavelet analysis (a) Healthy bearing (b) Inner race defect (c) Outer race defect (Ravikumar et al. 2020)

## 2.7 FAULT DIAGNOSIS BY MACHINE LEARNING

The condition of fault would be many in numbers. In such cases, the monitoring system must learn from previous experience and recognize its faults as and when they occur. These pre-recorded (by previous experience) faulty conditions serve as reference signatures for fault identification during the actual running condition. TCM, through machine learning, was applied to various machining operations such as drilling, milling and turning, turbomachinery, wind mill and all other critical rotating machinery. ML follow three basic steps; feature extraction, feature selection and classification. Figure 2.9 shows the steps and process flow involved in fault diagnosis of machinery equipment through machine learning. The literature about each step of ML is addressed in the following subsection.

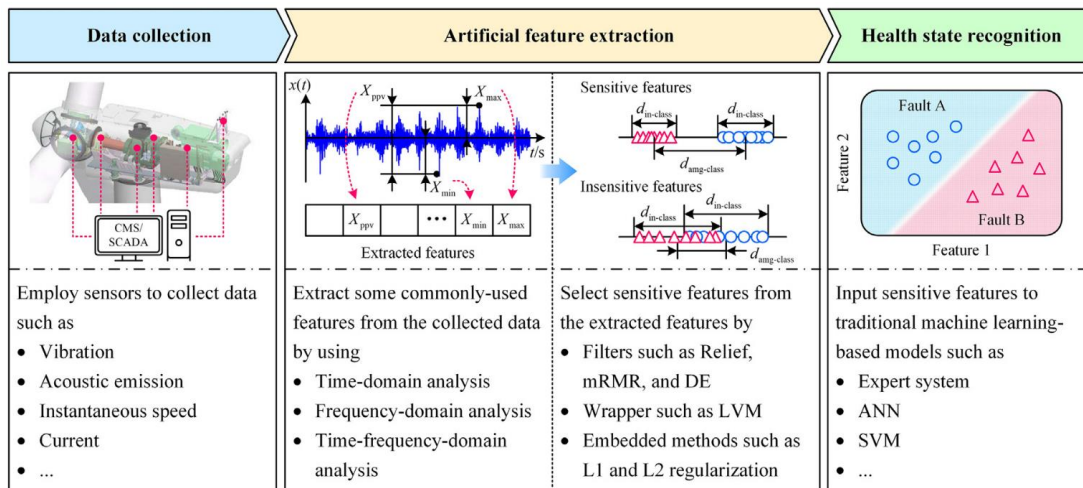


Figure 2.9 Fault diagnosis procedure using machine learning (Lei et al. 2020)

### 2.7.1 Feature extraction

Understanding deeply hidden information in a signal is achieved by extracting remarkable features such as Discrete Wavelet Transform (DWT), statistical, histogram, and empirical mode decomposition (EMD) features. Kuljanic and Sortino (2005) introduced torque force indicator (TFD) and normalized cutting force indicator (NCF) as on-line tool wear indicators for the milling process by studying the feature vector parameters of the cutting force signal obtained using a rotating dynamometer. Li et al. (2010) incorporated Empirical mode decomposition (EMD) into chatter feature

extraction by examining the energy spectrum of each IMF obtained by decomposing the vibration signal for the chatter symptom feature. The findings demonstrate that a feature derived from the boring bar's vibration by EMD can be used as a feature vector for quickly identifying chatter.

#### **2.7.1.1 Statistical features**

Statistical features are typically derived from time domain signals. There have been at least seven statistical features extracted in the current study using ANOVA in MS-Excel: mean, variance, standard deviation, maximum, minimum, sum, kurtosis and skewness, and co-variance. Li et al. (2015) developed a novel method to extract statistical features based on the central limit theory to diagnose the faults in rotating machinery. The feature extraction method was found to improve the effectiveness of the classification.

#### **2.7.2 Empirical mode decomposition features**

Wavelet transform (WT) and wavelet packet transform are time-frequency methods used to identify the chatter frequency based on the gradual increase of the chatter component (Anisheh M. 2009; Yao et al. 2010). However, these methods require designating wavelet basis and decomposition level for each signal which may vary the results based on the wavelet type. Empirical mode decomposition (EMD) is relatively better than WT, where a prior selection of parameters is not required (Wang and Fang 2019). Spindle current variation, tool vibration, acoustic emission, and sound signals can all be used to monitor the condition of a machining process. However, no well-defined mathematical model specifies which signal should be analysed; many follow EMD to distinguish just the chatter band.

##### **2.7.2.1 Discrete wavelet transform features**

Wavelets provide an effective tool for nonstationary signal analysis. Particularly during cutting, the appearance of irregular momentary disturbances renders the recorded signal nonstationary in vibration monitoring. Transients can be broken down via wavelet analysis into several wavelet components corresponding to a particular frequency octave. Gangadhar et al. (2017) diagnosed SPCT using DWT features in vibration signals. The MATLAB program was used to extract the DWT features. Bessous et al.

(2018) diagnosed bearing faults by decomposing the vibration signal through a discrete wavelet transform. The high pass filter and low pass filter allow the approximation coefficient and detailed coefficient to be derived. DWT allows multiple decomposition levels; the threshold is decided based on the energy level in detail of wavelet decomposition.

### **2.7.2.2 Histogram features**

Madhusudana et al. (2016b) carried out condition monitoring of the face milling tool under different conditions of the tool using vibration signals. They extracted histogram features from the signals for classification. Elangovan et al. (2010) classified tool wear using histograms and statistical features in turning operations. They extracted 20 histogram features from the vibration signal. They found that feature classification using statistical features was better than histogram features.

### **2.7.3 Feature selection**

The feature selection process plays the following roles in machine learning systems: It makes machine learning algorithms train more quickly. If the proper subset is selected, it enhances a model's accuracy, simplifies interpretation, decreases overfitting, and minimises model complexity. The following sections further detail how the feature selection technique is used. Elangovan et al. (2011) compared fault classification based on feature selection using the J48 algorithm and principal component analysis to monitor the turning tool using vibration information.

#### **2.7.3.1 Decision tree J-48**

The decision tree technique is frequently utilised in classification and machine learning. Both feature selection and feature classification can be made using decision trees. A decision tree is a technique for representing knowledge based on trees. Weka's adaptation of the J48 algorithm is frequently used for creating decision trees.

Madhusudana et al. (2016b; a) experimented with diagnosing milling tool conditions through vibration signals. A decision tree was used to capture significant histogram features in the dataset. The k-star algorithm was used as a classifier to identify various fault classes in the milling tool. The decision tree used for diagnosing the fault in the milling tool insert using histogram features is shown in Figure 2.10. Sugumaran et al.



(2007) used a decision tree to monitor the health condition of roller bearings using a vibration signal. Features of vibration signals were deduced using statistical analysis.

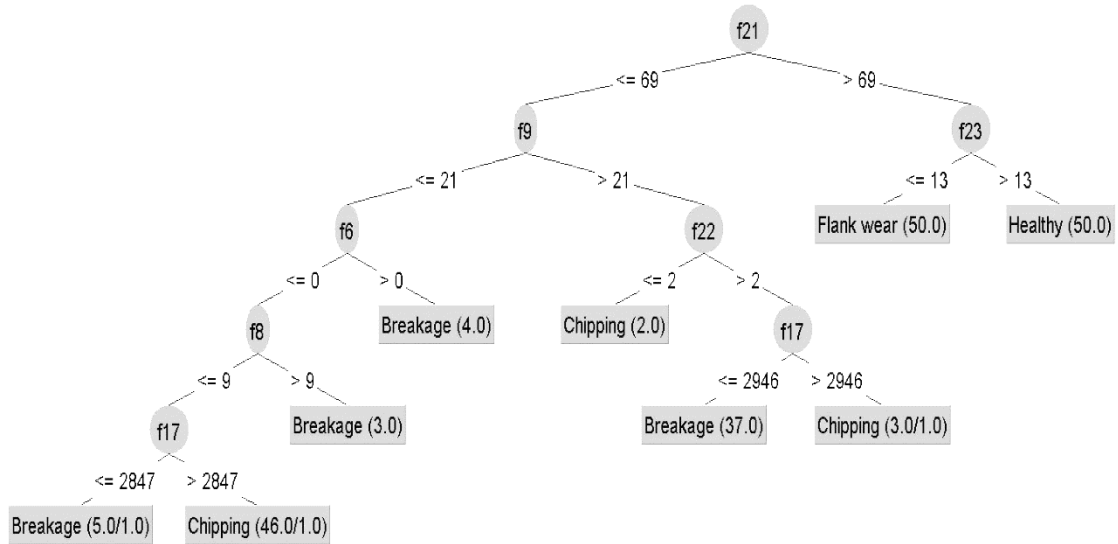


Figure 2.10 Decision tree used for milling tool insert fault diagnosis using histogram features (Madhusudana et al. 2016b)

## 2.7.4 Classification of features

The preceding feature extraction and selection steps are followed by a classification where the classifier builds an algorithm based on the significant feature selected with 66 % training data set and 34 % of the testing data set. 10-fold cross-validation is applied to the classifier for iterative improvement of the algorithm. The primary fault classifiers in various engineering applications are dealt with in subsequent sub-sections.

### 2.7.4.1 Rotation forest algorithm

The rotational forest (RF) ensemble method is relatively recent. It uses a boosted gradient descent algorithm designed by Rodriguez et al. (2006) to improve the efficiency of underperforming machine learning methods like trees. The J-48 algorithm cultivates the trees from a decision tree classifier. Due to its resistance to background noise, RF can provide swifter and more precise classification results. In place of a single classifier, it uses multiple them. The research by Jha et al. (2022) uses latent semantic analysis to provide an efficient method for transforming experimental attributes of a breast cancer dataset using a publicly available breast cancer dataset; the proposed method is verified using a multilayer perceptron, support vector machine. Using the

same set of features, other classifiers such as naive Bayes, rotation forest, simple linear logistic regression, and logistic model tree produce recognition accuracies between 96.75% and 99.30%.

#### **2.7.4.2 Naïve Bayes algorithm**

Due to its efficiency and ease of implementation, the naive Bayesian classification algorithm has found widespread application in big data analysis and other domains. The cutting force of end-milling tests at varying spindle speeds was collected by Karandikar et al. (2015). The Naive Bayes classifier was trained using an evaluation of how tool wears changes force features over time and across frequencies. The Naive Bayes classifier was used to predict the degree of tool wear.

#### **2.7.4.3 Random forest**

Ma et al. (2016a) used the random forest algorithm to predict the tool life of the milling cutter with 315 number milling test data. The results were compared with artificial neural network (ANN) algorithms and support vector regression (SVR). It was found that RF had better tool life prediction accuracy than rest two. Rajini and Jabbar (2021) suggested a lung cancer prediction model by employing the random forest classifier, which aims at assessing symptoms (gender, age, air pollution, weight loss) for the early prediction of lung cancer. The random forest algorithm showed higher accuracy compared with previous approaches.

#### **2.7.4.4 SVM**

Kothuru et al. (2018) compared SVM and convolution neural network (CNN) techniques in machining operations. The progression of wear rate in the cutting tool and variation of hardness in the workpiece was analysed using the above techniques as decision-making models. Wang et al. (2018) studied the application of a support vector machine (SVM) in multi-class gear fault diagnosis. Classification accuracy was excellent when the training data set, and testing dataset had identical rotational speeds. Since the training dataset was not available at all rotational speeds, interpolation and extrapolation of test data were used to help the SVM classifier perform fault diagnosis.

#### **2.7.4.5 K-star algorithm**

One of the instance-based classification methods is the K-star algorithm. According to a few similarity methods, this is the class of a test instance that is based on training instances that are identical to it. Compared to other instance-based learners, it is different in how it uses a distance function based on entropy. An instance is classified by comparison to a database of previously classified examples.

Vibration analysis was used by Painuli et al. (2014) to investigate defect diagnosis of lathe tool monitoring. Utilizing the K-star approach, statistical features were collected from the received signals and classification was carried out. Results indicate that K Star could classify the tool's conditions with a 78% degree of accuracy. Using vibration signals, Singh and Amarnath (2016) studied wavelet transform, decision tree, and K star algorithms for helical gear box problem diagnostics using vibration signals.

#### **2.7.4.6 Artificial neural networks (ANN)**

Regarding ANN, the artificial nodes are highly related to one another. These links are referred to as neurons. It's an adaptive system that shapes itself in response to data streaming via the network. The multilayer feed-forward back propagation technique is one of many designs used for rotating machinery components. An artificial neuron consists of synapses, a summing function, and an activating function (Sharma et al. 2017).

### **2.8 CONTROLLING VIBRATION IN MACHINING**

Machining instability is caused due to chatter with the lack of relative stiffness of the tool and its supporting structure. Tool chatter can be mitigated by increasing the tool stiffness or isolating the source of vibration (Pour and Behbahani 2016). Increasing stiffness shifts the damping resonant frequency to other machine components. Isolating the source of vibration is not viable as the shearing of the chip is a dynamic process. Theoretical modelling and analysis of tool vibration is a complex process and is a topic of many recent studies, but its complete elimination is very costly (Rivin 2000). Hence many machinists follow practical alternatives which are cost-effective such as employing spindle speed variation (SSV) in high-speed machining (Yamato et al. 2020), vibration-assisted cutting (Xiao et al. 2002), using tuned mass damper (Biju and

Shunmugam 2014), incorporating vibration damping technology (Som et al. 2015; Sørby 2017) and incorporating active vibration technology (Park et al. 2007). Recent research on vibration control has proved that smart materials play a vital role in vibration control without altering the system design. Many researchers have used several vibration suppression techniques involving passive, active and semi-active damping of tool vibration for reliable machining processes. Figure 2.11 shows the schematic of three damping techniques employed for tool vibration control considering the cutting tool as a single degree of freedom model.

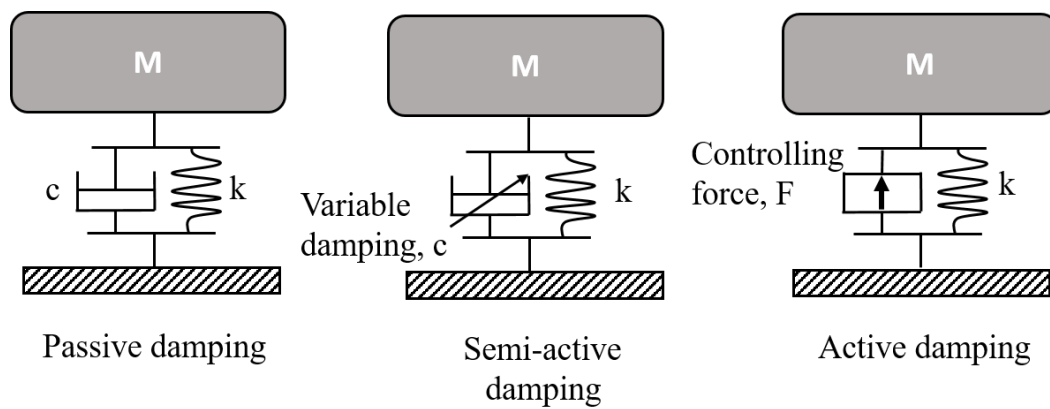


Figure 2.11 Damping methods employed for tool vibration

### 2.8.1 Passive damping techniques

A passive damping system couples an auxiliary mass to the vibrating tool; thus, oscillations of mass in negative cycles of chatter cycles form the damping and inherent stiffness of the tool holder as a spring Munoa et al. (2016). However, it is not adjustable to a wide frequency range. Ma et al. (2021) developed a pre-tuned damping system in the tool adaptor that houses a heavy mass supported by rubber springs that absorbs the vibration energy produced during the machining. The parts and components of the tool holder are shown in Figure 2.12. However, the technique was applied to a long slender milling tool. The cost of the tool was seemingly high; also, the tool holder was required to have a unique fixture and software integration. Biju and Shunmugam (2014) investigated the particle impact damper in attenuating the regenerative chatter and surface finish in boring by filling the cavity in the bar with various particle sizes and particle volumes.

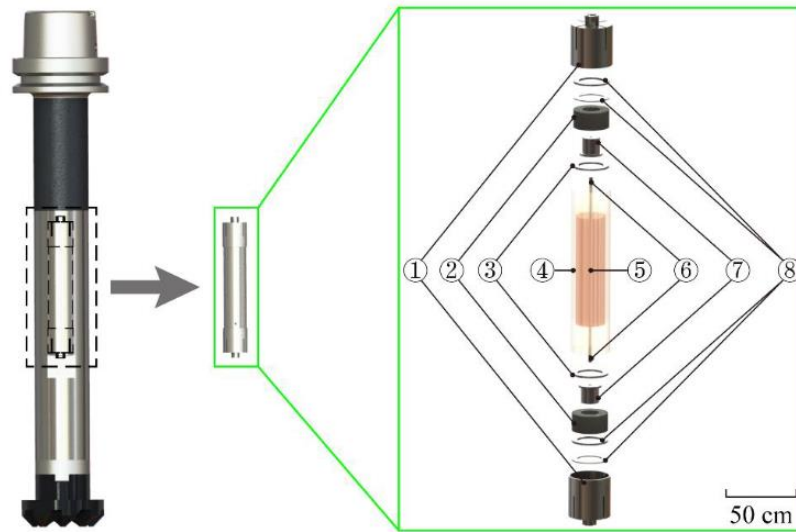


Figure 2.12 Milling tool embedded with passive damping unit. 1—end cover; 2—damping element; 3 and 8—gasket; 4—shell; 5—mass block; 6—steel rod; 7—support block (Ma et al. 2021)

### 2.8.2 Active damping techniques

Active damping employs sensors to sense the vibration level and send the control signal to the actuator, such as a piezoelectric, magnetostrictive or electromagnetic actuator with a more robust and stable control scheme to counter the vibration to control the vibration. A review of the application of active materials and their development of in-process control was carried out by Park et al. (2007) in detail suggests that the multifunctional capability and unobtrusive nature of active material had made them the integral of machine tools; however, the cost involved in such component was seemingly huge. Monnin et al. (2014) presented the effective control of vibration in machining by

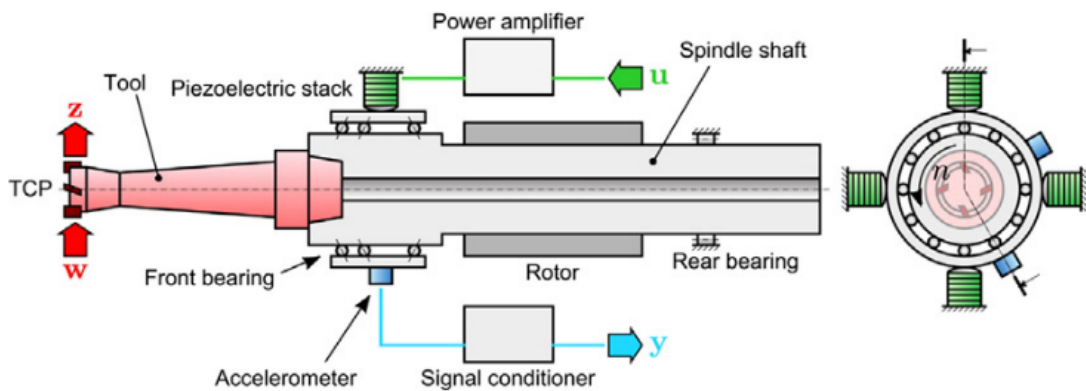


Figure 2.13 Active spindle (Monnin et al. 2014)

using piezoelectric stacks in the spindle unit to minimise the influence of cutting force on tool tip deviation by considering the dynamics of the machine structure. Figure 2.13 shows the schematic of the active force generator in the spindle unit.

### 2.8.3 Semi-active techniques

Many researchers have worked on tool chatter control by designing various methods and components. Vibration control using smart material can be referred to as semi-active vibration control, where the advantage of both active and passive systems are brought together while overcoming the disadvantages of both, such as requiring minimal power for functioning and in case of failure they could still perform as a passive system with no need of a complex controller. Recent research on vibration control has proved that smart materials such as MR fluid in a damper and mount have effectively controlled the vibration with easy installation and no structural modification. Kolluru et al. (2013) developed a magnetorheological shock absorber bed to minimize chatter developed during milling thin-walled features at high speed. A good

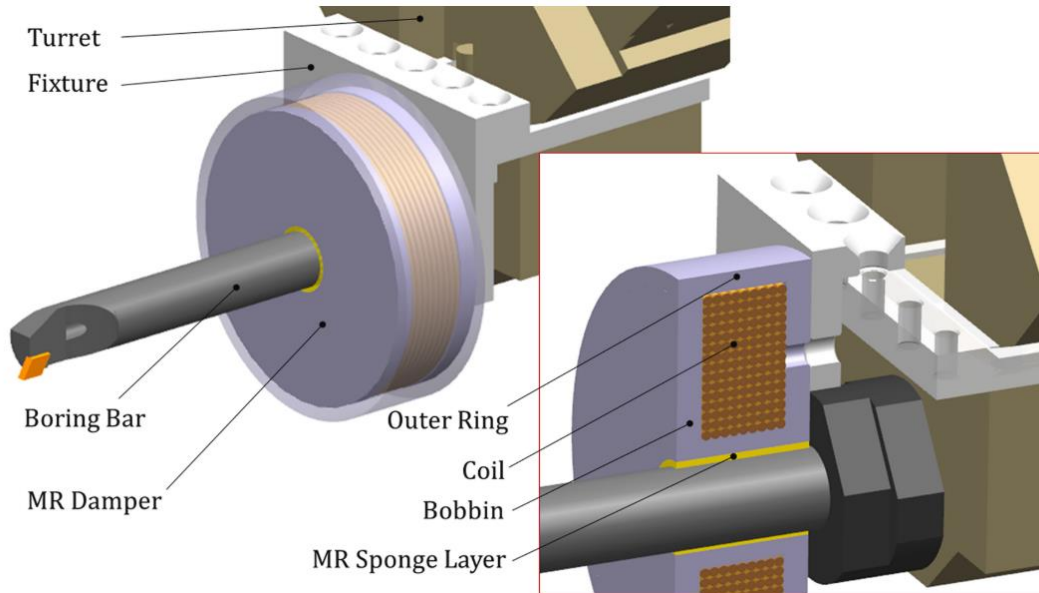


Figure 2.14 MR sponge used for vibration control in boring operation (Saleh et al. 2021)

quality product was produced with the shock absorber bed, which isolated the instabilities of machining. Eem et al. (2019) developed an adaptive elastomer mount to suppress machine vibration transmitting to the isolation table. A hybrid simulation test

was conducted to evaluate the performance of the developed MR elastomer mount with the passive counterpart using a shaking table and equipment over the elastomers. The adaptive elastomer outperformed its counterpart. In another independent research, a flexible fixture was made to suppress the vibration of a thin-walled workpiece. The workpiece was immersed in the tub of MR fluid; an appropriate magnetic field was supplied to secure the workpiece during machining (Ma et al. 2016b). Saleh et al. (2021) used an MR sponge as a damper to improve the stability of the boring bar for machining Inconel 718 and AL 7075 with improvement in both dynamic stiffness and damping.

The 3D model of the installation of the MR sponge on the cutting tool is shown in Figure 2.14. Biju and Shunmugam (2019) developed a tunable boring bar as an inverse cantilever inside the primary structure with MR fluid in the bar cavity and tuning the oscillation frequency by activating the magnetic field. The schematic of the tool holder is shown in Figure 2.15. Mohan and Natarajan (2016) employed an MR damper to control the chatter of boring tools. The boring tool was attached to the piston rod of the MR damper (which was a modified pneumatic damper). Cutting experiments were conducted in the presence and absence of an MR damper. It was observed that the vibration amplitude of the tool was decreased by up to 24%; also, the surface amplitude of the workpiece was reduced by up to 31% after using the MR damper.

The literature survey shows spindle speed variation, active tool holder, passive tuned mass damper and many other techniques to address tool vibration however, the need to implement such techniques economically on the conventional lathe is desired. Hence an attempt is made to design the MR damper with optimal MRF composition to suppress the tool vibration. The study also includes the design of experiments and techniques to arrive at better fluid composition.

## **2.9 DESIGN OPTIMIZATION AND APPLICATION OF MR DAMPER**

Parlak et al. (2013) performed geometric optimisation of the MR damper using the Taguchi design of experiments. The work was concentrated on maximising the magnetic flux density at the annular gap of the MR damper and classifying the design variables, which strongly influenced the objective function. The optimal damper configurations obtained from the study were fabricated and tested for verification. The

FEM images of the different design configurations obtained are shown in Figure 2.16. Parlak et al. (2012) geometrically optimized the MR damper using goal-driven optimisation based on maximum damper force and magnetic flux density as objective functions. Gurubasavaraju et al. (2017) geometrically optimized the monotube MR damper under shear mode with the ANSYS optimization tool; surface response techniques were used to optimise the MR geometrical parameters damper. Xu et al. (2013) conducted multi-objective optimization of an electromagnetic circuit of an MR damper to minimize the area of the magnetic circuit and enhance the damper force using the finite element method. Electrorheological and magnetorheological fluid devices were compared based on the electrical power requirement and an optimized MR damper to minimize the electrical power consumption.

Farjoud and Bagherpour (2016) presented a procedure to develop electromagnets with optimum design for MR devices using the finite element technique. Both steady-state design and dynamic design methods were discussed. The magnetic energy density (MED) and magnetic field efficiency (MFE) were used as performance parameters to assess MR electromagnets. Goldasz (2013) developed a model which can be extended to any monotube MR damper of multi-parallel annular flow paths. The model demonstrated the simulation of fluid flow through the piston. Kishore et al. (2018) developed an MR damper to suppress tool chatter in turning operation. The damper had a magnetic coil wound around the cylinder, and voltage was varied to control the damping co-efficient of the damper. A finite element analysis of the cutting tool was carried out, which simulated the effect of a damper on tool deflection during machining. The developed damper had reduced the tool wear, improved the surface finish and reduced cutting force.

The MR damper in the current study is designed with optimal geometric dimensions through a multi-objective genetic algorithm using a central composite design of experiment in ANSYS magnetostatic analysis.



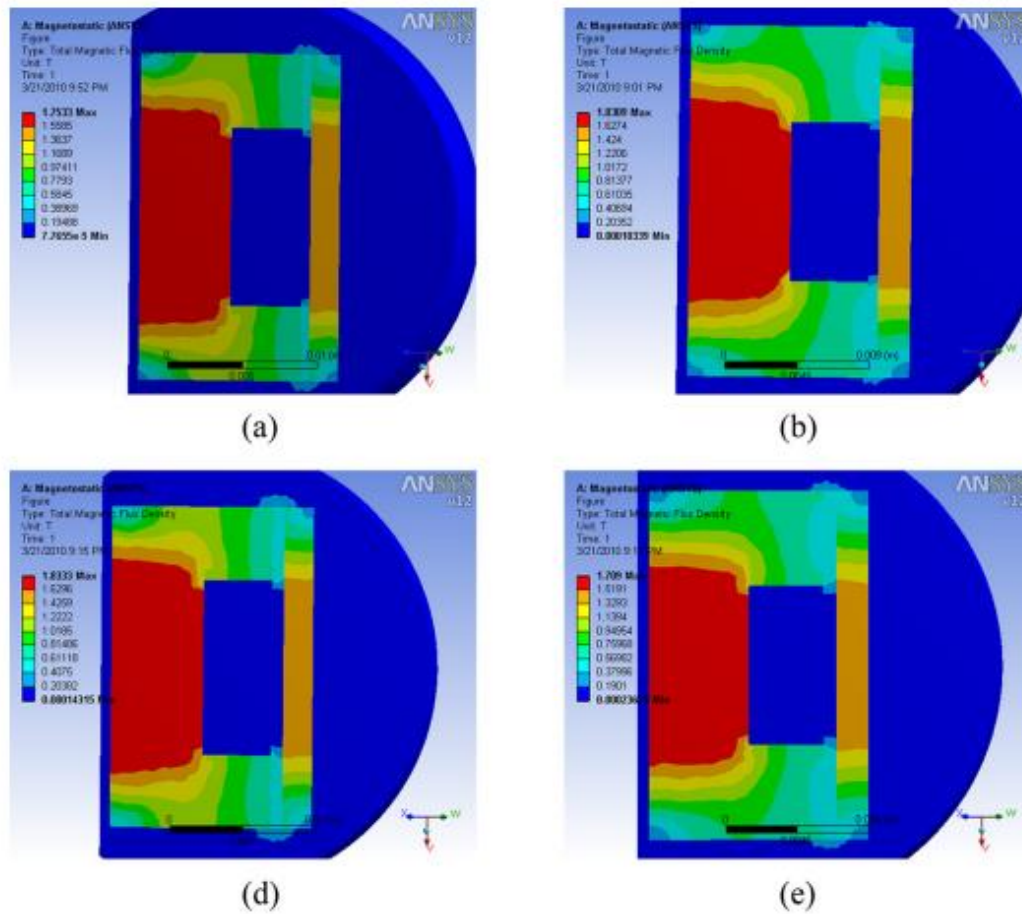


Figure 2.15 Magnetic flux density for various design configuration (Parlak et al. 2013)

## 2.10 MAGNETORHEOLOGICAL FLUID

MRF has proved its effectiveness in various engineering applications such as dampers (Parlak et al. 2012), clutches (Rabinow 1948), brakes (Acharya et al. 2021), engine mount (Nguyen et al. 2013) and surface grinding/polishing of optical lenses (Poynor and Reinholtz 2001). The preparation, rheological study and optimization of MR fluid are briefly discussed in this section.

### 2.10.1 Preparation and characterisation

The typical base oil used for the preparation of MRF is silicone oil (Osial et al. 2022), mineral oil ((Lim et al. 2004) and hydraulic oil (Acharya et al. 2019). The size of solid particles (carbonyl iron particles) may vary from  $1\mu\text{m}$  to  $10\mu\text{m}$  (Ashtiani et al. 2015).

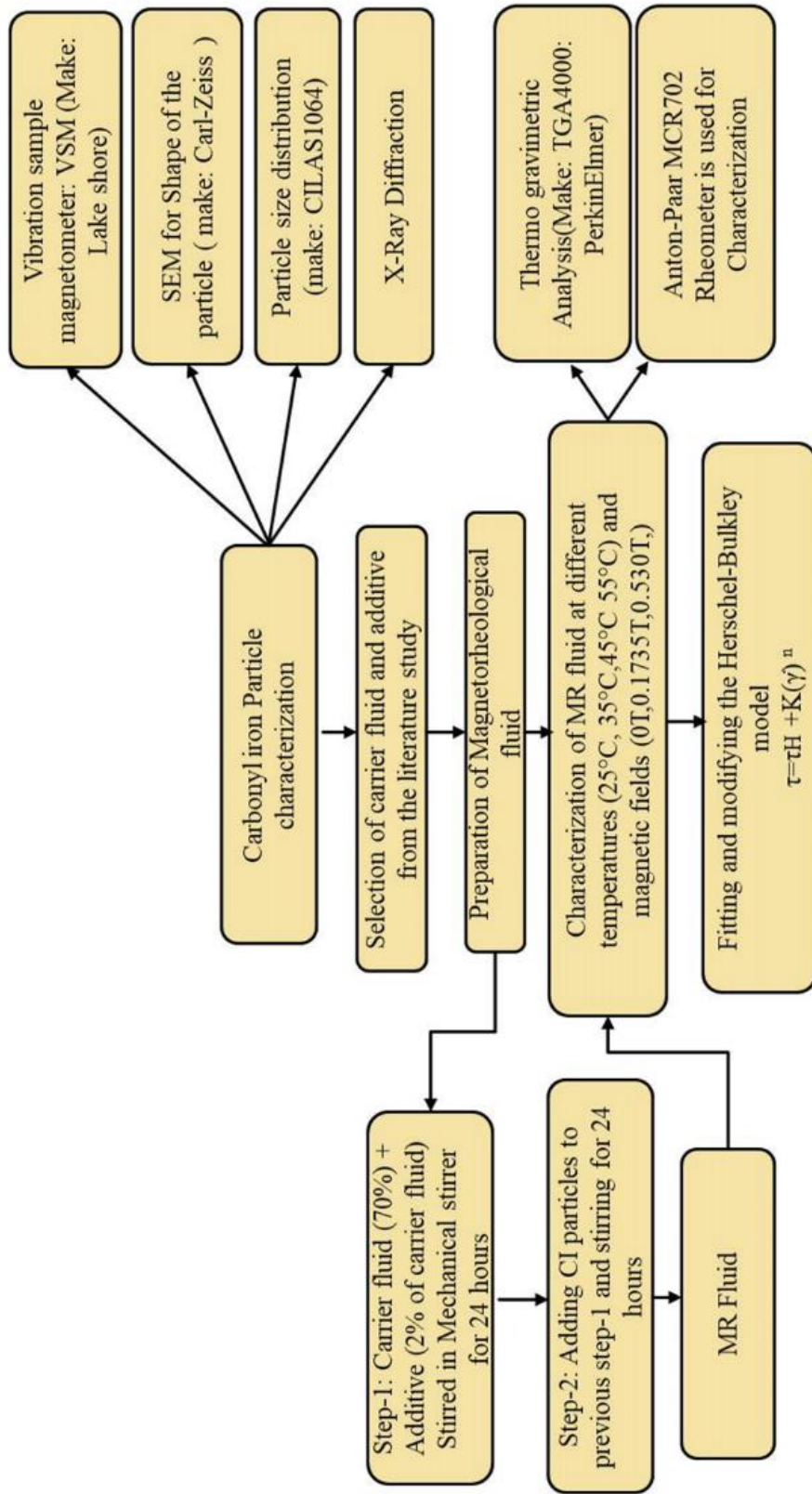


Figure 2.16 Iron Particle characterisation and preparation of MR fluid (Kumar Kariganaur et al. 2022)

Paul et al. (2015) investigated the effect of nanoparticles on the performance of an MR fluid damper when employed in turning. An attempt was made to minimize the temperature and improve the viscosity of MR fluid by infusing the aluminium and titanium oxide particles. The steps involved in preparing and characterising MR particles and MR fluid using various techniques have been shown in detail by (Kumar Kariganaur et al. (2022) in Figure 2.17.

### **2.10.2 Rheological study**

Kamble and Kolekar (2014) used silicon as a carrier fluid with different amounts of iron carbonyl particles to synthesize a new MR fluid and studied its rheological properties. A plate and cone type rheometer was used to determine shear stress, shear strain rate, viscosity and shear modulus. Song et al. (2009) synthesized a magnetic nano-sized additive made by decomposing penta carbonyl iron and studied the effect of adding this material in MR fluid under the influence of magnetic material.

### **2.10.3 Optimization of composition of MRF**

It is difficult to find the exact composition of MRF based on the design equations as unknown practical parameters influence their behaviour; hence, optimization by experimental techniques is necessary. Achieving the optimal rheological properties of MRF for each application requires a detailed evaluation of its constituents, composition and preparation method. MRF delivers varying damping coefficients based on the magnetic field induced in them (Phule et al. 1997).

(Acharya et al. 2019) obtained optimal composition of MR fluid for a shear mode mono tube damper by considering three different particle loading and two different particle size to obtain maximum damping force with minimum off-state viscosity through a multi-objective genetic algorithm. (Acharya et al. 2021) Finding optimal MR fluid composition for MR brake by considering particle mass fraction, base oil viscosity, and mean particle diameter of carbonyl iron particle using the multi-objective genetic algorithm by maximising field induced brake and minimizing off-state torque.

## **2.11 DYNAMIC MODELLING OF MRD**

Seung-Bok and Young-Min (2013) compiled dynamic modelling and control methodology to design MR devices for various vehicle applications, such as MR damper, MR brake, MR clutch, MR mount, and MR valves which help scientists and engineers in developing new devices.

## **2.12 MATHEMATICAL MODELLING OF CUTTING TOOL**

Turkes et al. (2011) developed a mathematical model to predict chatter frequency for orthogonal cutting by assuming turning as a single degree freedom system. The chatter frequency prediction model was developed by applying the orient transfer function (OTF) and tau- decomposition technique to Nyquist criteria. OTF and tau- decomposition techniques predicted the chatter frequency with a 3.3% and 2.12% deviation with the experimental value, respectively. Ramesh et al. (2013) designed a boring tool which was attached to different damping materials such as copper, cast iron and brass. Experimental results were compared with the analytical model developed using an artificial neural network. It was identified that experimental results conformed with analytical results. Ahmed et al. (2014) designed the MR operated end mill cutter and developed an FE model for the end mill cutter with an MR damper using the Euler beam model. Mohan et al. (2017) conducted a harmonic analysis of a boring tool incorporated with an MR damper. The effect of the MR damper on the peak amplitude of tool vibration was studied. It was identified that the peak value was reduced significantly after using the MR damper. Chiou and Liang (1998) developed a mathematical model for chatter stability for both sharp and worn tools. Experimental results verified analytical stability limits. Budak and Ozlu (2007) developed an analytical model for boring operation using multi –a dimensional approach and showed the effect of nose radius on the chatter stability. Experimental tests were also conducted to verify the analytical results.

## **2.13 CONTROL STRATEGIES**

Ramesh et al. (2013) investigated chatter stability in the boring bar and predicted tool wear using ANN. 3D plots and ANOVA tables were used to understand the influence

of cutting parameters and their interactions on tool wear. An experiment was conducted on a boring tool with an impact damper to validate the predictive model.

### **2.13.1 PID control**

Devikiran et al (2022) designed and simulated a custom-built MR damper for a two-wheeler application. The Kwok model was chosen to represent the MR damper mathematically. The supply of current to the MR damper was regulated by a PID controller on the basis of the damper's deflection. The ride comfort and road holding was improved with the PID control. Using an intelligent PID controller with an iterative learning algorithm, a simulation study of a magneto-rheological (MR) damper and hydraulic actuator for suspension system was conducted by (Talib and Darus 2013). Based on the force-displacement and force-velocity characteristics, the needed damper force was calculated using the Bouc Wen model of MR damper.

### **2.13.2 Fuzzy control**

Pour and Behbahani (2016) developed semi –active fuzzy control for chatter stability using an MR damper in turning in which the Chatter stability index (CDI) was used to analyse the stability of the process and fuzzy control to give the best voltage signal based on the measured vibration signals. It was observed that stability in the turning has increased up to 50% using a fuzzy controlled MR damper model. Sajedipour et al. (2010) developed the lumped model for MR damper using the Bouc-Wen model for turning operation. The turning process was analysed with the help of integrated simulation software and fuzzy control to calculate suitable voltage for the MR damper to suppress the chatter based on the vibration signal. It was observed that simulation results conformed with experimental results, also fuzzy controller significantly improved the system stability characteristics.

### **2.13.3 ANN**

Cao et al. (2008) demonstrated the feasibility of the ANN and Probabilistic Moving Near Neighbor (PMNN) as the scalable and invertible MR damper model, which can be applied to system design. It was suggested that PMNN is not a universal approach which requires physical principle structure knowledge.

## **2.14 RESEARCH GAP**

The current research trends show various methods to damp the vibrations induced during the cutting operation. The list of publications and patents involved in this field show the need to address this problem. Some have attempted in applying the passive and MR fluid damper technology to reduce tool vibration for boring operation and milling operation, however no attempt has been made to apply suitable control strategy for the semi-active system for hard turning operation. Thus there is a need to develop a tool specific MR damper and to apply a suitable control strategy to reduce the vibration and improve the surface finish of the workpiece and evaluate machining performance with external damper on stability limit of machining, chip morphology, tool life, and cutting force. The proposed research enables to develop a variable damping MR tool damper which adjusts to changing cutting conditions to improve the machining performance and reduce surface roughness. From the literature survey, it is found that there is no attempt made to control the damping force of damper online during machining. Existing damper of Paul et al. (2012) was manual controlled. In the proposed work, MR damper designed for cutting tool vibration control can do lot more than the existing design such as online prediction of surface roughness by using accelerometer signal, a robust controller designed to change the stiffness of the damper to control deteriorating surface finish at varying cutting condition along with correcting strategy. This damping technique enables stable machining, delays the tool wear in aggressive cutting conditions, and enables a higher material removal rate.

## **2.15 MOTIVATION FROM THE LITERATURE SURVEY**

The literature review concludes that signal processing and machine learning are effective tool fault identification and diagnosis techniques during machining processes for early tool failure detection to avoid unsteady vibration and poor surface finish. It is also evident from the literature that MR fluid devices have improved the machining performance in various operations, such as milling and boring. A similar approach is followed in this thesis to dampen the tool vibration in turning hard steels in addition to real-time control, unlike many researchers who attempted to reduce tool vibration

manually. The predefined machining parameters do not meet the modern machining requirement, which is becoming more automatic due to dynamic changes in the tool and workpiece. Therefore, it is essential to monitor and correct the cutting process online by identifying deviations from the actual machining regime to unstable by properly adjusting the structural support of the machining operation.

## **2.16 OBJECTIVES OF RESEARCH WORK**

1. To identify tool faults in hard turning operation based on vibration and cutting force through signal processing and machining learning techniques
2. To design, develop and characterise a magnetorheological fluid damper to control the vibration of the cutting tool
3. To synthesise and characterise the optimal composition of magnetorheological fluid for magnetorheological tool damper
4. Implementation and evaluation of damper performance in controlling the tool vibration

## **2.17 SCOPE OF CURRENT RESEARCH**

The scope of the current research work are drawn as follows

- Signal processing techniques such as time domain, spectrum and wavelet analysis under various tool fault conditions are evaluated using cutting force and vibration signal.
- In the present work, the experiment will be carried out on all geared precision panther lathe equipped with cutting force measuring dynamometer and vibration measuring accelerometer under different cutting conditions.
- Machine learning techniques such as Rotation forest, Naïve Bayes and Random tree are used to classify the features to diagnose the tool fault conditions—determination of best feature and classifier combination for diagnosing the tool faults.
- Based on the results of fault diagnosis, the vibration level and amplitude of cutting force for healthy and faulty conditions are identified and a suitable

vibration damping technique, preferably MR damper, is designed, developed and characterized.

- Detailed steps of optimizing the geometric dimensions with better magnetic properties of the damper materials; optimal MR fluid composition that results in maximum yield stress and damping force are carried out.
- The developed MR damper is implemented on the lathe for turning operation to evaluate the machining process's tool wear, surface roughness and stability limit.
- Real-time control is implemented to control the MR damper to achieve effective controllability.
- A novel tool holder containing MR fluid in the axial hollow section is developed that can reduce tool vibration by changing the damping coefficient of the MR fluid contained in the tool holder.

## **2.18 SUMMARY**

This chapter deals with literature on signal processing and machine learning techniques for tool fault identification and classification, respectively—the application of MR fluid in some engineering fields, specifically machining. The chapter lists the literature discussing chatter identification and avoidance technique used in machining operations. The literature referred to in this chapter forms the basis for identifying the research gap and formulating the objectives to achieve the thesis title.



## **CHAPTER 3**

### **METHODOLOGY**

#### **3.1 INTRODUCTION**

In the present study, fault classification of single point cutting tools for hard turning has been carried out by employing signal processing and machine learning technique using cutting force signals and vibration signals. A comparison of the performance of classifiers was made between cutting force and vibration signal to choose the best signal acquisition method in classifying the tool fault conditions using the machine learning technique.

Tool wear is inevitable in machining; however, one can delay the tool wear and increase the tool life by selecting optimal and stable machining conditions by using vibration suppression techniques that aid aggressive cutting conditions. An MR damper is sought as a vibration suppression device fitted onto a lathe machine with the optimal MR fluid composition to evaluate its performance in controlling the tool vibration. The L9 Taguchi design of the experiment opted to arrive at minimal machining parameters to evaluate the performance of the damper in machining two workpiece materials, namely oil hardened nickel steel (OHNS) and high carbon high chromium (HCHCR) die steel. The stability lobe diagram is obtained analytically with experimental validation to mark the stability limit of the machining condition. The designed MR damper is controlled by a real-time controller considering the vibration-limiting feedback approach. The tool wear, surface roughness, and amplitude of tool vibration are evaluated with and without a semi-active MR damper. To improve the design configuration of the MR damper, an internally damped novel tool holder is designed that houses MR fluid in its axial hollow section. The developed MR tool damper reduces the tool vibration with the electric current supply.

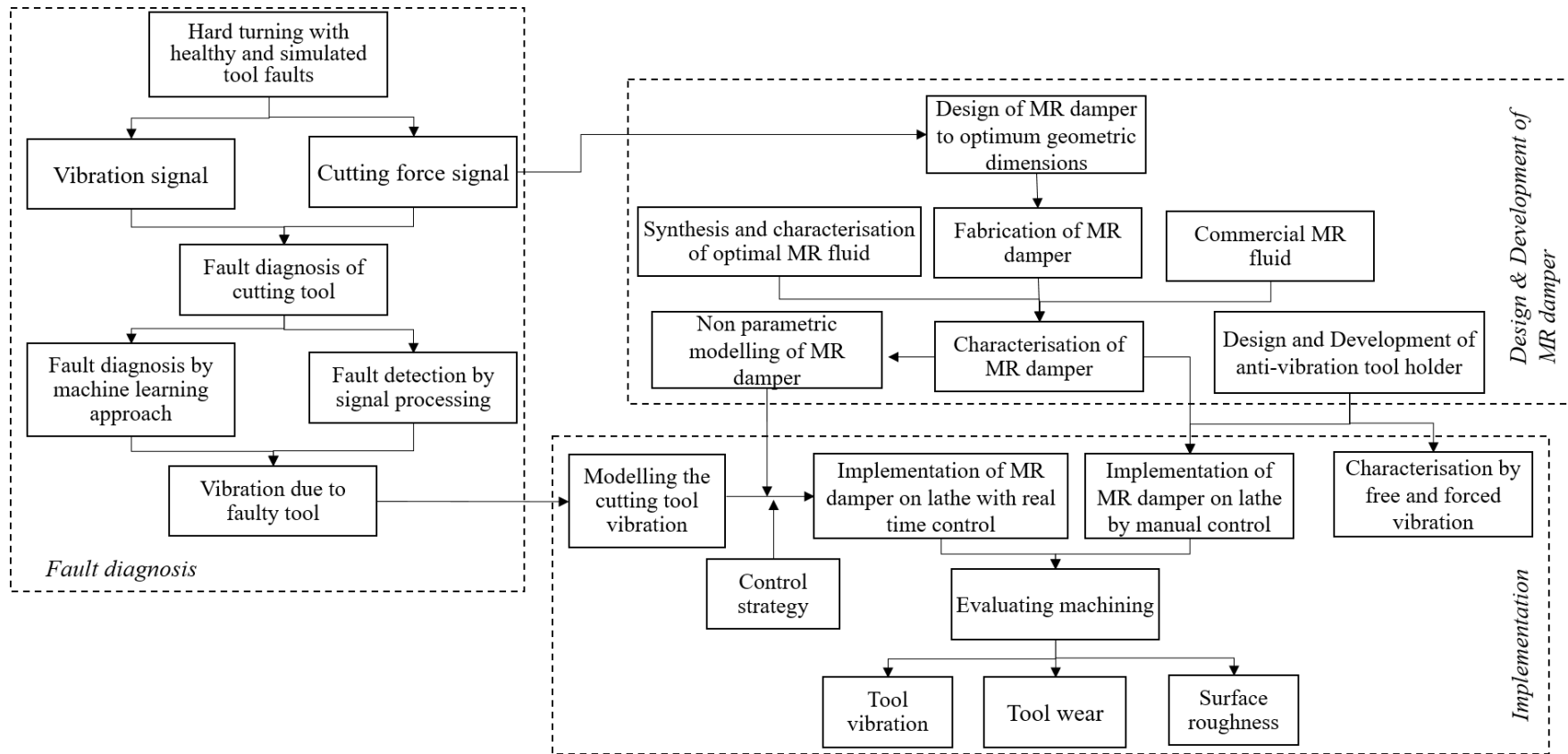


Figure 3.1 Flowchart of overall research methodology

## **3.2 METHODOLOGY**

The proposed research work involves three stages. They are as follows

1. Fault diagnosis using signal processing and machine learning
2. Design and development of MR damper to suppress the tool vibration
3. Implementation of MR damper on the lathe to evaluate machining performance

### **3.2.1 Fault detection based on signal processing**

The current study considers four tool conditions: a healthy tool, a tool with extended overhang, a tool with flank wear and a broken tool. These faults are induced naturally to simulate the practical scenario. Vibration signals and cutting force signals are acquired to monitor tool condition. Spectrum and wavelet analyses are applied to these time domain signals to identify the tool state. Spectrum analysis reveals the frequency component of fault, while the wavelet spectrogram represents fault by a magnitude and characteristic frequency. Wavelet analysis reveals both time localisation and frequency component of the signal

### **3.2.2 Fault diagnosis based on machine learning**

Machine learning is gaining importance in the current world due to its ability to identify and classify parameters based on the training data set. A set of trial runs are run with each tool's condition, and both vibrational and cutting force signals are acquired simultaneously. Machine learning is employed over these data set to classify the tool faults by following three basic steps of ML, namely feature extraction, feature selection and classification. The DWT and statistical features are extracted from vibration and cutting force signals. A decision tree is used to select the significant features from the features extracted. Finally, classification of tool conditions using two classifiers, namely Naïve Bayes and Rotation forest. The ML used in the current study is a supervised ML with a 66 % training data set and 34 % testing data set with 10 fold cross validation.

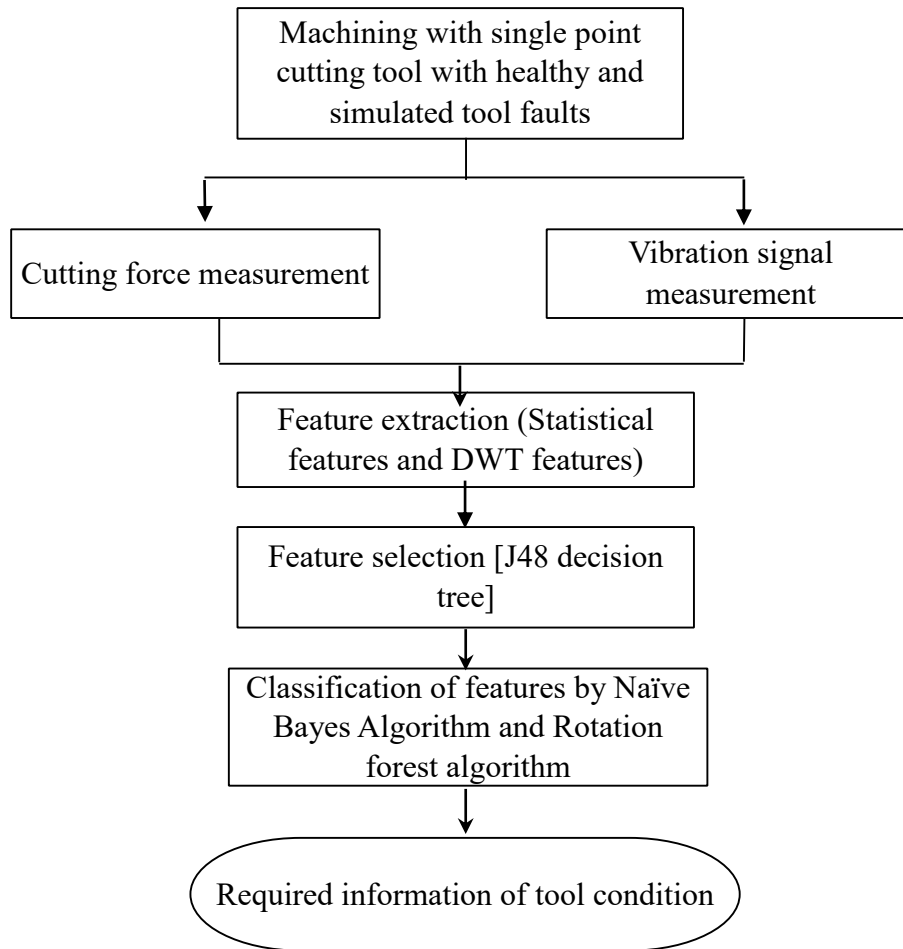


Figure 3.2 Flowchart of fault diagnosis using machine learning

### 3.2.3 Design, development and characterisation of MR damper

Referring to the literature on the vibration suppression techniques by a passive, active and semi-active techniques it is found that semi-active is a feasible solutions for tool vibration control; hence an external MR damper is designed and developed to be implemented on a lathe.

An MR damper is designed, developed and implemented by considering design input parameters obtained from preliminary turning experiments. Design of MR damper initiated with magnetostatic analysis of flow valve where geometric dimensions of flow valve of the damper are assigned and optimized. The magnetic material best suitable for achieving maximum flux density is evaluated by assigning material properties to the ANSYS model

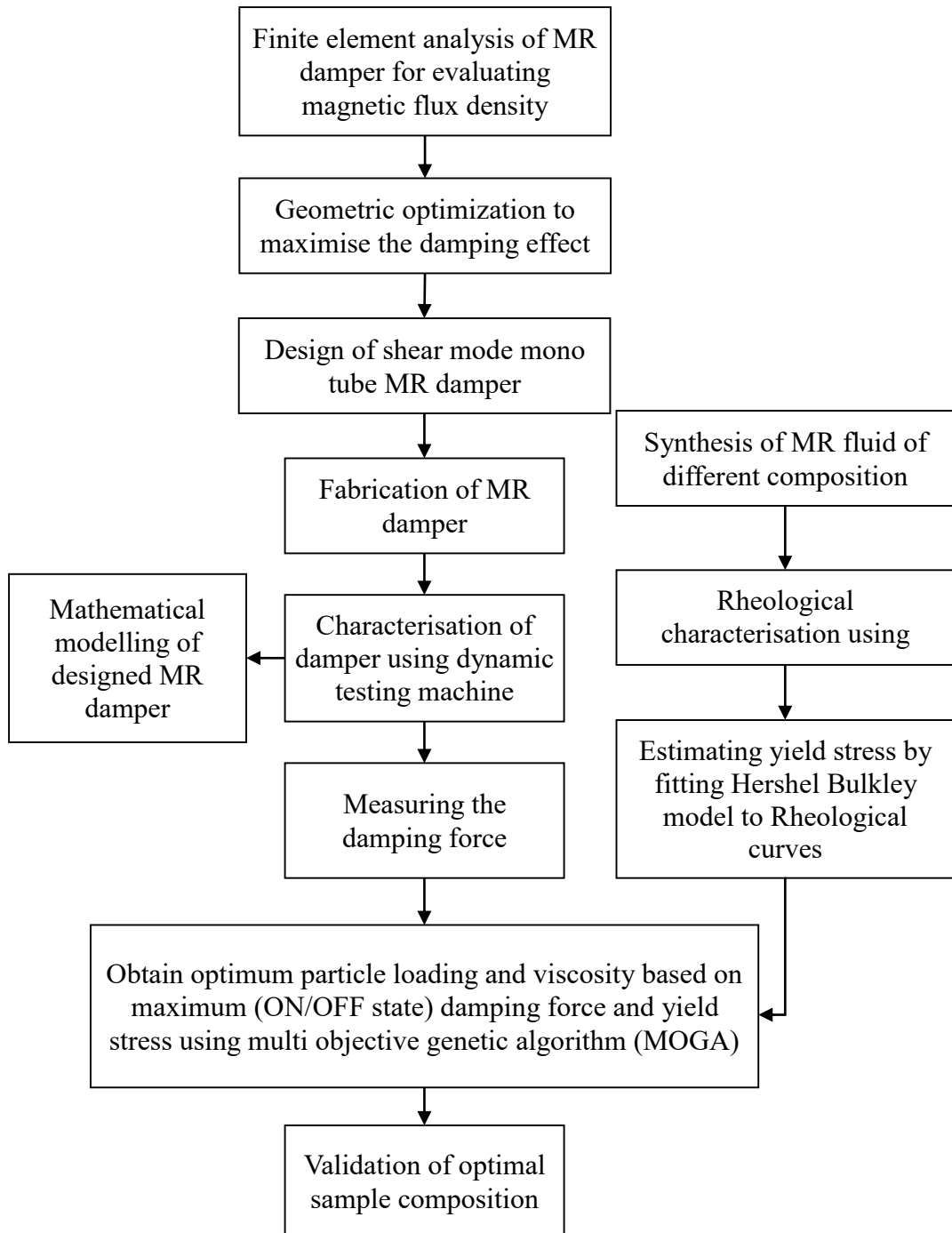


Figure 3.3 Flowchart of damper design and fluid synthesis

### 3.2.4 Synthesis and characterisation of MR fluid

The optimal composition of MR fluid is selected based on the desired shear stress from various samples prepared in-house. MR fluids are characterized on a rheometer to evaluate their rheological characteristics suitable for the damper. Commercial MR

Fluid is used to compare the performance of in-house MR fluid. The damper is fabricated to optimized design parameters and tested on a dynamic testing machine to evaluate its dynamic behaviour under various current supplies.

### **3.2.5 Implementation of MR damper to evaluate machining performance**

The machining study is carried out with the augmentation of a Magnetorheological (MR) fluid damper to suppress tool vibration in hard turning with easy installation without much structural modification. The optimal composition of MR fluid prepared in-house and is used in the damper. The in-house MR fluid is compared with commercial MR fluid. The L9 Taguchi design of the experiment opted to arrive at minimal machining parameters to evaluate the performance of the damper in machining two workpiece materials, namely oil hardened nickel steel (OHNS) and high carbon high chromium (HCHCR) die steel. The tool wear study is also carried out to monitor the influence of external damping over tool life. The stability lobe diagram is obtained analytically with experimental validation to mark the stability limit of the machining condition.

### **3.2.6 Implementation of current control**

An accelerometer is placed on the tool holder to acquire the vibration in the tangential direction. Vibration signals of the cutting tools were acquired and analysed using NI DAQ 9230 & NI LabVIEW. The piston rod of the MR damper was connected securely to the bottom of the tool holder, and the base of the MR damper was rigidly fitted on the lathe carriage to provide upward reaction force and neutralise the tool displacement. The Block diagram of the experimental setup is shown in Figure 3.4 for a detailed understanding of the connection between data acquisition and damper control. The digital control signal developed in the LabVIEW software is sent to the current controller through a digital-to-analogue converter NI 9403 with a DSUB module mounted on NI cDAQ 9174. The current controller acts as a switch to continuously turn ON/OFF the power supply from the DC power source to the MR damper. The activated MR damper changes its damping coefficient according to the limiting vibration feedback.

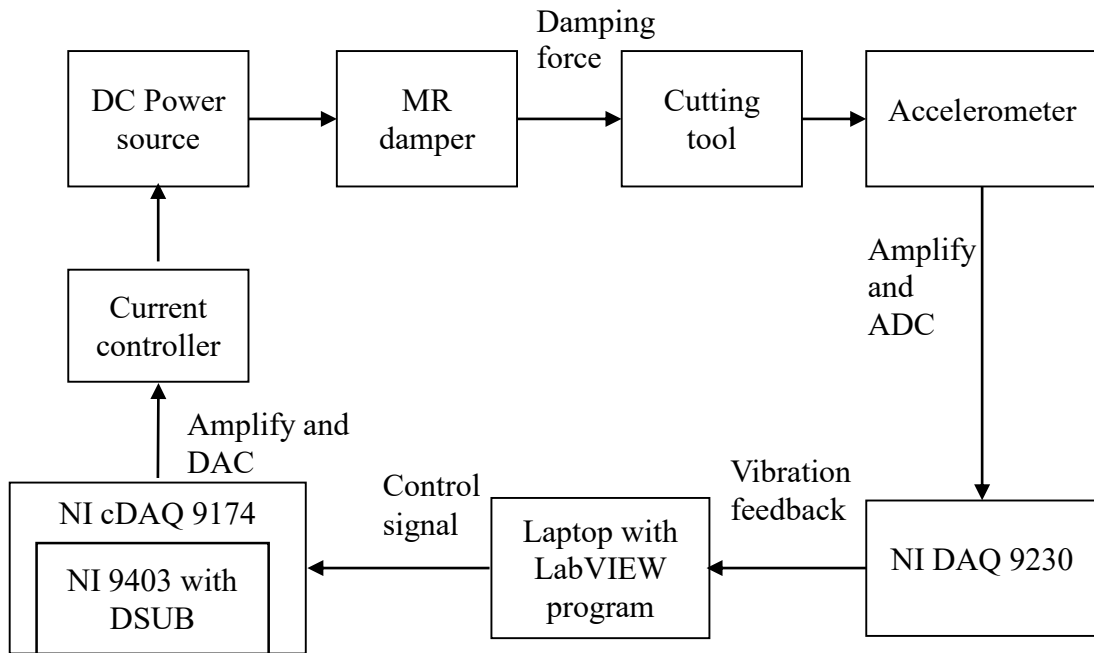


Figure 3.4 Block diagram of effective control of tool vibration with NI DAQ and accelerometer

### 3.2.7 Design of a novel anti-vibration tool holder

We have seen that an external damper can reduce the tool vibration effectively, enabling a good surface finish. Similarly an internal damper embedded into the tool holder is conceptualised. The tool holder is designed, and developed featuring MR fluid which can change its damping coefficient with a change in viscosity of contained MR fluid. The tool holder is one of a kind and use for turning operations with a magnetic circuit inside the tool holder. More details on the design, development and characterisation of the novel tool holder are dealt with in chapter 7. The dynamic response of the tool holder is evaluated through free and forced vibration study to reveal the damping ratio and controllability. The tool holder is later installed on the lathe to study the machining performance. The vibration amplitude and surface roughness are evaluated.

### 3.3 SUMMARY

This chapter deals with the methodology followed to achieve fault diagnosis using signal processing and machine learning. The vibration induced by these faulty tools are suppressed using the MR damper. This damping technique enables stable machining, delays the tool wear in aggressive cutting conditions, and enables a higher material removal rate. The existing methodology mainly focus on passive damping techniques applied to boring operation and milling operation, whereas the current study addresses the violent vibration induced in hard turning operation without much structural modification to machine tool. The method is adaptable to cutting conditions unlike passive damping which are tuned to specific frequency. The detailed evaluation of machining performance brings out the added advantages achieved with the adaptable external damping for machining operation. The adopted methodology ensures effect of external damping on machining performance by detailed evaluation of stability lobe diagram, chip morphology, tool life, vibration level, cutting force and surface finish produced on the workpiece which are not addressed comprehensively in the literature. The limitation of the current study requires sensors and signal analyser that are to be accurate to send control signal in real time to control tool vibration online. The MR damper suffers gravitational settling instability which makes it ideal for continuous usage rather than delay or long time idle. However, the settling instability could be addressed by continuously keeping the MR fluid in active condition with minimal power usage.

The whole system of control, cutting tool, sensors, battery supply and signal analyser could be miniaturised using a programmable micro controller for easy and convenient handling. One of the strong point associated with the current design and methodology is variable damping that adapts to changing cutting conditions and hard workpiece materials. All literature have used either single material or single cutting condition to evaluate the machining performance whereas in the current study two hard steels operated at three different depth of cut, three different speed and three different feed rate are evaluated.



## **CHAPTER 4**

### **FAULT DIAGNOSIS OF SINGLE POINT CUTTING TOOL BY SIGNAL PROCESSING AND MACHINE LEARNING**

#### **4.1 INTRODUCTION**

Tool fault diagnosis with limited human intervention is essential in the modern machining process to witness automation and precise manufacturing. Automation increases productivity and efficient job handling ability. Online tool condition monitoring enables the fault diagnosis of cutting tools. A sensor is employed to acquire the information on the tool condition. The sensor data will be in raw form, which needs to be processed using a signal processing technique to derive useful information about the tool fault. In the present work, a single point cutting tool of carbide tip is used to machine oil hardened nickel steel. Various tool conditions are considered: healthy, extended overhang, worn flank and broken tool. Vibration signals corresponding to each tool's condition are acquired using the accelerometer to monitor the tool conditions. The time domain signals are transformed to the frequency domain by employing a fast Fourier transform (FFT)—other signal processing techniques, such as wavelet analysis used to understand the ailment of the tool.

#### **4.2 SIGNAL PROCESSING TECHNIQUE**

##### **4.2.1 Time domain analysis**

The following statistical features describe a time domain signal, namely maximum value, mean value, standard deviation. Eqn. 4.1 and Eqn. 4.2 represent the general form of mean and standard deviation. A low standard deviation signifies the data points are close to the mean value, whereas a high standard deviation signifies the data points are scattered away from the mean value.

$$\mu = \bar{X} = \frac{1}{n} \sum_{i=1}^n X_i \quad (4.1)$$

$$\sigma = \sqrt{\mu} = \sqrt{\frac{1}{n} \sum_{i=1}^n (X_i - \bar{X})^2} \quad (4.2)$$

#### 4.2.2 Frequency domain analysis

The frequency components of rotating members is identified by employing Fourier transform on the time domain signal (Bae et al. 2019). Fourier transform for angular frequency  $\omega$  is given by,

$$X(\omega) = \int_{-\infty}^{+\infty} x(t) e^{-j\omega t} dt \quad (4.3)$$

$X(\omega)$  is the Fourier transform of the time domain signal  $x(t)$ .

In turning process tool vibration signal is periodic, and its characteristic frequency is spindle frequency (SF), so the spectrum plot of the vibration signal shows peaks at SF and its harmonics while the appearance of peaks at other frequencies indicates chatter

$$SF = \frac{n}{60} = \frac{1000v}{60\pi D} \quad (4.4)$$

Where  $n$  is spindle speed in RPM and  $v$  linear speed in m/min.  $D$  is the diameter of the workpiece (Madhusudana et al. 2016d).

#### 4.2.3 Wavelet analysis

Fourier transform does not apply to non-stationary signals, even though they are most common in real life. Online condition monitoring requires tools that handle non-stationary signals to give real-time system information (Büssow 2007). Fourier transform cannot reveal the frequency component corresponding to a particular time. The spectra reveal only the existence of various frequency components in a system concerned. Wavelet analysis provides the frequency component and its location on the time strap with a magnitude of frequency (Mallat 2002). Wavelet transform is an

effective tool for damage localisation. A continuous wavelet transform of time domain signal  $x(t)$  is defined as,

$$CWT X_{\psi}(a,b) = \frac{1}{\sqrt{|a|}} \int_{-\infty}^{\infty} x(t)\psi^*\left(\frac{t-b}{a}\right)dt, \quad \{a,b \in R, a \neq 0\} \quad (4.5)$$

In Eqn. 4.7,  $\Psi(t)$  is the mother wavelet,  $\Psi^*(t)$  is the complex conjugate of  $\Psi(t)$ . 'a' is the scaling parameter and 'b' is the translation parameter.  $X_{\psi}(a,b)$  is a transformed signal with the function of 'a' and 'b'.  $\frac{1}{\sqrt{|a|}}$  is divided with wavelet coefficients at each scale to normalise the signal energy (Benkedjough and Rechak 2018).

The morlet wavelet transform belongs to the family of CWT. Mother Wavelet of Morlet is given by

$$\psi(t) = \frac{1}{\sqrt[4]{\pi}} (e^{j\omega t} - e^{-\frac{\omega_0^2}{2}}) e^{-\frac{t^2}{2}} \quad (4.6)$$

In the Eqn. 4.8  $\omega_0$  is the central frequency of the mother wavelet, the term  $e^{-\frac{\omega_0^2}{2}}$  is used for correcting the non-zero mean of the complex sinusoid. It is ignored if  $\omega_0 > 5$ . The redefined mother wavelet when  $\omega_0 > 5$  is given in Eqn. 4.9.

$$\psi(t) = \frac{1}{\sqrt[4]{\pi}} e^{j\omega_0 t} * e^{-\frac{t^2}{2}} \quad (4.7)$$

### 4.3 EXPERIMENTAL WORK

Experiments were conducted on all geared high-precision universal lathe machines powered by a three-phase induction motor with cutting conditions mentioned in Table 4.2.

Table 4.1 Chemical composition of Oil hardened nickel steel

Element	C	Si	Mn	Cr	W	V	Mo	Ni	Fe
Weight percentage (%)	0.82	0.18	0.52	0.49	-	0.19	0.13	0.05	Rest

Table 4.2. Details of cutting conditions

Parameters	Specifications
Work material	Oil hardened nickel steel
Tool holder	Sandvik PCLNR2020K12
Insert material	Coated carbide (diamond shape)
Cutting speed	56 m/min
Feed	0.3 mm/rev
Depth of cut	2 mm
Various conditions of the tool	Healthy, overhang, worn flank and broken tool

Oil hardened nickel steel was used as a workpiece material for the study. It is a hard steel whose chemical composition is listed in Table 4.1. It finds numerous applications in the manufacturing of stamping dies, thread cutting tools, reamers and blanking tools.

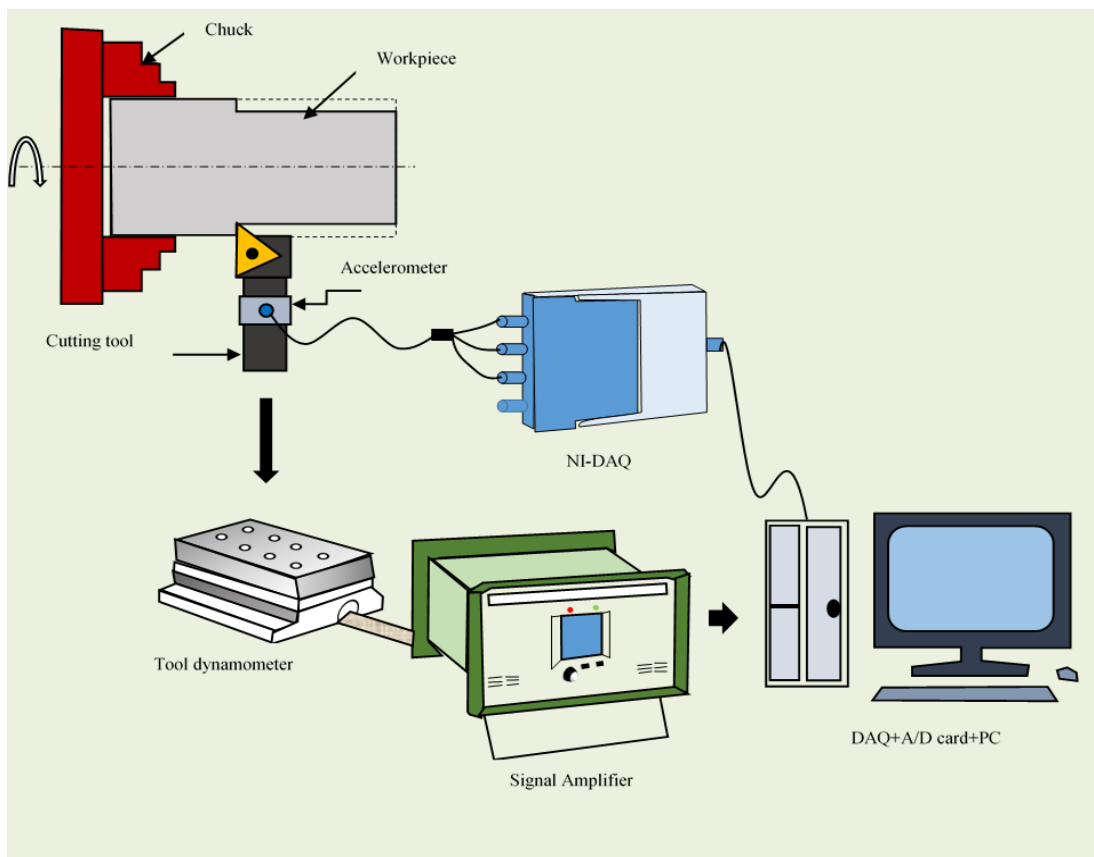


Figure 4.1 Schematic representation of experimental setup

Fig. 4.1 shows the schematic representation of the experimental setup for understanding the acquisition and recording of cutting force and tool vibration during the machining process.

Kistler dynamometer type 9257B was used to acquire cutting force during machining, whose specifications are shown in Table 4.3 with the sensitivity of the dynamometer in various directions, range of measuring the cutting force and operating temperature of the device. Dynamometer had a sampling frequency of 11.6 kHz. The signal generated by the piezoelectric dynamometer flows to a multi channel charge amplifier type 5070A to condition the signal. The conditioned signal flows into data acquisition system 5697A with an integrated A/D card. Finally, the data is visualised on the computer screen.

Table 4.3. Specification of Kistler 9257B Dynamometer

Range $F_x, F_y, F_z$ (kN)	Sensitivity (Pc/N)		Natural Freq.(kHz) $F_n(x,y,z)$	Capacitance (pF)	Operating Temperature Range
	$F_x, F_y$	$F_z$			
-5 to 10	-7.5	-3.7	3 to 5	220	0 to 70°C

Vibration signals are acquired using a tri-axial accelerometer sensor (YMC145A100). The analogue output of the accelerometer is converted into voltage by a National Instruments data acquisition (DAQ) device. Specifications of the sensor are shown in Table 4.4.

Table 4.4 Specification of the accelerometer used in the experiment

Parameter	Modal Number	Sensitivity(mV/g)			Measuring Range(g)
Specification	YMC121A100	X:104.1	Y: 99.28	Z:106.3	$\pm 50$

#### 4.4 EXPERIMENTAL PROCEDURE

Single point cutting tool was mounted on the tool dynamometer, which was secured firmly on the tool post, as shown in the inset of Figure 4.3. The direction of various force components  $F_x, F_y$  and  $F_z$  can be seen in the inset of Figure 4.3. Cutting conditions

were set according to the test plan (such as speed = 572 RPM, feed = 0.3 mm/rev and depth of cut = 0.5 mm). A data acquisition system was used for acquiring force signals from the tool dynamometer, which was amplified by a charge amplifier and sent to DynoWARE software for post-processing. The force measuring system was calibrated prior to measurement. Rough machining was done to remove the unevenness over the workpiece and to remove the rust layer formed on the workpiece. Machining was started and measurement of cutting force for the set cutting condition and tool condition was taken. Machining time is set for 40 seconds, out of which 30 seconds was the time for data acquisition, to stabilise the system prior to measurement. Tool conditions were changed keeping cutting conditions constant.

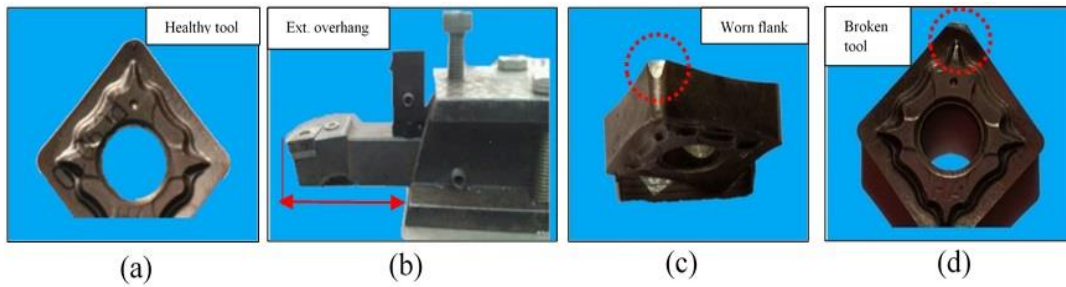


Figure 4.2 Photographic image of various tool wear (a) Healthy tool (b) Extended overhang (c) Worn flank (d) Broken tool

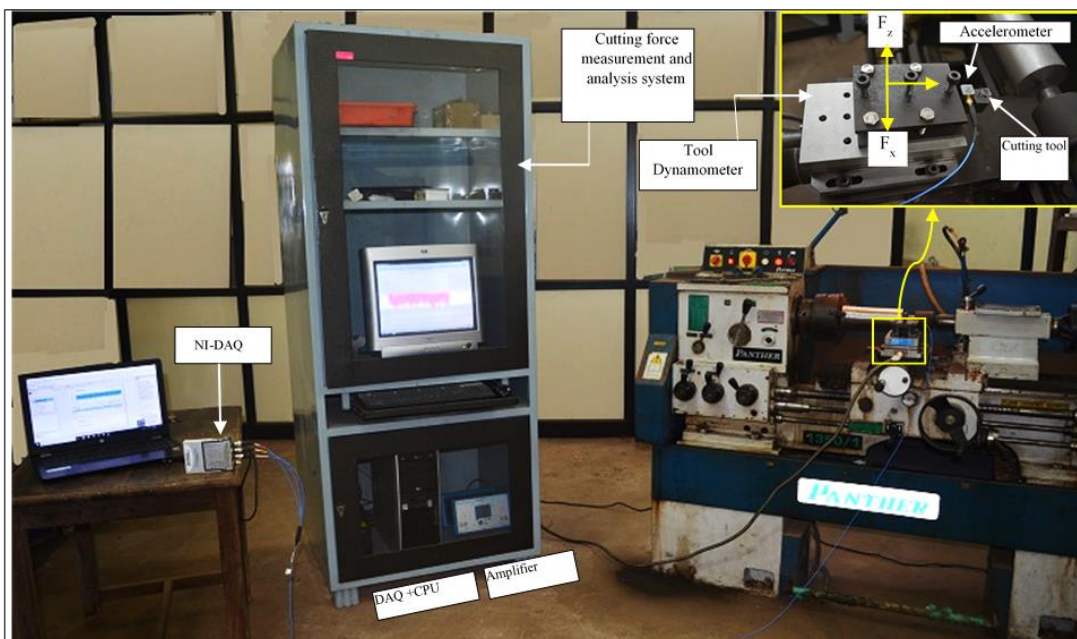


Figure 4.3 Experimental setup containing lathe machine with force measuring and analysing system

The experiments were carried out for four different tool conditions.

Different conditions of the tool insert considered in the present study are shown in Figure 4.2.

- Case 1. A healthy tool with proper mounting (Figure 4.2 (a))
- Case 2. Healthy tool but extended overhanging (Figure 4.2 (b)).
- Case 3. Worn flank with proper mount (Figure 4.2 (c))
- Case 4. Broken tool while mounted properly (Figure 4.2 (d))

A fresh and brand new tool insert was used for case 1. However, in case 2, the insert used was healthy but tool holder was extended by 45mm extra to simulate the condition of the tool mounted with an extended overhang. A worn flank insert was selected in case 3. Similarly, a broken tool while machining a similar workpiece was chosen in case 4. Case 1, case 3 and case 4 were mounted properly without an extended overhang. Case 2 to case 4 are the typical tool condition experienced in machining industries.

## **4.5 RESULTS AND DISCUSSION ON VIBRATION SIGNAL**

### **4.5.1 Time domain analysis**

The following figure signifies the time domain signals of various tooling conditions, acquired using an accelerometer. The amplitude of tool vibration can be observed in the time domain. The range of time domain signal for proper is  $\pm 1$  g, for overhang  $\pm 2$  g. If the signal is not labelled, one cannot say which signal corresponds to what tool condition. The difference between the flank wear and broken tool in the Figure. 4.4 is the RMS amplitude of the time domain signal. The RMS of flank wear is 2.9 g, whereas the RMS amplitude of the broken tool is 4.01 g. They look the same because a severely worn flank leads to a broken tool. The broken tool shows higher amplitude in the time domain because of the rubbing of the broken cutting edge. However, FFT and CWT analysis allows one to know the tool condition by frequency components and time-frequency components. As time progresses, the acceleration signal vary but this was not visualised nor evident in the time domain signal as large one masked small frequency components. A frequency domain plot solves this problem and represents

every component of frequency in the spectrum. Some characteristic frequencies appear at a particular condition of the tool which can be identified and monitored in a spectrum plot for tool fault severity check.

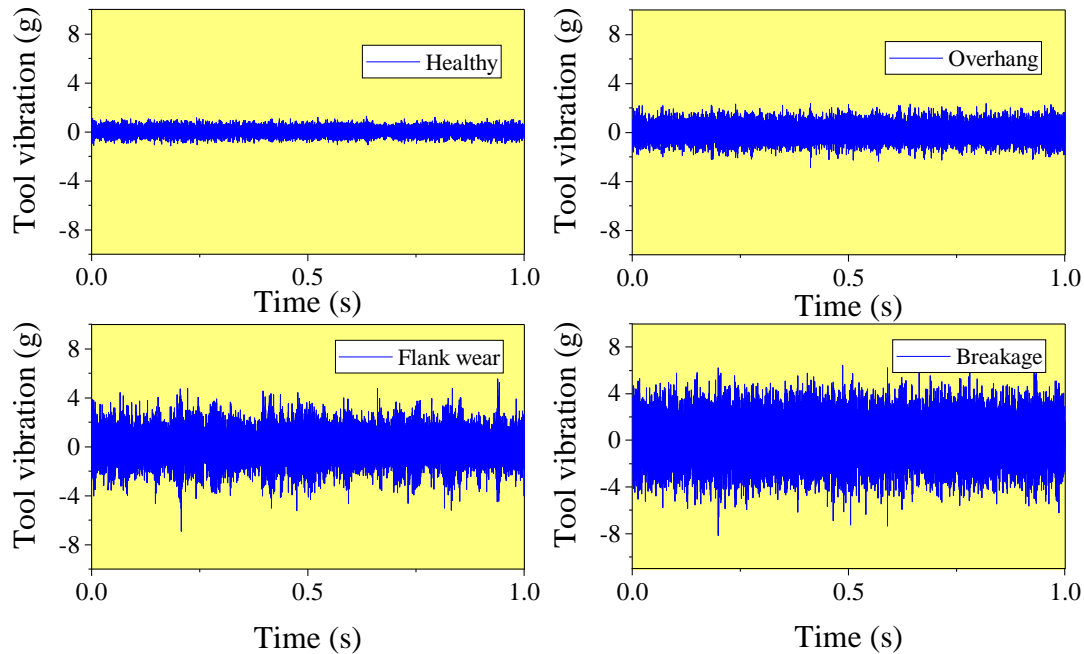


Figure 4.4 Time domain signals of various tool conditions

#### 4.5.2 Frequency analysis

The variation of harmonic and non-harmonic frequency present in vibration signal is analysed to detect tool fault. Many frequency components with high amplitude for worn flank and broken tool could be due to friction between non-cutting edges and workpieces. The tool fault information may be in low-frequency or high-frequency regions. The vibration signal of the healthy tool depicts harmonic and non-harmonic frequency components clearly at nominal frequencies.

The dominant peak value appears at low harmonics of SF, 48 Hz and 100Hz (1x and 2x); when tool fault changes, high harmonics of SF also appear besides low harmonics. Maximum amplitude occurs at 48 Hz, which can be seen in every plot. Some peaks appear at different frequencies besides multiplies of SF for healthy tool condition and the amplitude are at nominal value and shows no marked spectrum periodicity. In case of faulty tools either these harmonics varied or were absent. The spectrum of the faulty tool contains many sidebands with a spacing of approx—20 Hz. FFT shows the presence of additional frequencies. Newly occurred frequencies that differ from



multiplies SF correspond to chattering, so the chatter occurred for broken and worn flank tools. Chatter frequencies are complex as a tool has worn out and more complex vibration has been induced. However, FFT does not provide any clear indication of tool wear, which can be considered as conclusive evidence. Referring to Figure 4.5 the frequency amplitude of the broken tool is lesser than the worn flank because the broken tool creates sharp edges, whereas the worn flank smudges the cutting edge

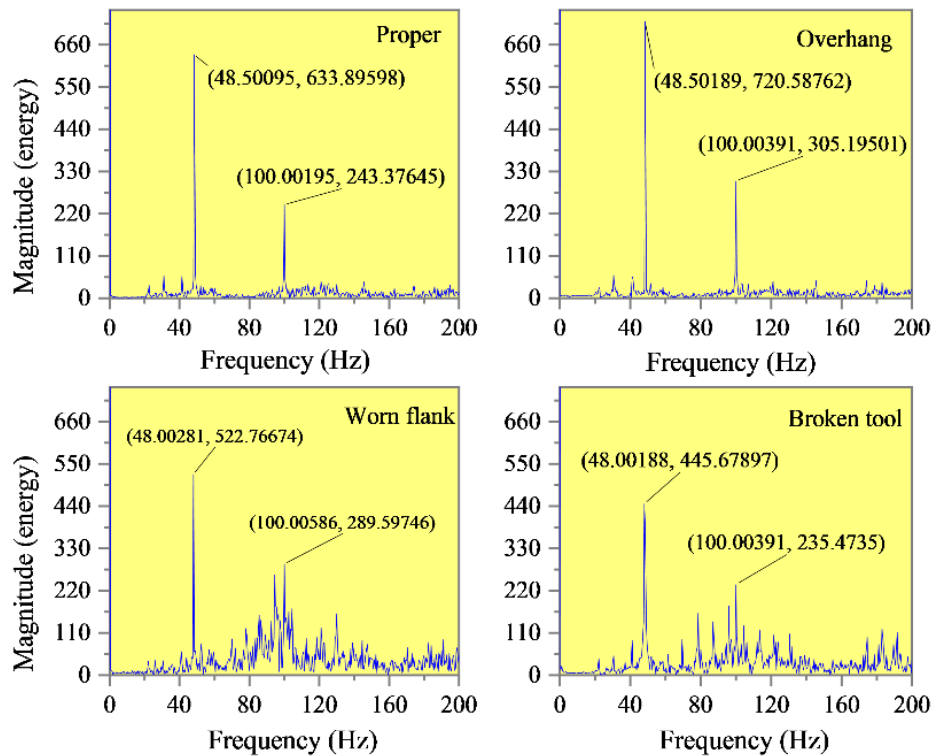


Figure 4.5 Spectrum plot of different tool conditions

### 4.5.3 Time-frequency analysis/ wavelet analysis

Usually, Morlet wavelets are suitable for detecting gradual frequency changes in a signal (Büssow 2007). Figure 4.6 to Figure 4.9 shows wavelet decomposition of vibration signal for various tool conditions. Analysing the CWT plot of healthy tool in Figure 4.6 reveals the presence of low amplitude frequency components between 0 and 500 Hz. However, there were narrow, low-frequency components at the beginning but they decreased from a time scale of 0 to 1 second. There were broader frequency

components between 500 to 1000 Hz with an amplitude of around 1.5 g. Frequency amplitude decreased with time in 500 to 1000 Hz.

The CWT of overhang frequency components raised in magnitude from 10 to 1000 Hz. The frequency band spread broader in the 0 to 500 Hz range than healthy, with an increase in amplitude from 2 g to 4 g, as seen in Figure 4.7. The quantity in Figure., 4.6 to Figure. 4.9, represents the vibration acceleration level in ‘g’.

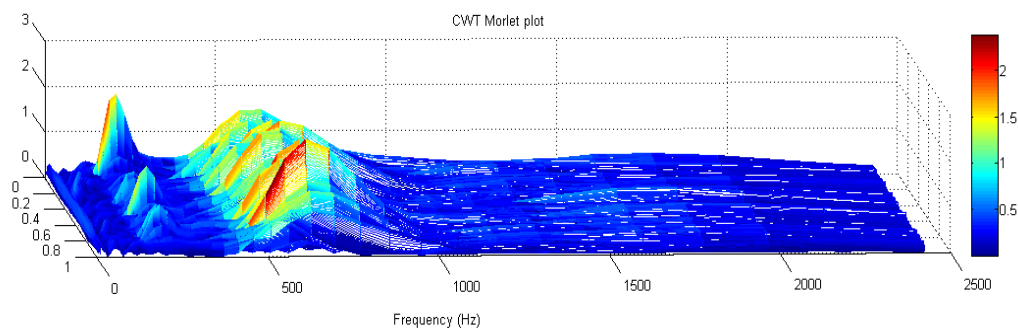


Figure 4.6 CWT plot for Healthy tool

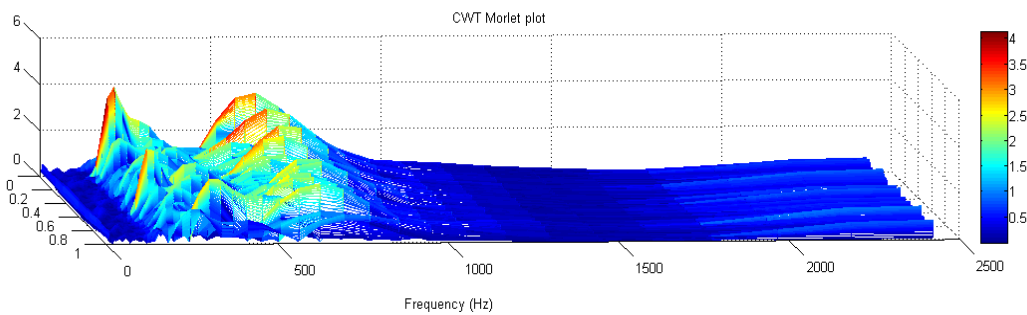


Figure 4.7 CWT plot for extended overhanging tool

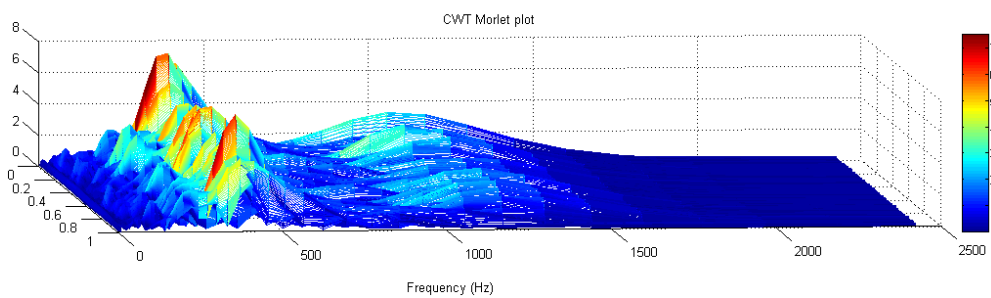


Figure 4.8 CWT plot for worn flank

The CWT of flank wear in Figure 4.8 shows the further increase of amplitude from 2 g to 8 g in all frequency ranges. Also, the band increased up to 1750 Hz. As the tool flank wears, the tool rubbing the workpiece sets additional frequency to come into existence. The amplitude of tool vibration also increases due to the high cutting force being put onto the tool.

The CWT of the broken tool in Figure 4.9 has a higher amplitude of tool vibration in the 200 Hz to 700 Hz range; there are no much frequency components in the 800 Hz to 1000 Hz.

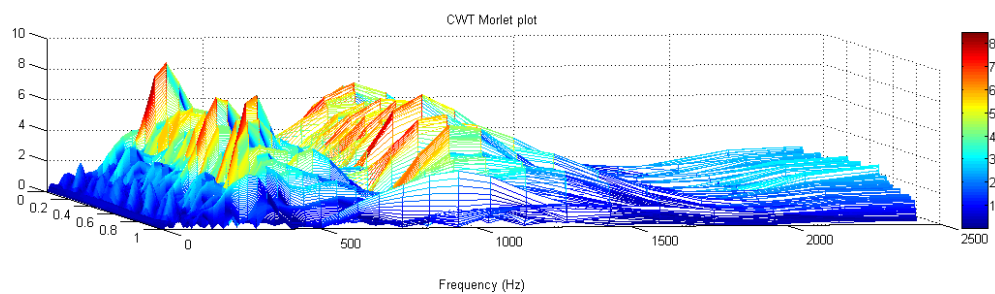


Figure 4.9 CWT plot for broken tool

## 4.6 RESULT AND DISCUSSION ON CUTTING FORCE SIGNAL

### 4.6.1 Time domain cutting force signals

Cutting force signals were recorded for healthy tool, the tool with extended overhang, insert with flank wear and a broken insert at a constant cutting speed of 572 RPM, 0.3 mm/rev feed and 0.5 mm depth of cut. For each tool condition, 30 samples were recorded. Cutting force signals acquired for various conditions of tool are shown in Figure 4.10 to Figure 4.13.

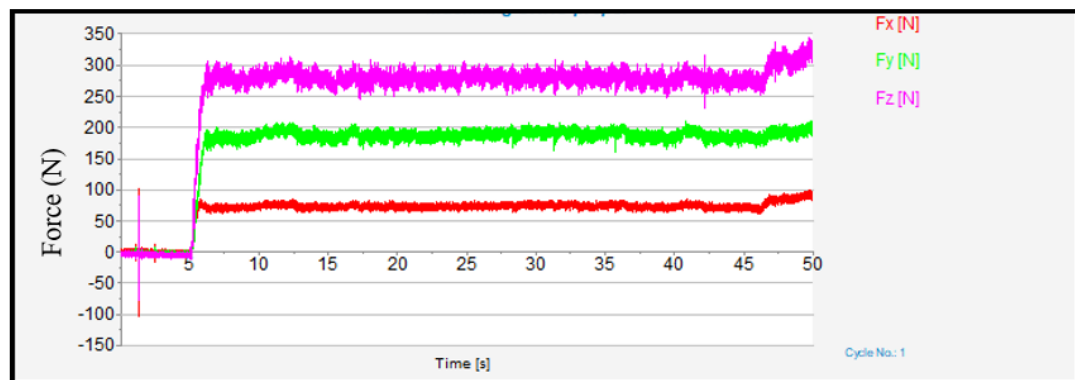


Figure 4.10 Time domain plot of cutting force signal of healthy tool

The sampling frequency was 16.66 kHz. As tangential force is the major cutting force with maximum amplitude, it was considered for the machining process analysis. Z-direction implies tangential direction where the cutting force is maximum. The effect of tool deflection due to tool failure is more prominent in the tangential direction. The

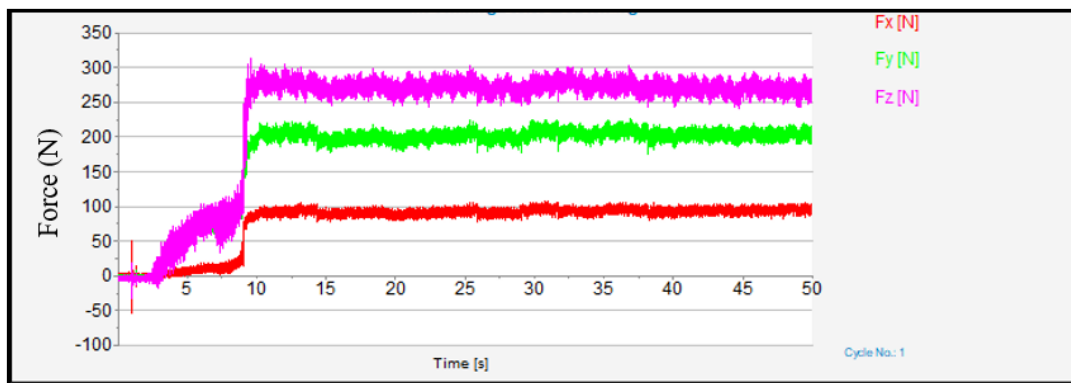


Figure 4.11 Time domain plot of cutting force signal of healthy tool mounted with extended overhang

amplitude of peaks was changing and the range of the signal was also changing but it does not give any information of the tool diagnostics.

Figure 4.10 corresponds to a healthy tool mounted properly; Figure 4.11 corresponds to an extended overhang. The cutting condition was maintained the same for all the cases of tool state. The variations observed in signals were not significant to distinguish between the proper mount and extended overhang. In such a condition, it was necessary to opt for a signal processing technique, which takes minor changes in signal to distinguish accurately. However, signal processing yields result about classification; if

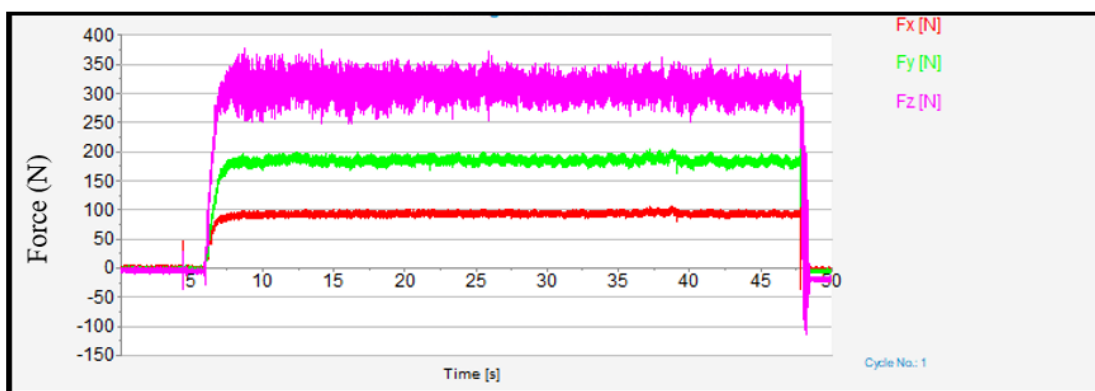


Figure 4.12 Time domain plot of cutting force signal of worn flank

good sensor and programming are established in the system (to be monitored while machine learning makes the system learn automatically with the examples).

Figure 4.12 corresponds to the signal of flank wear, which induces high cutting force. Figure 4.13 is the force signal for tool breakage. With tool breakage, the tool loses its geometry, and rises cutting force. A pictorial representation of cutting force is not just enough to classify the tool condition. These signals have to be analysed further to get the in-depth information buried in the signal to classify the tool state accurately.

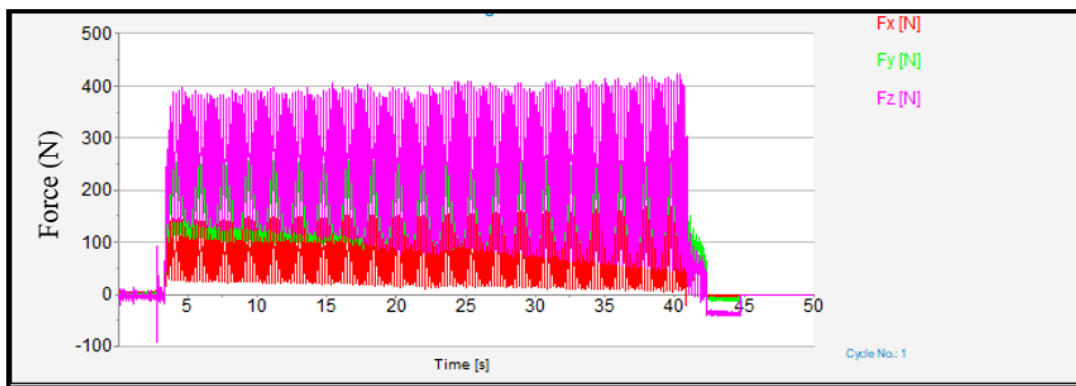


Figure 4.13 Time domain plot of cutting force signal of broken tool

#### 4.6.2 Frequency domain analysis

The spectrum of cutting force for all four tool conditions is shown in Figure 4.14. A dominant frequency component of 4.44 Hz and its 2x harmonics is seen in all four conditions—the amplitude of this frequency is seen to be varying with tool condition. The amplitude at 4.44 Hz for a broken tool is 105 N much larger compared to other tool conditions. A broken tool consumes more energy compared to the rest other conditions. However, for the healthy conditions the amplitude is 1.39 N and it increased to 1.71 N for overhanging case, whereas it reduced to 1.15 N for flank wear. The level of flank wear is seen reduced due to process damping achieved with flank wear land, as evident from the study of Tunç and Budak (2012). The spectrum plot resulted in frequency band of up to 5 kHz; however, only up to 50 or 100 Hz are shown in here for convenient discussion, as sharp peaks appeared in these ranges.

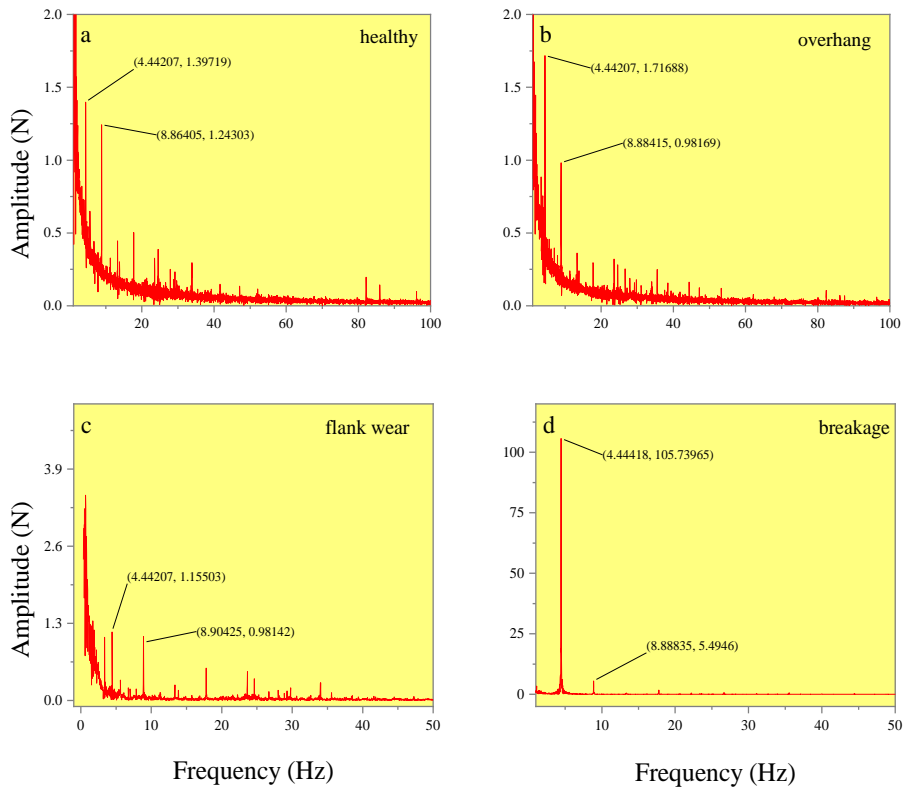


Figure 4.14 Spectrum plots of cutting force signal for various tool conditions

### 4.6.3 Wavelet analysis of cutting force

Figures 4.15 to 4.18 show the wavelet analysis of cutting force signal for healthy, overhang, flank wear and broken tool, respectively. Only low-frequency components were present in the plot in all time stamps. However, the amplitude level kept increasing from healthy to overhang, flank wear, and broken tool. Additional frequency components were seen in flank wear due to rubbing of a worn flank face with the machined parts. The broken tool has only low frequency but high amplitude due to sharp edges formed after breakage. These sharp edges get blunt and form newer sharp edges, which is evident from the reduction of amplitude from 0 to 0.6 s which further increases from 0.6 s to 1 s in Figure 4.18.

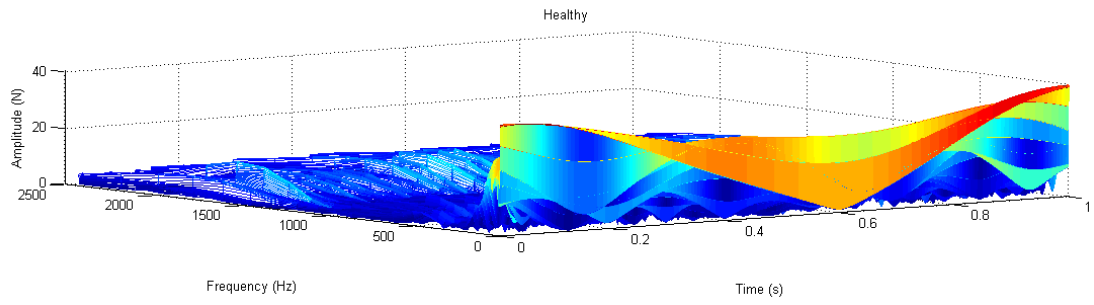


Figure 4.15 Wavelet plot of healthy tool – cutting force

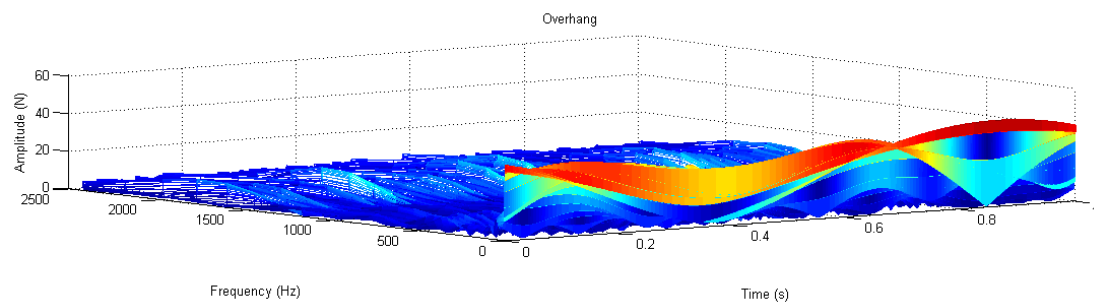


Figure 4.16 Wavelet plot of overhanging tool – cutting force

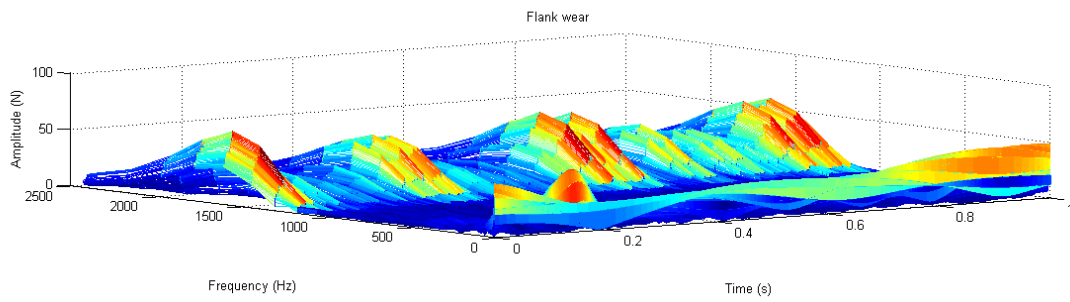


Figure 4.17 Wavelet plot of worn flank – cutting force

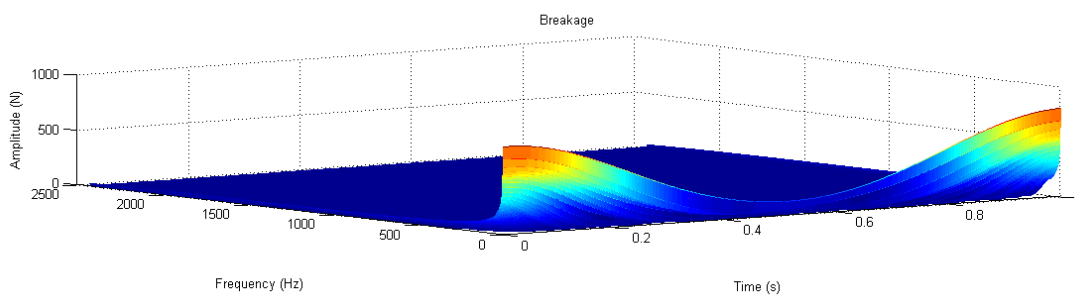


Figure 4.18 Wavelet plot of broken tool - cutting force

#### 4.7 TOOL FAULT DIAGNOSIS BY MACHINE LEARNING

Sequential steps followed for fault diagnosis of single point cutting tool during hard turning are shown in Figure 4.11. Both healthy and simulated faulty tools were used for machining oil-hardened nickel steel workpieces. Cutting force and vibration

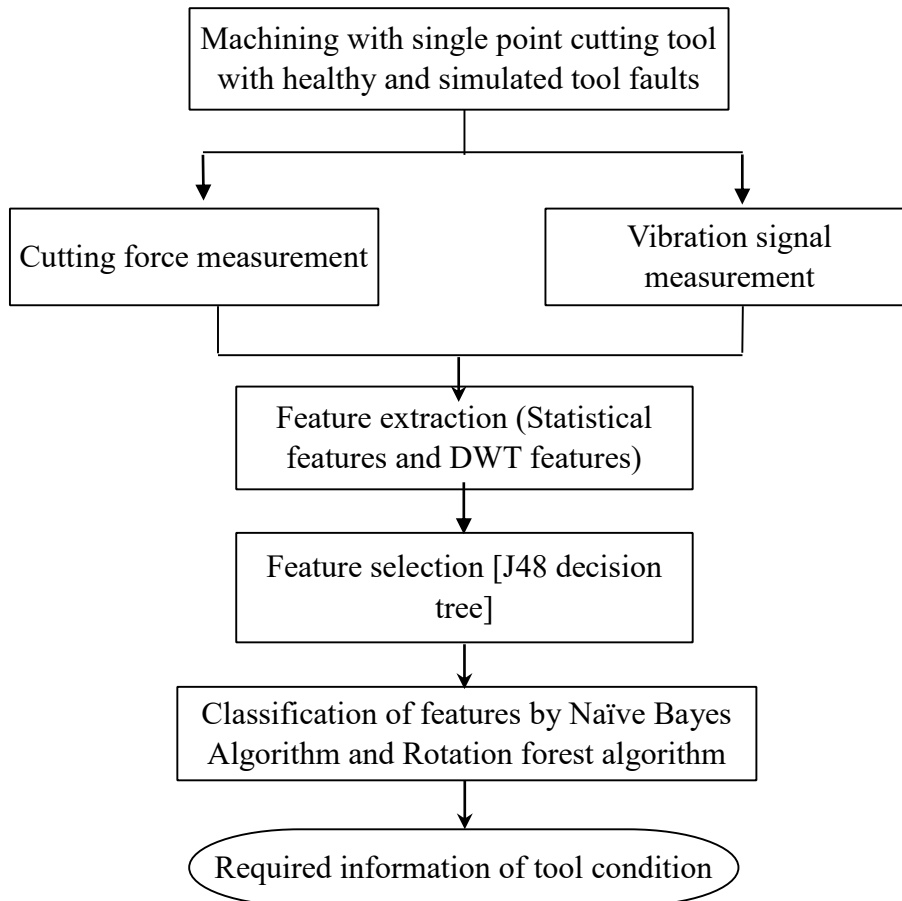


Figure 4.19. Methodology followed to classify tool faults using machine learning technique.

signals were acquired using a cutting tool dynamometer and accelerometer. Pre-processing of the signal was carried out independently for each signal type to feed to the transformation tool. Discrete wavelet features were extracted from the signals through discrete wavelet transform (DWT), a MATLAB code. DWT yields 8 wavelet coefficients (features) for each single second of data. Significant features are selected from the coefficients yielded by DWT. This selection of significant features was made by the J48 decision tree algorithm. The tree represents the significant features for classification in pictorial form with the logic of classification visible explicitly. A



decision tree can be used as a feature selector as well as a classifier if, it provides good classification accuracy; else, different other classifiers are tested to classify the tool conditions. In the current study Naïve Bayes algorithm to classify the tool faults. Since two signal types are used, the classification accuracy obtained with vibration and cutting force signals were compared to see which sensor signal is more suitable for tool fault classification.

#### **4.7.1 Wavelet Transform Analysis**

Wavelet as a mathematical tool that divides a continuous-time signal into different scale components. The wavelets are scaled and translated over a finite-length waveform. This finite length waveform is known as a mother wavelet and scalable and translatable wavelets are called daughter wavelets. Wavelet transforms can represent functions that have discontinuities and sharp peaks. Wavelet transformation deconstructs and reconstructs non-stationary signals accurately, whereas traditional Fourier transform fails to do so (Wang et al. 2007).

Wavelet transforms are used to transform data, and then encode the transformed data. Wavelet transforms can be of two types. First, discrete wavelet transforms (DWTs); second, continuous wavelet transforms (CWTs). DWTs use a specific subset of scale and translation values. CWTs operate over every possible scale and translation and CWT are generally used for signal analysis (Sugumaran et al. (2016), Kumar, H., Sugumaran, V., Amarnath, M. (2016)).

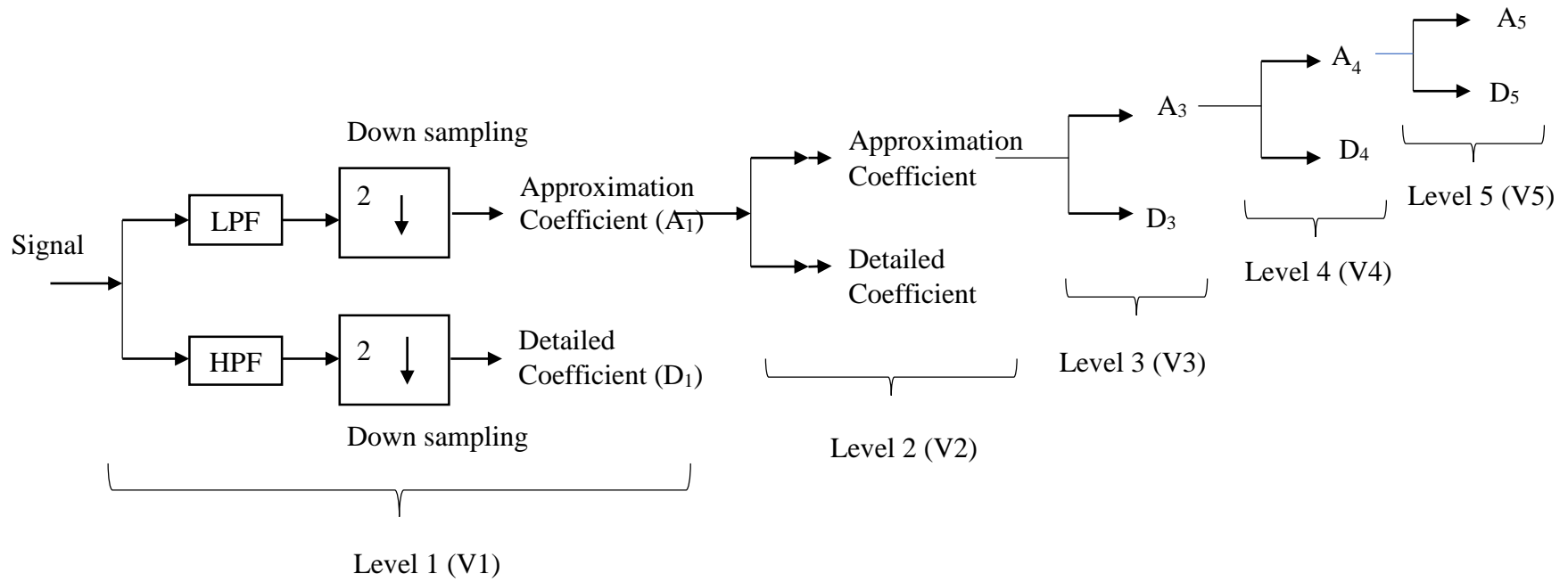


Figure 4.20 Signal decomposition to obtain approximation coefficient and detailed coefficient

#### 4.7.2 Feature extraction using discrete wavelet transform

The effective way of representing large data (signal) is achieved by correlating with approximation coefficients. These coefficients contain the most useful information in the dataset (Madhusudana et al., 2016a). Decomposed signal has detail coefficients and approximation coefficients. Detailed coefficients describe high-frequency coefficients, while approximation coefficients describe low-frequency coefficients Sundararajan, D. (2015). Approximation coefficients will be considered in each feature vector for the formation of the vector which is shown in pictorial form in Figure 4.20. Feature V1 is level one decomposition. V2 is level two decomposition and so on.

Wavelet considered for the present study is the Haar wavelet. Haar low pass filter computes simple average while Haar high pass filter computes simple difference. The basis function for the DWT is the filter coefficients.

The DWT feature vector is given by,

$$v^{dwt} = \{v_1^{dwt}, v_2^{dwt}, \dots, v_n^{dwt}\}^T \quad (4.8)$$

$v_i^{dwt}$  is the element associated with the different resolutions and can be calculated as follows,

$$v_i^{dwt} = \frac{1}{n_i} \sum_{j=1}^{n_i} W_{i,j}^2; i = 1, 2, \dots, 8 \quad (4.9)$$

$$n_1 = 2^8, n_2 = 2^7, \dots, n_8 = 2^0 \quad (4.10)$$

$v_i^{dwt}$  is  $i^{\text{th}}$  feature vector element in a DWT vector,

$n_i$  is the number of samples in the sub-band,

$w_{i,j}^2$  is the sub band for the  $j^{\text{th}}$  detailed coefficient.

The pictorial representation of the decomposition is shown in Figure 4.21. The details of the DWT feature with its feature vector can be found in studies. The wavelet tree representation of the vibration signals gives a clear idea about how the original signal is reconstructed using the approximations and details at various levels. The coefficients obtained using this wavelet transforms are further subjected to statistical analysis and

the statistical features are extracted for all the signals and for all the wavelet coefficients from “D1” to “D8”. These features are used for classification and fault diagnosis. (Saravanan and Ramachandran 2010)

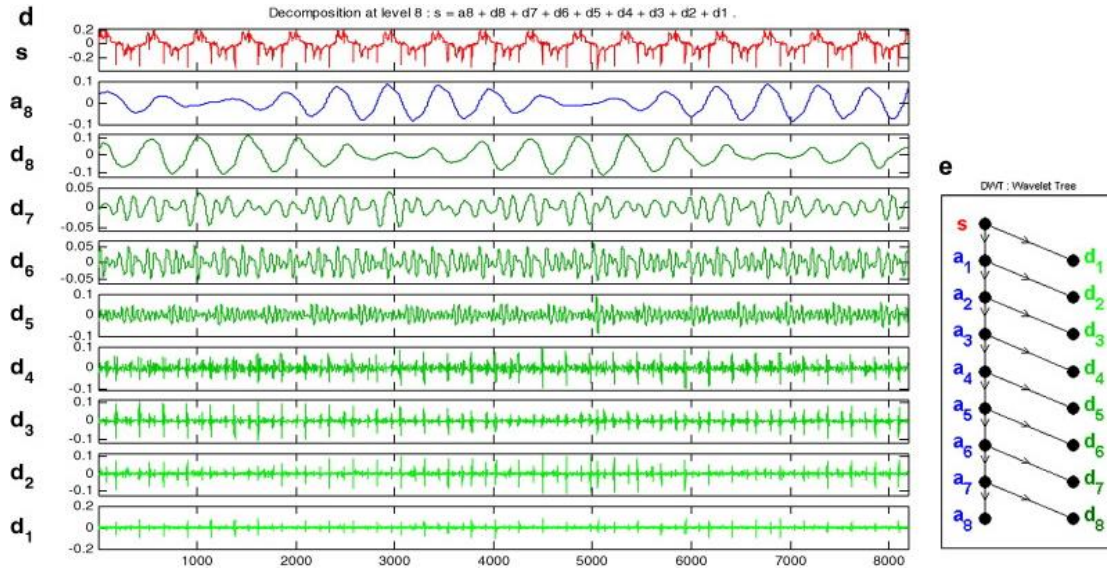


Figure 4.21 Decomposition level of signal using DWT (Saravanan and Ramachandran 2010)

DWT has different wavelet types: Haar, Daubechies, and Newland transform.

The mother wavelet function  $H(l)$  of the Haar wavelet is represented as Eq. 4.11(Chui 1992)

$$H(l) = \begin{cases} 1 & 0 \leq l < 0.5 \\ -1 & 0.5 \leq l < 1 \\ 0 & \text{else} \end{cases} \quad (4.11)$$

The scaling function  $S(l)$  of the mother wavelet is represented as

$$S(l) = \begin{cases} 1 & 0 \leq l < 1 \\ 0 & \text{else} \end{cases} \quad (4.12)$$

The **Haar function**  $H_{m,n}$  for every pair belonging to  $\mathbf{R}$  is

$$H_{m,n}(l) = 2^{\frac{m}{2}} H(2^m l - n), l \in R \quad (4.13)$$

Haar function supported on the right-open interval. It has integral 0 and norm 1 in the Hilbert space  $L^2(\mathbf{R})$ ,

$$\int_{\mathbf{R}} H_{m,n}(l) dl = 0, \|H_{m,n}\|_{L^2(\mathbf{R})}^2 = \int_{\mathbf{R}} H_{m,n}(l)^2 dl = 1 \quad (4.14)$$

$$\int_{\mathbf{R}} H_{m_1,n_1}(l) H_{m_2,n_2}(l) dl = \delta_{m_1,m_2} \delta_{n_1,n_2} \quad (4.15)$$

$\delta_{i,j}$  Represents Kronecker delta.

### 4.7.3 Selection of features using a decision tree

The decision tree represents decisions and decision-making rules visually and explicitly. Decision trees are simple to understand and make a reasonable interpretation of data and are effective ways of decision-making. They reduce ambiguity in decision-making. A decision tree displays the logic of classification for interpretation, unlike a neural network (NN) which uses a black box algorithm Sugumaran et al. (2013).

A decision tree has nodes, branches, and roots to represent the classification of samples. A node represents a feature (attribute), a branch represents a decision rule and a leaf represents an outcome. A decision tree will have a single root node for a whole training set of data (Anoop and Sugumaran 2017)). A new node is added to the tree for every partition.

The detailed steps involved in developing the decision tree are listed below:

- a. The tree starts with a node representing the training samples of data collected.
- b. If the samples are all of the same class, then they are labelled as a leaf.
- c. Otherwise, the algorithm will divide the samples into individual classes based on the entropy-based measure known as information gain by discretizing attributes to select the optimal threshold.
- d. To create the branch, samples are portioned for each interval.
- e. The algorithm uses the same steps mentioned above repeatedly to form the decision tree.
- f. This repetition process to form the tree stops only after one of the following criteria is met

- i. When all the samples of a node given belong to one class.
- ii. When there is no attribute remaining to partition the samples.
- iii. When samples get exhausted for the branch test attribute.

#### 4.7.4 Classification using Naïve Bayes classifier

Naïve Bayes classifier (NBC) belongs to a family of probabilistic classifiers built on the Bayes theorem of probability. It predicts the class of an unknown dataset. It is a simple but highly effective probabilistic learning method, applied to predictive diagnosis and other applications. The classifier relates the attribute set to the class variable by applying knowledge of probability and statistics. The classifier learns features of the training data set while analysing them. Madhusudana et al. (2014) used the Naïve Bayes algorithm to classify the healthy and faulty milling tool conditions, resulting in 96.9% classification accuracy. The algorithm assumes that all attributes ( $T_i$ ) are independent when given the class ( $K$ ) value.

Naïve Bayes uses the following steps for classification:

- Learning conditional probability of each attribute  $T_i$  from the class label  $K$ .
- Classification is done by applying the Bayes rule to compute the probability of  $K$  when  $T_1, \dots, T_n$  are given.
- The probability of a class  $K_i$  given an instance  $I = \{T_1, \dots, T_n\}$  for  $n$  observations is given by:

$$p(K_i|I) = p(I|K_i) \times p(K_i) / p(I) \quad (4.16)$$

$$\propto p(T_1, \dots, T_n | K_i) \times p(K_i) \quad (4.17)$$

$$= \prod_{j=1}^n p(T_j | K_i) \times p(K_i) \quad (4.18)$$

where,

- $p(I)$  = probability of predictor,
- $p(K_i)$  = prior probability of the class,
- $p(K_i/I)$  = posterior probability of class ( $C_i$ ) when predictor ( $I$ ) is given.

- $p(I/K_i)$  = probability of predictor when class is given

It is assumed that features are independent of each other for a set of random variables. It is impossible to estimate all the parameters without such an assumption  
Espinilla, M., Montero, J., Rodríguez, J. T. (2014). Naive Bayes is fast in response and, thus, could be used for making real-time predictions. It has a higher success rate while classifying multi-class predictions.

#### **4.7.5 Classification using rotation forest algorithm**

Rotation forest (RF) goals at constructing accurate and varied classifiers. RF is an ensemble technique that can distinctly train the ‘L’ number of decision trees. It transforms the data set while retaining all the information in the set. An ensemble classifier unites the predictions of several classifiers instead of only one classifier. Because ensemble reduces the variance and bias. It is essential to alter the data set bagging, boosting or learning method to create different classifiers.

Let  $X = [x_1, x_2 \dots x_n]^T$  a data point with n features and  $X$  is an  $N \times n$  matrix containing the training examples.  $Y = [y_1, y_2 \dots y_n]^T$  is a class label with c classes. Assuming that true class labels of all training examples are also provided. The ensemble vector is  $D = \{D_1, D_2 \dots D_L\}$ , where L is a number of different classifiers in the ensemble and F, is the feature set. All classifiers can be trained in parallel. A detailed study was carried out by Rodríguez et al.(2006)

### **4.8 RESULTS AND DISCUSSION**

The detailed discussion of the results of feature extraction, feature selection and classification of the tool faults using cutting force signal data is explained in this section.

#### **4.8.1 Feature extraction for cutting force using DWT**

In the current study, the ‘Haar’ wavelet was used in the discrete wavelet transformation. The DWT extracted 8 features (V1 to V8) from each signal. There were a set of 120 signals with 30 signals for each class. The classes considered are healthy, overhang, flank wear and broken tool. Table 4.6 shows only 4 signals for each class for reference.

Table 4.5. Discrete wavelet features extracted from the cutting force signal

Wavelet coefficients								Class
V1	V2	V3	V4	V5	V6	V7	V8	
14.30	11.80	13.10	20.50	46.50	102.00	40.40	130.00	Healthy
15.40	12.00	12.70	24.00	62.00	142.00	41.60	112.00	
19.50	13.40	14.00	25.00	53.00	145.00	55.00	204.00	
17.30	13.00	14.30	23.30	52.80	123.00	66.20	183.00	
16.00	12.80	14.10	27.00	82.10	240.00	74.70	187.00	Overhang
18.00	14.40	14.70	24.50	60.10	127.00	61.20	185.00	
17.50	14.60	14.30	31.80	89.50	244.00	76.30	194.00	
16.50	14.10	13.50	24.30	55.60	111.00	51.80	158.00	
345.0	240.0	66.90	99.50	66.10	173.00	49.40	122.00	Flank wear
269.0	187.0	52.60	80.40	55.70	133.00	46.10	154.00	
199.0	141.0	41.20	65.90	70.30	197.00	57.20	141.00	
278.0	194.0	62.90	133.0	381.0	1210.0	103.0	424.00	
9.05	8.36	10.80	28.30	103.0	556.00	2700	19600	Broken tool
9.08	7.84	10.40	26.50	118.0	588.00	2930	21400	
9.19	8.32	10.50	25.20	97.60	530.00	3010	22400	
8.54	7.98	9.80	23.90	98.00	437.00	2890	21300	

#### 4.8.2 Feature extraction for vibration signal using DWT

As for the cutting force signal, the vibration signal was transformed to obtain wavelet coefficients tabulated in Table 4.7. The tool condition and feature extraction method also remained the same for the vibration signal.



Table 4.6 Discrete wavelet features extracted from the vibration signal

Wavelet coefficients								Tool condition / Class
V1	V2	V3	V4	V5	V6	V7	V8	
0.051	0.144	0.260	0.074	0.068	0.049	0.040	0.046	Healthy
0.050	0.142	0.271	0.073	0.069	0.043	0.037	0.048	
0.052	0.148	0.267	0.071	0.067	0.049	0.029	0.051	
0.050	0.149	0.240	0.078	0.071	0.048	0.028	0.039	
0.157	0.510	1.110	0.837	0.391	0.160	0.151	0.070	Overhang
0.151	0.486	1.090	0.932	0.365	0.157	0.149	0.091	
0.157	0.479	1.050	0.905	0.420	0.161	0.144	0.105	
0.163	0.506	1.110	0.926	0.450	0.170	0.126	0.079	
0.248	0.979	2.340	2.730	1.170	1.080	0.356	0.241	Flank wear
0.253	0.959	2.440	2.870	1.130	1.100	0.373	0.308	
0.266	1.010	2.370	3.010	1.030	0.963	0.310	0.245	
0.278	1.060	2.490	3.060	0.994	0.925	0.260	0.275	
1.980	4.770	4.150	4.750	0.901	1.250	0.441	0.337	Breakage
2.020	4.590	3.540	3.880	1.040	0.986	0.426	0.267	
2.290	4.970	3.960	4.610	1.260	1.610	0.531	0.327	
2.210	4.570	3.740	4.020	1.210	1.210	0.371	0.335	

### 4.8.3 Decision tree for feature selection

The J48 algorithm was used to form the decision tree. The algorithm was fed with labelled wavelet coefficients to classify the classes which were derived from DWT. Out of 8 features extracted in DWT, only 6 features were used by the decision

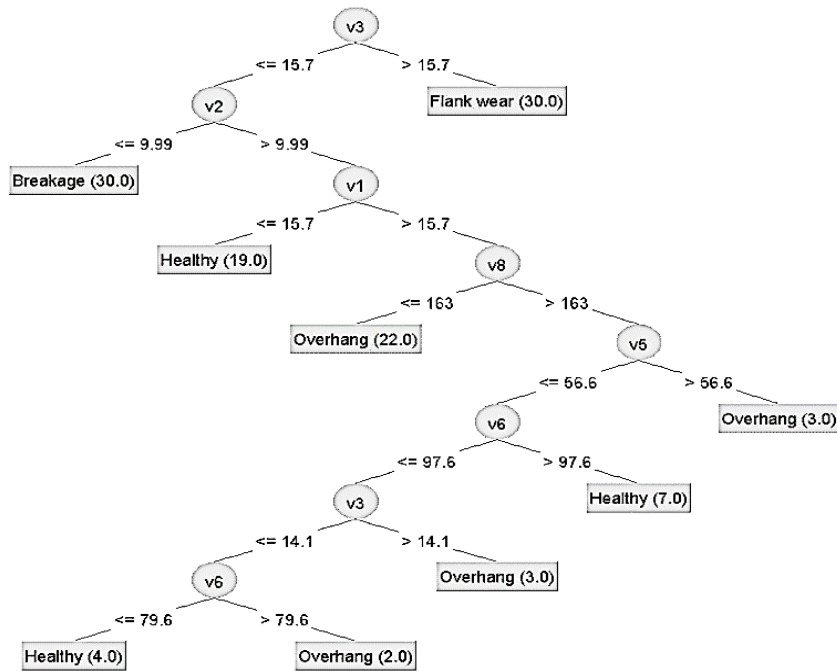


Figure 4.22 J48 decision tree for cutting force

tree to classify the tool state. In a decision tree, the classes are represented by rectangular boxes. The box contains several instances classified correctly and those classified incorrectly using the rule mentioned in the branch. The decision tree formed is shown in Figure 4.22. All instances of flank wear were classified using a single feature, V3, and all instances of the broken tools were classified using two features, V3 and V2. Healthy and overhang were classified using 6 features with 14 branches. These two classes required more features and branches because of data similarity in both classes. To classify the flank wear feature, V3 should be greater than 15.7. To classify breakage, V3 should be less than or equal to 15.7, and V2 should be less than or equal to 9.99. Flank wear and broken tool used one and two features, respectively, because of their well-distinguished pattern in their signal and feature. However, six features

were used to classify overhang and healthy because of data overlap. Thus, they required feature inside feature to classify them.

Figure 4.23 represents a decision tree formed from the wavelet coefficients of vibration signals. In Figure 4.22, V1 is the root node through which the whole tree is formed.  $V1 > 0.058$  among  $V1 < 0.168$  are classified as overhang else healthy or breakage. Similarly, flank wear is classified using V1, V2 and V5 and so on for the other classes.

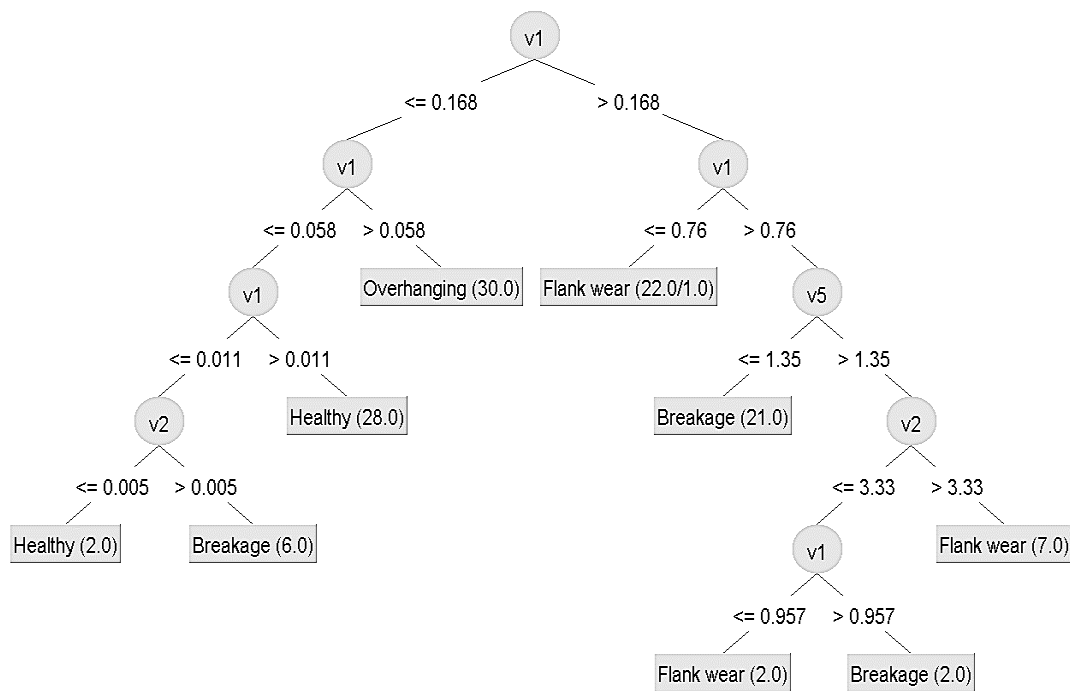


Figure 4.23 J48 Decision tree used for feature selection for vibration signal

#### 4.8.4 Classification using the Naïve Bayes algorithm for vibration signal

The Naïve Bayes algorithm used 10 fold cross-validation method, with 66% training data set and 34% testing data set. The confusion matrix in Table 4.7 represents the number of instances classified. Across the row are classes, and down the column are classified into various classes. Referring to the first row, out of 30 instances of a healthy class, 29 were classified as healthy, and one was misclassified as an overhang. In the second row, 27 out of 30 were correctly classified as overhang, while 3 were misclassified as healthy. Referring to the third row, all instances of flank wear were

correctly classified as flank wear. Referring to the fourth row, all instances of broken tools are classified correctly. The overall classification accuracy was 96.6 %.

Table 4.7 Confusion matrix for Naive Bayes classifier – vibration signal

classified as →	Healthy	Overhang	Flank wear	Broken tool
Healthy	29	1	0	0
Overhang	3	27	0	0
Flank wear	0	0	30	0
Broken tool	0	0	0	30

#### 4.8.5 Classification using Naive Bayes for cutting force

Table 4.8 shows the confusion matrix for cutting force signal where Naïve Bayes classified tool faults using vibration signal at 70% accuracy. i.e., 84/120 were correctly classified to their respective classes, and 36/120 were misclassified to other classes. This misclassification is due to data similarity in both classes and also an inefficient classification algorithm.

Table 4.8 Confusion matrix for Naive Bayes classifier for cutting force

classified as →	Proper	Overhang	Flank wear	Breakage
Healthy	30	0	0	0
Overhang	0	30	0	0
Flank wear	0	0	6	24
Breakage	6	0	6	18

#### 4.8.6 Classification using Rotation forest algorithm for cutting force

The classification using the significant features from the decision tree resulted in the following confusion matrix. The classifier is fair in classifying the flank wear and broken tool but poor in classifying the healthy and overhang conditions. Looking at Table 4.9, samples 25/30 have been classified correctly as healthy, whereas 5 are classified as an overhang. Similarly, 27/30 are classified as overhang, and 3 are

misclassified as healthy. The classification accuracy of the rotation forest for cutting force signal using DWT statistical features is 93.33 %.

Table 4.9 Confusion matrix of rotation forest algorithm for cutting force signal

classified as →	Healthy	Overhang	Flank wear	Broken tool
Healthy	25	5	0	0
Overhang	3	27	0	0
Flank wear	0	0	30	0
Broken tool	0	0	0	30

#### 4.8.7 Classification using Rotation forest algorithm for Vibration signal

The classification accuracy of the rotation forest algorithm for vibration signal using DWT features is also 93.33 %. However, none of the tool conditions is classified with 100 % confidence. Broken tool condition is misclassified as healthy as well as flank wear. Other such tool classifications can be referred to in Table 4.10

Table 4.10 Confusion matrix of rotation forest algorithm for vibration signal using DWT features

classified as →	Healthy	Overhang	Flank wear	Broken tool
Healthy	28	0	2	0
Overhang	0	29	1	0
Flank wear	0	0	29	1
Broken tool	2	0	2	26

#### 4.8.8 Classification using Random tree algorithm for cutting force

The random tree also gave a classification accuracy of 93.33% for the random trees using a cutting force signal with 100 % confidence in classifying flank wear and broken tool and 83.33 % confidence in classifying healthy state and 90 % confidence in classifying overhang.

Table 4.11 Confusion matrix of the random tree for cutting force signal using DWT features

classified as →	Healthy	Overhang	Flank wear	Broken tool
Healthy	25	5	0	0
Overhang	3	27	0	0
Flank wear	0	0	30	0
Broken tool	0	0	0	30

#### 4.8.9 Classification using Random tree algorithm for vibration signal

Random tree classified the tool conditions for vibration signal using DWT features at 93.33 % accuracy with 100 % confidence in classifying the healthy and overhang, whereas 90 % and 83.33 % confidence in classifying flank wear and broken tool, respectively. The confusion matrix is shown in Table 4.12.

Table 4.12 Confusion matrix of the random tree for vibration signal using DWT features

classified as →	Healthy	Overhang	Flank wear	Broken tool
Healthy	30	0	0	0
Overhang	0	30	0	0
Flank wear	0	0	27	3
Broken tool	0	0	5	25

#### 4.8.10 Comparison of various classifiers for their classification accuracy

Referring to Table 4.13, Random tree and rotation forest yielded the same classification accuracy of 93.33 %, whereas Naïve Bayes resulted in 96.6 % accuracy using a cutting force signal and 70 % using a vibration signal. The Naïve Bayes algorithm with DWT features using cutting force signal is recommended for better classification accuracy.

Table 4.13 Comparison of classification accuracy of various classifiers

Classifier	Rotation forest algorithm	Random tree	Naïve Bayes
Classification accuracy for cutting force (%)	93.33	93.33	70.00
Classification accuracy for vibration signal (%)	93.33	93.33	<b>96.6</b>

## 4.9 TOOL FAULT DIAGNOSIS BY MACHINE LEARNING USING STATISTICAL FEATURES

### 4.9.1 Statistical feature extraction

Statistical feature extraction is one basic signal processing technique that uses mathematical tools to transform raw non-linear signals into informative signatures against noise. A feature is a distinguishing property obtained from a section of a pattern (here, vibration signal). Features are extracted to represent the important information hidden in the signal by decomposing the signal. Statistical features extracted in the current study are mean, sum, minimum, maximum, variance, standard deviation, kurtosis, and skewness (Tiwari 2000). These features are described in Table 4.13.

Table 4.14 Statistical features and their definition.

Sl. No.	Terminology	Statistical formula	Description
1	Mean	$\mu_1 = \bar{X} = \frac{1}{n} \sum_{i=1}^n X_i$	A dimensional quantity that measures the central tendency of the distribution (a measure of location)

2	Variance	$\mu_2 = \sigma^2 = \frac{1}{n} \sum_{i=1}^n (X_i - \bar{X})^2$	A dimensional quantity that measures the spread about the mean or power of fluctuation from the mean
3	Higher statistical moments about mean	$\mu_k = \frac{1}{n} \sum_{i=1}^n (X_i - \bar{X})^k \text{ where } k = 3, 4, 5$	Higher moments
4	Standard deviation	$\sigma = \sqrt{\mu_2} = \sqrt{\frac{1}{n} \sum_{i=1}^n (X_i - \bar{X})^2}$	A dimensional quantity that measures the variability of the distribution or fluctuation from the mean
5	Skewness	$\chi = \frac{\mu_3}{\sigma^3} = \frac{\frac{1}{n} \sum_{i=1}^n (X_i - \bar{X})^3}{\sigma^3}$	A non-dimensional feature that measures the degree of asymmetry of the distribution (or shape of the distribution) about the mean.
6	Kurtosis	$\kappa = \frac{\mu_4}{\sigma^4} = \frac{\frac{1}{n} \sum_{i=1}^n (X_i - \bar{X})^4}{\sigma^4}$	A non-dimensional feature that



			reflects the peakedness of the distribution
7	Standard error	$Y = \sqrt{\frac{1}{(n-2)} \left[ \sum (y-\bar{y})^2 - \frac{\left[ \sum (x-\bar{x})(y-\bar{y}) \right]^2}{(x-\bar{x})^2} \right]}$	The standard error is a measure of the amount of error in the estimation of y

## 4.10 RESULTS AND DISCUSSION

### 4.10.1 Statistical feature extraction for the experimental dataset

Statistical features were extracted by Analysis of variance (ANOVA). The labelled dataset containing vibration signal information in tabular form is given to the software. Only tangential vibration was considered for the study, which was more dominant than the other directions. A one-second data of vibration signal of a class (tool condition) had 25600 data points. There were thirty seconds of data for each class; four classes were in the experiment. One second data set is reduced to twelve statistical features. There are 20 data sets for each case; however, only 5 samples for each case of vibration signal are shown for reference in Table 4.14 and cutting force data in Table 4.15.

Table 4.15 Statistical features extracted from the vibrational signal

Mean	Std Dev.	SE of mean	Variance	Sum	Skewness	Kurtosis	Mode	Min	Median	Max	Range	Case
0.045	0.311	0.002	0.097	1154.296	-0.003	0.089	-0.132	-1.303	0.045	1.302	2.605	Healthy
0.045	0.304	0.002	0.092	1143.689	0.003	0.018	-0.057	-1.087	0.044	1.220	2.308	Healthy
0.046	0.313	0.002	0.098	1165.604	-0.009	0.034	-0.187	-1.120	0.047	1.288	2.408	Healthy
0.045	0.313	0.002	0.098	1147.899	-0.003	0.098	-0.139	-1.306	0.045	1.340	2.646	Healthy
0.044	0.319	0.002	0.102	1132.472	-0.041	0.038	-0.088	-1.264	0.047	1.328	2.592	Healthy
0.044	1.702	0.011	2.896	1136.415	-0.007	0.010	-1.154	-8.834	0.038	6.716	15.550	Breakage
0.043	1.800	0.011	3.239	1089.782	0.022	0.033	1.134	-7.071	0.035	7.050	14.121	Breakage
0.045	1.740	0.011	3.029	1143.698	0.001	0.080	-1.261	-9.017	0.047	6.707	15.725	Breakage
0.044	1.741	0.011	3.032	1127.773	0.035	0.181	0.502	-7.467	0.053	7.658	15.125	Breakage
0.044	1.702	0.011	2.896	1136.415	-0.007	0.010	-1.154	-8.834	0.038	6.716	15.550	Breakage
0.042	0.943	0.006	0.890	1085.294	-0.032	0.140	-0.201	-3.782	0.051	3.953	7.735	flank wear
0.044	0.953	0.006	0.908	1118.085	-0.033	0.019	0.583	-4.222	0.052	3.911	8.132	flank wear
0.042	0.959	0.006	0.919	1087.680	-0.006	0.112	0.016	-3.882	0.048	4.743	8.625	flank wear
0.043	0.977	0.006	0.954	1108.934	-0.011	0.085	-0.678	-3.813	0.046	4.594	8.408	flank wear
0.043	0.972	0.006	0.944	1105.077	-0.025	0.011	-0.423	-4.001	0.050	4.150	8.151	flank wear
0.045	0.643	0.004	0.414	1153.358	-0.003	0.044	-0.057	-2.857	0.045	2.347	5.204	Overhang
0.044	0.638	0.004	0.408	1131.619	0.023	0.035	-0.343	-2.683	0.042	2.677	5.360	Overhang
0.044	0.635	0.004	0.404	1134.998	-0.004	0.080	0.155	-2.529	0.043	2.573	5.102	Overhang
0.044	0.650	0.004	0.422	1118.950	-0.025	-0.060	0.150	-2.410	0.049	2.613	5.023	Overhang
0.044	0.665	0.004	0.442	1137.582	-0.016	0.139	-0.189	-2.793	0.049	2.686	5.478	Overhang

Table 4.16 Statistical features extracted for cutting force signals

Mean	Std Dev.	SE of mean	Variance	Sum	Skewness	Kurtosis	Mode	Min	Median	Max	Range	Case
280.786	6.51024	0.0504	42.3832	4.68E+06	-0.066	-0.08936	281.128	251.831	280.884	304.443	52.612	Healthy
281.667	7.63723	0.0591	58.3273	4.69E+06	-0.006	-0.60375	281.128	258.911	281.738	305.054	46.143	Healthy
275.821	6.72561	0.0521	45.2337	4.60E+06	0.102	-0.25895	277.344	254.761	275.757	302.612	47.851	Healthy
276.880	5.43767	0.0421	29.5682	4.61E+06	0.118	-0.21511	274.414	257.446	276.611	299.561	42.115	Healthy
272.935	7.60061	0.0588	57.7693	4.55E+06	-0.039	-0.21117	273.071	247.437	273.071	301.758	54.321	Healthy
273.907	5.96785	0.0462	35.6152	4.56E+06	0.015	-0.08019	275.391	251.831	273.926	298.096	46.265	overhang
276.652	5.49332	0.0425	30.1765	4.61E+06	0.042	0.17858	278.442	255.859	276.611	303.101	47.242	overhang
270.239	6.519	0.0505	42.4973	4.50E+06	0.224	-0.12163	270.02	249.512	269.897	294.922	45.41	overhang
271.819	6.58445	0.051	43.3549	4.53E+06	-0.064	-0.30119	271.24	241.821	271.851	295.288	53.467	overhang
271.413	5.205	0.0403	27.0920	4.52E+06	-0.133	0.10844	271.362	249.268	271.484	291.992	42.724	overhang
243.196	108.181	0.8379	11703.2	4.05E+06	-0.188	-1.44366	380.859	69.8242	258.667	405.884	336.059	flank wear
233.244	112.044	0.8679	12553.8	3.89E+06	-0.031	-1.50529	83.0078	64.8193	240.479	412.598	347.778	flank wear
233.549	110.239	0.8539	12152.6	3.89E+06	-0.105	-1.4883	376.831	62.8662	244.995	400.269	337.402	flank wear
239.089	113.786	0.8814	12947.3	3.98E+06	-0.109	-1.49428	71.5332	60.791	250.61	412.109	351.318	flank wear
226.818	114.336	0.8856	13072.7	3.78E+06	-0.006	-1.49508	71.4111	58.2275	231.567	408.081	349.853	flank wear
308.635	12.3694	0.0958	153.002	5.14E+06	0.022	0.06305	308.716	261.108	308.228	354.37	93.262	Breakage
312.544	11.2685	0.8729	126.979	5.21E+06	-0.092	0.07851	312.988	270.386	312.744	353.149	82.763	Breakage
312.363	11.6424	0.0901	135.547	5.21E+06	0.062	0.13988	312.378	267.822	312.5	355.347	87.525	Breakage
310.556	12.6979	0.0983	161.237	5.18E+06	0.095	-0.06706	303.345	267.578	310.425	363.525	95.947	Breakage
306.706	12.5416	0.0971	157.292	5.11E+06	0.019	0.07877	304.81	261.475	306.763	354.736	93.261	Breakage

### 4.10.2 Feature selection using the J48 decision tree

Figure 4.24 shows the decision tree which used seven features namely, SE of mean, Standard deviation, variance, Kurtosis, sum, maximum and skewness for the classification of features. These features serve as input to the classification algorithm. Looking at the decision tree diagram, one can observe that the ‘overhang’ class has been classified with two features; the ‘proper’ class has been classified with three features; the ‘Flank wear’ is classified with five features, and the ‘breakage’ is classified using seven features. The class, which uses more features, have data similarity with other classes.

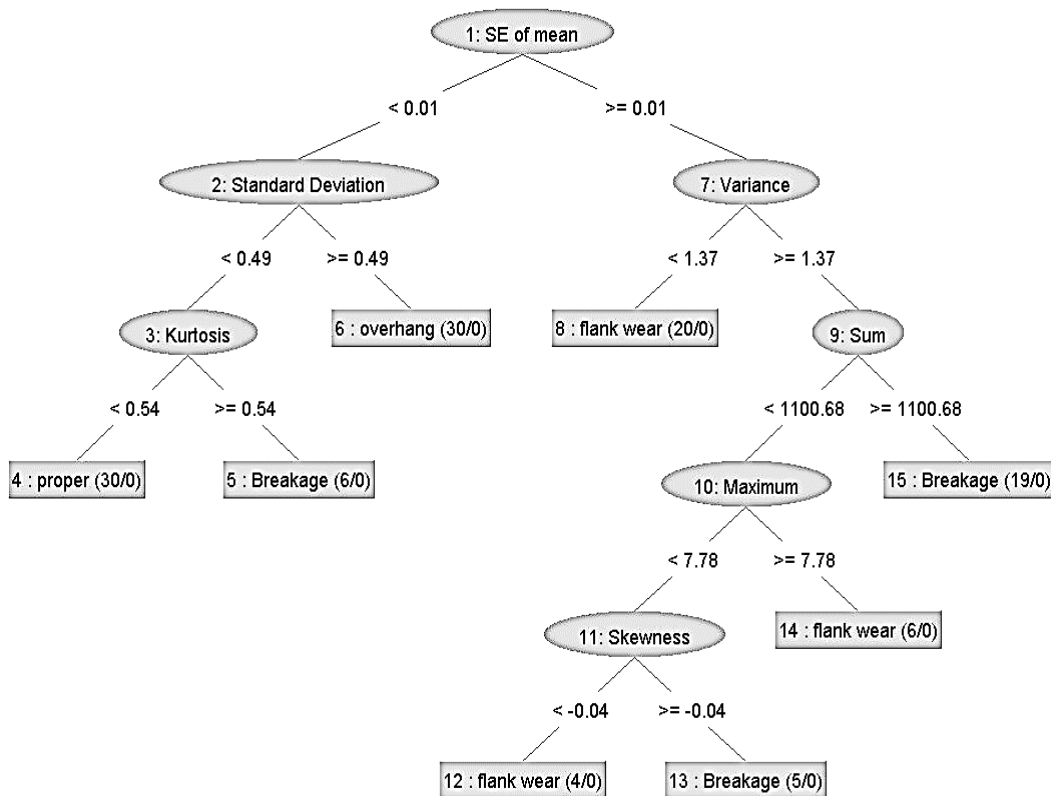


Figure 4.24 Decision tree (J-48) based on statistical features of vibration data

Similarly, Figure 4.25 shows the decision tree based on statistical features of the cutting force signal. Only two significant features are selected (Maximum, Sum).

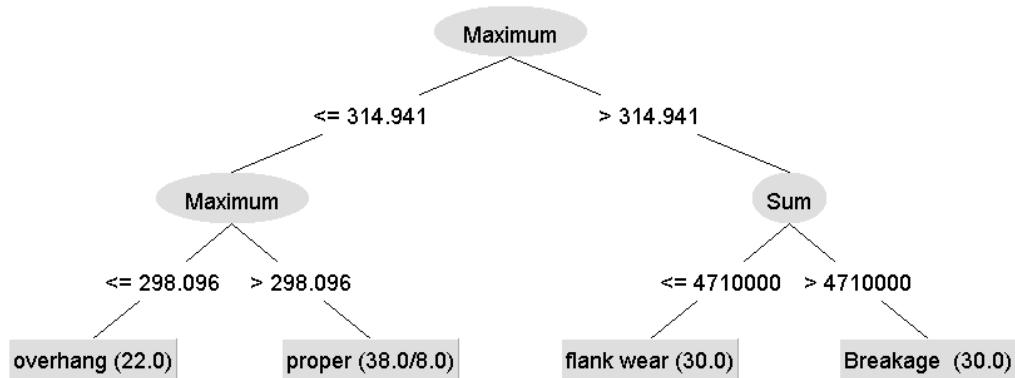


Figure 4.25 Decision tree based on statistical features of cutting force signal

### 4.10.3 Classification using various classifiers

#### 4.10.3.1 Random tree

Table 4.16 shows the confusion matrix of the Random tree for vibration signal. The overall classification accuracy achieved by a random tree is 92.5 %, lesser than a random forest with 8 instances out of 120 miss classified. Similarly, the confusion matrix of a random tree for cutting force is shown in Table 4.17, which shows 89.16 % classification accuracy. Flank wear and breakage are classified without any miss classification, whereas healthy and overhang are classified with 76.6 % and 80.0 % confidence, respectively.

Table 4.17 Confusion matrix of Random tree – vibration signal

<b>j</b>	<b>k</b>	<b>l</b>	<b>m</b>	<b>← classified as</b>
29	0	1	0	j=healthy
0	30	0	0	k=overhang
0	0	29	1	l=breakage
0	0	6	24	m=flank wear

Table 4.18 Confusion matrix of Random tree-cutting force

<b>j</b>	<b>k</b>	<b>l</b>	<b>m</b>	<b>← classified as</b>
23	7	0	0	j=proper
6	24	0	0	k=overhang
0	0	30	0	l=breakage
0	0	0	30	m=flank wear

#### 4.10.3.2 Naïve Bayes classifier

Table 4.18 tabulates the classification chart of the Naïve Bayes classifier with an overall classification accuracy of 75.83 %, with 29 instances miss classified and 91 instances correctly classified. Naïve Bayes yielded the lowest classification accuracy using vibration signal compared to the rest of the classifiers. Table 4.19 tabulates the confusion matrix of the Naïve Bayes algorithm using a cutting force signal with an overall classification accuracy of 91.66 %. There is no confusion in classifying the breakage and flank wear; however, 4 samples of healthy are confused with overhang, and similarly, 6 of the overhang are confused with healthy.

Table 4.19 Confusion matrix of Naïve Bayes classifier – vibration signal

<b>j</b>	<b>k</b>	<b>l</b>	<b>m</b>	<b>← classified as</b>
28	0	2	0	j=healthy
0	30	0	0	k=overhang
0	0	10	18	l=breakage
0	0	7	23	m=flank wear

Table 4.20 Confusion matrix of Naïve Bayes classifier – cutting force

<b>j</b>	<b>k</b>	<b>l</b>	<b>m</b>	<b>← classified as</b>
26	4	0	0	j=healthy
6	24	0	0	k=overhang
0	0	30	0	l=breakage
0	0	0	30	m=flank wear

### 4.10.3.3 Rotation forest algorithm

In Table 4.20, the rotation forest algorithm has correctly classified all 30 instances of proper mount-healthy-state of tool. Extended overhang instances are also classified accurately. Breakage: 26 instances are correctly classified as Breakage. The rest four instances are misclassified as flank wear. Flank wear: 26 instances are correctly classified as flank wear, and the rest 4 are misclassified as Breakage. This misclassification is due to the similarity in features of Breakage and flank wear. The overall classification accuracy of the algorithm is 95.00 %.

Table 4.21 shows the confusion matrix of the rotation forest using the statistical features of the cutting force signal. The classification accuracy of the algorithm is 90.83 %. The algorithm is good at classifying the flank wear and breakage at 100 % confidence using a cutting force signal, whereas poor at classifying the healthy and overhang case.

Table 4.21 Rotation forest` confusion matrix – vibration signal

<b>j</b>	<b>k</b>	<b>l</b>	<b>m</b>	<b>← classified as</b>
30	0	0	0	j=proper
0	30	0	0	k=overhang
0	0	26	4	l=breakage
0	0	4	26	m=flank wear

Table 4.22 Rotation forest` confusion matrix – cutting force

<b>j</b>	<b>k</b>	<b>l</b>	<b>m</b>	<b>← classified as</b>
28	2	0	0	j=healthy
9	21	0	0	k=overhang
0	0	30	0	l=breakage
0	0	0	30	m=flank wear

#### 4.10.4 Comparison of classifiers

The comparison of all three classifiers for their classification accuracy is tabulated in Table 4.22. The Rotation forest algorithm gives the highest classification accuracy of 95 % using the statistical features of the vibration signal. It can be seen in Tables 4.16, 4.18, 4.20 that vibration signal is preferred for achieving reasonable confidence in classifying the healthy and overhang, whereas cutting force is preferable to achieve the highest confidence in classifying the flank wear and broken tool (Table 4.17, 4.19, 4.21). None of the cutting force, vibration signal, classifier, or statistical DWT features could give 100 % accuracy.

Table 4.23 Classification accuracy comparison using statistical features

Sl. No.	Classifier	Classification accuracy for vibration data (%)	Classification accuracy for cutting force data (%)
1	Rotation forest	<b>95.00</b>	90.83
2	Random tree	93.33	93.33
3	Naïve Bayes	75.83	91.66

The classification accuracy of all three classifiers corresponding to vibration and cutting force through DWT and statistical features are tabulated in Table 4.24. The classification accuracy of the vibration signal is better than the cutting force signal for both DWT and statistical features. However, Naïve Bayes gives good classification accuracy with DWT features, whereas Rotation forest gives good classification accuracy with statistical features.

Table 4.24 Classification accuracy of various classifiers for vibration and cutting force signal

Features	Signal	Rotation forest	Naïve Bayes	Random tree
DWT	Cutting force	93.33	70.0	93.33
	Vibration	93.33	<b>96.6</b>	93.33
Statistical	Cutting force	90.83	91.66	93.33
	Vibration	<b>95.0</b>	75.83	93.33



#### **4.10.5 SUMMARY**

The chapter discusses the tool fault diagnosis using signal processing and machine learning techniques applied to vibrational and cutting force signals. Accelerometer is easy to mount without any structural modification of the tooling structure, whereas a dedicated setup is to be established for installing the dynamometer for cutting force measurement. The tool faults can be diagnosed using the statistical parameters and visual inspection of the time domain signal. The rotational frequency and chatter frequency components could be identified, and their amplitude could be tracked using the frequency domain analysis. Wavelet analysis reveals both the time resolution and frequency resolution of the tool fault, making it the best way to identify the time of occurrence of the tool fault and the kind of tool fault.

In the current study, supervised machine learning with a labelled data set is used to train and test the vibrational and cutting force signals. Machine learning follows three steps for classification, namely feature extraction, feature selection and classification. Statistical features and wavelet features have been extracted for classification. The decision tree J48 algorithm is used for feature selection. Random tree, rotation forest, and Naïve Bayes algorithm are employed as the classifier, and their classification accuracy is compared. The results show that the vibration signal gives better classification accuracy than the cutting force signal; moreover, mounting the accelerometer and acquiring the vibrational signal is portable and versatile.

The next chapter discusses the damper design based on the level of vibration and cutting force produced by healthy and faulty tools. The healthy tool has a steady vibration pattern with the least standard deviation in the cutting force signal. Similarly, unsteady vibration with a large standard deviation is observed in faulty tools. The damping coefficient of the damper is to be adjusted to shift the unsteady machining state to a steady state. The detailed study of improved tool life can be achieved using the damper in the machining operation. The damper's ability to improve the machining operation's stability limit is also detailed in the next chapter.



## **CHAPTER 5**

### **DEVELOPMENT AND CHARACTERISATION OF MR DAMPER WITH OPTIMAL COMPOSITION OF MR FLUID**

#### **5.1 INTRODUCTION**

The MR damper is designed, developed and implemented by considering design input parameters obtained from preliminary turning experiments of healthy tools and faulty tools. Design of MR damper initiated with magnetostatic analysis of flow valve where geometric dimensions of flow valve of the damper are assigned and optimized. The magnetic material best suitable for achieving maximum flux density is evaluated by assigning material properties to the ANSYS model. The optimal composition of MR fluid is selected based on the desired shear stress from various samples prepared in-house. MR fluids are characterized on a Rheometer (Make: Anton Paar) to evaluate their rheological characteristics suitable for the damper. Commercial MR fluid (Make: Lord Corporation, 132 DG) is also used to compare the performance of in-house MR fluid. The damper is fabricated to optimise design parameters and tested on a damper testing machine to evaluate its dynamic behaviour under various current supplies.

#### **5.2 DETERMINING THE OPTIMAL COMPOSITION OF MRF FOR THE MR DAMPER**

Figure 5.1 shows the flowchart of the methodology followed to achieve the optimal particle loading and suitable viscosity of base oil that can result in maximum yield stress in ON-state concurrently with the maximum effective damping range. A preliminary study of solid particles is carried out with SEM characterisation, vibration sample magnetometer and particle size distribution to understand the morphology and magnetic properties of the carbonyl iron particles used in the study.

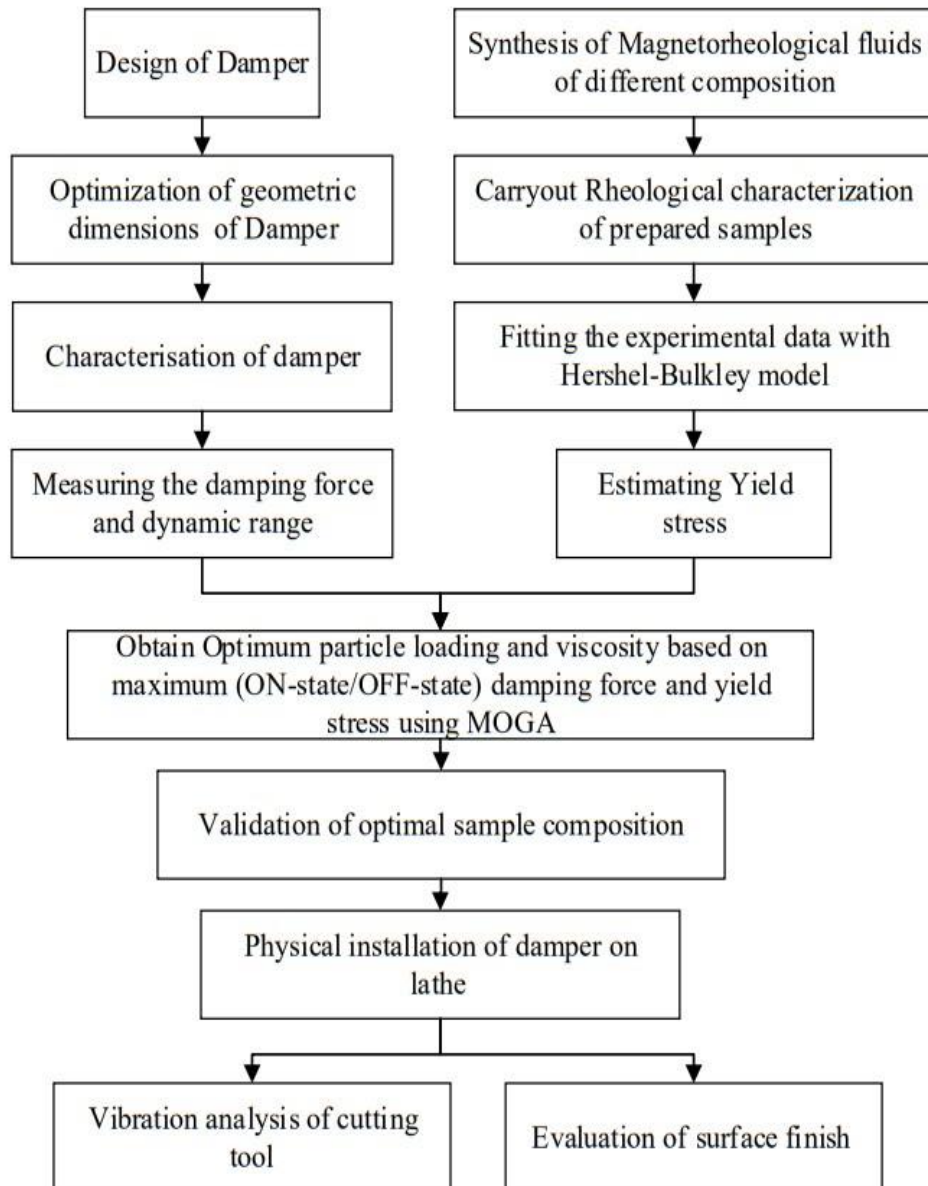


Figure 5.1 Methodology of fluid synthesis and evaluation of its performance

### 5.3 CHARACTERIZATION OF CARBONYL IRON PARTICLE (CIP)

The magnetisable solid particles dispersed in a liquid medium must possess significant properties that define the rheological characteristics of the MRF. It is referred from the literature that larger particle sizes have higher magnetic saturation than smaller carbonyl iron particles (Lemaire et al. 1998). Hence the particles considered for the study are tested for their particle size distribution. Figure 5.2 shows the mean diameters of CIP as 8.27  $\mu\text{m}$  with narrow distribution range.

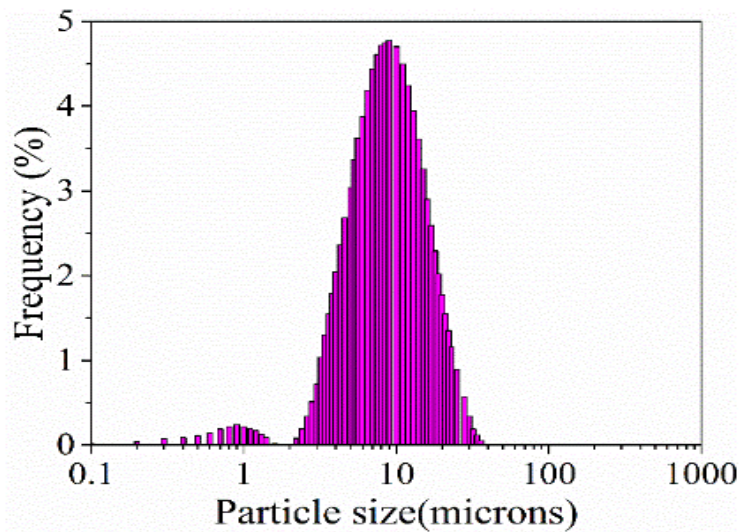


Figure 5.2 Particle size distribution of CIP

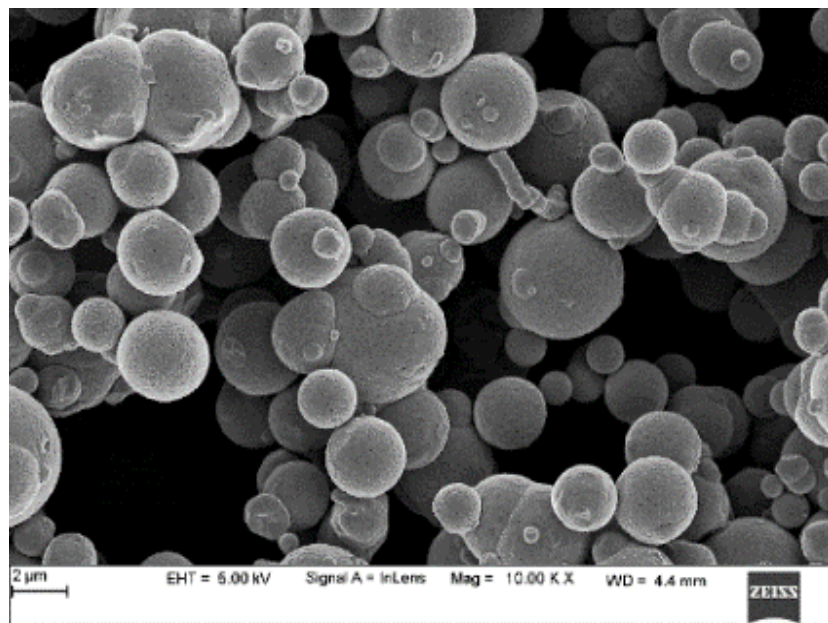


Figure 5.3 SEM image of CIP

Figure 5.3 shows the FESEM image of these CIP particles taken to reveal their shape morphology. They are spherical in shape and have better abrasion and adhesive wear resistance (Cho et al. 2002; Lemaire et al. 1998).

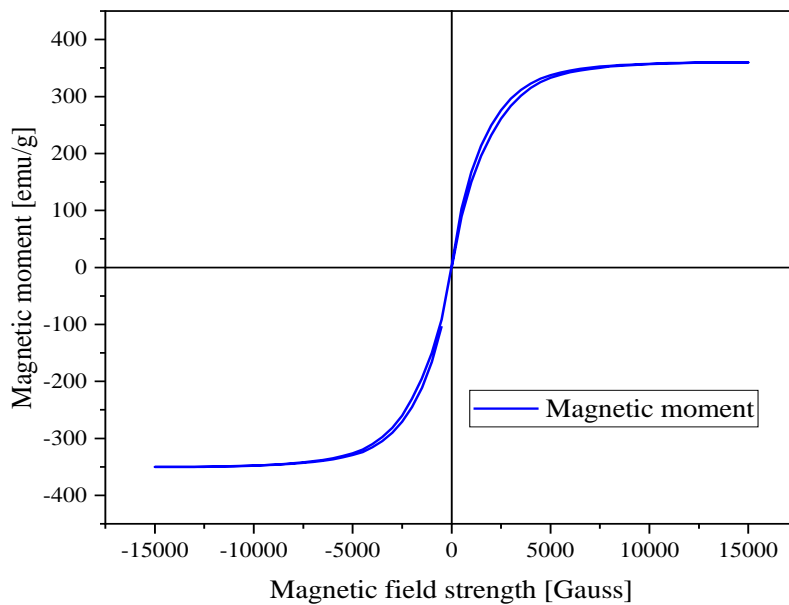


Figure 5.4 Magnetization curve of CIP

The magnetic permeability of MRF is proportional to the saturation magnetization of iron particles dispersed in them. For higher yield stress, the iron particles should have high saturation magnetization (Genç and Phulé 2002). The magnetic hysteresis curve of 8.27  $\mu\text{m}$  sized CIP has magnetic saturation at 15000 Gauss, as shown in Figure 5.4. The particles achieve a saturation limit at 6000 Gauss. To have a larger effective damping range, the iron particles must possess good reversibility of the MR effect with low coercivity and low residual magnetization. For good magnetic properties of CIP, MRF show little or no hysteresis. The crystal lattice structure of CI particles was found to be body centred cube (BCC) which is shown through peaks at  $45^\circ$ ,  $65.7^\circ$  and  $83^\circ$  as shown in Figure 5.5

#### 5.4 SYNTHESIS AND CHARACTERISATION OF MR FLUID

Silicone oil of 350 cSt (Si-350), hydraulic oil of 57 cSt (Hyd-57) (shock absorber oil) and silicone oil of 32 cSt (Si-32) are considered as a dispersed medium for the study. Silicone oil has high-temperature stability, whereas hydraulic oil has high

load-bearing capacity. Lower viscosity silicone oil is chosen to achieve low OFF-state viscosity, ensuring maximum effective damping range.

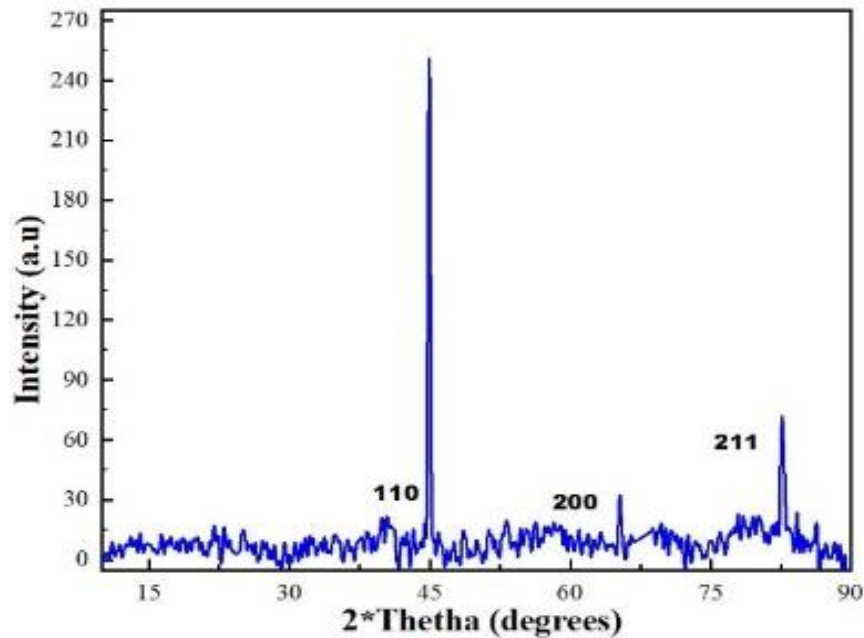


Figure 5.5 XRD image of the CIP

Nine MRF samples are prepared, as shown in Table 5.1, with a specification of samples and their nomenclature. The levels of parameters in synthesising the MRF samples are tabulated in Table 5.2. The OFF-state viscosity of MRF should be as low as possible to achieve maximum effective damping range with the MR damper; hence viscosity of oil has been chosen as one of the design parameters. A lower viscosity also supports a faster MRF reaction time and better iron particle re-dispersibility (Genç and Phulé 2002). White lithium grease at 2% of the base fluid mass was used as an additive to prevent agglomeration and sedimentation for all MRF samples. Initially, the proper mass of each base fluid, additive, and CIP is precisely measured. White lithium grease is mixed with base oil for about 8 hours, then CIP is mixed and stirred at 800 rpm for 12 hours.

Table 5.1 Nomenclature of MRF samples prepared for the experiment

Sample no	Base oil	Wt. fraction. (%)
S1	Hyd-57	70
S2	Hyd-57	60
S3	Hyd-57	50
S4	Si-350	70
S5	Si-350	60
S6	Si-350	50
S7	Si-32	70
S8	Si-32	60
S9	Si-32	50

Characterisation of these nine samples of MRF at 3 current inputs (0A, 0.7 A and 1.4 A) will result in 27 test samples. To reduce the number of test trials, DOE with central composite design (CCD) is employed. Table 5.6 with columns 2 and 3 were deduced from CCD (placed in section 5.7).

Table 5.2 Various levels of the parameters for DOE

Parameters	Levels		
	L1	L2	L3
Base oil viscosity (cSt)	32	57	350
Weight fraction (%)	50	60	70
Supply current to the electromagnet	0	0.7	1.4

Shear stress vs shear rate was measured for all nine MRF samples according to the sample set obtained by CCD using a parallel plate Rheometer (Figure 5.6) (Anton Paar MCR-702) in controlled shear rate (CSR) for different magnetic fields. A gap of 0.45 mm between the parallel plates and the temperature maintained at 30 °C. This same annular fluid flow gap is maintained between the piston and the cylinder in the damper. MRF's post-yield magnetorheological properties are typically modelled under sustained shear using the Herschel-Bulkley model (HBM) (Gołdasz and Sapiński 2015).



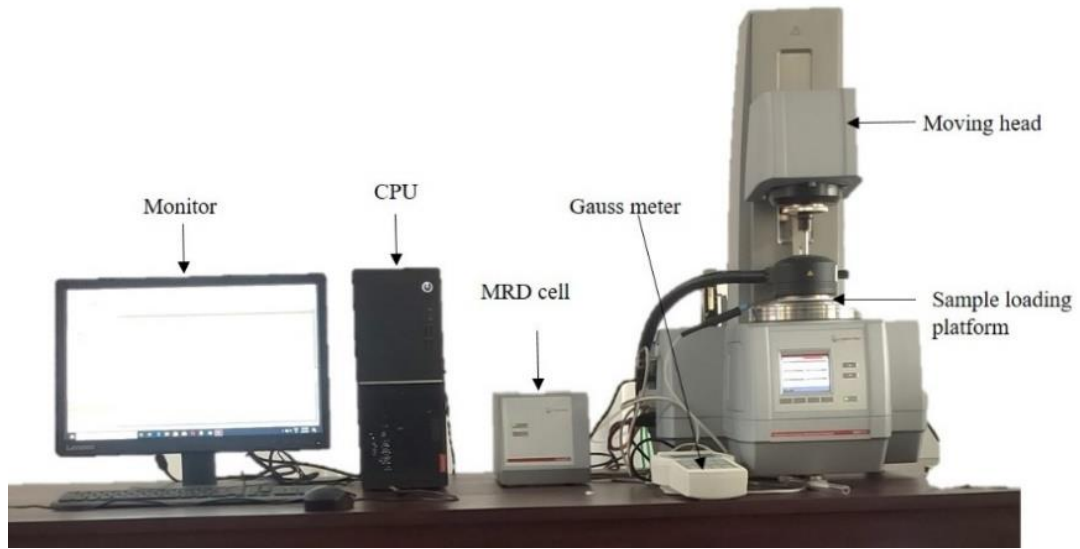


Figure 5.6 Rheometer to characterise MRF samples

Eq. 5.1 describes the HBM, which has three parameters: yield stress, consistency, and flow index. The model describes viscoplastic materials exhibiting a power-law relationship (Herschel and Bulkley 1926). Where  $\tau$  is applied shear stress,  $\tau_o$  is yield stress,  $K$  is consistency index,  $(du/dt)$  is the shear rate,  $n$  is the flow behaviour index. Fitting this equation to flow curves results in parameter values.

$$\tau = \tau_o + K \left( \frac{du}{dt} \right)^n \quad (5.1)$$

Figure 5.7 shows the plots of MRF characterised on the rheometer as a variation of shear stress against shear rate. The fluid samples were tested for 0 A, 0.7 A and 1.4 A currents corresponding to 0 kA/m, 30.647 kA/m and 56.588 kA/m field strength on the test platform of the rheometer. Each curve is fitted by Herschel–Bulkley model for all nine samples. Shear stress increases as particle loading of CIP and magnetic field strength. MRF with Si-350 displays higher shear stress than Si-32 and Hyd-57 at all particle loading except at 70 % wt fraction, indicating the particle loading has an equal influence on shear stress as the viscosity of the fluid. A similar trend is seen in the experimental work of Acharya et al. (2019) where shear stress increases with particle loading from 6000 Pa to 8000 Pa and then to 12000 Pa with particle loading increasing from 60 % to 70 % and then to 80 % respectively for particle size around 10  $\mu\text{m}$ . However, looking at the shear stress value at 1.4 A of 70 % wt fraction of Si 350 is less

than 60 % wt fraction indicating the MRF is saturated with particle loading. However, the 32 cSt and 57 cSt oil can accommodate still more particles. Hence 32 cSt oil and 57 cSt oil are further used to prepare 75%, 80 % and 85 % wt fraction samples. Table 5.3 shows increased yield stress, whereas, they attain saturation level at 80 % wt fraction. Hence it could be concluded that 80 % is the threshold loading value for 32 cSt and 57 cSt base oils and 60 % is the threshold particle loading for 350 cSt oil.

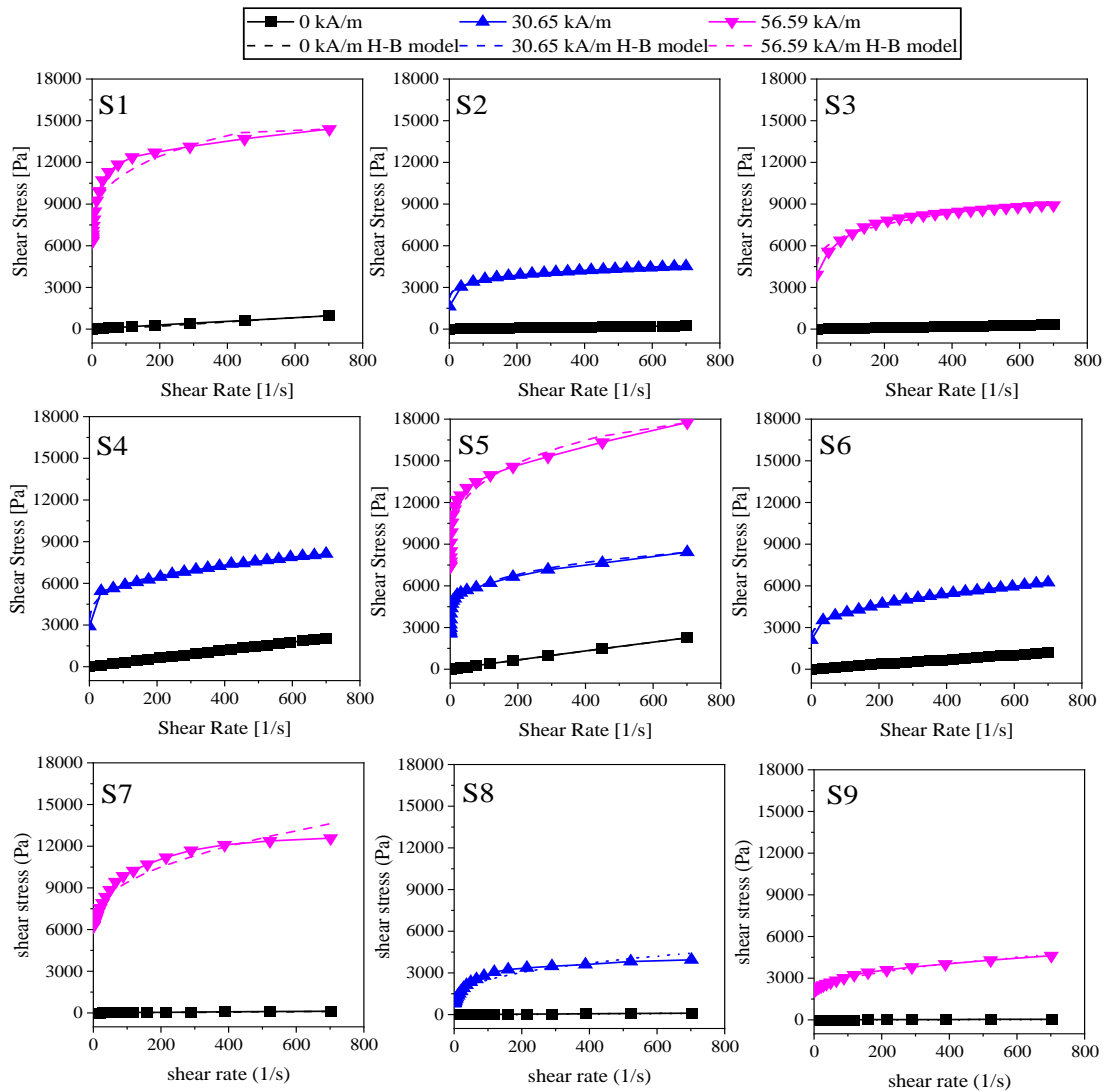


Figure 5.7 Flow curves of MRF samples

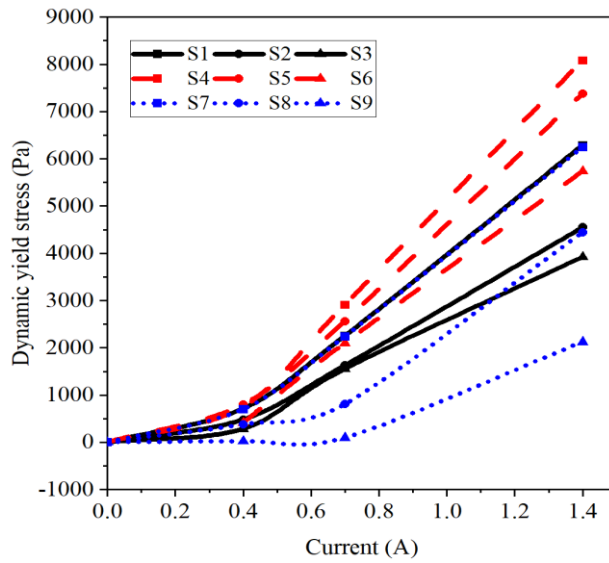


Figure 5.8 Plot of dynamic yield stress for fluid samples under magnetic field (for input current)

Figure 5.8 shows the variation of dynamic yield stress with varying magnetic fields. The yield stress is primarily influenced by the viscosity of base oil and then by particle loading. The least viscosity of base oil ensures adequate liquidity and minimal damping force at zero-field. Moreover, particle loading has a greater influence on shear stress for low-viscosity base oil, whereas marginal influence for high-viscosity base oil.

Figure 5.9 depicts the off-state viscosity vs. shear rate plot for prepared MRF samples. MRF viscosity decreases with increasing shear rate, indicating that the fluid shows shear thinning behaviour. Shear thinning behaviour approaches an asymptotic value as the shear rate increases.

Table 5.3 Estimating the saturation limit of particle loading

Sample name	Particle loading (%)	Base oil	Yield stress at 1.4 A
S10	75	Hyd-57	6896.4
S11	80	Hyd-57	7258.3
S12	85	Hyd-57	7025.1
S13	75	Si-32	6587.2
S14	80	Si-32	6912.6
S15	85	Si-32	6898.2

The equation obtained by fitting the curves to the plots in Figure 5.7 is used in estimating the damper's damping force, which is discussed in the further section.

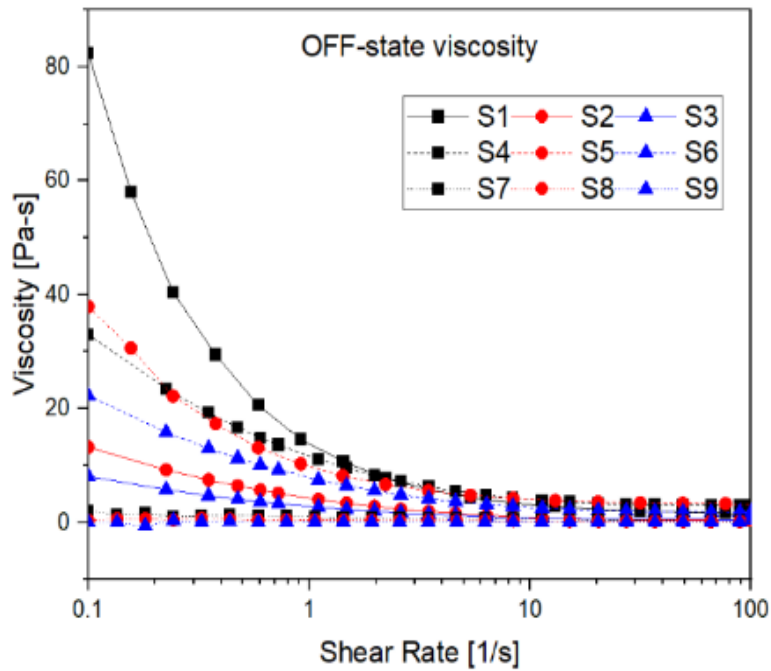


Figure 5.9 Viscosity curves of MRF under no magnetic field

## 5.5 DESIGN OF MR DAMPER

The MR damper consists piston–a cylinder system with modification at the piston head and fluid involved. The piston head has got electromagnet capable of providing a desired magnetic field to restrict the flow of MR fluid through the passage. The material used for the piston core and cylinder should be ferromagnetic to keep the magnetic flux line close to the restricted passage. In the present study, four different ferromagnetic materials are selected for both the piston and cylinder. The schematic diagram of the MR damper depicting the cylinder, piston, and electromagnet and MR fluid is shown in Figure 5.10. The constraints primarily are the size and shape of the

damper which can be accommodated in the limited space under the tool holder without compromising the machining process.

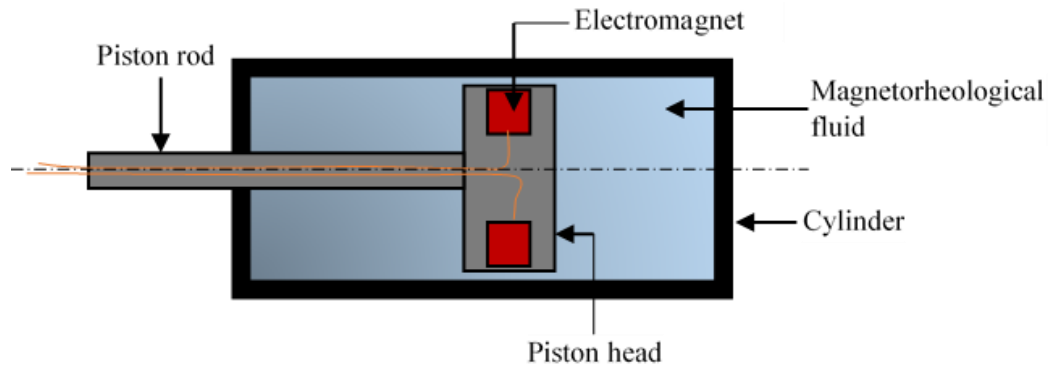


Figure 5.10 Schematic representation of MR damper in shear mode

### 5.5.1 Design of Magnetic Circuit

Designing an MR damper for an estimated damping force is achieved by developing a magnetic circuit which involves determining Ampere-turns ( $NI$ ) required to produce magnetic flux through the piston. The designed magnetic circuit can produce maximum flux density and allows maximum flux lines in the working zone.

The induction of magnetic flux and magneto motive force (MMF) in the circuit is explained using Ohm's law given as

$$\Phi = NI\mu A \quad (5.2)$$

Where,  $\Phi$  = magnetic flux produced in the coil,  $NI$  designates magneto-motive force with  $N$  being the number of turns and  $I$  the electric current passing through the coil,  $\mu$  = magnetic permeability of coil material,  $A$  = cross-sectional area.

The damper is made as compact as possible to accommodate it in limited space while considering all functional aspects. The number of coils calculated for the designed damper is 95, with a maximum current of 1.4 A. The gauge of the wire being used decides the electric current limit. Since a lower-diameter wire is desired to accommodate a maximum number of turns, the current is limited to 1.4 A.

The magnetic flux conservation rule establishes the relation between magnetic field intensity and the applied current as follows.

$$H_{MR} = \frac{NI}{2g} \quad (5.3)$$

The magnetic flux density developed at the annular gap of fluid flow is

$$B = \frac{\mu_o \mu_{MR} NI}{2g} \quad (5.4)$$

Where  $g$  = fluid flow gap,  $\mu_{MR}$  = relative permeability of MR fluid,  $\mu_o$ =magnetic permeability of free space

### 5.5.2 Designing finite element models of MR damper

The finite element model of the MR damper is shown in Figure 5.11, which is modelled and analysed using FEA. As the damper is geometrically symmetric, only one-fourth portion of the computational domain is considered for the analysis.

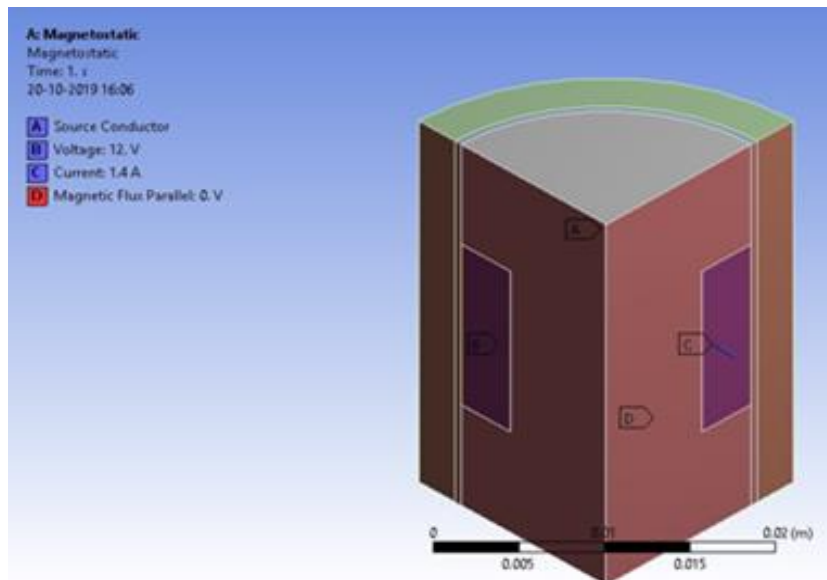


Figure 5.11 Electric boundary condition applied to magnetic circuit

Following assumptions are made during magneto static analysis,

- Flux lines pass through the cylinder and there is little leakage into the surrounding space.
- The magnetic flux lines are parallel to the surface.
- The model is axisymmetric; only one-quarter of a damper is analysed.

Magnetic flux density induced in the annular fluid flow gap depends on the material used for the piston and cylinder. In shear mode, the fluid lies between the cylinder and the piston. Choosing the material for the cylinder and piston of proper magnetic properties is also crucial apart from designing the electromagnet coil. Ferromagnetic materials allow magnetic flux lines to pass through the fluid gap, flow through cylinder material, cross across the fluid gap, and reach the piston again, thus closing the magnetic field path. Figure 5.11 also shows the feature selected for assigning electric boundary conditions.

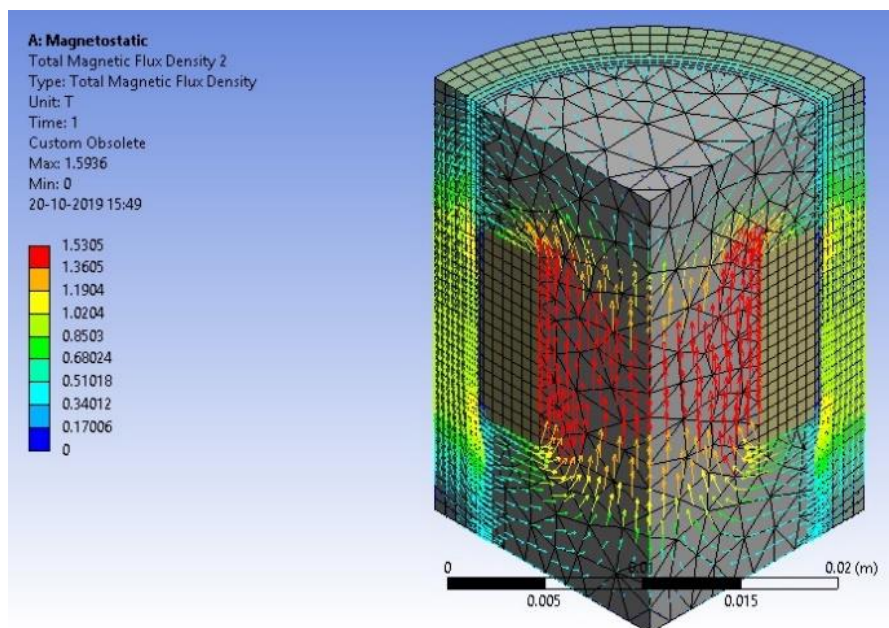


Figure 5.12 Flux lines around the MR flow valve

The magnetic field flow depends on the magnetic permeability of a material. The magnetic permeability of MR fluid is lesser than ferromagnetic material. According to electromagnetic field theory, field lines are parallel to the surface vector. The flux lines pass across the flow path, creating the required resistance to the flow of MR fluid through the passage while remaining parallel in the cylinder. The explanation is shown

in pictorial form in Figure 5.12, representing the flow of magnetic flux lines, and their directions in the magnetic circuit.

### 5.5.3 Comparison of finite element models

The magnetic flux density at the fluid gap is visualized by taking MR fluid elements separately for different materials, as shown in Figure 5.13 – 5.16. The magnetic flux density is maximum at the flange region. The plots also show the variation of flux density along the length of MR fluid (axially). Figure 5.13 shows the variation of magnetic flux density along the active region for various current inputs. The active region is the annular MR fluid surrounding the piston.

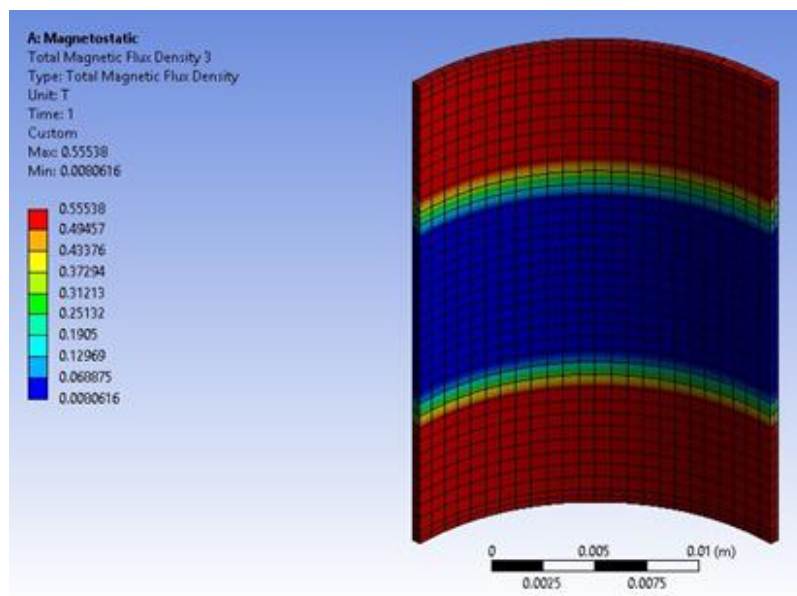


Figure 5.13 Magnetic flux density distribution in MR fluid element between piston and cylinder of material AISI 1008



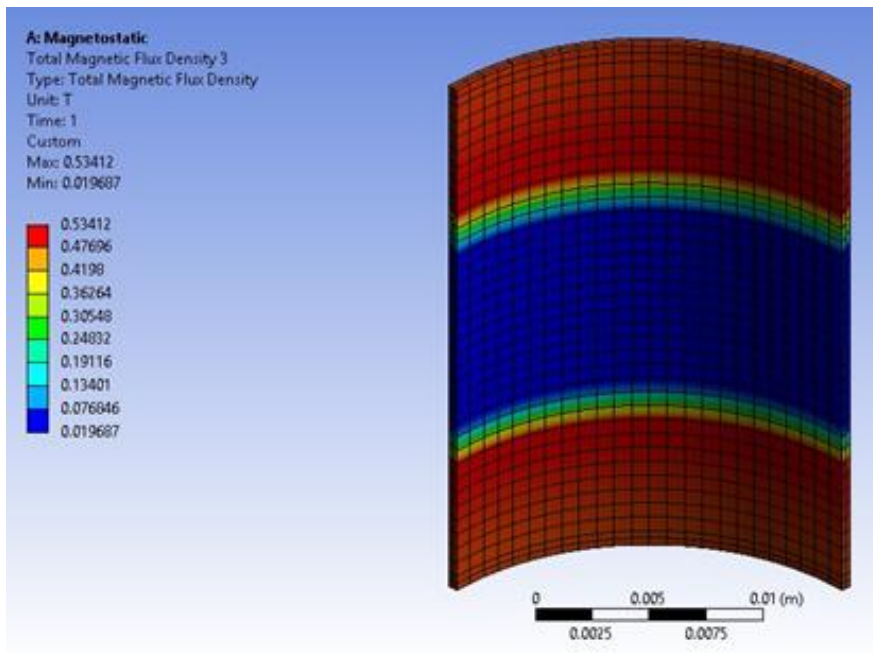


Figure 5.14 Magnetic flux density distribution in MR fluid element between piston and cylinder of material AISI 1010

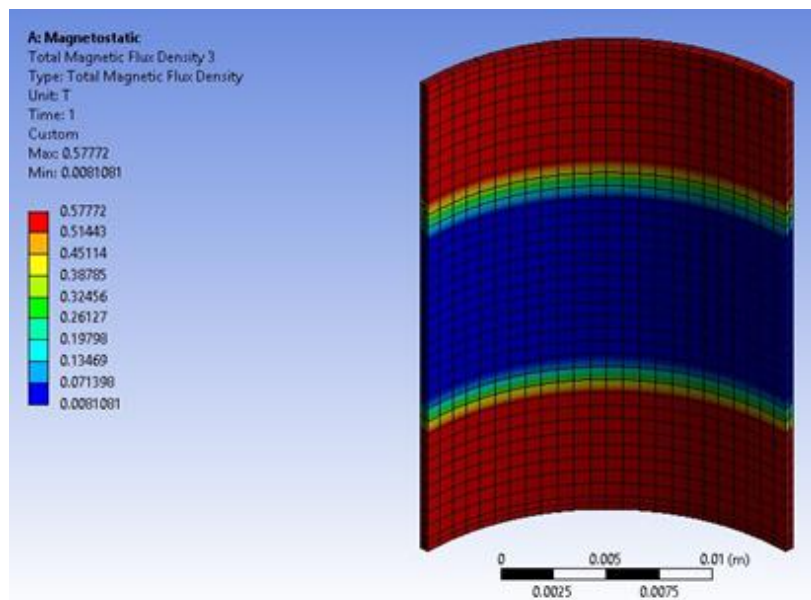


Figure 5.15 Magnetic flux density distribution in MR fluid element between piston and cylinder of material AISI 1018

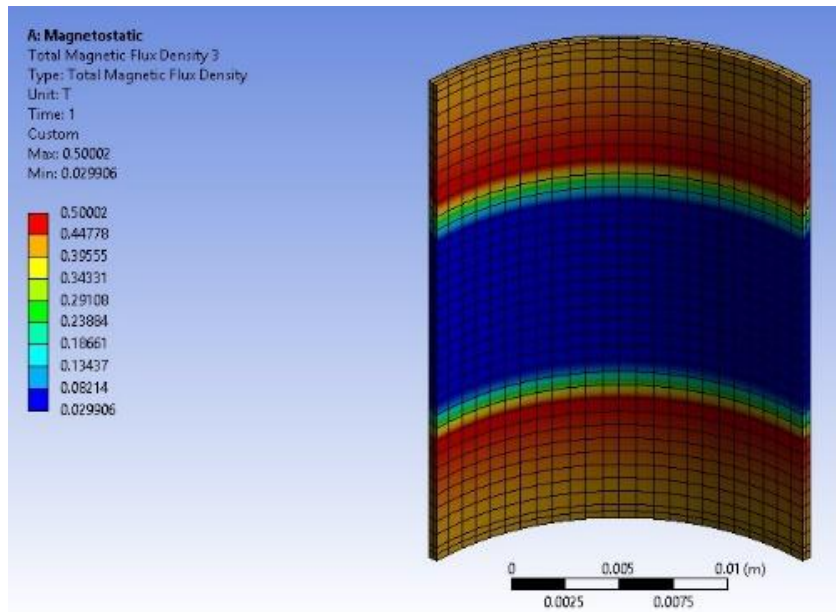


Figure 5.17 Magnetic flux density distribution in MR fluid element between piston and cylinder of material AISI 1020

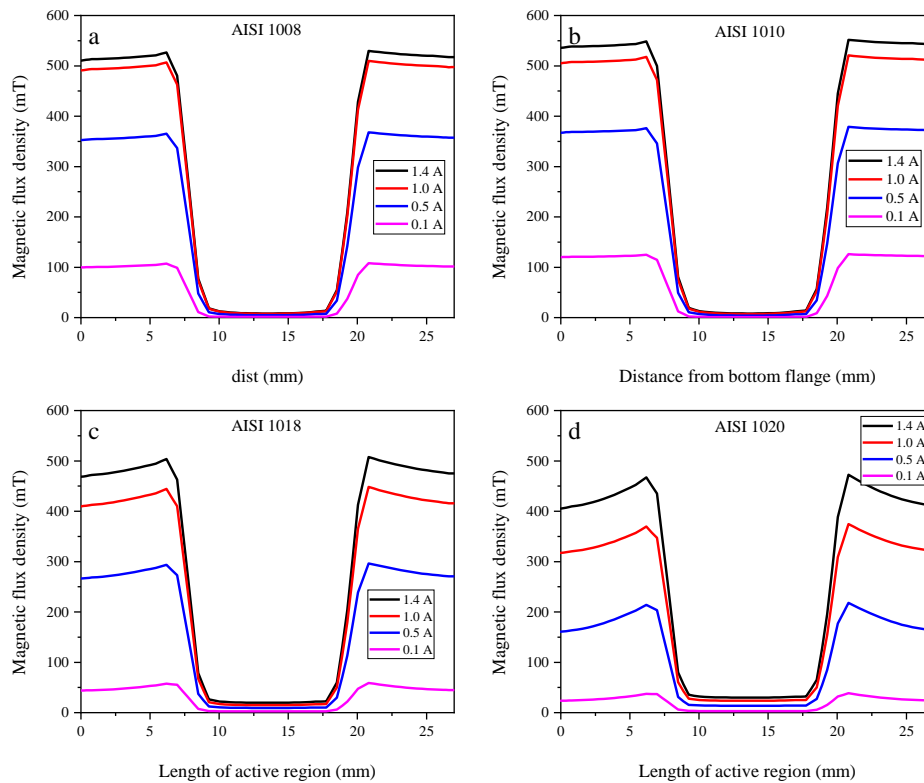


Figure 5.16 Magnetic flux density distribution for various current input (a) AISI 1008 (b) AISI 1010 (c) AISI 1018 (d) AISI 1020

The flux density across the length of the piston for various current is shown in Figure 5.17. The X-axis is the length of the piston from the bottom to the face end. All four magnetic materials are evaluated for increasing the current. The saturation limit could be clearly seen in AISI 1008 and AISI 1010. AISI 1020 gives minimum flux density and minimal dynamic range, whereas AISI 1010 gives 550 mT at 1.4 A.

### 5.5.4 Estimation of damping force

If the viscosity of a fluid is controlled, then the damping force can be varied accordingly. Yield stress ( $\tau_B$ ) developed at the annular gap between piston and cylinder due to magnetic field  $B$  is given as in Eqn. 5.4. The magnetic field  $B$  is obtained from FEA performed in ANSYS.  $\tau_B$  in Eq. 5.4 is obtained by curve fitting the plot obtained through current sweep in Figure 5.7 (section 5.4) with constant shear in the rheometer for in-house prepared MRF (here is an instance of an S5 fluid sample)

$$\tau_b = 39.7B^4 - 132.4B^3 + 119.1B^2 + 10.3B + 0.1 \quad (5.5)$$

Damping force ( $F_d$ ) in an MR damper is computed through the Eqn. (5.5) to (5.9). The damping force for a shear mode is the summation of frictional, shear, and viscous forces. Shear force can be controlled using electric current, while frictional and viscous

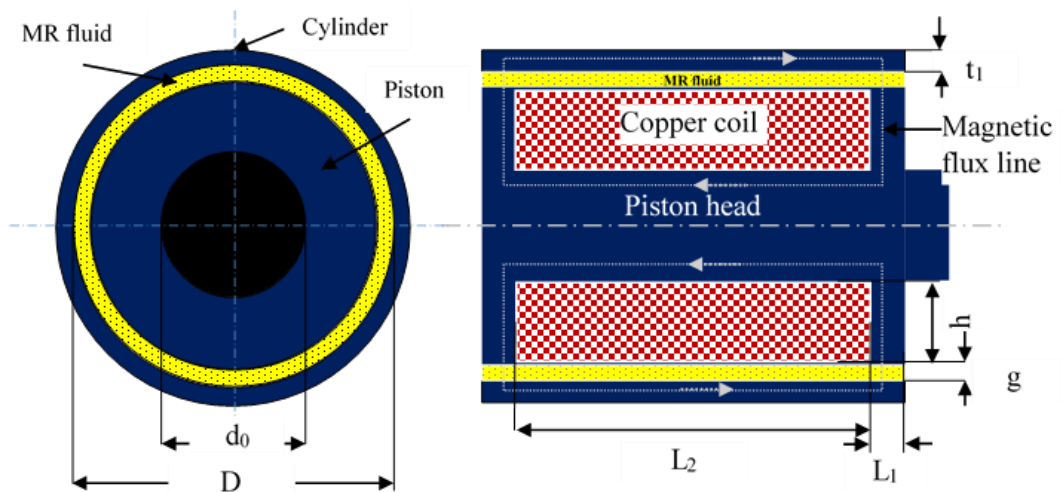


Figure 5.18 Nomenclature and dimensions of the magnetic circuit

forces are uncontrollable and inevitable. The geometric parameters of the damper are marked in the schematic sketch in Figure 5.18.

$$F_d = \left( 2.07 + \frac{12Q\mu}{12Q\mu + 0.4wg^2\tau_y} \right) \frac{\tau_y LA_p}{g} \text{sgn}(\dot{u}) + \left( 1 + \frac{wg\dot{u}}{2Q} \right) \frac{12\mu QL_i A_p}{wg^3} \quad (5.6)$$

L=effective pole length (mm)=2L<sub>1</sub>

$$w = \pi \left( \frac{g}{2} + D + \frac{g}{2} \right) \quad (5.7)$$

Where  $w$ = Annular gap (mm),  $g$ =fluid flow gap, and  $D$  = diameter of piston (mm).

$$A_p = \frac{\pi(D^2 - d_o^2)}{4} \quad (5.8)$$

$A_p$  = Area of Piston (mm<sup>2</sup>),  $d_o$  = diameter of piston rod (mm)

$$\text{Apparent viscosity, } \mu = 0.0006\dot{\gamma}^{-0.6091} \quad (5.9)$$

$$\dot{\gamma} = \frac{\text{velocity}}{2 \times \text{fluid flow gap}} \quad (5.10)$$

The force induced in the MR damper is calculated for various current inputs at a 12 V DC supply. The maximum force obtained in AISI 1008, AISI 1010, AISI 1018 and AISI 1020 is 152 N, 160 N, 140 N and 121 N, respectively. The damper with higher flux gives a higher damping force. Figure 5.19 shows the variation of damping force for all four material models for various current inputs. The comparison shows the AISI 1010 produces max damping force for the current 1.4 A, 12 V supply. AISI 1020 is the least suitable for damper material as it produced 120 N force at 1.4 A supply. AISI 1008, AISI 1010 and AISI 1018 got saturated at 1.4 A current which is evident from Figure 5.19 with no significant difference between 1 A and 1.4 A. There could be an increase in force through an increase in flux density by increasing the current input to

AISI 1020. However, the wire gauge 28 AWG does not support 1.4 A current pass through it.

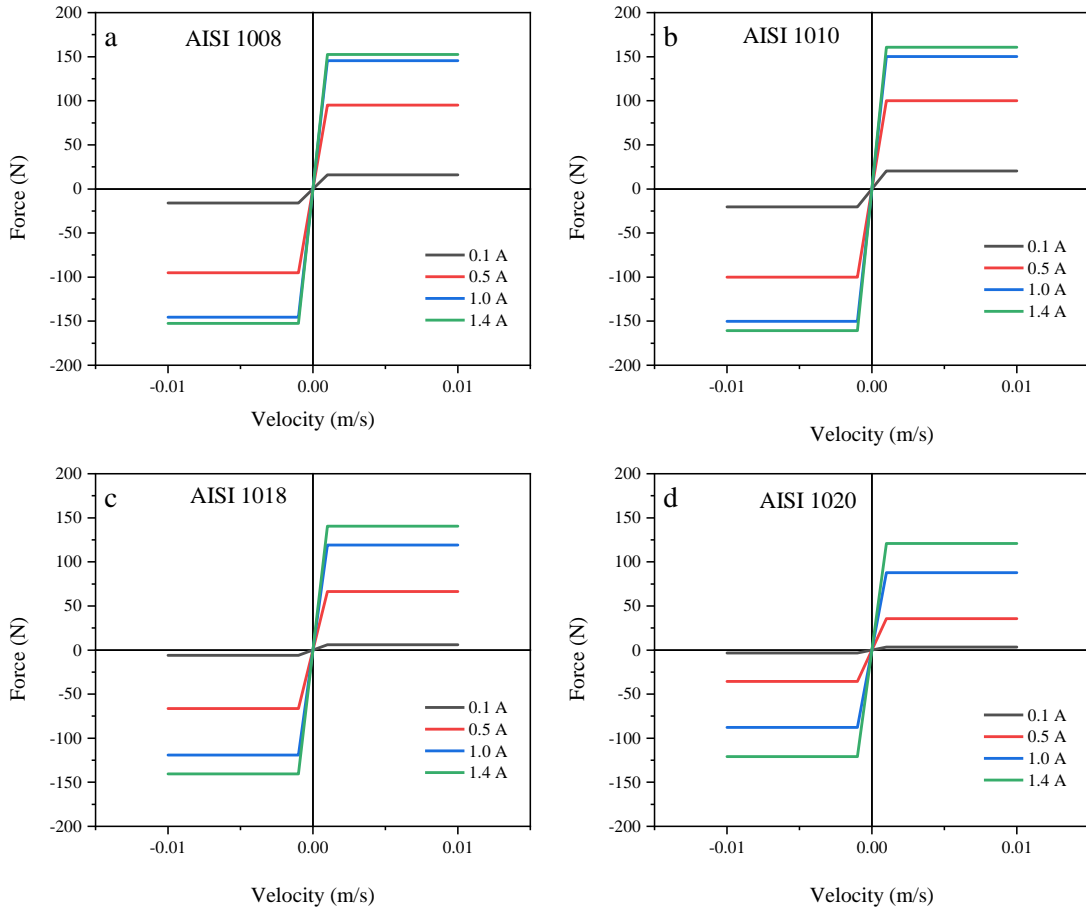


Figure 5.19 Force –Velocity plot of MR damper for various input current (a) AISI 1008 (b) AISI 1010 (c) AISI 1018 (d) AISI 1020

## 5.6 OPTIMIZING THE GEOMETRIC DIMENSIONS OF MR DAMPER

Optimal geometric dimensions of the MR damper are obtained by performing magnetostatic analysis in ANSYS workbench with Magnetostatic toolbox. The geometric modelling of the MR valve is carried out with initial design variables. A quarter portion of the computational domain of MR fluid in the annular flow gap is shown in Figure 5.20 with initial design variables. A maximum of 0.3 T magnetic flux density was achieved in the fluid flow gap with the optimized dimensions. Fluid flow gap, copper coil width and flange length (input design variables) are assigned as

parameter sets. The magnetic flux density developed at the annular fluid gap is set as a response parameter.

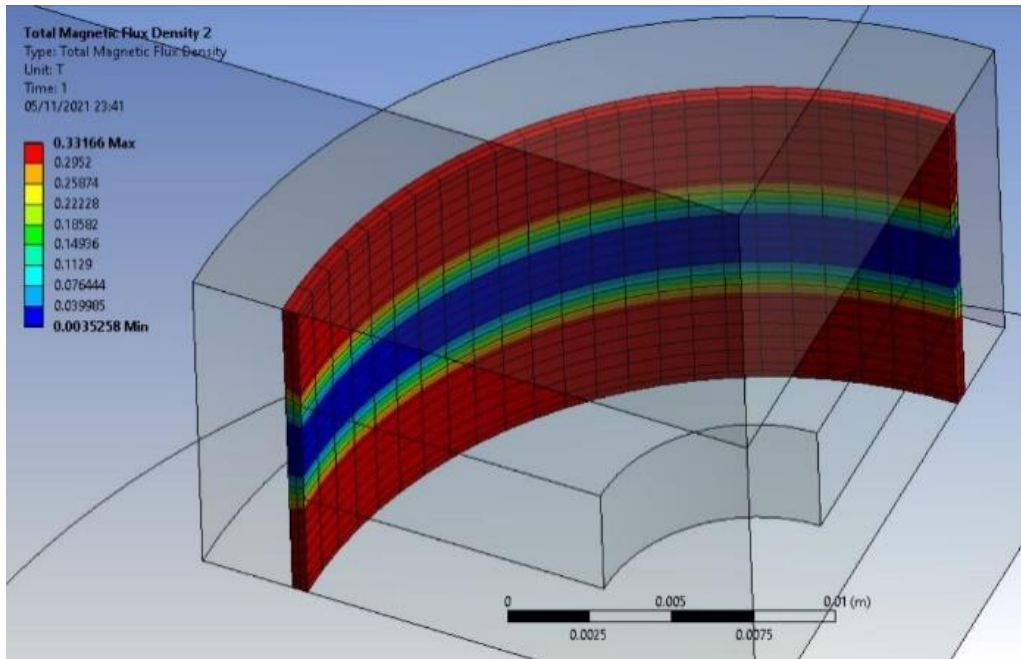


Figure 5.20 Computational domain of annular fluid flow gap

The input design variables are assigned upper and lower bound through central composite design to obtain design points tabulated in Table 5.4. Maximum magnetic flux density achieved at the fluid flow gap is evaluated for all design points generated in DOE. Surface response plots evaluate the influence of design input parameters over magnetic flux density. A full second-order polynomial regression model was used to obtain the surface response plots. The sensitivity of these input parameters over output response could be examined by plotting a sensitivity chart since three input variables influence the magnetic flux density; the optimal design parameters are obtained by adopting multi-objective genetic algorithm (MOGA) optimization to maximize the magnetic flux density and minimize the design input parameters. The MOGA optimization earmarks three candidate points achieving maximum magnetic flux density at the flow gap, and the possible candidate point is chosen as the final design parameter.

The initial, lower and upper design values are chosen based on the space constraints and cutting force measured in the preliminary turning experiment. The space available between the tool holder and saddle was 81 mm. The preliminary study was carried out to measure the vibration of the cutting tool in hard turning and the roughness produced on the machined surface. The amplitude level is higher in the tangential direction than in the feed and radial directions. The maximum cutting force produced was 236.9 N for speed 572 RPM, 0.125 mm/rev feed and a depth of cut of 0.3 mm. Hence, the authors designed the damper based on maximum cutting force and tool oscillation.

Current,  $I$  is considered by the gauge of the copper wire used. The gauge is considered based on the number of turns required to produce the desired magnetic flux density. The voltage supplied to the magnetic circuit is 12 V DC; hence the permissible value of current to the AWG 28 coil is 1.5 A, if exceeded this value the wire fuses. To accommodate a maximum number of turns, the current is limited to 1.5 A

$B$  is the value obtained by the magnetostatic analysis for the initial design values. The response of the design parameters depends on the current and properties of the MR fluid used in the model.

The response surface plotted the correlation between input design parameters and output response. Figure 5.21 and Figure 5.22 shows a correlation between fluid flow gap vs coil width and flange length vs coil width, respectively. Coil width has a more significant influence on flux density than flange length also, fluid gap influences in achieving maximum flux density.

Table 5.4 Parametric boundaries and optimal dimensions

Parameters	Initial design variables	Lower bound	Upper bound	Optimal dimension
Width of piston coil (l)	10 mm	4 mm	6 mm	4.6 mm
Flange length (t)	4 mm	3.6 mm	4.4 mm	3.6 mm
Fluid flow gap (g)	0.5 mm	0.45 mm	0.55 mm	0.45 mm
Current magnitude (I)	0.8 A	0.5 A	1.5A	1.4 A
Mag. Flux den. (B)	0.33 T	-	-	0.51 T

Figure 5.23 shows the correlation between fluid gap vs flange length against flux density. The minimal flange length and minimal fluid gap result in maximum flux density. The damping force is calculated for the optimum values obtained from the above optimization process. The physical damper fabricated to optimal design dimensions is shown in Figure 5.24.

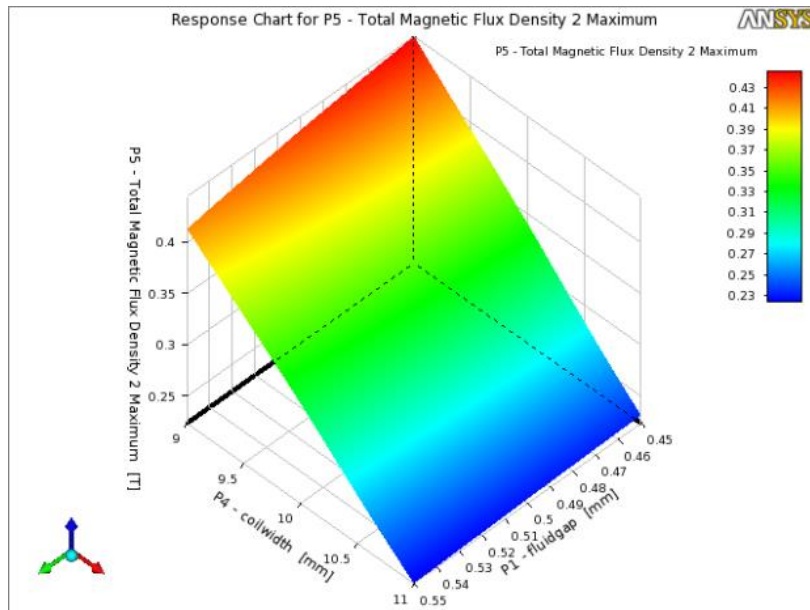


Figure 5.21 Response surface of coil width vs fluid gap

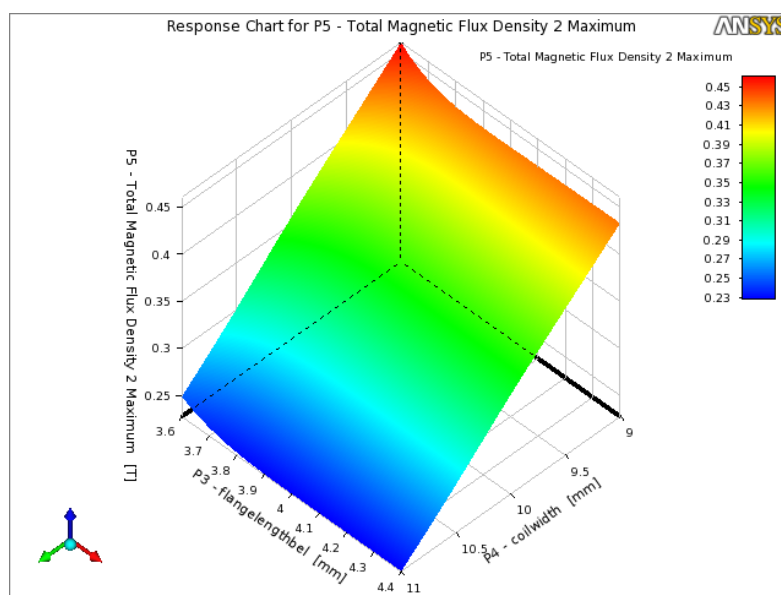


Figure 5.22 Response surface of coil width vs flange length



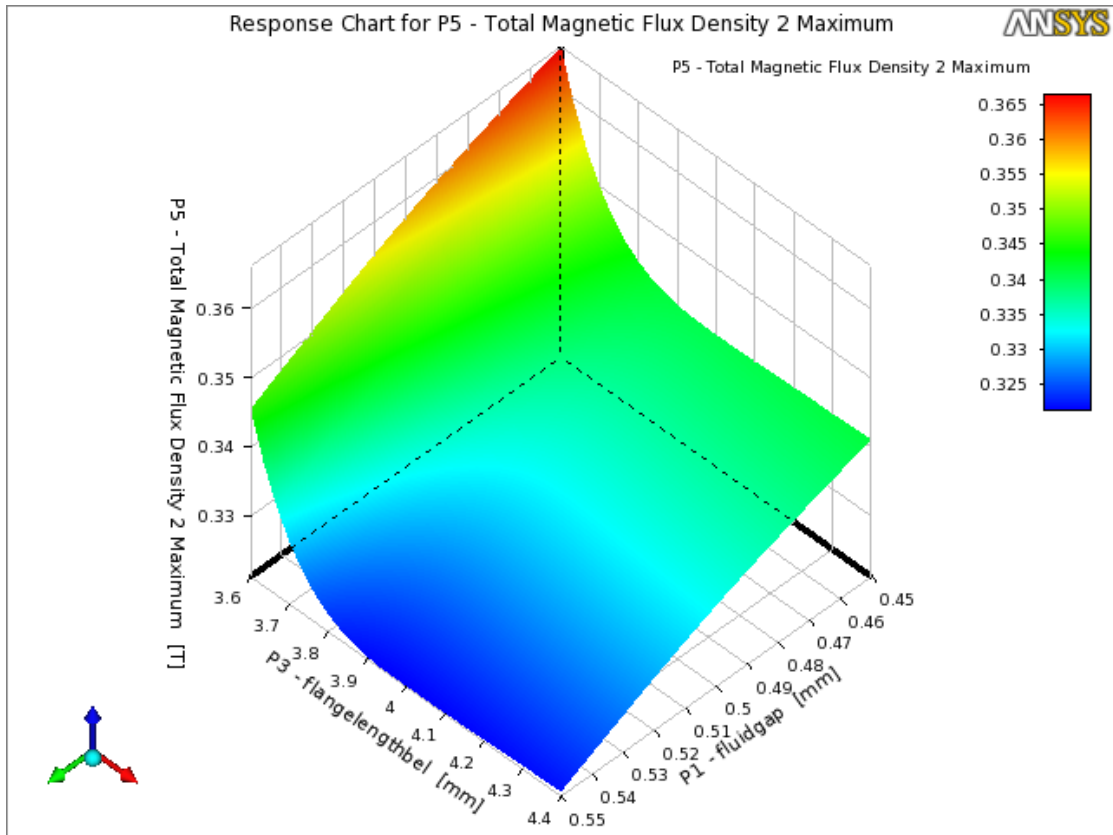


Figure 5.23 Response surface of fluid gap vs flange length

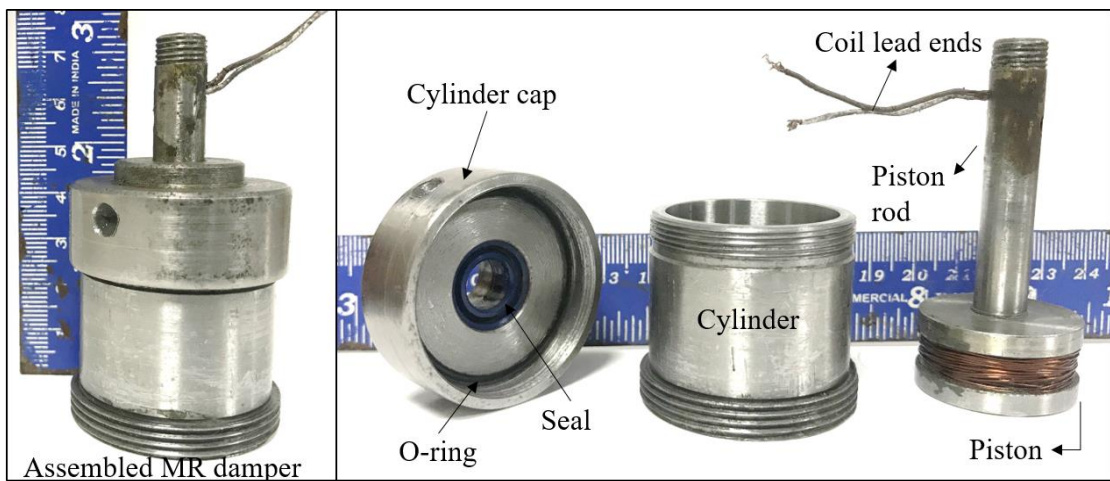


Figure 5.24 The damper fabricated to optimal design dimensions with its parts labelled

## 5.7 CHARACTERISATION OF MR DAMPER

The damper testing machine characterises the short-stroke damper fabricated to optimal dimensions to record the nature of force against displacement. Figure 5.25 shows the dynamic test set up to characterise the MR Damper. All nine fluid samples in Table 5.1 were tested on the damper testing machine (DTM) to obtain damping force and effective damping range. The DTM comprises two jaws, one movable and another fixed. The movable jaw was actuated by a servo-controlled linear hydraulic actuator fitted with LVDT. The fixed jaw was fitted with a load cell to measure the force. The force-displacement curve is obtained by setting the amplitude and velocity of oscillations via MOOG™ controller. The readings are recorded on the local dedicated desktop. The hydraulic power pack supplies the desired pressure difference for actuation. The damper is held between these two jaws. The piston rod was held in a movable jaw and the cylinder was on a fixed jaw. The damper is actuated by a programmable DC power supply. The voltage was set at 12 volts and a 0.7 A and 1.4 A current was supplied.

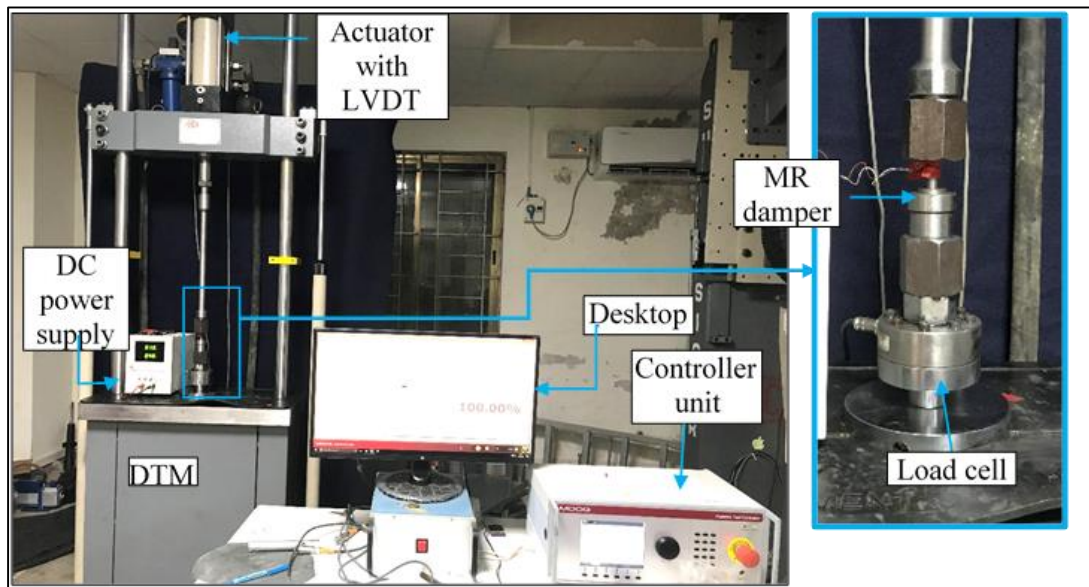


Figure 5.25 Damper testing machine with all its supporting elements

The force-displacement curves for all nine samples operated at three DC supply currents are plotted in Figure 5.26. The effective damping range is estimated. These values are tabulated in Table 5.5. Similarly, yield stress values corresponding to Figure

5.9 is also tabulated in Table 5.5. The maximum yield stress and ratio are highlighted **boldly** in Table 5.5. These are individual best values however, not the optimal values. Because a high yield stress may not always produce a max ratio of damping force and vice versa, optimization is necessary to obtain the optimum fluid composition and current supply for maximizing yield stress and the ON/OFF damping force ratio.

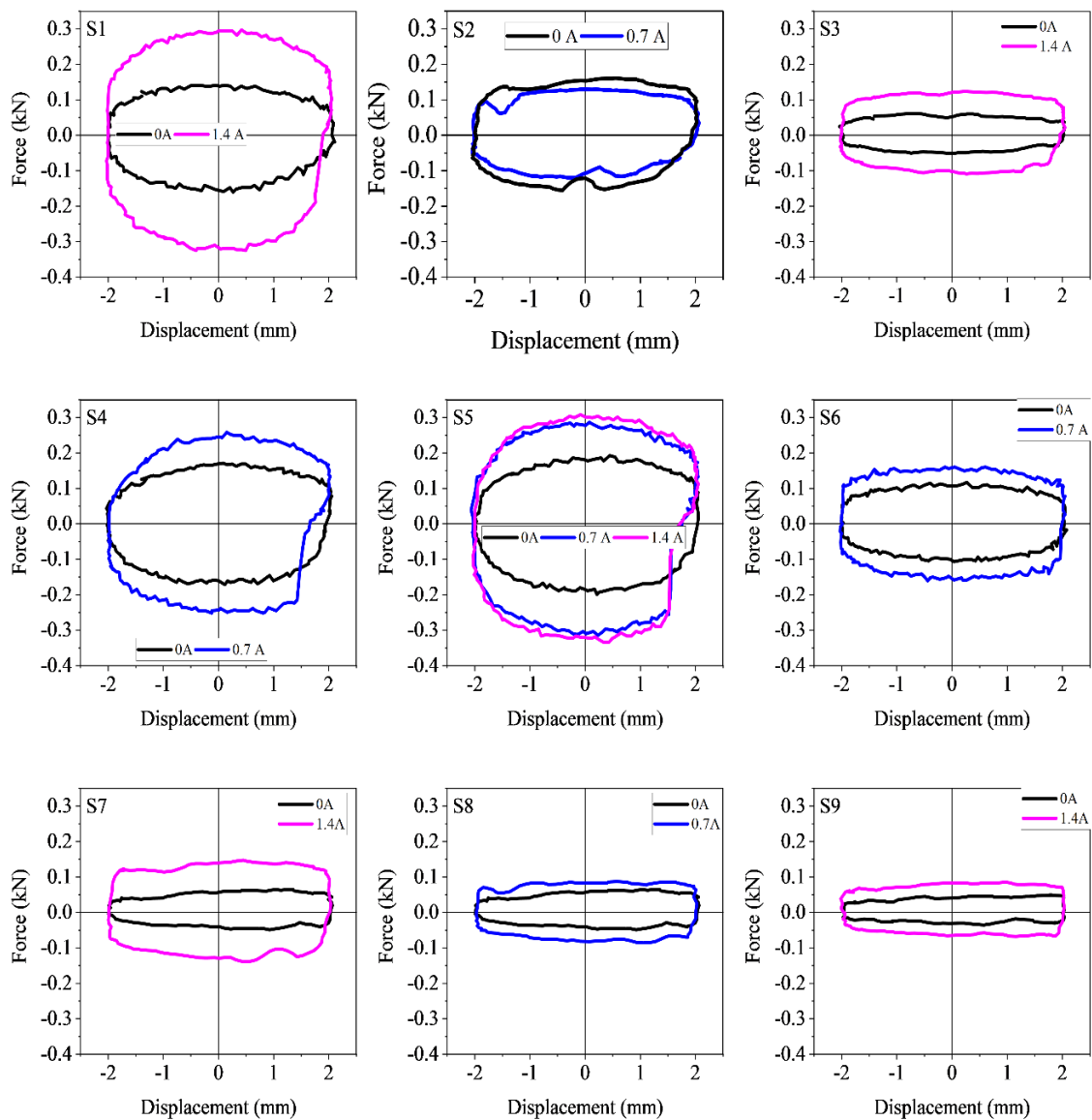


Figure 5.26 Force-displacement curves of MRD with various fluid samples

Table 5.5 DOE result obtained by CCD and its responses

Sl. No.	Sample No.	Current (A)	Yield stress (Pa)	Effective damping range
1	S9	1.4	115.49	1.84267
2	S9	0	0	1
3	S3	1.4	3922.1	1.8732
4	S6	0.7	2103	1.37021
5	S3	0	0	1
6	S5	0.7	2560.1	1.30599
7	S8	0.7	802.46	1.52715
8	S5	0.7	2560.1	1.30599
9	S5	0	0	1
10	S5	0.7	2560.1	1.30599
11	S5	0.7	2560.1	1.30599
12	S2	0.7	1625.1	<b>2.34449</b>
13	S5	1.4	<b>7379.4</b>	1.37736
14	S5	0.7	2560.1	1.30599
15	S5	0.7	2560.1	1.30599
16	S7	0	0	1
17	S4	0.7	2906.5	1.58882
18	S1	0	0	1
19	S1	1.4	6286	1.97456
20	S7	1.4	6246.1	2.3536

## 5.8 ANALYSIS OF VARIANCE (ANOVA) AND MULTI-OBJECTIVE OPTIMIZATION

The influence of input factors on responses (i.e. yield stress and effective damping range) can be identified using analysis of variance (ANOVA). The responses were analysed with different modes of modelling. In this sense, the types of equations are changed to check model suitability. Three modelling methods were implemented: linear, linear+interactions and full quadratic equations. All the models were created with a 95% confidence level. The ANOVA for both responses is illustrated below.

The influence of linear, interactions and square terms over the yield stress is provided in Table 5.6. The full quadratic model yielded the best result for yield stress

response in terms of weight\_fraction, current and base oil viscosity. The full quadratic model for yield stress is given as Eq. 5.11.

$$\begin{aligned}
 \text{yield\_stress} = & 3419 - 67 \times \text{weight\_fraction} - 5100 \times \\
 & \text{current} - 179 \times \text{viscosity} + 0.71 \times \text{weight\_fraction}^2 + \\
 & 2567 \times \text{current}^2 + 6.34 \times \text{viscosity}^2 + 70.9 \times \\
 & \text{weight\_fraction} \times \text{current} - 1.09 \times \text{weight\_fraction} \times \\
 & \text{viscosity} + 73.1 \times \text{current} \times \text{viscosity}
 \end{aligned} \tag{5.11}$$

The R<sup>2</sup> value for this model was noted as 99.04 %. Linear and linear + interactions model showed less feasibility when compared to the full quadratic model in terms of R<sup>2</sup>. It can be seen through the ANOVA table that weight\_fraction was less significant in both linear and square terms.

Table 5.6 ANOVA for yield stress

Source	DF	Adj SS	Adj MS	F-Value	P-Value
Model	9	92940920	10326769	115.19	0.000
Linear	3	3885717	1295239	14.45	0.001
Weight_fraction	1	37908	37908	0.42	0.530
current	1	2509777	2509777	28.00	0.000
viscosity	1	1338032	1338032	14.93	0.003
Square	3	5493600	1831200	20.43	0.000
Weight_fraction <sup>2</sup>	1	13802	13802	0.15	0.703
Current <sup>2</sup>	1	4349896	4349896	48.52	0.000
Viscosity <sup>2</sup>	1	1273398	1273398	14.20	0.004
2-Way Interaction	3	3505390	1168463	13.03	0.001
weight_fraction x current	1	1971095	1971095	21.99	0.001
Weight_fraction x viscosity	1	66472	66472	0.74	0.409
Current x viscosity	1	1467823	1467823	16.37	0.002
Error	10	896499	89650		
Lack-of-Fit	5	896499	179300	*	*
Pure Error	5	0	0		
Total	19	93837419			

Similarly, the analysis of variance is illustrated in Table 5.7 for the effective damping range. The best feasible model was obtained using linear terms rather than full

quadratic and linear + interaction models. The best fit was again decided using the R<sup>2</sup> value of the equation. Again, current and base oil viscosity is more significant than the weight fraction.

Table 5.7 ANOVA for effective damping range

Source	DF	Adj SS	Adj MS	F-Value	P-Value
Model	3	2.40594	0.80198	12.93	0.000
Linear	3	2.40594	0.80198	12.93	0.000
Weight_fraction	1	0.06904	0.06904	1.11	0.307
current	1	1.95487	1.95487	31.51	0.000
viscosity	1	0.38203	0.38203	6.16	0.025
Error	16	0.99253	0.06203		
Lack-of-Fit	11	0.99253	0.09023	*	*
Pure Error	5	0.00000	0.00000		
Total	19	3.39847			

The regression equation for the effective damping range is shown in Eq. 5.12

$$\begin{aligned}
 & \textit{Effective damping range} \\
 & = 0.889 + 0.00831 \times \textit{weight\_fraction} + 0.632 \quad (5.12) \\
 & \quad \times \textit{current} - 0.01667 \times \textit{viscosity}
 \end{aligned}$$

The yield stress, an essential feature of the MRF, decides the dynamic responses through its application. The effective damping range decides the intensity of the magnetic effect in the MRF. Hence, both responses are essential in selecting MRF for an application. Understanding the combined effect and the corresponding optimal quantities of input parameters is necessary to arrive at the best suitable fluid combination. The genetic algorithm, a benchmark optimization technique, is used for multi-objective optimization of the fluid combination. The regression equations obtained for yield stress and the effective damping range using the response surface method are objective functions. The multi-objective optimization process was performed using the toolbox available in the MINITAB software and the genetic parameters were kept default as available in the toolbox. The crossover fraction was set to 0.8 and the stopping criteria were limited to 100 generations since no further

improvement was found above that. The Pareto front generated using multi-objective optimization is shown in Figure 5.27.

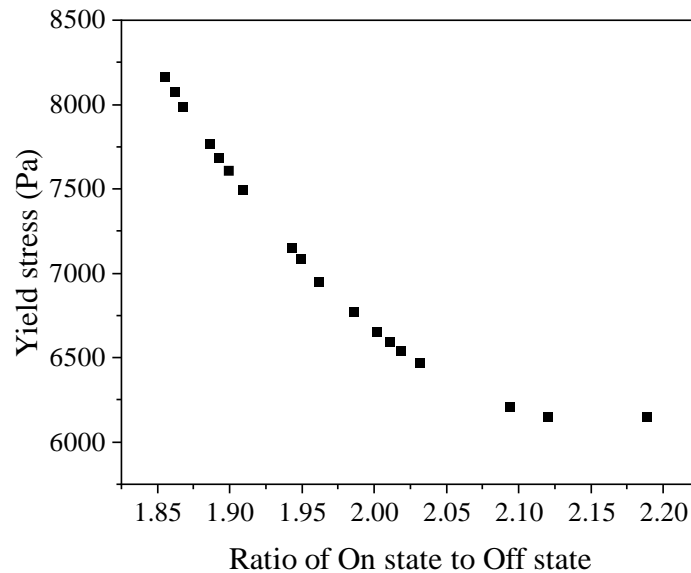


Figure 5.27 Pareto front plot generated by multi objective optimization

The combined best responses and the corresponding optimal input parameters are provided in Table 5.8.

Table 5.8 The optimal parameters and their response obtained by MOGA

Response		Optimal Parameters		
Yield Stress (Pa)	Effective damping range	Weight fraction (%)	Current (A)	Base oil viscosity (cSt)
7495.372	1.909	69.999	1.399	240.8

The results obtained through MOGA show that a 70% weight fraction of CIP in 240 cSt base oil, when actuated at 1.4 A, results in yield stress of 7495.372 Pa and a ratio of ON-state to OFF-state as 1.9. To confirm the effectiveness of the multi-objective optimization, a validation experiment was carried out considering the exact input parameters towards the rheology and dynamic experiments. Figure 5.28 shows the rheological curve of the S10 sample with Silicone oil viscosity 240 cSt weight fraction 70 % of CIP at supply current 1.4 A results yield stress of 6081 Pa. The S10 sample is filled into the MR damper to characterise the damper. Figure 5.29 shows the Force-

displacement curve indicating the maximum damping force in ON-state (1.4 A) and OFF-state. Table 5.9 shows the closeness of the optimal parameters obtained through MOGA and the validation experiment.

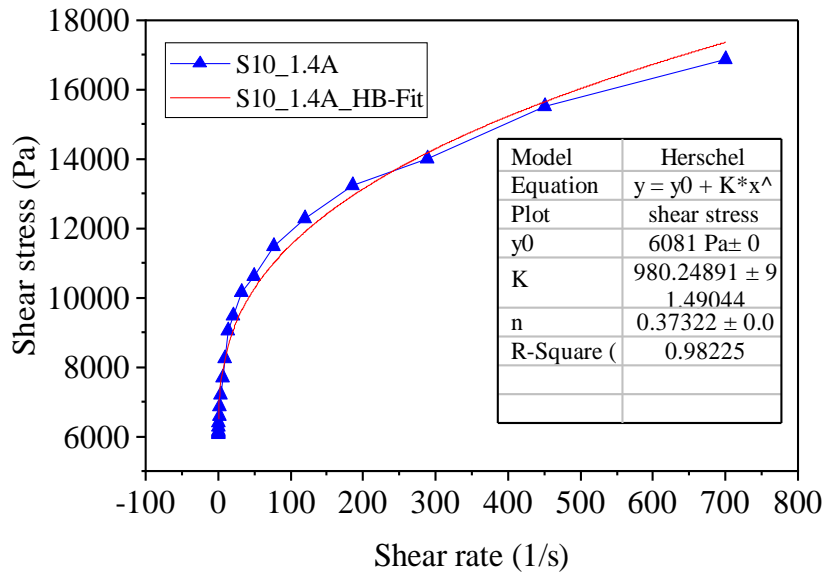


Figure 5.28 Shear curve of S16 MRF sample

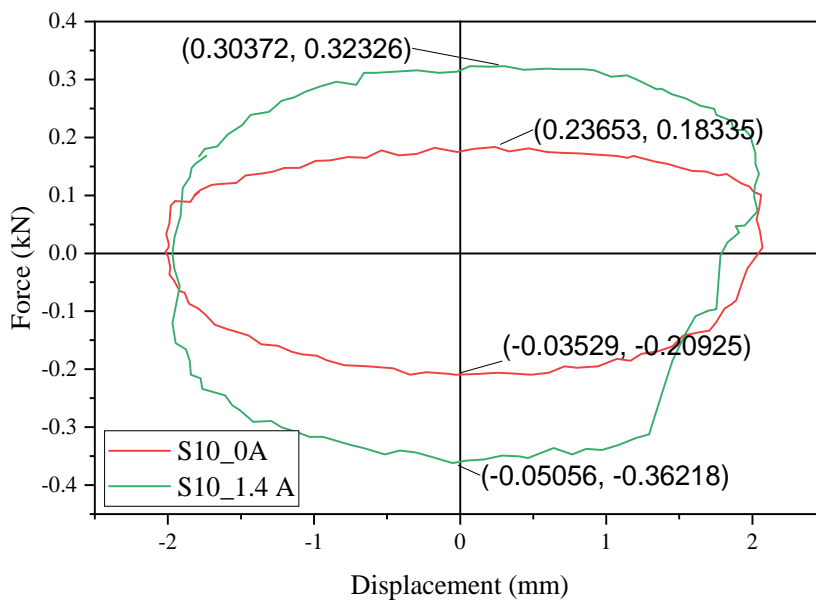


Figure 5.29 Damper characterised with S16 MRF sample



Table 5.9 Comparison of MOGA output and validation experiment

Parameters	Through MOGA	Validation experiment	% error
Weight fraction (%)	69.999	70	0
Current (A)	1.399	1.4	0
Base oil viscosity (Pa-s)	240.8 cSt	240 cSt	0.3
Yield Stress (Pa)	7495.372	6081	18.8
Effective damping range	1.909	1.8	5.71

## 5.9 SUMMARY

The chapter discusses designing and developing an MR damper that can be implemented on lathe machines to suppress tool vibration. The magnetostatic analysis of the flow valve and selecting the magnetic material of the piston and cylinder that delivers maximum flux density. The optimal dimensions of the damper are obtained through geometric optimization. The MR fluid is synthesised in-house with the optimal particle loading composition, base oil viscosity, and additives. There have been 12 fluid samples prepared with different combinations of particle loading and viscosity of the base oil. The design of experiment is employed to reduce the number of testing. The fluids are tested for rheological characteristics and hysteresis curve. The developed MR damper is characterised by a damper testing machine with optimal and commercial fluid in-house. The in-house fluid performed as equally well as commercial fluid. The developed MR damper delivers sufficient damping force to combat chatter vibration in hard turning.



## **CHAPTER 6**

### **EVALUATION OF MACHINING PERFORMANCE WITH MR DAMPER**

#### **6.1 INTRODUCTION**

This chapter discusses the machining study carried out with the augmentation of a Magnetorheological (MR) fluid damper to suppress tool vibration in hard turning with easy installation without much structural modification. The MR fluid damper changes its damping coefficient with a supply of magnetic field to regulate variable cutting conditions. An optimal composition of MR fluid has been prepared in-house to be used in the damper. In-house MR fluid is compared with commercial MR fluid. The L9 Taguchi design of the experiment opted to arrive at minimal machining parameters to evaluate the performance of the damper in machining two workpiece materials, namely oil-hardened nickel steel (OHNS) and high carbon high chromium (HCHCR) die steel. Tool wear studies are also carried out to monitor the influence of external damping over tool life. The stability lobe diagram is obtained analytically with experimental validation to mark the stability limit of the machining condition.

MR damper is effective when it is controlled using a controller to utilise its adaptability effectively; hence, real-time control is implemented to control the damping force of the MR damper for machining applications for different cutting conditions and different materials. The timely activation of the damper is possible by monitoring the real-time acceleration signal of the tool vibration as vibration feedback. The surface roughness and vibration amplitude of the tool are evaluated with and without real-time control.

#### **6.2 MACHINING STUDY WITH MR DAMPER**

The damper performance was evaluated by conducting a series of tests on rough turning using the design of experiments. Two workpiece materials namely, Oil

hardened nickel steel and high carbon high chromium die steel of 60 mm diameter and 250 mm length, were machined using CNMG120408 insert, which PCLNR2020K12 tool holder held. Vibration signals were acquired using NI DAQ 9234 and analyzed using the LabVIEW-Signal Express module.

The piston rod of the MR damper was fastened to the bottom of the tool holder, and the MR damper was rigidly fitted on the lathe carriage with a unique cement bond adhesive. The damper provides an upward reaction force opposing tool vibration to suppress the displacement. An experimental setup on the lathe for evaluating the MR damper connected with a programmable DC power source is shown in Figure 6.1. The MR tool damper, when connected with a programmable DC power source (PSD 3005), display of it indicates the electric current (bottom row) and voltage drawn by the damper (top row).

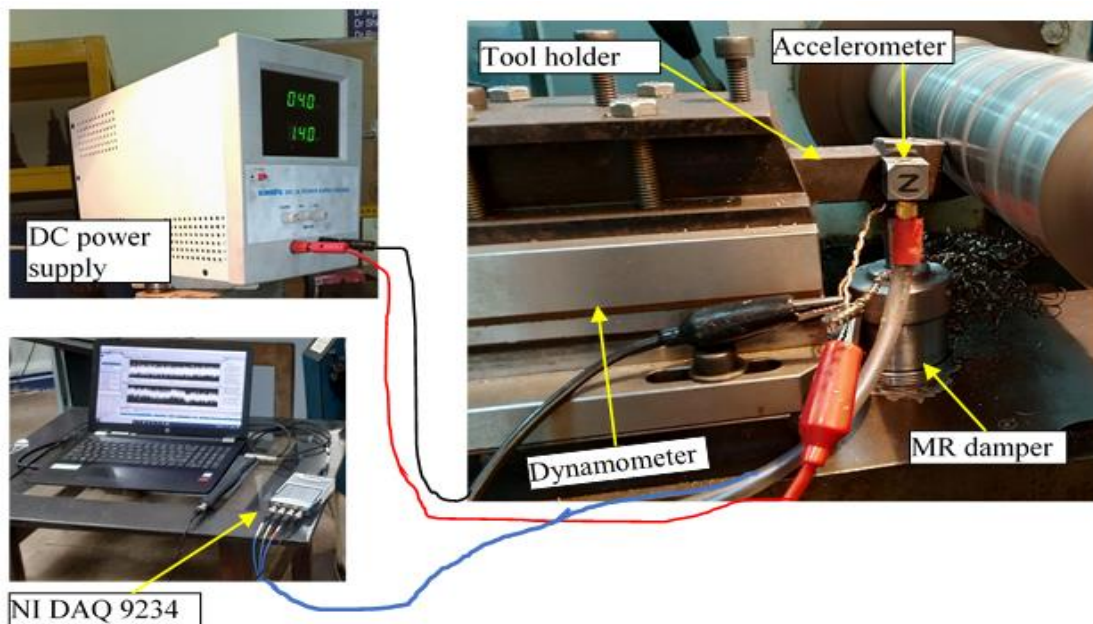


Figure 6.1 Experimental setup to evaluate the performance of the MR fluid damper

The machining performance with an MR damper is evaluated by analysing the acceleration signal and measuring the surface roughness, tool wear and chip morphology. This chapter discusses the influence of external damping on these responses for two different workpiece materials, namely OHNS and HCHCR D2 steel, with both in-house prepared MR fluid and commercial MR fluid. The stability lobe

diagram for the said tool-workpiece conditions is also evaluated to study the influence of external damping on the stability limits of machining.

Nine sets of tests were conducted with different feed rates, different depths of cut and different spindle speeds using the L9 Taguchi design of the experiment from a set of 27 populations. The levels of each factor are shown in Table 6.1. The derived experiment trials from DOE are tabulated in Table 6.2. Further vibration level and surface roughness analysis are analysed according to the cutting conditions in Table 6.2.

Table 6.1 Levels and factors of DOE for machining trials

PARAMETERS	LEVELS		
	L1	L2	L3
Speed (RPM)	192	384	572
Feed (mm/rev)	0.046	0.093	0.156
DOC (mm)	0.2	0.3	0.4

Table 6.2 Cutting conditions derived from DOE

Expt. No	Speed (RPM)	Feed (mm/rev)	Depth of cut (mm)
1	192	0.046	0.2
2	384	0.138	0.2
3	576	0.092	0.2
4	192	0.092	0.3
5	384	0.046	0.3
6	576	0.138	0.3
7	192	0.138	0.4
8	384	0.092	0.4
9	576	0.046	0.4

### 6.3 EVALUATION OF TOOL VIBRATION

Figure 6.2 compares the vibration level with increasing the damping coefficient of the damper by increasing the current to the damper. Plots (a)-(c) for in-house fluid and Plots (d)-(f) for commercial fluid. Both commercial fluid [Lord Corp. 132 DG] and in-house MR fluid were found to be effective in reducing the tool vibration; however, looking at Figure 6.3, in-house MR fluid is better than commercial fluid; however, the settling rate of in-house fluid is lower than commercial fluid. The settling rate of in-house MR fluid is 0.02 ml in 24 hrs, and that of commercial fluid is 0.05 ml in 48 hrs. The vibration amplitude reduces linearly with increasing the current to the damper. A similar trend is observed while machining HCHCR D2 steel, as shown in Figure 6.4.

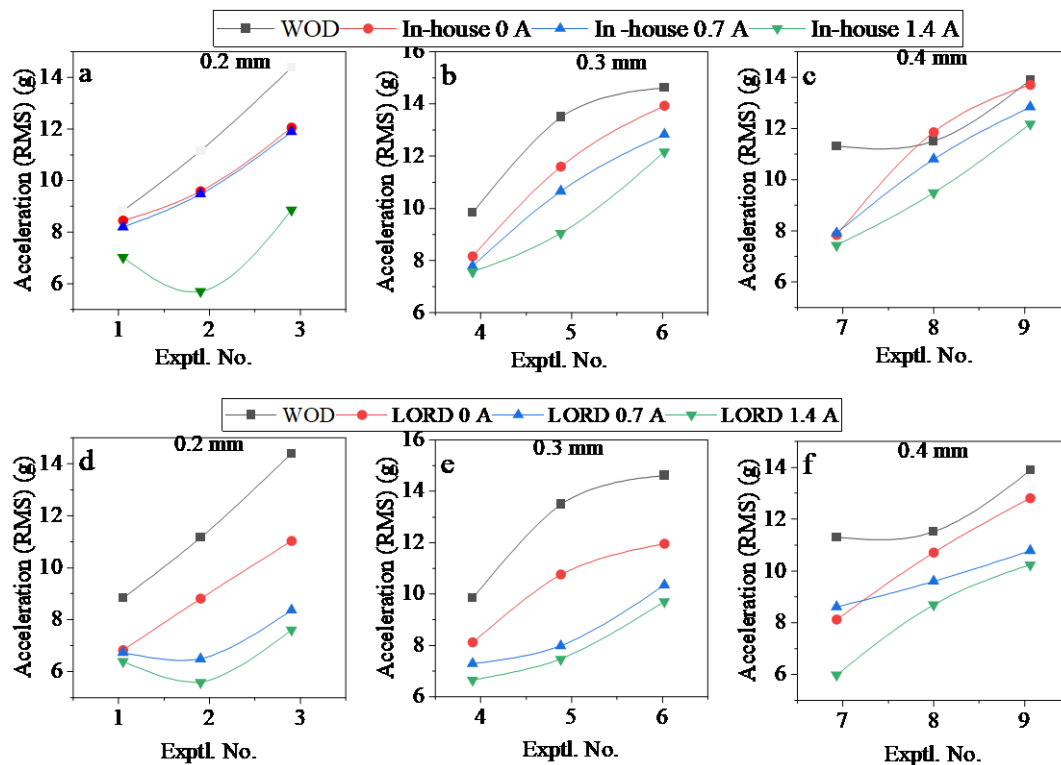


Figure 6.2 Vibration produced on OHNS workpiece with damper at various current for (a)-(c) in-house MR fluid, (d)-(f) commercial MR fluid

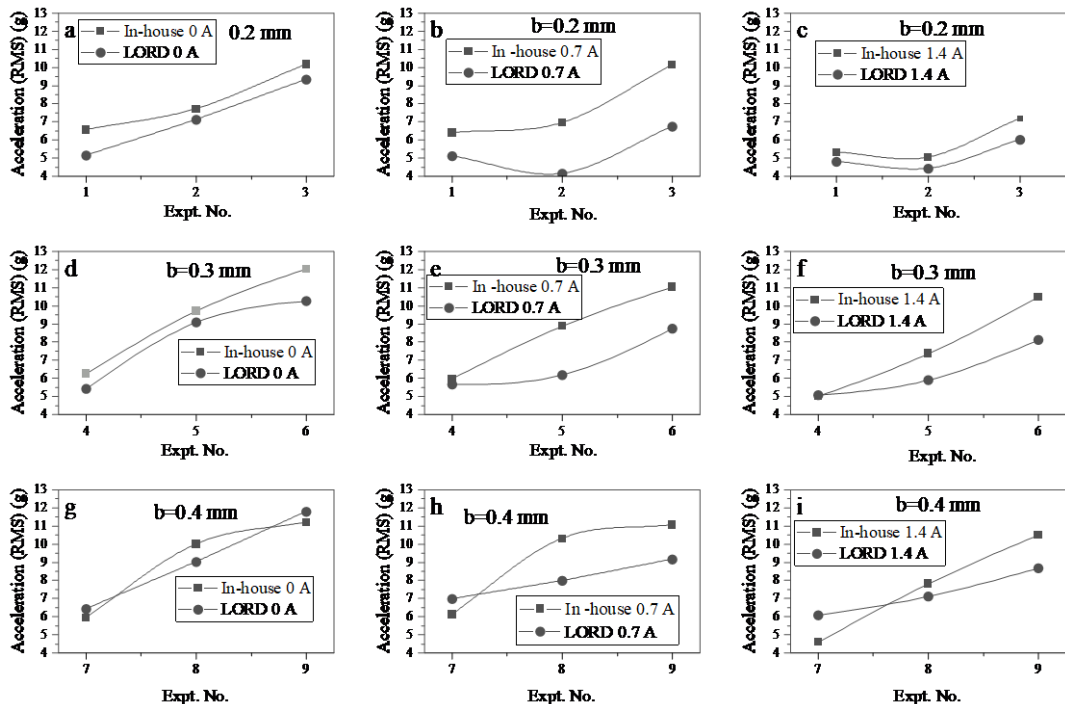


Figure 6.3 Comparison of vibration levels at various cutting conditions when in-house MR fluid and lord fluids are used in the damper while machining OHNS

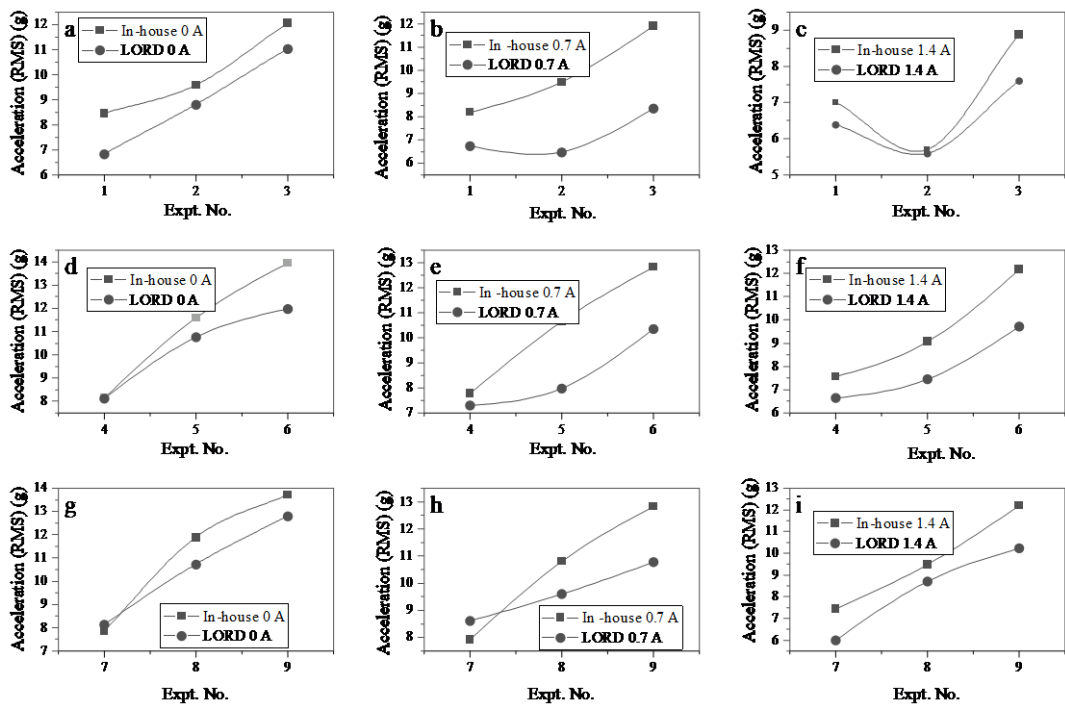


Figure 6.4 Comparison of vibration level at various cutting conditions when in-house MR fluid and lord fluids are used in the damper while machining HCHCR D2 steel

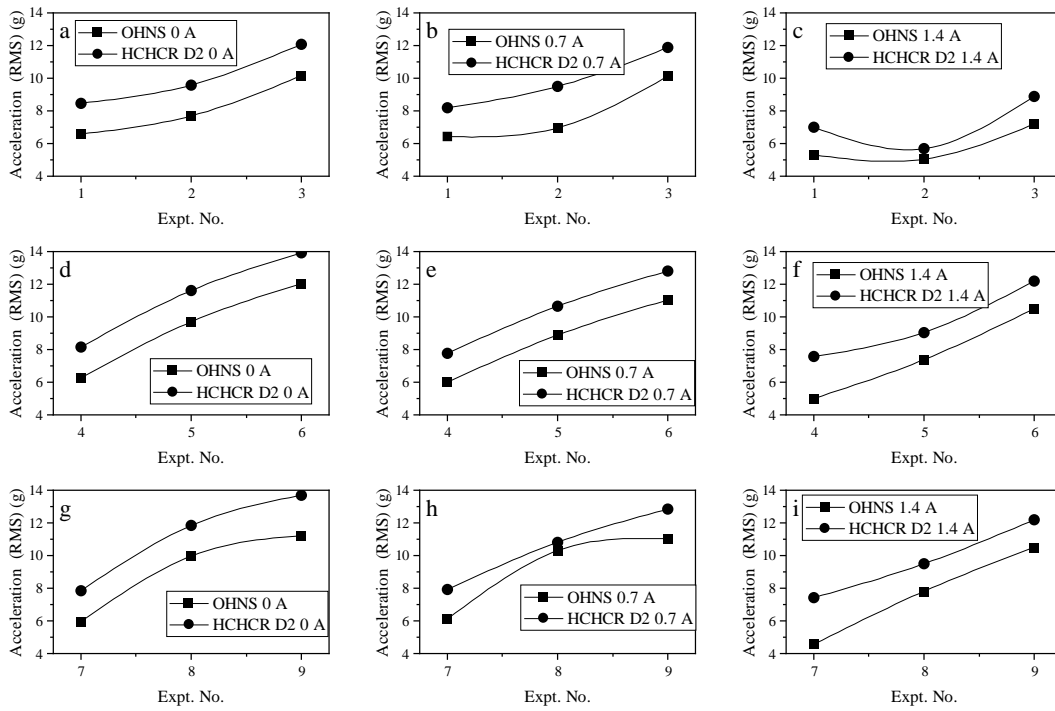


Figure 6.5 Comparison of vibration level between OHNS and HCHCR D2 steel when in-house fluid is used in the damper

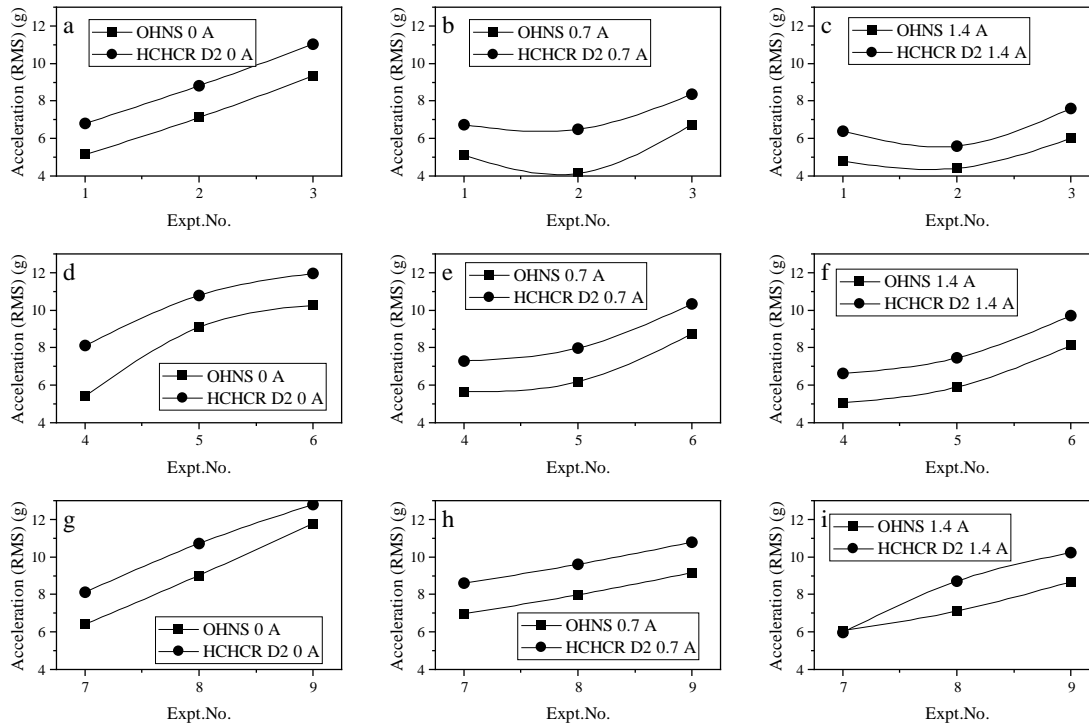


Figure 6.6 Comparison of vibration level between OHNS and HCHCR D2 steel when commercial fluid [Lord 132 DG] MR fluid is used in the damper



Figure 6.5 compares the vibration between OHNS and HCHCR D2 steel for in-house prepared MR fluid for various cutting conditions obtained from DOE. Similarly, Figure 6.6 shows the comparison of vibration for commercial lord fluid as is seen from both Figure 6.5 and Figure 6.6 that the vibration level of HCHCR D2 is more than OHNS due to the inherent hardness of the material. External damping has a greater influence in suppressing the vibration value.

#### **6.4 EVALUATION OF SURFACE ROUGHNESS**

Figure 6.8 shows the axis of vibration measurement (Y-axis) and Figure 6.7 illustrates the direction of roughness measurement (X-axis). There is no concurrent relation between vibration and roughness because the vibration is measured in the lateral direction of tool deflection, whereas the roughness is measured in the longitudinal direction of the workpiece.

Figure 6.9 and Figure 6.10 depicts the comparison of roughness when machining OHNS and HCHCR D2 steel respectively. The roughness increases with increase in speed for depth of cut 0.2 mm, whereas for depth of cut 0.3 and 0.4 mm it decreases with increase in speed. This shows that the damper is effective in producing a better surface finish for a higher depth of cut. The vibration level increases by 0.2 mm because the depth of cut is less than the nose radius, which oscillates the tool inducing the chatter marks on the workpiece. As the speed increases, violent vibration is induced, increasing surface roughness and vibration. The vibration decreases with increasing speed for depth of cut 0.3 mm and 0.4 mm due to process damping achieved with deeper cut ensuring the continuous engagement of the chip with the tool. The shear energy increases with increasing speed; hence the tool oscillation and surface roughness decrease with increasing speed. Figure 6.11 and Figure 6.12 shows the comparison of surface roughness between materials when in-house fluid and commercial fluid [Lord corp. 132 DG] used in the damper, respectively.

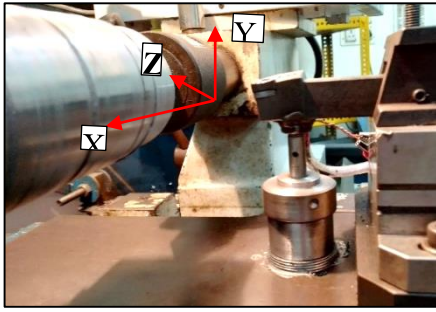


Figure 6.7 Direction of measurement of vibration

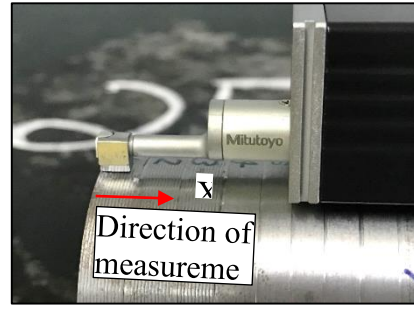


Figure 6.8 Direction of measurement of surface roughness

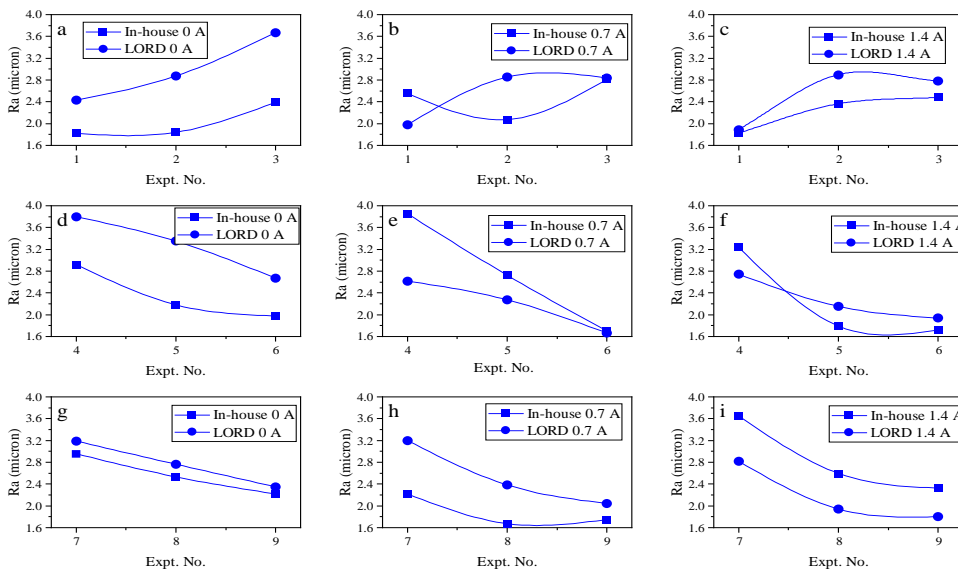


Figure 6.9 Comparison of surface roughness between in-house MR fluid and lord fluid while machining OHNS

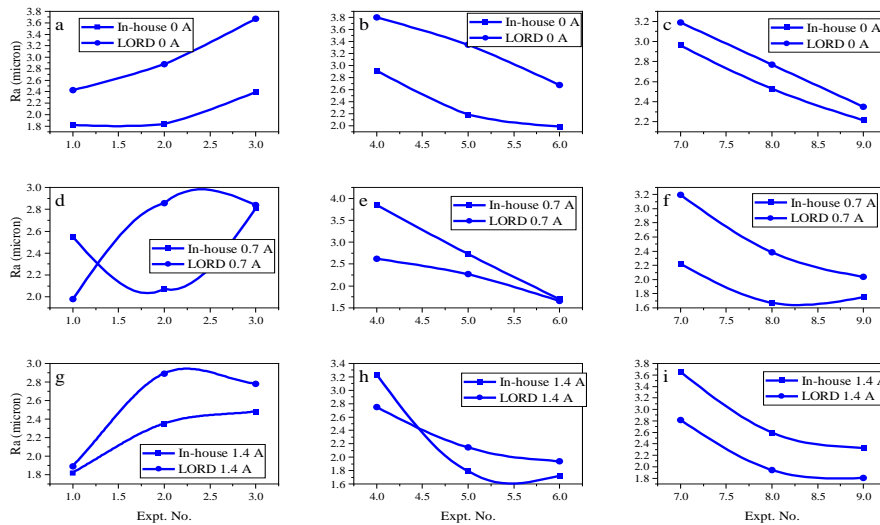


Figure 6.10 Comparison of surface roughness between in-house MR fluid and lord fluid while machining HCHCR D2 steel

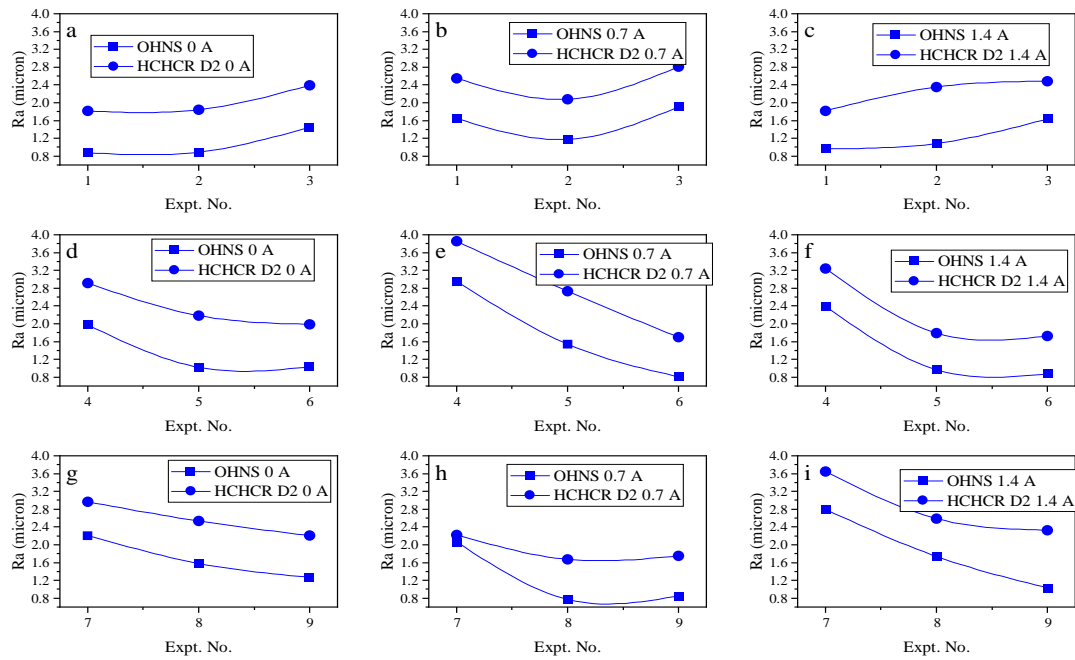


Figure 6.8 Comparison of surface roughness between OHNS and HCHCR D2 steel when in-house fluid is used in the damper

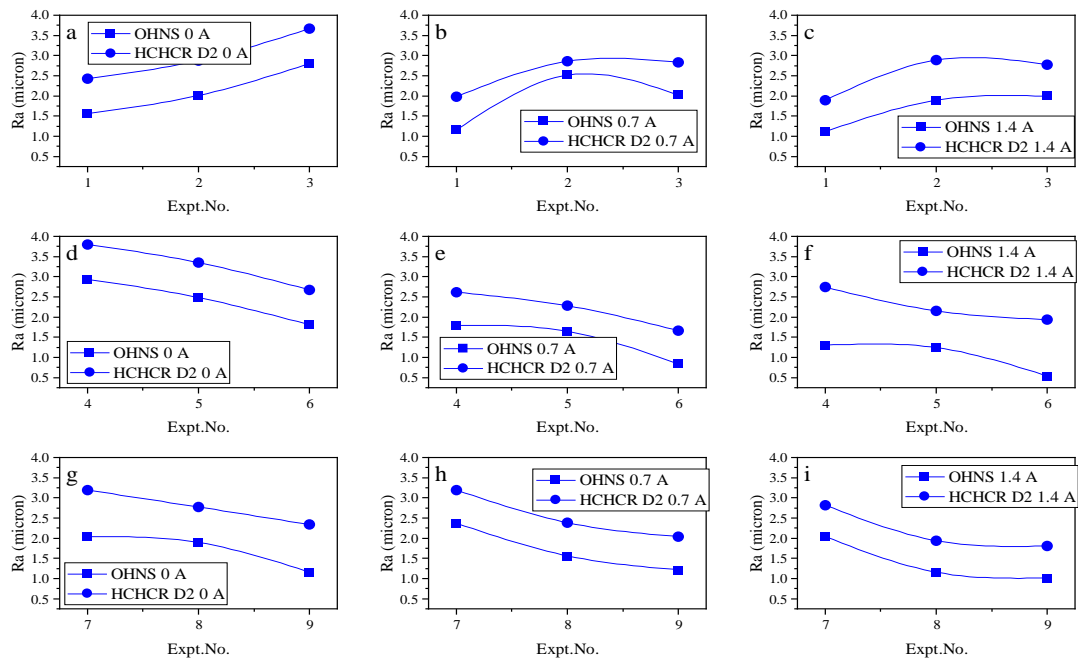


Figure 6.7 Comparison of surface roughness between OHNS and HCHCR D2 steel when LORD fluid is used in the damper

## 6.5 TOOL WEAR RATE

Tool wear has more influence in hard turning, which is studied through life tests by conducting a flank wear test. The cutting condition that resulted in the least vibration is used for the tool wear study. Flank wear of 0.4 mm was set as the tool failure criterion (Astakhov 2004). These tool failure criteria can be extended in shop floor industries to draw a good tool life for economical production. The tool wear is measured in an optical microscope fitted with a micrometre. The insert is machined till 0.4 mm flank wear is achieved. Figure 6.13 shows tool life without any damper, with the damper containing in-house fluid and LORD fluid when machining the OHNS workpiece. The wear test reveals that the tool life is enhanced with the damper due to external damping. The in-house MR fluid could enhance the tool life from 23 to 28 min while commercial MR fluid enhanced it from 23 to 34 min. An extra 6 min tool life is observed with in-house fluid compared to commercial MR fluid. A similar observation of enhanced tool life with damper while machining HCHCR D2 steel is observed in Figure 6.14 with improved tool life of 2 min with commercial MR fluid and 5 min with in-house fluid. The cost-effective in-house prepared MR fluid can be recommended for tool vibration suppression and life enhancement to turn hard steels. In the experiment, the coated tool never failed by mechanical breakage or plastic deformation but by gradual flank wear.

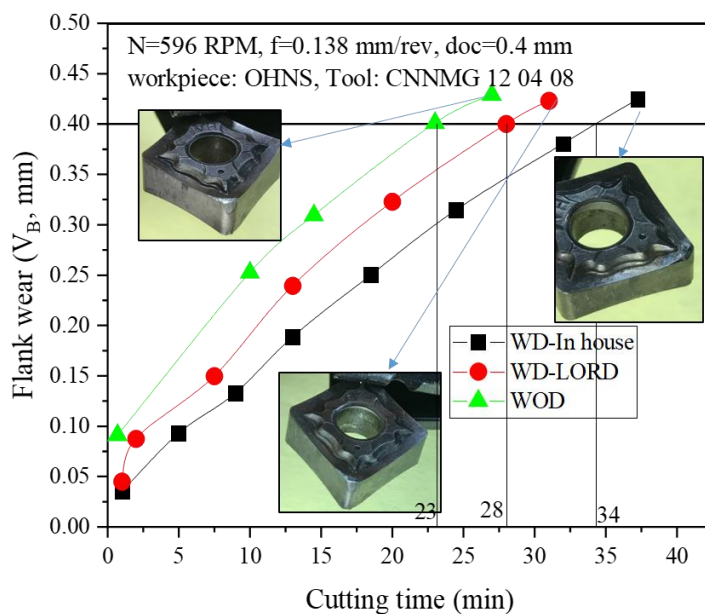


Figure 6.9 Comparison of tool life of OHNS material

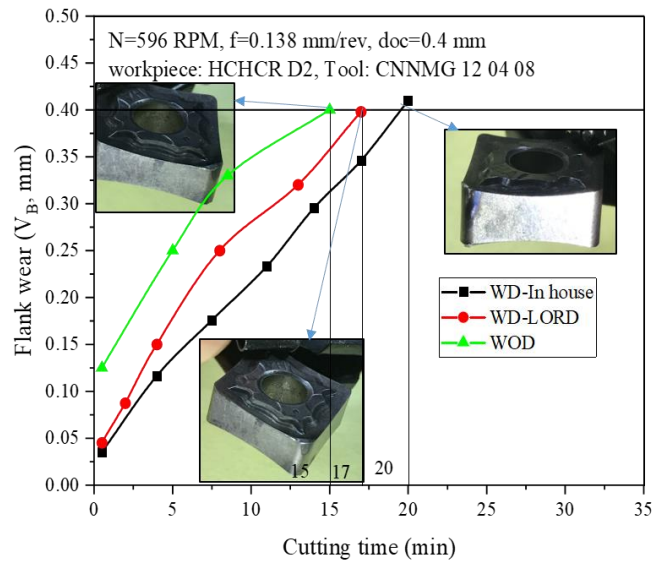
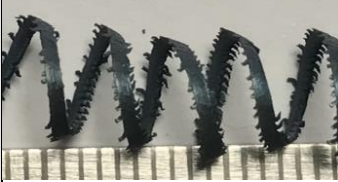




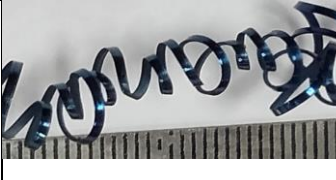


Figure 6.10 Comparison of tool life of HCHCR D2 steel

## 6.6 CHIP MORPHOLOGY

Cutting conditions are chosen in a range that does not allow built-up edge formation. The damper-enabled machining produces smooth continuous chips enabling effective heat transfer without much affecting the workpiece or tool. Minimal heat transfer to the tool ensures its longevity of tool life. Table 6.3 shows chips formed without a damper, with a damper containing in-house MR fluid and commercial fluid. Cutting conditions maintained are cutting speed=576 RPM, feed=0.136 mm/rev, depth of cut=0.3 mm. The chips appear blue, indicating maximum heat is carried away by the chip, which is the ideal feature for carbon alloy steel. The chip profile shows a smooth edge on the long string chips with the damper, whereas there are serration edges without the damper. Along with the ploughing action of the tool on the workpiece, the damper enables the breaking of chips to dispose of the chips as short continuous chips marking effective chip evacuation. Long smooth continuous chips produce fewer micro-vibrations, evidently shiny chips.

Table 6.3 Chip morphology without damper and with damper while machining OHNS and HCHCR D2 steel

Workpiece	Without damper	Damper with In-house fluid	Damper with LORD fluid
OHNS			
HCHCR D2			

## 6.7 STABILITY LOBE DIAGRAM

The stability lobe diagram (SLD) is an effective tool based on regenerative chatter theory to predict and control tool chatter. It represents the limiting depth of cut for increasing spindle speed. The interest of the machine tool designers is to increase the limiting depth of cut and area under the lobes. Figure 6.15 compares the SLD obtained with the damper and without the damper of OHNS. Yellow indicates a stable machining zone while black and grey regions indicate unstable cutting conditions. The damper increased the stable region by shifting the boundary of lobes. As the speed increases,, the lobe widens, leading to more space between the lobes, allowing desirable machining conditions. The SLD plot is obtained using Eq. 6.1 and 6.2 (Yue 2006).

$$b_{lim} = \frac{-1}{2k_s Re[FRF]} \quad (6.1)$$

$$Re[FRF] = \frac{1}{k} \left[ \frac{1 - r^2}{(1 - r^2)^2 + (2\zeta r)^2} \right] \quad (6.2)$$

Where,  $b_{lim}$  is the limiting depth of cut,  $k_s$  is the cutting stiffness of the cutting tool ( $k_s = 1$ ),  $Re[FRF]$  is a real part of the frequency response function,  $k$  is static stiffness ( $k=F/x$ ),  $k=10$ ,  $x$  is the displacement of cutting tool normal to cut,  $r$  is the ratio of chatter frequency to the natural frequency,  $\zeta$  is the ratio of damping coefficient to critical damping coefficient.  $\zeta$  changes for a tool with MR damper, which improves the stable region.  $\zeta = 0.05$  the parameters used in generating the SLD are:  $n_t = 1$ , and  $f_n = 250$  Hz. The lowest points on the lobes are the minimum chip widths, a horizontal border line connecting these points can be formed at  $b=b_{min}$ , any point below this line is unconditionally stable, and any point inside the lobe is unstable. The region between  $b_{min}$  and lobe boundary is conditionally stable. The incorporation of a damper improves the  $b_{min}$  which shifts to the higher doc. Figure 6.16 shows  $b_{min} = 0.51$  mm without damper,  $b_{min} = 0.58$  mm for current 0.7 A,  $b_{min} = 0.64$  mm for current 1.4 A. The stability limit for machining OHNS is the same for in-house and commercial fluids. Experimental validation is carried out by measuring the vibration amplitude by machining at 384 rpm, with varying the depth of cut, keeping a constant feed rate of 0.138 mm/rev. When  $b=0.48$  mm (point 1), the vibration was observed to be unconditionally stable, and the decaying amplitude of tool vibration was observed for  $b=0.56$  mm (point 2) was unstable with resonating vibration; however, when the

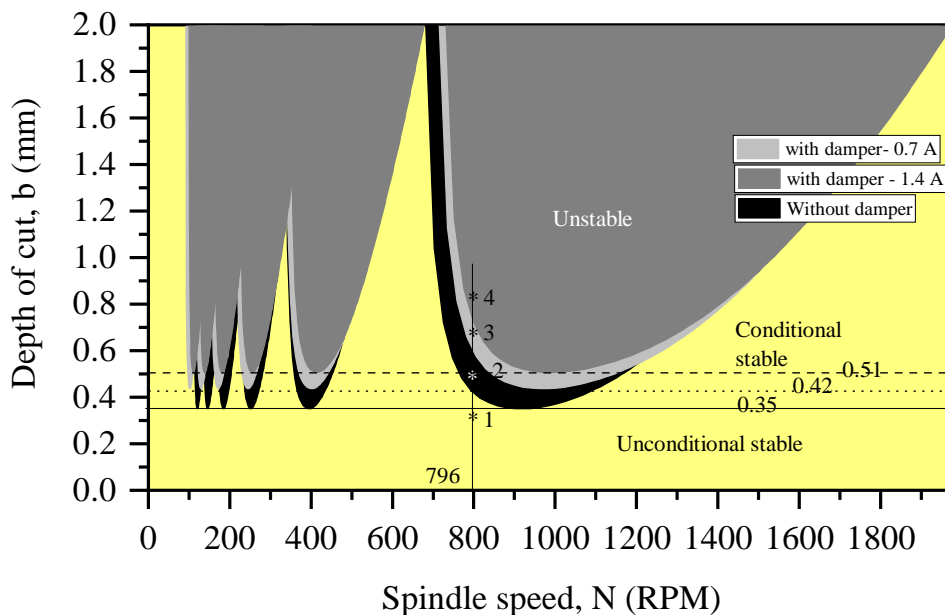


Figure 6.11 Stability lobe diagram for OHNS workpiece (a) Without damper (b) With damper

damper is activated at 0.7 A with commercial fluid or in-house fluid, the lobe shifts to higher value making the point from unstable to stable.

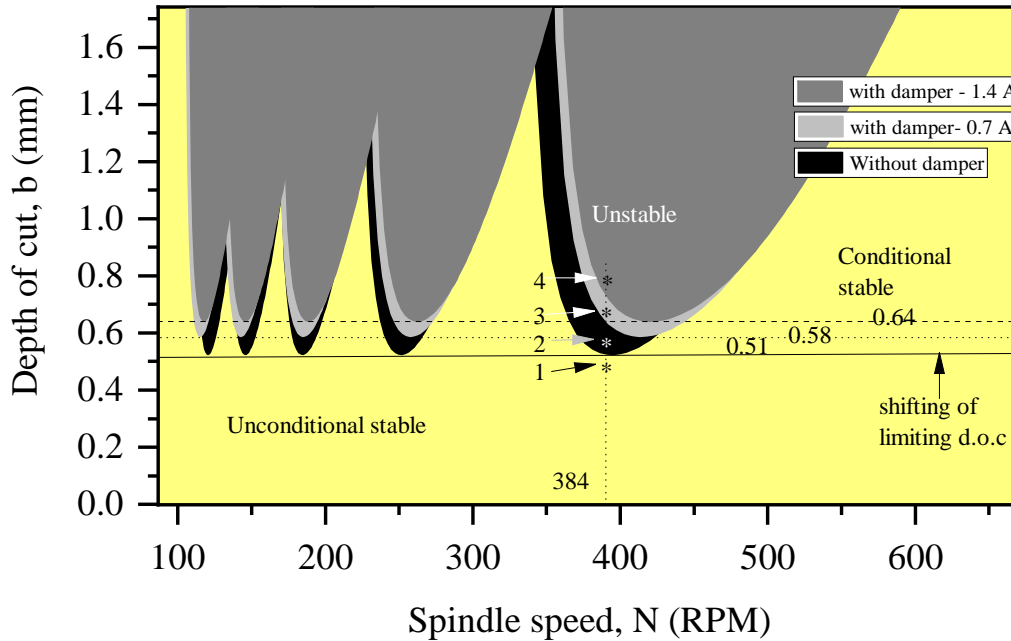


Figure 6.12 Stability lobe diagram for HCHCR D2 workpiece (a) Without damper (b) With damper

Similarly, the  $b$  is increased to 0.68 mm; the system behaved unstable without a damper; however, when the damper is activated with current 1.4 A, the system shifts to a stable zone (point 3). Hence the system behaviour is analogous to spindle speed variation to bypass or shift the chatter frequency by changing the natural frequency of the tooling structure. Point 4 is unconditionally unstable. A similar discussion holds good for SLD for HCHCR D2 steel with a limiting width of cut lesser than OHNS for all damper conditions.

## 6.8 EVALUATION OF MACHINING PERFORMANCE WITH MR DAMPER BY REAL-TIME CONTROL

Semi-active devices and controllers for vibration reduction on machine tools is a newly reported strategy that faces significant modelling and control challenges. The developed MR damper is controlled by a real-time controller considering the vibration-limiting feedback approach. The vibration response of the cutting tool is analysed before and after incorporating the semi-active MR damper to identify the performance



in machining OHNS and HCHCR D2 steel. The tool wear, surface roughness, and amplitude of tool vibration are evaluated with and without a semi-active MR damper.

### 6.8.1 Methodology

The control current to the damper is estimated by limiting vibration feedback. The vibration feedback of the cutting tool is analysed in LabVIEW to generate a digital pulse signal to the controller, which regulates the current from the DC power source to the MR damper. The influence of MR damper on surface roughness, tool wear, and amplitude of tool vibration in machining OHNS and HCHCR D2 are evaluated. The flowchart of the implementation of control to MR damper is shown in Figure 6.16.

### 6.8.2 Control logic for the damper

The control logic is formulated based on the amplitude of tool vibration. The maximum current flows to the damper when the acceleration level crosses the set threshold for 10 consecutive cycles. The controller sends no current if the threshold is not reached. As the control logic is straightforward, a speedy control action is anticipated.

$$I = \begin{cases} I_{max}, & A > A_{threshold} \\ I_{min}, & A < A_{threshold} \end{cases}$$

This control logic decides the supply of maximum current (1.4 A) or minimum current (0 A) by monitoring tool tip acceleration. The tool response regarding acceleration is the deciding factor for comparing the damper and control logic performance. Hence a

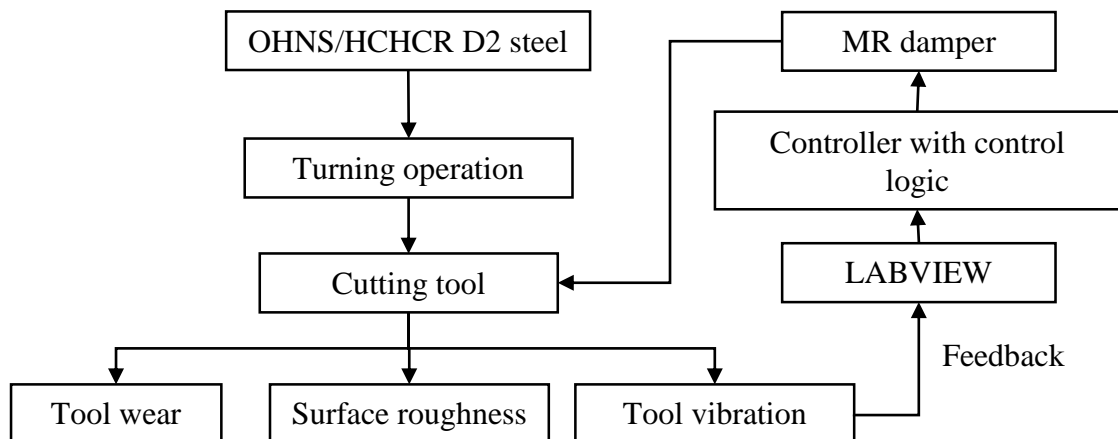


Figure 6.13 Flowchart of implementing control to MR damper

feedback system is developed to monitor the tool vibration with signal processing (RMS tracking) of real-time sensor data, which identifies the amplitude of vibration in the time domain signal.

## **6.9 MACHINING STUDY: IMPLEMENTATION OF MR DAMPER ON LATHE WITH CONTROLLER**

OHNS workpiece of 60 mm diameter and 250 mm length is machined using CNMG 120412 insert, which was held in PCLNR 2020K 12 tool holder. Vibration signals were acquired and analysed using NI DAQ 9230 and NI LabVIEW. Cutting force along tangential, radial and axial direction were recorded using Kistler 9257B dynamometer; however, only tangential direction was considered for designing the damper. A uniaxial accelerometer is placed on the tool holder to acquire the vibration in the tangential direction while placing it 50 mm away from the tool tip. The piston rod of the MR damper was connected securely at the bottom of the tool holder, and the MR damper was rigidly fitted on the lathe carriage to provide upward reaction force and neutralise the tool displacement. The block diagram of the experimental setup is illustrated in Figure 6.18 for a detailed understanding of the connection between data acquisition and damper control. A photographic image of the experimental setup showing the MR damper installed underneath the tool with a current controller is shown in Figure 6.19. The tool holder is secured on a dynamometer, and the accelerometer is on the tool holder to measure cutting force and vibration. The digital control signal developed in the LabVIEW software is sent to the current controller through a digital-to-analogue converter NI 9403 with a DSUB module mounted on NI cDAQ 9174.

## **6.10 RESULTS AND DISCUSSION**

The machining was carried out without the damper for cutting conditions 384 rpm at 0.046 mm/rev and 572 rpm at 0.093 mm/rev with a constant depth of cut of 0.5 mm to machine OHNS and HCHCR D2 steel, respectively. The tool vibration and surface roughness for these cutting conditions are measured and tabulated in Table 6.4. The tool wear is monitored considering the 0.4 mm flank wear as the tool failure criteria. The procedure is repeated for machining with a damper using online control.

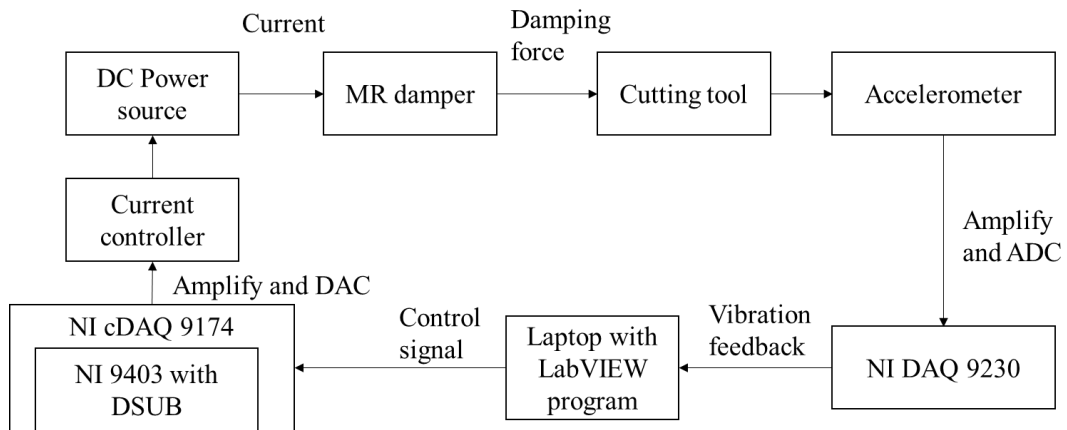


Figure 6.14 Block diagram of the experimental setup

Table 6.4 Tool acceleration, surface roughness and tool wear measurement with damper and without damper

Expt. No.	1	2	
<b>Workpiece Material</b>	OHNS	HCHCR D2	
<b>Cutting speed/surface velocity (rpm) (m/min)</b>	384 (72.39)	572 (107)	
<b>Spindle rotational frequency</b>	6.4 Hz	9.53 Hz	
<b>Feed rate(mm/rev)</b>	0.046	0.093	
<b>Tangential cutting force (N)</b>	360	441	
<b>RMS Acceleration of tool (g)</b>	Without damper	12.16	15.62
	With constant current 1.4 A	9.02	10.25
	With control ON	5.12	6.89
<b>Surface Roughness, Ra, (µm)</b>	Without damper	6.72	9.78
	With constant current 1.4 A	5.02	6.27
	With control ON	3.58	4.58
<b>Tool wear, V<sub>B</sub> (mm)</b>	Without damper	0.5	0.5
	With constant current 1.4 A	0.38	0.46
	With control ON	0.31	0.39

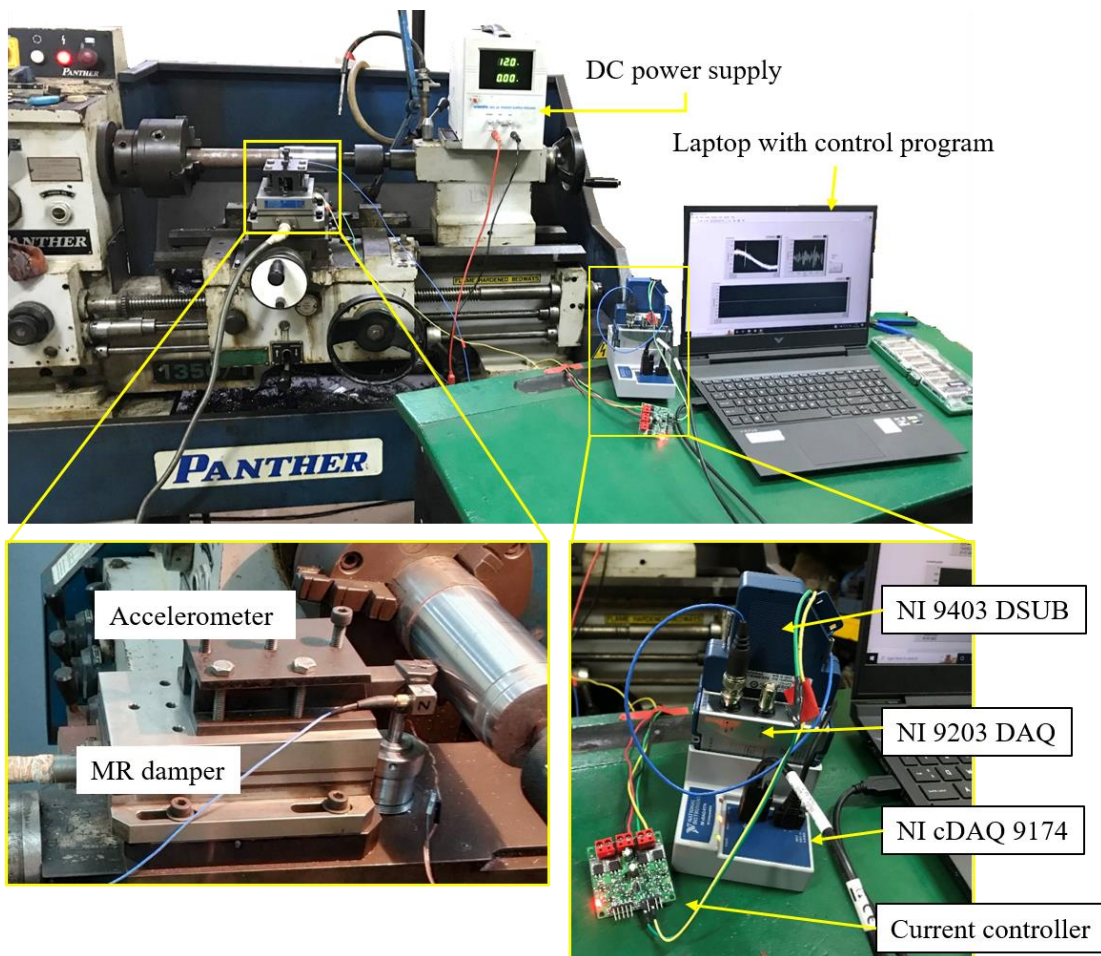


Figure 6.15 Experimental setup showing data acquisition, controller and MR damper

### 6.10.1 Vibration analysis of cutting tool with MR damper

Figure 6.20 (a) shows the tool vibration measured during the turning of OHNS in the presence of the MR damper, and Figure 6.20 (b) depicts the control pulse signal generated by the controller based on a vibration limiting approach for cutting condition 384 rpm, 0.053 mm/rev, 0.5 mm depth of cut. Similarly, Figure 21 (a) and Figure 21 (b) are the vibration signal and control signal for HCHCR D2 steel at 0.093 mm/rev, and 572 rpm, respectively. The amplitude of acceleration along the tangential direction was reduced with the damper by timely activation by control. s 6.20 (c) and 21 (c) depict frequency spectrum plots for both machining circumstances.

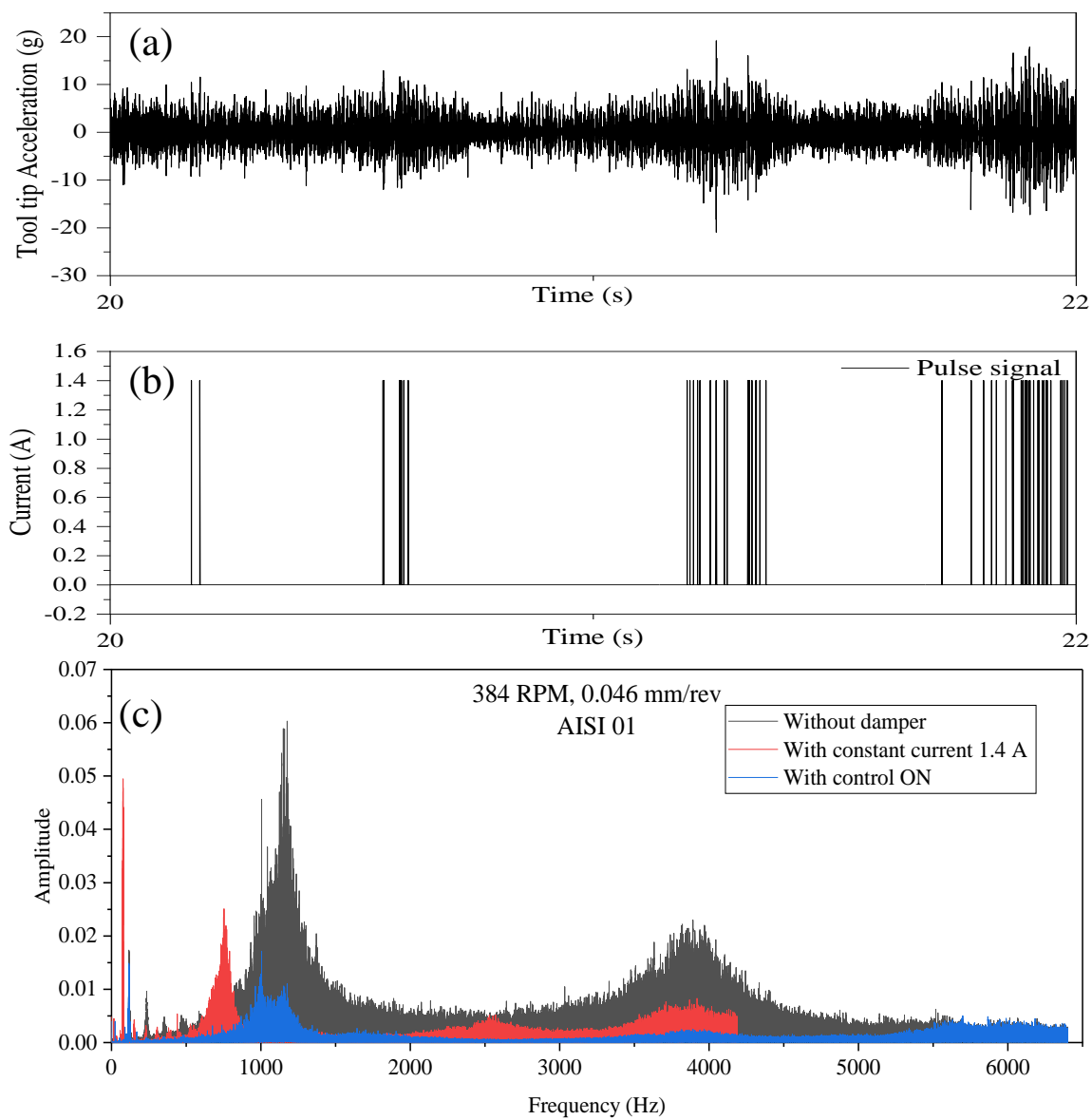


Figure 6.16 (a) vibration signal of OHNS (b) Control pulse signal OHNS (c) Spectrum plot of OHNS

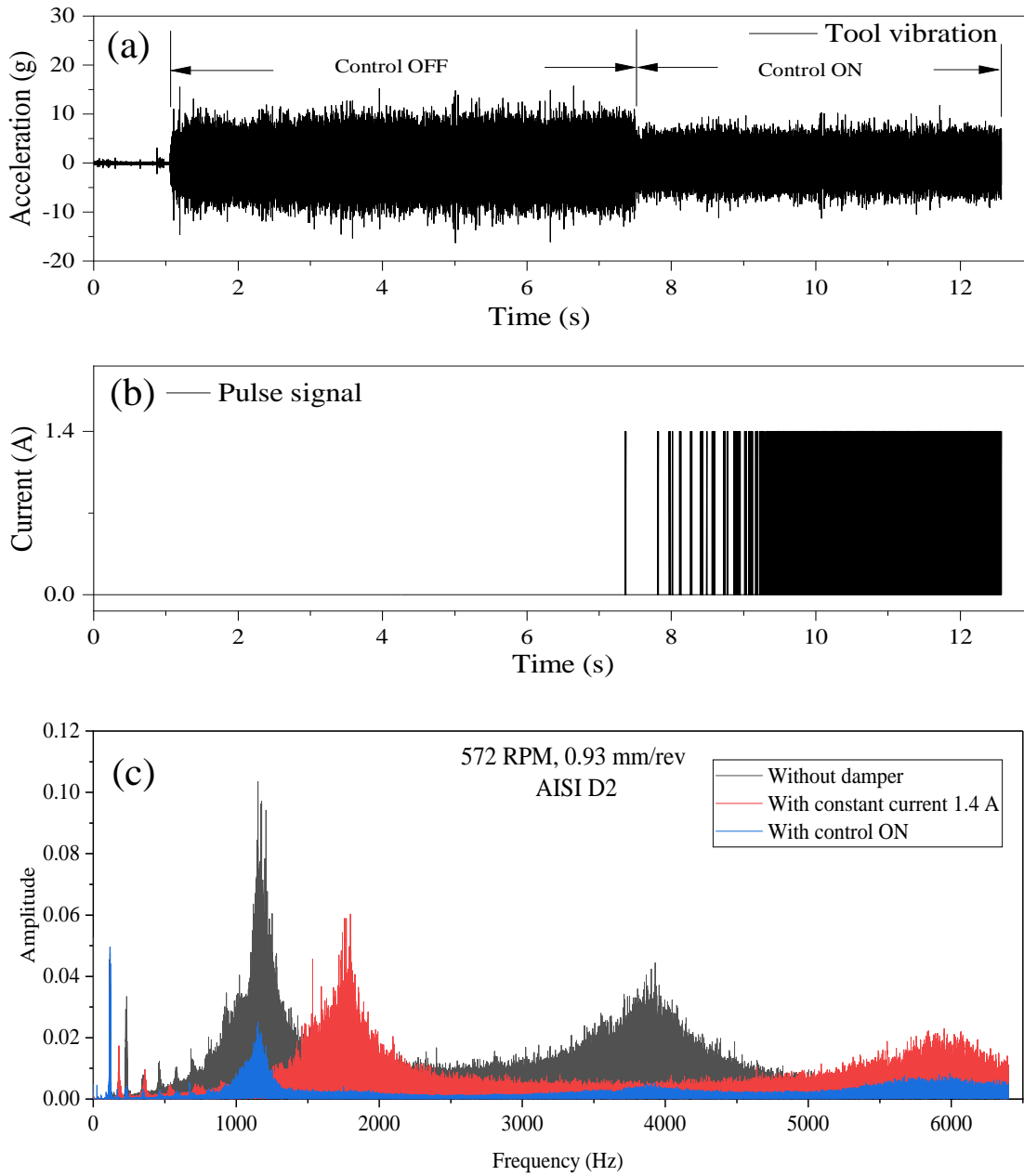


Figure 6.17 (a) Vibration signal of HCHCR D2 steel (b) Control pulse signal for HCHCR D2 (c) Spectrum plot of HCHCR D2

The area under the spectrum plot reveals the vibration energy, which is reduced with the damper at constant current and active control. The reduced amplitude of vibration is primarily due to the damper's higher dynamic stiffness, which improves the overall stability of the machining process. The average reduction in vibration level for 0.046 mm/rev is 57.9% and 55.8% for 0.093 mm/rev.

### 6.10.2 Comparison of surface roughness

Surface roughness is an important parameter highly influenced by tool vibration in machining. Figure 6.22 compares the surface profile produced with control ON and control OFF for two cutting conditions. It is seen that the timely activation of the MR damper has invariably improved the surface finish for both workpiece materials.

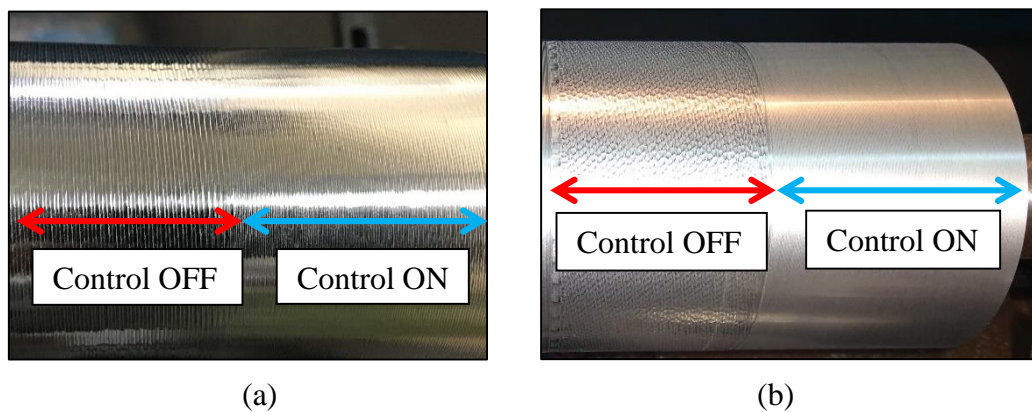


Figure 6.18 Roughness profile produced on workpiece with control ON and control OFF (a) 384 RPM, 0.043 mm/rev (b) 572 RPM, 0.093 mm/rev

### 6.10.3 Comparison of tool wear of the cutting tool

Flank wear significantly impacts the cutting process as it can change the tolerance over machined parts. According to ASME Standards, inserts are replaced as the maximum width of flank wear land reaches 0.4 mm. A tool wear test was conducted by machining the workpiece for 40 minutes in the presence and absence of an MR damper. The flank wear was measured using AXION optical microscope.

Table 6.4 lists the comparison of flank wear of the cutting tool during the turning operation. The flank wear is more at high speed and feeds due to increased temperature

due to abrasion of the flank face with the workpiece. Decrease in tool flank wears with damper mainly due to reduction of tool vibration, especially at the point of contact between tool and workpiece. The physical measurement of flank wear without a damper is shown in Figure 6.23.

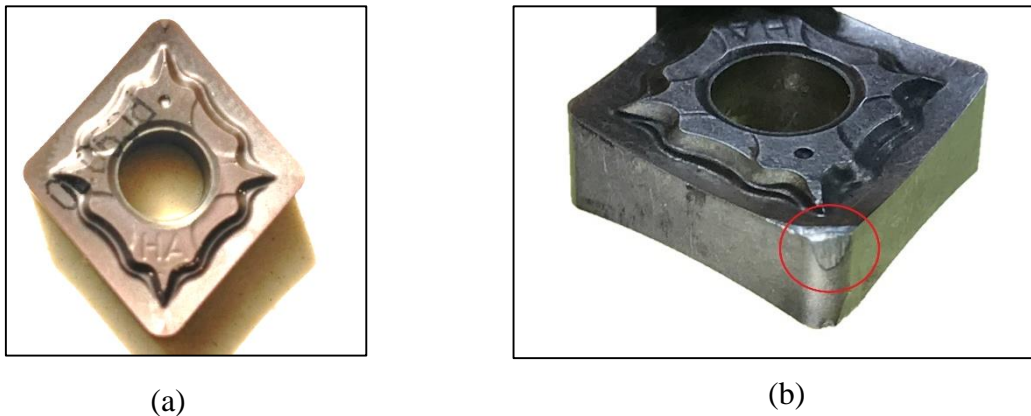


Figure 6.19 (a) Healthy tool and (b) Worn flank

## 6.11 SUMMARY

The chapter discusses the evaluation results of the MR damper installed on the lathe. The machining is carried out on two hard steel rods: OHNS and HCHCR D2 die steel. The machining is carried out without the MR damper and with the MR damper on both workpiece materials. The MR damper is evaluated with both optimal MR fluid and commercial MR fluid. The RMS value of tool vibration, surface roughness produced and tool wear rate with and without MR damper are evaluated. The L9 Taguchi experiment design on cutting conditions of three levels and three factors have been considered. Tool wear study on machining OHNS and HCHCR D2 steel with and without damper is evaluated. The stability lobe diagram for the tool-work combination with and without the damper was obtained by analytical calculation with coefficients obtained by frequency response test. The stability boundary of the machining increases with the activation of the damper enabling aggressive cutting conditions with the damper.

Cutting speed is the largest factor influencing the tool life, leading to rapid flank wear. Feed rate has less effect than cutting speed; however, if increased, invariable can



lead to chip hammering, chip welding, and loss of chip control. Similarly, depth of cut has little effect on tool life; however, if increased than allowed, it leads to increased cutting force, insert breakage and high power consumption; if maintained less, it causes vibrations.

The damper is implemented with real-time control to suppress chatter vibration. The experimental validation is carried out by machining OHNS and HCHCR D2 steel workpieces, commonly used in manufacturing dies and tools. Machining tests under various cutting conditions demonstrated that real-time control of the magnetorheological fluid damper could significantly improve surface finish and tool life compared to constant current.



## **CHAPTER 7**

### **DEVELOPMENT OF AN NOVEL ANTI-VIBRATION TOOL HOLDER FEATURING MR FLUID**

#### **7.1 INTRODUCTION**

Chapter 7 explores the possibilities of imbibing internally damped, controllable tool holders based on the insight obtained from the previous chapter about external damping. The internal damper is much more convenient and easy to use than the external damped tool holder without any structural modification to the machine tool. This chapter is the better version or configuration of the tool vibration control device featuring MR fluid. The results show the controllability and performance evaluation of the internal damped MR tool holder

A novel anti-vibration cutting tool holder has been designed to combat vibration induced during machining—the unique tool houses an inverse cantilever beam inside the primary structure with MR fluid in the chamber. A lumped mass is attached to this inverse beam at its free end. The lumped mass is surrounded by a viscous medium whose viscosity can be changed by an external magnetic field, thus achieving a tunable damped mass damper. The passive absorber with a constant mass ratio can control the self-excited oscillation within a specific instability range. For the higher intensity of instability, the parameters of the absorber are changed, such as the inverse beam's damping coefficient by changing the fluid's viscosity around the suspended mass. The vibration induced in the tool tip gets attenuated by the inertial movement of suspended mass. The dynamic characteristics of the unique tool holder are evaluated by conducting free and forced vibration tests to arrive at the shortest settling time and the highest resistance to chatter vibration. The machining performance of the unique tool holder is

comprehended with improvement in surface finish and a reduction in the amplitude of vibration signals.

## 7.2 DESIGN OF TOOL HOLDER

The tunable tool holder has a simple configuration that makes it simple to build and install. The tool holder comprises a hollow section at the axial centre with a suspended mass attached to a slender cantilever. The tool is modelled as shown in Figure 7.1; the outer structure of the holder has a shank size of 25x25 mm and an effective length of 175 mm. A slender beam supports the mass. The slender portion is wound with copper coil. The coil leads are taken through the opening in the end cap with sealant. Numerical symbols denote all significant damper components.

The oscillation frequency of the suspended mass is adjusted to a structural frequency, and when that frequency is triggered, the damper resonates out of phase with the structural motion. This happens when the tool chatters. The inertia force exerted by the mass on the primary structure dissipates energy. The suspended mass generates a reaction force proportionate to the tool holder's vibration amplitude, enabling dynamic vibration absorption.

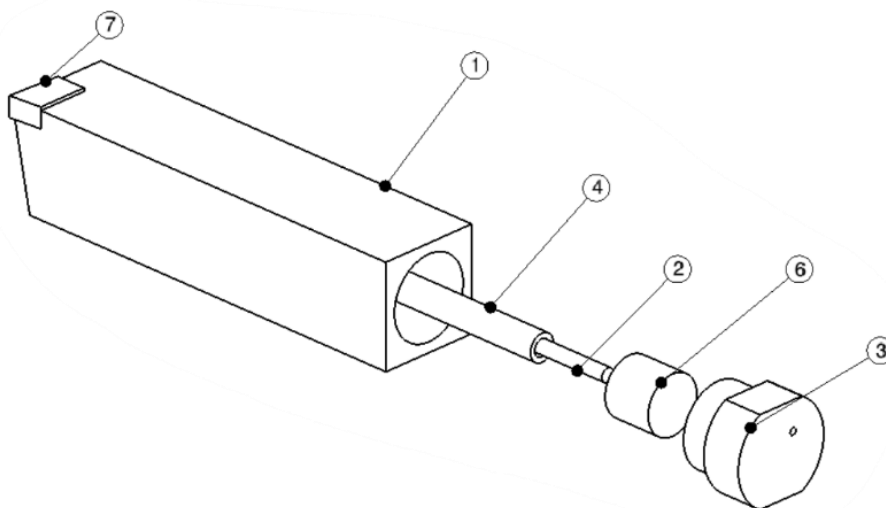


Figure 7.1 Parts label of the tool holder (1) outer tool body (2) slender bar (3) end cap (4) copper coil (5) fluid volume inside tool body (6) suspended mass (7) Insert

To enhance the vibration-damping ability of the suspended mass, the MR fluid is introduced into the hollow space between the slender bar and the tool holder's inner peripheral walls. A copper coil is wound around the slender bar to induce the magnetic field in the oscillating path of suspended mass. The dynamic vibration absorber is designed to dampen the resonance between the tool holder and the weight member, attenuate the vibration induced at the tooltip, and reduce the chatter vibration of the tool holder. The damping performance can be steadily maintained by changing the viscosity of the MR fluid.

### 7.3 NUMERICAL CALCULATION FOR DESIGNING THE TOOL MASS DAMPER FOR UN-DAMPED STRUCTURE

The system of a single degree of freedom transforms into two degrees of freedom by incorporating the vibration damping technique.

The system vibrates at resonance when the exciting frequency ( $\omega$ ) coincides with the resonance frequency ( $\omega_n$ ) of the system

$$\omega = \omega_n = \sqrt{\frac{k_p}{m_p}} \quad (7.1)$$

An additional spring mass ( $m_s, k_s$ ) system is coupled to the primary structure, which acts as the vibration absorber to dampen the vibration of the mass,  $m_p$ .

If the excitation frequency is equal to the natural frequency (which is also chatter frequency)

$$\omega = \sqrt{\frac{k_s}{m_s}} \quad (7.2)$$

Thus  $\frac{m_s}{k_s} = \frac{m_p}{k_p}$

Achieving this condition is called a tuned mass absorber—the system of single degrees changes to two degrees of freedom.

$$m_p \ddot{x}_p + k_p x_p + k_s (x_p - x_s) = F \sin \omega t \quad (7.3)$$

$$m_s \ddot{x}_s + k_s(x_s - x_p) = 0 \quad (7.4)$$

Solution assumed is

$$x_p = A_1 \sin \omega t ; x_s = A_2 \sin \omega t \quad (7.5)$$

Since

$$\dot{x}_p = -\omega A_1 \sin \omega t ; \dot{x}_s = -\omega A_2 \sin \omega t \quad (7.6)$$

Substituting these in Eq. 7.3 and 7.4

$$(k_p + k_s - m_p \omega^2)A_1 - k_s A_2 = F \quad (7.7)$$

$$-k_s A_1 + (k_s - m_s \omega^2)A_2 = 0 \quad (7.8)$$

Solving the above equations, we get

$$A_1 = \frac{k_s - m_s \omega^2}{\beta} ; A_2 = \frac{k_s F}{\beta} \quad (7.9)$$

Where

$$\beta = [m_p m_s \omega^4 - \{m_p k_s + m_s (k_p + k_s)\} \omega^2 + k_p k_s] \quad (7.10)$$

To get the amplitude of mass  $m_p=0$  equate the Eq. (7.9) to zero

$$A_1 = \frac{(k_s - m_s \omega^2)^2}{\beta} = 0 \quad (7.11)$$

$$\omega = \sqrt{\frac{k_s}{m_s}} = \omega_n \quad (7.12)$$

From equation 7.12, it is found that the amplitude of the secondary mass is larger than the primary mass. Thus, the design should accommodate a large amplitude of mass. However, the space around the secondary mass is filled with viscous fluid due to constricted space in the tool holder. Further, to improve the damping of the secondary mass oscillation, MR fluid is used, whose viscosity can be changed by applying a magnetic field. The magnetic field induced in the fluid chamber is made possible by winding the inverse cantilever beam with a copper coil. The field lines pass through the suspended mass, thus changing the fluid's viscosity in the direction of oscillation of the mass.

## 7.4 DEVELOPMENT OF MR TOOL HOLDER

### 7.4.1 Magnetostatic analysis

Figure 7.2 is the magnetostatic analysis of the MR tool holder, which reveals the flux density produced at the working gap. It is the basis for the design of the MR tool holder. The number of turns, the AWG of the wire, the power supply and rheological properties are decided based on the magnetostatic analysis. The suspended mass in the primary structure oscillates more than the primary mass (tooltip), which must be damped by enclosing it using the viscous fluid with variable viscosity. If we could measure the magnetic flux density produced at the gap between suspended mass and inner walls of the primary structure through magnetostatic analysis, then by rheological data of MR fluid, we can estimate the viscosity value corresponding to the magnetic field. Thus a changing viscosity gives a variable damping coefficient. The viscosity values are inserted in finite element harmonic analysis to analyse the system's response for variable viscosity and input excitation.

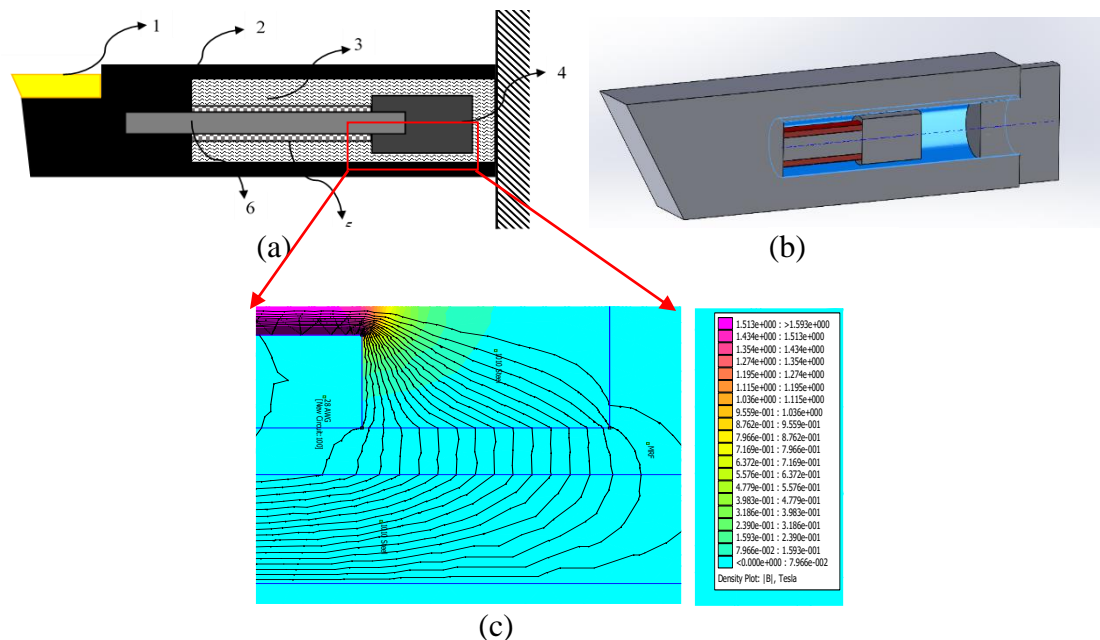


Figure 7.2 (a) Schematic of cross sectional view of MR tool holder 1-insert, 2-outer structure,3-MR fluid, 4-suspended mass, 5-copper coil, 6-inverse beam (b) 3D cross sectional view of MR tool holder (c) Magnetostatic analysis of active region in tool holder

The schematic of the cross-sectional view of the MR tool holder is shown in Figure 7.2 (a), indicating its parts and labels as the numerical designation. The vivid isometric cross-sectional view is also shown in Figure 7.2 (b). The red colour is a copper coil, and the blue colour is MR fluid. First, an axisymmetric FE model of the damper is created. The model used finite linear elements based on the modified magnetic potential technique. The flux lines and flux density produced at the oscillating path are shown through the finite element method magnetics (FEMM) tool in Figure 7.2 (c). The flux density produced at the fluid gap is 0.07966 T when 28 AWG of 100 turns is used as the electromagnetic coil at a supply current of 1.4 A, 12 V DC supply. The figure also shows that there aren't many secondary flux leakage paths that cross the functioning gap of the damper. One main objective was to produce a suitable amount of homogeneous flux density in the damper's working gap and to guarantee a functional performance range. The properties of commercial MR fluid MRF 132 DG from Lord Corp. were used in the tool holder.

#### 7.4.2 Structural analysis of the MR tool holder

The tool holder with a damping system is modelled in ANSYS, as shown in Figure 7.3. The tool is fixed at the end face, and harmonic excitation is applied at the tooltip. The response of the tool tip is recorded as shown in Figure 7.4. The damping ratio of the tool changed with the change in the viscosity of the MR fluid. The amplitude of the tool response damped with the increase in current.

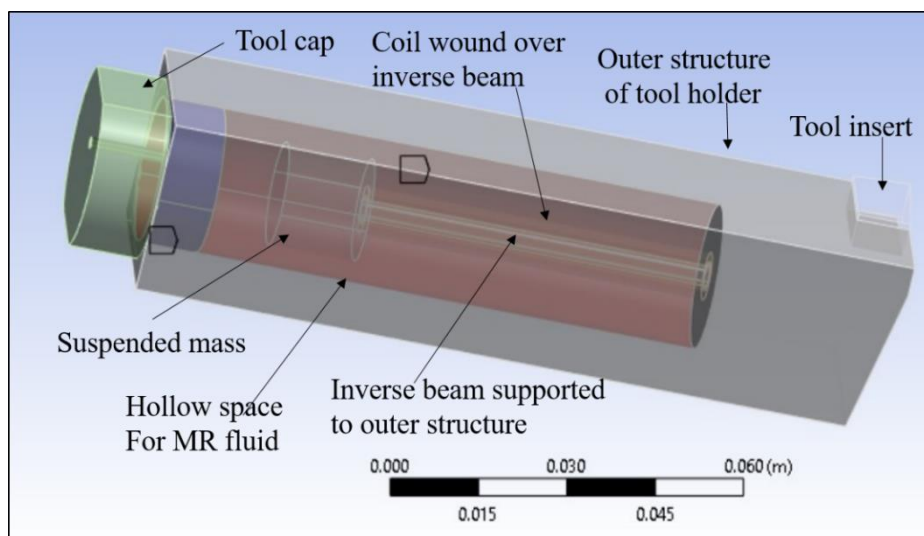


Figure 7.3 ANSYS model of the tool holder showing hidden parts and outer structure



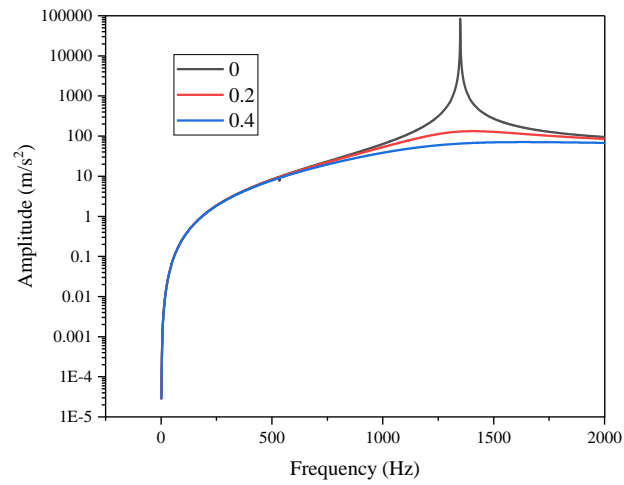
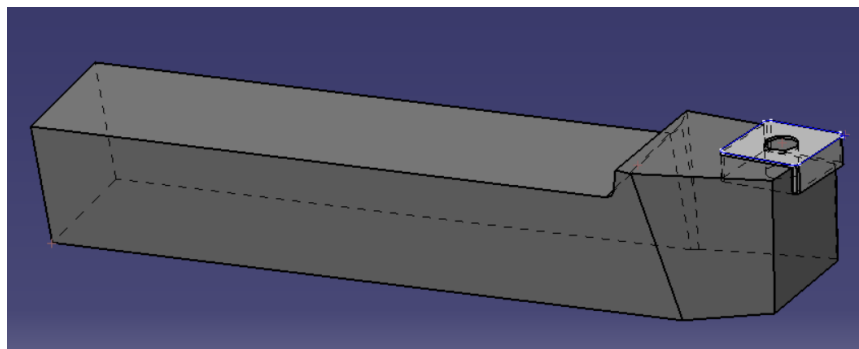
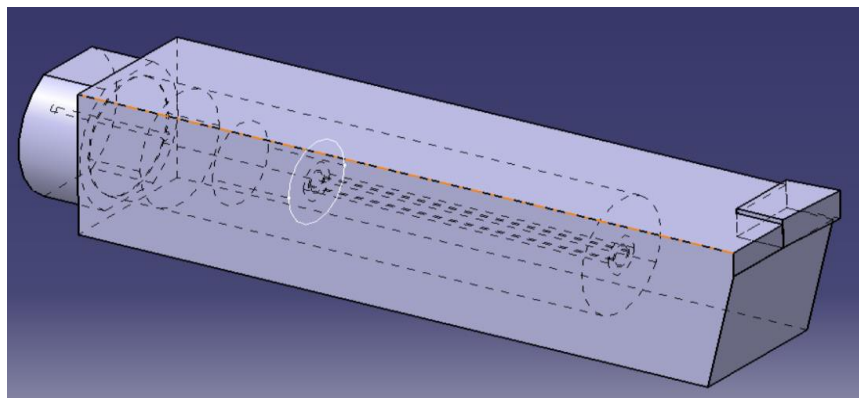


Figure 7.4 Harmonic response of the tool holder modelled in ANSYS for different damping ratio

Comparison of solid shank with new MR tool holder is modelled as shown in Figure 7.5 and compared experimentally for weight and natural frequency.



(a)



(b)

Figure 7.5 Solid model of (a) Solid shank tool holder and (b) MR tool holder

### 7.4.3 Fabrication of the tool holder

The tool holder is fabricated to the design configuration mentioned in the previous section. The parts of the developed tool holder are shown in Figure 7.6. The outer structure houses the tool insert at one end and an opening at the other. The tool tip's relief and clearance angles are provided as per the standard tool designation. The size of the rectangular shank is 25x25 mm, designed as the right-hand tool with a functional length of 150 mm, width of 25 mm and height of 25 mm. The body material is a tool steel. The tool can accommodate the insert of type CNMG. The insert is assembled with standard components of PCLNR 2020K 12, such as a lever, screw, shim, shim pin and an Allen key. The secondary structure is attached to the primary structure at the axial wall with a copper coil wound over it. The hollow space is filled with MR fluid. The end of the tool closed with the end cap. The copper leads come out through the hole in the end cap. The assembled image of the tool holder is shown in Figure 7.7. The mass of the solid shank tool holder was 0.37 kg, whereas the mass of the MR tool holder was 0.52 kg.

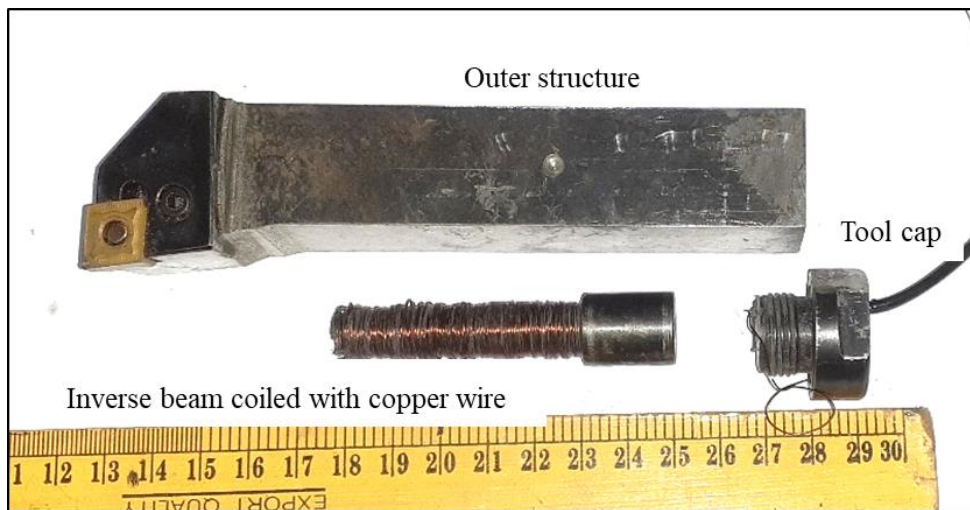


Figure 7.6 Dismantled components of MR tool holder fabricated

The tool holder is analysed for its frequency response for impulse excitation, which helps identify the natural frequency and tool damping ability. The free vibration is carried out for the overhanging length of 67 mm when the tool holder is held at its end. The overhanging of 67 mm is set to bring the advantage of primary oscillation. If not maintained, additional overhanging of the MR tool holder may not be effective. The tool holder works fine for extended overhanging to machine parts that require overhanging, such as flange, shoulder and deep grooves.

The experimental setup showing the impact hammer and data acquisition system to obtain the frequency response using the LABVIEW program is shown in Figure 7.8. The electric current supply to the electromagnetic coil induces the magnetic



Figure 7.7 Assembled image of the fabricated tool holder

field in the tool holder using the programmable DC power supply (0 - 2.0 A in steps of 0.4 A). The frequency response depicts the natural peak frequency at 968 Hz and 1400 Hz. The maximum peak amplitude at 1400 Hz reduced from 1.425 g/N to 1.317 g/N (8.2 %), as shown in Figure 7.10. The frequency response of the solid

tool is shown in Figure 7.9, indicating the peak at 2981 Hz. The natural frequency of the new tool holder is reduced due to the hollow portion in the shank; however, the damping capability is improved. The damping ratio of the tool holder with MRD was estimated by the 3 dB method using Eq. 7.1. The values of the damping ratio are tabulated in Table 7.1. The FRF plot appreciates the viscoelastic behaviour of MR fluid. The amplitude of frequency response reduces with the external damper.

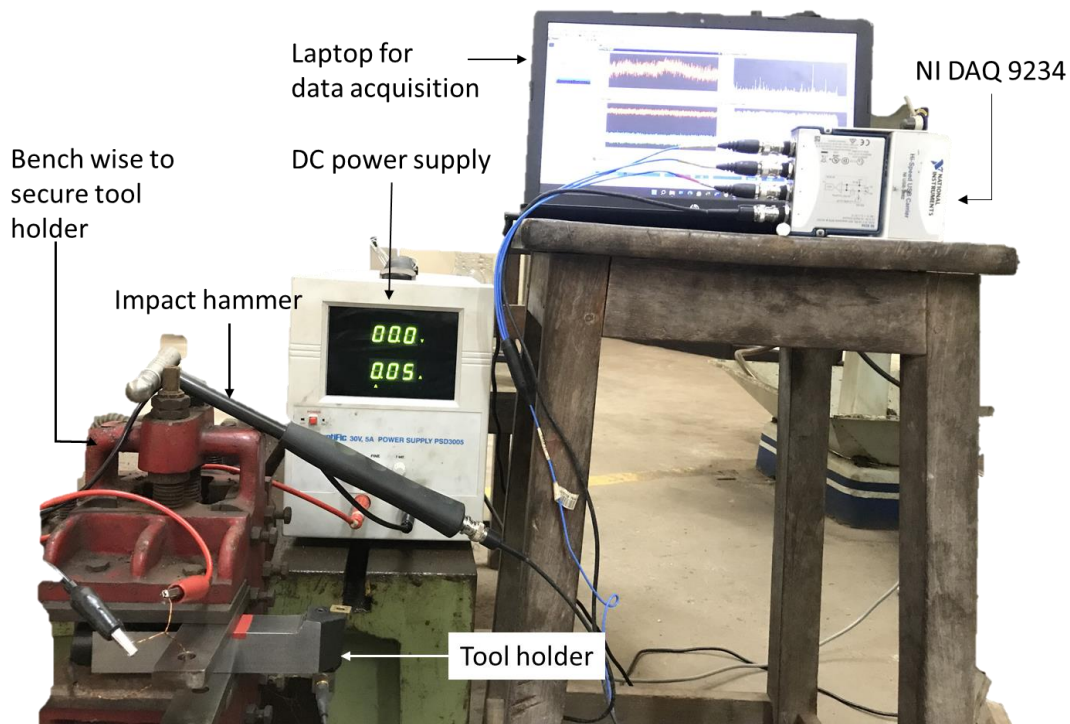


Figure 7.8 Experimental setup showing the free vibration study

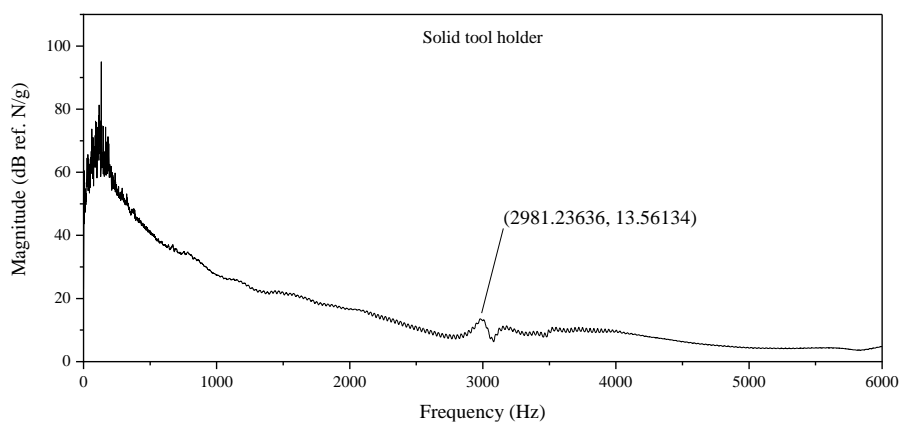


Figure 7.9 Frequency response of Sold tool holder for impulse excitation

The frequency shift observed is marginal, indicating no change in the stiffness of

the tool holder; however, there is a reduction of amplitude in the frequency response plot indicating damping due to the damper. Similarly, calculating the damping ratio from Figure 7.11 for the internal damped MR tool holder, the damping ratio achieved is 3.75, almost the same as external damping (3.43).

$$Q = \frac{f_0}{f_2 - f_1}; \text{ damping ratio, } \zeta = (1/2Q) \quad (7.1)$$

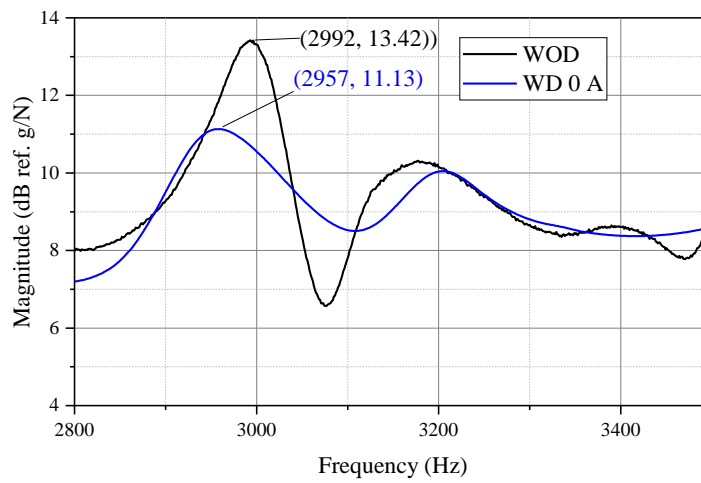


Figure 7.10 Estimating damping ratio for solid tool with external damping

Table 7.1 Estimation of damping ratio with damper

Condition	Damping factor (Q)	Damping Ratio ( $\zeta$ (%))
The solid tool holder (WOD)	29.05	1.72
The tool with external damping	14.42	3.43
The tool with internal. Damping	13.31	3.75

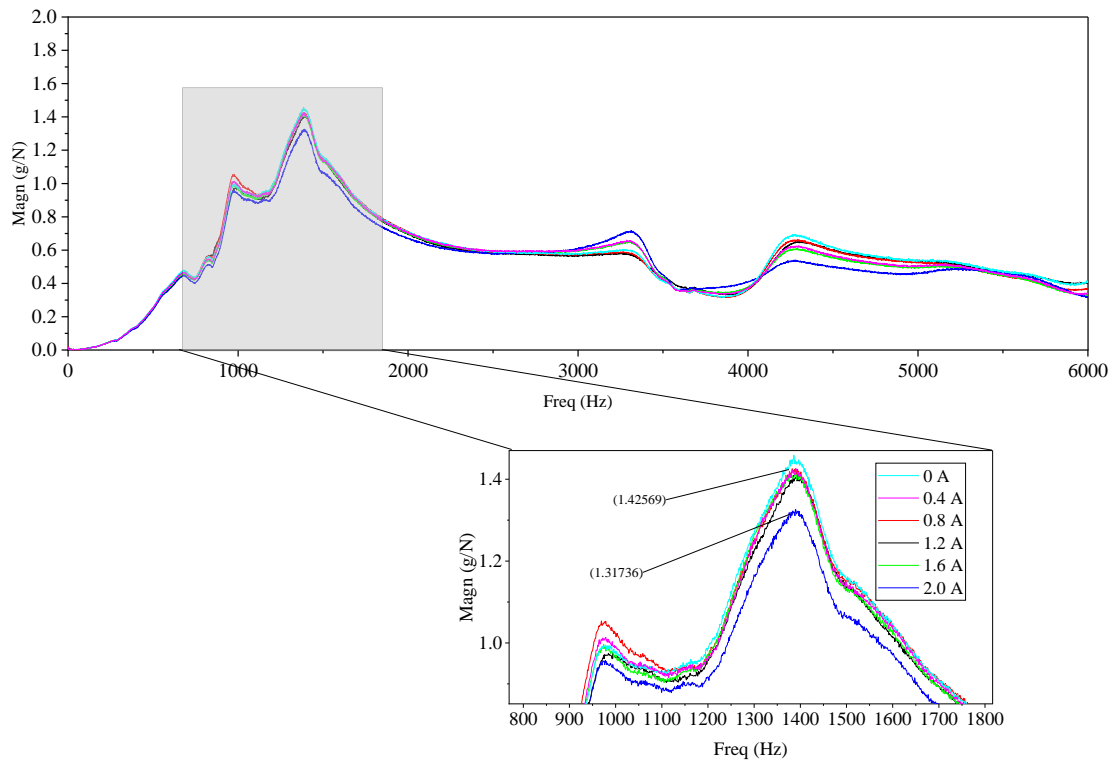


Figure 7.11 Frequency response of MR tool holder

## 7.5 FORCED VIBRATION STUDY

Experimental setup of the forced vibration testing of the magnetorheological tool holder, which consists of a power amplifier, electrodynamic shaker, data acquisition device (NI 9234, Make: National Instruments), accelerometer (Make: PCB Piezotronics), impedance sensor, programmable DC power source and stinger with fixture for holding the tool holder as shown in Figure 7.12.

A LabVIEW program was interfaced with sensors using DAQ. The tool was subjected to sinusoidal excitation at a natural frequency of 968 Hz, and the RMS acceleration at the tooltip at no current and at current 2.0 A reduced from 4.03 g to 1.145 g, as seen in Figure 7.13.

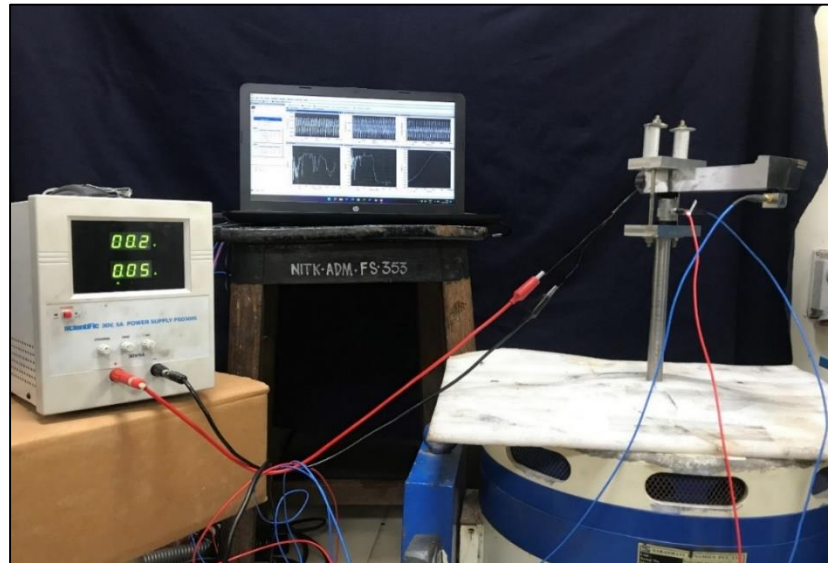


Figure 7.12 Experimental setup of the forced excitation study

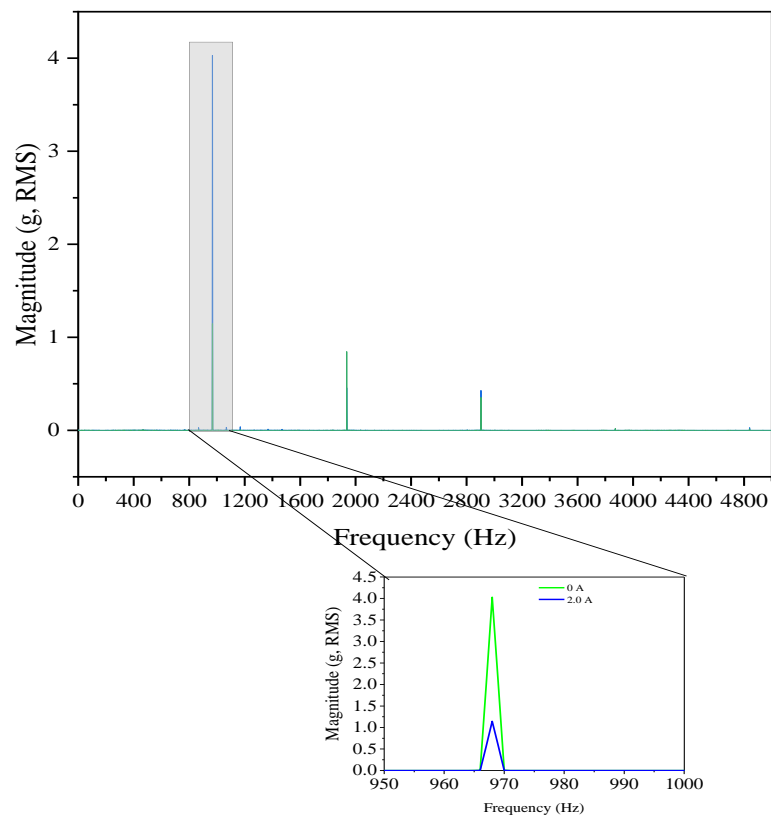


Figure 7.13 Acceleration response to forced excitation frequency of 968 Hz



## 7.6 MACHINING WITH MR TOOL HOLDER

The machining with the developed tool holder is carried out on a conventional lathe. The tool is connected to a DC power source which supplies variable current to the electromagnetic coil in the tool holder. The whole experimental setup with data acquisition and power supply is shown in Figure 7.14. An accelerometer is mounted at the bottom of the tooltip, as shown in the close-up view in Figure 7.15, to measure the tooltip vibration. The mounting of the sensor at the tooltip base ensures safety from the chip. The machining of oil-hardened nickel steel workpiece at cutting condition 378 RPM, 0.5 mm depth of cut and 0.08 mm/rev feed is carried out. The vibration signals are recorded during machining to measure the level of acceleration. If violent vibration is observed, the current is supplied to the coil in incremental steps till the vibration level is reduced. Figure 7.16 shows the vibration signal of the machining described above, which is reduced with the supply of electric current to the tool holder. The tool vibration, which was  $\pm 9$  g, was reduced to  $\pm 4$  g with the damper activated at 0.5 A, which was further reduced to  $\pm 2.5$  g with activation of 1.0 A current.

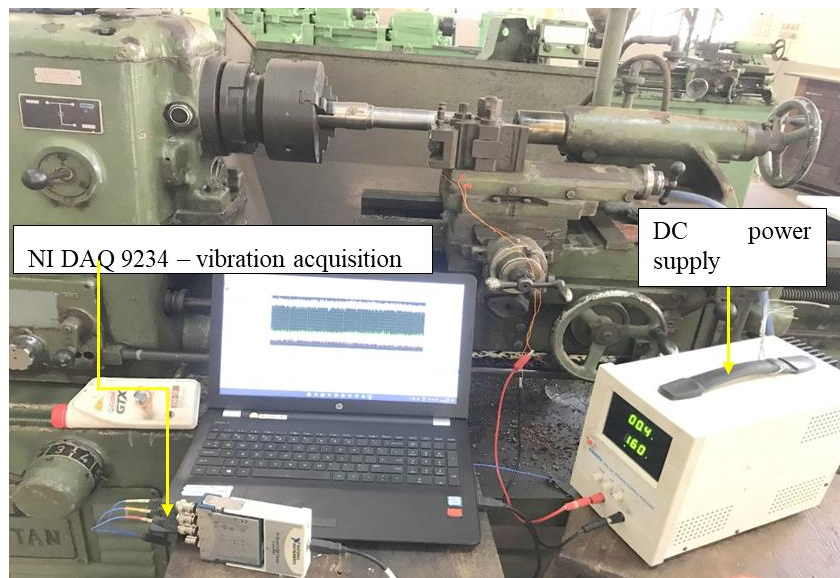


Figure 7.14 Experimental setup showing the vibration acquisition setup and DC power source to supply current to the tool holder

The surface roughness produced on the workpiece using the MR tool holder for cutting condition (speed: 576 RPM, feed: 0.053 mm/rev and depth of cut: 0.3 mm) without activation is  $6.02 \mu\text{m}$ , with 0.5 A supply current roughness reduced to  $4.52 \mu\text{m}$  further



increasing to 1.0 A roughness values reduced to 3.25  $\mu\text{m}$ . The vibration level and surface roughness values for a solid shank tool holder are  $\pm 7.88$  g and 5.98  $\mu\text{m}$ , respectively. The plot in Figure 7.16 compares the vibration level of the new MR tool holder with the solid shank tool. The vibration level and surface roughness values of the MR tool holder at 0 A are more than solid shank tools due to reduced stiffness; however, the vibration reduces with an increase in a magnetic field.

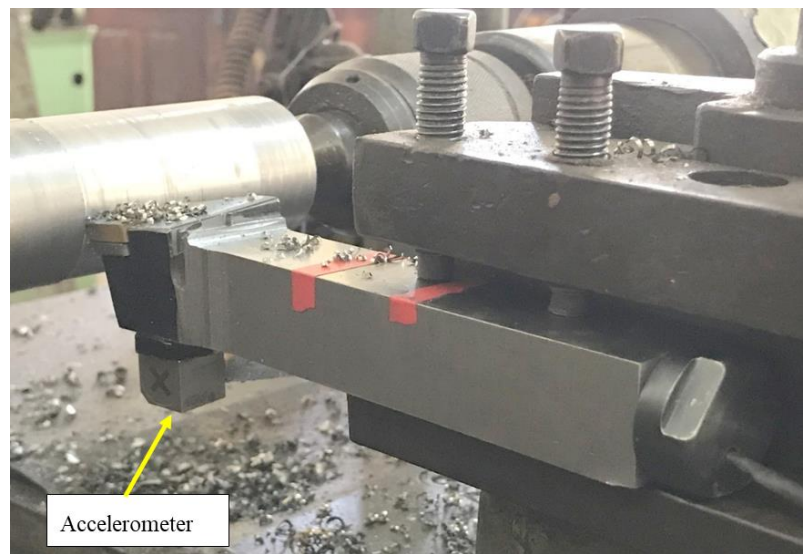


Figure 7.15 Close-up view of the tool holder secured on the lathe, accelerometer mounted under tooltip to acquire tool vibration.

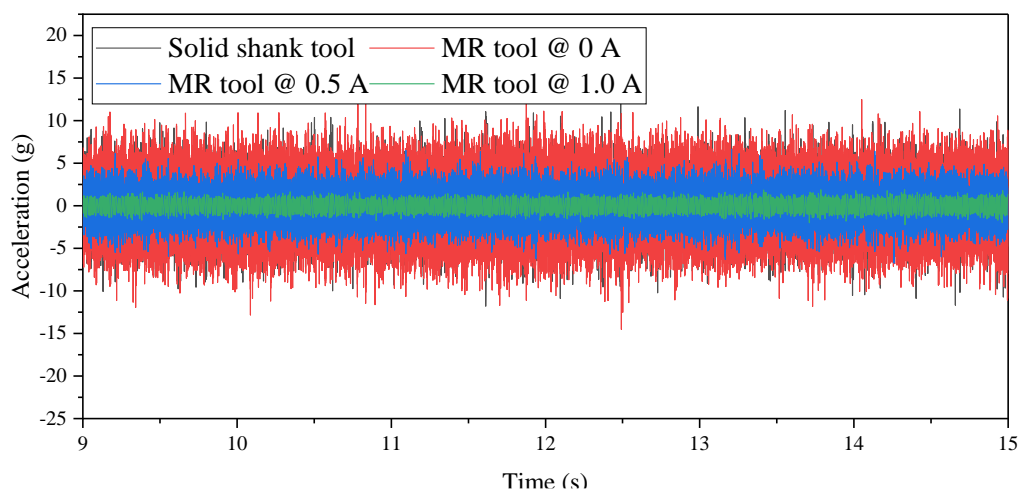


Figure 7.16 Vibration during machining with solid shank tool and new MR tool holder at varies current

## **7.7 SUMMARY**

A new tool holder with an inverse cantilever beam containing MR fluid is designed and developed to improve the tool holder's vibration suppression capability with variable damping and stiffness. The free vibration force vibration study is carried out to measure the natural frequency and damping ratio without activation and with activation. The tool holder is installed on the lathe to conduct machining, and the vibration amplitude reduces with the supply of current due to increased dynamic stiffness and improved internal damping by the magnetorheological effect.

## CHAPTER 8

### SUMMARY AND CONCLUSION

#### 8.1 SUMMARY

The tool fault identification and diagnosis were carried out using signal processing and machine learning techniques, using vibrational and cutting force signals. The tool faults were diagnosed using the statistical parameters and visual inspection of the time domain signal. The spindle rotational and chatter frequency components were identified, and their amplitude was tracked using the frequency domain analysis. Wavelet analysis revealed both time localisation and frequency resolution of the tool fault, making it the best to identify the time of occurrence of the tool fault and the nature of the tool fault.

The current study uses supervised machine learning with a labelled data set to train and test the vibrational and cutting force signals. Statistical features and wavelet features were extracted for classification. Significant features were selected from the J48 decision tree algorithm. Random forest, rotation forest, and Naïve Bayes algorithm were employed as the classifier; their classification accuracy was compared. The comparison shows that the vibration signal gives better classification accuracy than the cutting force signal; moreover, mounting the accelerometer and acquiring the vibrational signal is much easier, portable and versatile.

As seen in fault diagnosis, a faulty tool produces a poor surface finish; similarly, machining at aggressive cutting conditions results in chatter vibration. These vibrations were controlled by employing a variable viscosity damper to change its damping coefficient based on the applied magnetic field. The damper was designed based on vibration level and cutting force to calculate the amount of damping force and operating frequency of the damper. The flow valve of the damper was modelled in ANSYS

magnetostatic to obtain magnetic flux density achieved at the fluid flow gap. Various magnetic materials were assigned to the model to identify the maximum flux density in the fluid gap. The damper was characterised by a damper testing machine to evaluate its dynamic behaviour and maximum damping force. The optimal composition of the MR fluid for the MR damper was obtained by designing the experiment with particle loading of the carbonyl iron particle, viscosity of the base oil and the activation magnetic field as factors with three levels. The optimal composition was identified by employing ANOVA multi-objective optimization. The optimal composition delivered by the ANOVA was validated by further preparing the MR fluid and characterising it in the MR damper with good agreement between predicted values and validation results.

The developed damper was implemented on the lathe to evaluate its performance in suppressing the tool vibration and its influence on surface roughness. The damper was evaluated with optimal in-house MR fluid as well as commercial MR fluid [MRF 132 DG Lord Corp.]. Two workpiece materials were chosen for machining: OHNS and HCHCR D2 steel. A stability lobe diagram was constructed to mark the limiting depth of cut with and without the MR damper. Flank wear of 0.4 mm was considered a failure criterion to evaluate tool life. Cutting conditions of three levels of feed, speed and depth of cut were considered for evaluation; however, to reduce the number of test samples, Taguchi L15 design of the experiment was followed. An ON/OFF controller was implemented to control the damper in real-time by monitoring the tool vibration using vibration-limiting feedback. The pulse signal was generated when the limiting vibration crossed the set threshold level to activate the damper, making it an effective, efficient damper compared to the constant current to the damper.

In addition, an internally damped tool holder was designed and developed to improve the design configuration and easy installation with a built-in magnetic circuit. The novel MR tool holder was effective in controllability and reducing tool vibration.

## 8.2 CONCLUSIONS

### 8.2.1 Signal processing technique

Identifying the tool faults based on the signal processing applied to vibration and cutting force are listed as follows

- The state of the cutting tool is identified by the statistical parameters such as standard deviation, range, and maximum in the time domain signals. These statistical values were seen to be increasing by the fault conditions. The level of vibration for healthy was  $\pm 1$  g; for overhang  $\pm 2$  g; for flank wear  $\pm 4$  g and for the broken tool, it was  $\pm 6$  g. Similarly, the standard deviation for the cutting force signal for healthy was 49 N; overhang was 92 N; flank wear was 50 N, and the broken tool was 320 N. The process of damping due to flank wear land reduces the cutting force value.
- The dominant peak value appears at spindle frequency (SF), 48 Hz and its harmonics 100 Hz (approx. 2x). When tool fault changes, higher harmonics of SF appear. Maximum amplitude occurs at 48 Hz. The spectrum of the faulty tool contains many sidebands with a spacing of approximately 20 Hz. The spectrum shows the presence of additional frequencies, such as newly occurred frequencies that differ from multiples of SF corresponding to chattering; hence, chatter occurred for broken and worn flank tools. The level of flank wear is seen reduced due to process damping achieved with flank wear land.
- The CWT plot of the broken tool has only low frequency but high amplitude due to the sharp edge formed after breakage. These sharp edges get blunt and form newer sharp edges, which is evident from the reduction of amplitude from 0 to 0.6 s and increases from 0.6 s to 1 s.

The spectrum and wavelet analysis of the vibrational signals revealed better fault information than the cutting force signals.

### **8.2.2 Fault diagnosis by machine learning**

Comparison of the classification accuracy of all the three classifiers employed for both vibration and cutting force signal by utilising DWT and statistical features showed that the classification accuracy of the vibration signal is superior to that of the cutting force signal. However, Naive Bayes provides good classification accuracy of 96.6 % using DWT features, whereas Rotation Forest provides good accuracy of 95 % using statistical features using vibration signals.

The level of cutting force and vibration signal for healthy and faulty tools mark the input parameters for designing the MR damper. The damping force required in healthy conditions and the required in the faulty tool is estimated. The damper is designed for this range of damping force using the optimal composition of MR fluid.

### **8.2.3 MR fluid preparation and characterisation**

Nine samples of different viscosity and weight fractions of CIP were prepared. The maximum ON-state damping force is obtained for a higher viscosity (350 cSt) carrier fluid at 70% concentration of particles than the hydraulic oil (52 cSt) carrier fluid. It is also observed that increased particle concentration increases the MRF's dynamic yield stress, which has an inverse effect on the ratio of ON-state to OFF-state damping force. A carrier fluid viscosity of 240 cSt and a particle loading of 70 % resulted in the higher yield stress and the maximum effective damping range.

### **8.2.4 Development of MR damper**

The machining was performed by installing the damper on a lathe by fastening the piston rod to the tool holder and cylinder base to the saddle.

- The MR damper with in-house MR fluid delivers the desired damping force of 350 N at 1.4 A current, and commercial MR fluid (Make: 132 DG, Lord Corp.) fluid delivers 300 N at 1.4 A, which is sufficient to suppress the unstable cutting force

- The MR damper works effectively in suppressing the tool vibration at a higher depths of cut by increasing the current to the damper. The amplitude of tool vibration in the presence of the MR damper was 30 % lesser with the damper
- The MR damper improves the surface finish enabling aggressive cutting conditions with increased depth of cut both for the OHNS material and HCHCR D2 steel
- The tool life was enhanced with MR damper at a maximum of 9 min when machining OHNS workpiece and 5 min when machining HCHCR D2 steel
- The MR damper improved the chip morphology with the formation of continuous serration-free smooth edge chips enabling easy evacuation of chips and reducing abrasion of serrated chips
- Experimental verification via stability lobe diagram reveals the improvement of the limiting depth of cut from 0.51 mm to 0.64 mm for OHNS workpiece and improvement from 0.35 mm to 0.51 mm for machining HCHCR D2 steel

Real-time control allowed for the reduction of the surface roughness by approximately 46.7% for a cutting speed of 384 RPM and approximately 53.17% for 572 RPM. Additionally, the chatter marks on the machined surfaces were removed completely.

- In addition, the time domain signal and their frequency spectrum of tool vibration show that chatter is effectively damped by the MR damper at both normal and high-speed cutting parameters with real-time activation of the damper.
- The flank wear of the tool was reduced by 38 % when machined at feed 0.046 mm/rev and 22 % for feed 0.093 mm/rev with the timely activation of the control keeping the depth of cut and speed the same.

### **8.3 SCOPE FOR FUTURE WORK**

- The fault diagnosis of the cutting tool can be extended to real-time signal processing with online monitoring of the machining process by using an acoustic emission signal, sound signal, a current signal, temperature measurement and residual surface stresses

- The machine learning followed in the present study is supervised learning which can be extended to unsupervised learning
- The shear mode MR damper has been considered for the current study, which could be realised with a magnetorheological mount in place of a damper
- Other modes of damper, such as flow mode and squeeze mode, could be explored for their effectiveness



## REFERENCES

- Acharya, S., Radhe, T., Saini, S., and Kumar, H. (2019). "Determination of optimal magnetorheological fluid particle loading and size for shear mode monotube damper." *J. Braz. Soc. Mech. Sci. Eng.*, 41(10), 1–15.
- Acharya, S., Saini, T. R. S., Sundaram, V., and Kumar, H. (2021). "Selection of optimal composition of MR fluid for a brake designed using MOGA optimization coupled with magnetic FEA analysis." *J. Intell. Mater. Syst. Struct.*, 32(16), 1831–1854.
- Ahmed, G. M. S., Reddy, P. R., and Seetharamaiah, N. (2014). "FEA based Modeling of Magneto Rheological Damper to Control Vibrations During Machining." *Procedia Mater. Sci.*, 6(Icmpe), 1271–1284.
- Akan, A., and Karabiber Cura, O. (2021). "Time–frequency signal processing: Today and future." *Digit. Signal Process.*, 119, 103216.
- Alok, A., Kumar, A., and Das, M. (2021). "Hard Turning with a new HSN 2-coated carbide insert and optimization of process parameter." *Trans. Indian Inst. Met.*, 74, 1577–1591.
- Anisheh M., & H. H. (2009). "Adaptive Segmentation with Optimal Window Length Scheme using Fractal Dimension and Wavelet Transform." *Int. J. Eng.*, 22(3), 257–268.
- Anoop, P., and Sugumaran, V. (2017). "Classifying machine learning features extracted from vibration signal with logistic model tree to monitor automobile tyre pressure." *Struct. Durab. Health Monit.*, 11(2), 191.
- Arizmendi, M., Campa, F., Fernández, J., De Lacalle, L. L., Gil, A., Bilbao, E., Veiga, F., and Lamikiz, A. (2009). "Model for surface topography prediction in peripheral milling considering tool vibration." *CIRP Ann.*, 58(1), 93–96.
- Ashtiani, M., Hashemabadi, S. H., and Ghaffari, A. (2015). "A review on the magnetorheological fluid preparation and stabilization." *J. Magn. Magn. Mater.*, 374, 711–715.
- Astakhov, V. P. (2004). "The assessment of cutting tool wear." *Int. J. Mach. Tools Manuf.*, 44(6), 637–647.
- Bae, S. J., Mun, B. M., Chang, W., and Vidakovic, B. (2019). "Condition monitoring of a steam turbine generator using wavelet spectrum based control chart." *Reliab. Eng. Syst. Saf.*, 184, 13–20.

Barbieri, N., Sant, G. D., Vitor, A., Matos, B., Sant, L. D., Vitor, A., Fonseca, K., and Lima, D. (2019). "Analysis of automotive gearbox faults using vibration signal." *Mech. Syst. Signal Process.*, 129, 148–163.

Benkedjough, T., and Rechak, N. Z. S. (2018). "Tool wear condition monitoring based on continuous wavelet transform and blind source separation."

Bessous, N., Zouzou, S. E., Bentrach, W., Sbaa, S., and Sahraoui, M. (2018). "Diagnosis of bearing defects in induction motors using discrete wavelet transform." *Int. J. Syst. Assur. Eng. Manag.*, 9(2), 335–343.

Bhuiyan, M. S. H. H., Choudhury, I. A., and Dahari, M. (2014). "Monitoring the tool wear, surface roughness and chip formation occurrences using multiple sensors in turning." *J. Manuf. Syst.*, 33(4), 476–487.

Biju, C. V., and Shunmugam, M. S. (2014). "Investigation into effect of particle impact damping (PID) on surface topography in boring operation." *Int. J. Adv. Manuf. Technol.*, 75(5–8), 1219–1231.

Biju, C. V., and Shunmugam, M. S. (2019). "Performance of magnetorheological fluid based tunable frequency boring bar in chatter control." *Meas. J. Int. Meas. Confed.*, 140, 407–415.

Budak, E., and Ozlu, E. (2007). "Analytical modeling of chatter stability in turning and boring operations: A multi-dimensional approach." *CIRP Ann. - Manuf. Technol.*, 56(1), 401–404.

Büssow, R. (2007). "An algorithm for the continuous Morlet wavelet transform." *Mech. Syst. Signal Process.*, 21(8), 2970–2979.

Cao, M., Wang, K. W., and Lee, K. Y. (2008). "Scalable and invertible PMNN model for MagnetoRheological fluid dampers." *JVCJournal Vib. Control*, 14(5), 731–751.

Chiou, R. Y., and Liang, S. Y. (1998). "Chatter stability of a slender cutting tool in turning with tool wear effect." *Int. J. Mach. Tools Manuf.*, 38(4), 315–327.

Cho, Y. H., Cho, M. S., Choi, H. J., and Jhon, M. S. (2002). "Electrorheological characterization of polyaniline-coated poly(methyl methacrylate) suspensions." *Colloid Polym. Sci.*, 280(11), 1062–1066.

Chui, C. (1992). *An Introduction to Wavelets. Math. Comput.*

- Cuka, B., and Kim, D. (2017). "Robotics and Computer – Integrated Manufacturing Fuzzy logic based tool condition monitoring for end-milling." *Robot. Comput. Integr. Manuf.*, 47(January), 22–36.
- Desai, R. M., Jamadar, M. e.Hussain, Kumar, H., and Joladarashi, S. (2021). "Performance Evaluation of a Single Sensor Control Scheme Using a Twin-Tube MR Damper Based Semi-active Suspension." *J. Vib. Eng. Technol.*, 9(6), 1193–1210.
- Devikiran, P., Puneet, N. P., Hegale, A., and Kumar, H. (2022). "Design and development of MR damper for two wheeler application and Kwok model parameters tuning for designed damper." *Proc. Inst. Mech. Eng. Part J. Automob. Eng.*, 236(7), 1595–1606.
- Díaz-Tena, E., López De Lacalle Marcaide, L. N., Campa Gómez, F. J., and Chaires Bocanegra, D. L. (2013). "Use of magnetorheological fluids for vibration reduction on the milling of thin floor parts." *Procedia Eng.*, 63, 835–842.
- Dimla, D. E. (2002). "The Correlation of Vibration Signal Features to Cutting Tool Wear in a Metal Turning Operation." 705–713.
- Edhi, E., and Hoshi, T. (2001). "Stabilization of high frequency chatter vibration in fine boring by friction damper." *Precis. Eng.*, 25(3), 224–234.
- Eem, S. H., Koo, J. H., and Jung, H. J. (2019). "Feasibility study of an adaptive mount system based on magnetorheological elastomer using real-time hybrid simulation." *J. Intell. Mater. Syst. Struct.*, 30(5), 701–707.
- Elangovan, M., Devasenapati, S. B., Sakthivel, N. R., and Ramachandran, K. I. (2011). "Evaluation of expert system for condition monitoring of a single point cutting tool using principle component analysis and decision tree algorithm." *Expert Syst. Appl.*, 38(4), 4450–4459.
- Elangovan, M., Ramachandran, K. I., and Sugumaran, V. (2010). "Studies on Bayes classifier for condition monitoring of single point carbide tipped tool based on statistical and histogram features." *Expert Syst. Appl.*, 37(3), 2059–2065.
- Farjoud, A., and Bagherpour, E. A. (2016). "Electromagnet design for magneto-rheological devices." *J. Intell. Mater. Syst. Struct.*, 27(1), 51–70.
- Gangadhar, N., Vernekar, K., Kumar, H., and Narendranath, S. (2017). "Fault diagnosis of single point cutting tool through discrete wavelet features of vibration signals using decision tree technique and multilayer perceptron." *J. Vib. Eng. Technol.*, 5(1), 35–44.

- Gangsar, P., and Tiwari, R. (2014). "Multiclass Fault Taxonomy in Rolling Bearings at Interpolated and Extrapolated Speeds Based on Time Domain Vibration Data by SVM Algorithms." *J. Fail. Anal. Prev.*, 14(6), 826–837.
- Gangsar, P., and Tiwari, R. (2016). "Taxonomy of Induction-Motor Mechanical-Fault Based on Time-Domain Vibration Signals by Multiclass SVM Classifiers." *Intell. Ind. Syst.*, 2(3), 269–281.
- Genç, S., and Phulé, P. P. (2002). "Rheological properties of magnetorheological fluids." *Smart Mater. Struct.*, 11(1), 140.
- Ghule, G., Ambhore, N., and Chinchankar, S. (2017). "Tool condition monitoring using vibration signals during hard turning: A review."
- Goldasz, J. (2013). "Study of a magnetorheological fluid damper with multiple annular flow gaps." *International J. Veh. Des.*, 62(1), 21–41.
- Gołdasz, J., and Sapiński, B. (2015). *Insight into magnetorheological shock absorbers. Insight Magnetorheol. Shock Absorbers.*
- Gurubasavaraju, T. M. M., Kumar, H., and Arun, M. (2017). "Optimisation of monotube magnetorheological damper under shear mode." *J. Braz. Soc. Mech. Sci. Eng.*, 39(6), 2225–2240.
- Guyon, I., and Elisseeff, A. (2003). "An introduction to variable and feature selection." *J. Mach. Learn. Res.*, 3(Mar), 1157–1182.
- Hahn, R. (1951). "Design of Lanchester damper for elimination of metal-cutting chatter." *Trans. Am. Soc. Mech. Eng.*, 73(3), 331–335.
- Herschel, W. H., and Bulkley, R. (1926). "Konsistenzmessungen von Gummi-Benzollösungen." *Kolloid-Z.*, 39(4), 291–300.
- Hesser, D. F., and Markert, B. (2019). "Tool wear monitoring of a retrofitted CNC milling machine using artificial neural networks." *Manuf. Lett.*, 19, 1–4.
- Ingle, R., & Awale, R. (2018). "A Unique Approach of Noise Elimination from Electroencephalography Signals between Normal and Meditation State." *Int. J. Eng.*, 31(5), 719–728.
- Jha, S. K., Wang, J., and Shanmugam, R. (2022). "An accurate soft diagnosis method of breast cancer using the operative fusion of derived features and classification approaches." *Expert Syst.*, 39(7).

- Johansson, D., Hägglund, S., Bushlya, V., and Ståhl, J.-E. (2017). “Assessment of commonly used tool life models in metal cutting.” *Procedia Manuf.*, 11, 602–609.
- Jurkovic, J., Korosec, M., and Kopac, J. (2005). “New approach in tool wear measuring technique using CCD vision system.” *Int. J. Mach. Tools Manuf.*, 45(9), 1023–1030.
- Kamble, V. G., and Kolekar, S. (2014). “Analysis of Rheological Properties of MR Fluid Based on Variation in Concentration of Iron Particles.” *Am. J. Nanotechnol.*, 5(2), 12–16.
- Karandikar, J., McLeay, T., Turner, S., and Schmitz, T. (2015). “Tool wear monitoring using naïve Bayes classifiers.” *Int. J. Adv. Manuf. Technol.*, 77(9–12), 1613–1626.
- Kim, Y., Ha, J. M., Na, K., Park, J., and Youn, B. D. (2021). “Cepstrum-assisted empirical wavelet transform (CEWT)-based improved demodulation analysis for fault diagnostics of planetary gearboxes.” *Meas. J. Int. Meas. Confed.*, 183.
- Kishawy, H. A., Hegab, H., Umer, U., and Mohany, A. (2018). “Application of acoustic emissions in machining processes: analysis and critical review.” *Int. J. Adv. Manuf. Technol.*, 98(5–8), 1391–1407.
- Kishore, R., Choudhury, S. K., and Orra, K. (2018). “On-line control of machine tool vibration in turning operation using electro-magneto rheological damper.” *J. Manuf. Process.*, 31, 187–198.
- Koenigsberger, F., and Tlustý, J. (1970). *Machine tool structures*. Pergamon series.
- Kolluru, K., Axinte, D., and Becker, A. (2013). “A solution for minimising vibrations in milling of thin walled casings by applying dampers to workpiece surface.” *CIRP Ann.*, 62(1), 415–418.
- Kothuru, A., Nooka, S. P., and Liu, R. (2018). “Audio-Based Tool Condition Monitoring in Milling of the Workpiece Material With the Hardness Variation Using Support Vector Machines and Convolutional Neural Networks.” 140(November), 1–9.
- Kuljanic, E., and Sortino, M. (2005). “TWEM, a method based on cutting forces—monitoring tool wear in face milling.” *Int. J. Mach. Tools Manuf.*, 45(1), 29–34.
- Kumar Kariganaur, A., Kumar, H., and Arun, M. (2022). “Influence of temperature on magnetorheological fluid properties and damping performance.” *Smart Mater. Struct.*, 31(5).

- Kus, A., Isik, Y., Cakir, M. C., Coşkun, S., and Özdemir, K. (2015). “Thermocouple and infrared sensor-based measurement of temperature distribution in metal cutting.” *Sensors*, 15(1), 1274–1291.
- Lemaire, E., Meunier, A., Bossis, G., Liu, J., Felt, D., Bashtovoi, P., and Matoussevitch, N. (1998). “Influence of the particle size on the rheology of magnetorheological fluids.” *J. Rheol.*, 39(5), 1011.
- Li, W., Zhu, Z., Jiang, F., Zhou, G., and Chen, G. (2015). “Fault diagnosis of rotating machinery with a novel statistical feature extraction and evaluation method.” *Mech. Syst. Signal Process.*, 50–51, 414–426.
- Li, X., Yao, Z. H., and Chen, Z. C. (2010). “An Effective EMD-Based Feature Extraction Method for Boring Chatter Recognition.” *Appl. Mech. Mater.*, 34–35, 1058–1063.
- Liang, B., Iwnicki, S. D., and Zhao, Y. (2013). “Application of power spectrum, cepstrum, higher order spectrum and neural network analyses for induction motor fault diagnosis.” *Mech. Syst. Signal Process.*, 39(1–2), 342–360.
- Lim, S. T., Cho, M. S., Jang, I. B., and Choi, H. J. (2004). “Magnetorheological characterization of carbonyl iron based suspension stabilized by fumed silica.” *J. Magn. Magn. Mater.*, 282(1–3), 170–173.
- Liu, C., Li, Y., Zhou, G., and Shen, W. (2018). “A sensor fusion and support vector machine based approach for recognition of complex machining conditions.” *J. Intell. Manuf.*, 29(8), 1739–1752.
- Lyu, Y., Jamil, M., He, N., Gupta, M. K., and Pimenov, D. Y. (2021). “Development and testing of a high-frequency dynamometer for high-speed milling process.” *Machines*, 9(1), 1–16.
- Ma, J., Zhang, D., Wu, B., Luo, M., and Chen, B. (2016a). “Vibration suppression of thin-walled workpiece machining considering external damping properties based on magnetorheological fluids flexible fixture.” *Chin. J. Aeronaut.*, 29(4), 1074–1083.
- Ma, J., Zhang, D., Wu, B., Luo, M., and Chen, B. (2016b). “Vibration suppression of thin-walled workpiece machining considering external damping properties based on magnetorheological fluids flexible fixture.” *Chin. J. Aeronaut.*, 29(4), 1074–1083.
- Ma, W., Yu, J., Yang, Y., and Wang, Y. (2021). “Optimization and tuning of passive tuned mass damper embedded in milling tool for chatter mitigation.” *J. Manuf. Mater. Process.*, 5(1).

- Madhusudana, C. K., Budati, S., Gangadhar, N., Kumar, H., and Narendranath, S. (2016a). "Fault diagnosis studies of face milling cutter using machine learning approach." *J. Low Freq. Noise Vib. Act. Control*, 35(2), 128–138.
- Madhusudana, C. K. K., Kumar, H., and Narendranath, S. (2016b). "Condition monitoring of face milling tool using K-star algorithm and histogram features of vibration signal." *Eng. Sci. Technol. Int. J.*, 19(3), 1543–1551.
- Madhusudana, C. K., Kumar, H., and Narendranath, S. (2016c). "Engineering Science and Technology , an International Journal Condition monitoring of face milling tool using K-star algorithm and histogram features of vibration signal." *Eng. Sci. Technol. Int. J.*, 19(3), 1543–1551.
- Madhusudana, C. K., Kumar, H., and Narendranath, S. (2016d). "Fault Detection of Face Milling Cutter through Spectrum , Cepstrum and Wavelet Analysis." 4(1), 10–28.
- Mallat, S. (2002). "A wavelet tour of signal processing." Academic Press, 1998." *Mojtaba Kosari Receiv. B Sc Degree Electr. Eng. Shiraz Univ. Fars Iran In.*
- Masood, I., Jahanzaib, M., and Haider, A. (2016). "Tool wear and cost evaluation of face milling grade 5 titanium alloy for sustainable machining." *Adv. Prod. Eng. Manag.*, 11(3), 239–250.
- Merritt, H. E. (1965). "Theory of self-excited machine-tool chatter: Contribution to machine-tool chatter research-1." *J. Manuf. Sci. Eng. Trans. ASME*, 87(4), 447–454.
- Mohan, E., and Natarajan, U. (2016). "Experimental Investigation on Boring Tool Vibration Control Using MR Fluid Damper." *J. Adv. Manuf. Syst.*, 15(01), 13–25.
- Mohan, E., Natarajan, U., and Prasanth, C. S. (2017). "Investigation of damping effect of magneto-rheological fluid damper on internal turning operation." *SSRG Int J Mech Eng ICEHS*, 23–28.
- Monnin, J., Kuster, F., and Wegener, K. (2014). "Optimal control for chatter mitigation in milling—Part 1: Modeling and control design." *Control Eng. Pract.*, 24, 156–166.
- Muhammad, A., Gupta, M. K., Mikołajczyk, T., Pimenov, D. Y., and Giasin, K. (2021). "Effect of tool coating and cutting parameters on surface roughness and burr formation during micromilling of inconel 718." *Metals*, 11(1), 1–18.
- Munoa, J., Beudaert, X., Dombovari, Z., Altintas, Y., Budak, E., Brecher, C., and Stepan, G. (2016). "Chatter suppression techniques in metal cutting." *CIRP Ann.*, 65(2), 785–808.

Neugebauer, R., Denkena, B., and Wegener, K. (2007). "Mechatronic Systems for Machine Tools." *CIRP Ann.*, 56(2), 657–686.

Nguyen, Q. H., Choi, S. B., Lee, Y. S., and Han, M. S. (2013). "Optimal design of high damping force engine mount featuring MR valve structure with both annular and radial flow paths." *Smart Mater. Struct.*, 22(11).

Norton, M. P., and Karczub, D. G. (2003). *Fundamentals of noise and vibration analysis for engineers*. Cambridge university press.

Osiak, M., Nowicki, M., Klejman, E., and Fraś, L. (2022). "Investigation of the well-dispersed magnetorheological oil-based suspension with superparamagnetic nanoparticles using modified split Hopkinson pressure bar." *Rheol. Acta*, 61(2), 111–122.

Painuli, S., Elangovan, M., and Sugumaran, V. (2014). "Tool condition monitoring using K-star algorithm." *Expert Syst Appl*, 41(6), 2638-2643.

Park, G., Bement, M. T., Hartman, D. A., Smith, R. E., and Farrar, C. R. (2007). "The use of active materials for machining processes: A review." *Int. J. Mach. Tools Manuf.*, 47(15), 2189–2206.

Parlak, Z., Engin, T., and Çalli, I. (2012). "Optimal design of MR damper via finite element analyses of fluid dynamic and magnetic field." *Mechatronics*, 22(6), 890–903.

Parlak, Z., Engin, T., and Şahin, I. (2013). "Optimal magnetorheological damper configuration using the taguchi experimental design method." *J. Mech. Des. Trans. ASME*, 135(8).

Paul, P. S., Iasanth, J. A., Vasanth, X. A., and Varadarajan, A. S. (2015). "Effect of nanoparticles on the performance of magnetorheological fluid damper during hard turning process." *Friction*, 3(4), 333–343.

Peng, W., Chen, J., and Zhou, H. (2009). "An implementation of ID3-decision tree learning algorithm." *Web Arch Usyd Edu AupengDecisionTree2 Pdf Retrieved Date May*, 13.

Phu, D. X., Shin, D. K., and Choi, S. (2015). "application to vibration control of a vehicle seat Design of a new adaptive fuzzy controller and its application to vibration control of a vehicle seat installed with an MR damper." *Smart Mater. Struct.*, 24.

Phule, P. P., Ginder, J. M., and Jatkar, A. D. (1997). "Synthesis and properties of magnetorheological (MR) fluids for active vibration control." *Mater. Res. Soc. Symp. - Proc.*, 459, 99–104.



- Plaza, E. G., and López, P. J. N. (2018). "Application of the wavelet packet transform to vibration signals for surface roughness monitoring in CNC turning operations." 98, 902–919.
- Plaza, E. G., López, P. J. N., García Plaza, E., Núñez López, P. J., Plaza, E. G., and López, P. J. N. (2017). "Surface roughness monitoring by singular spectrum analysis of vibration signals." *Mech. Syst. Signal Process.*, 84, 516–530.
- Pour, D. S., and Behbahani, S. (2016). "Semi-active fuzzy control of machine tool chatter vibration using smart MR dampers." *Int. J. Adv. Manuf. Technol.*, 83(1–4), 421–428.
- Poynor, J. C., and Reinholtz, C. (2001). "Innovative Designs for Magneto-Rheological Dampers." *Expedition*, 1–12.
- Preumont, A. (1997). *Vibration Control of Active Structures*. Solid Mechanics and Its Applications, Cham: Springer International Publishing.
- Rabinow, J. (1948). "The Magnetic Fluid Clutch." *Trans. Am. Inst. Electr. Eng.*, 67, 1308–1315.
- Rajini, A., and Jabbar, M. A. (2021). "Lung cancer prediction using random forest." *Recent Adv. Comput. Sci. Commun.*, 14(5), 1650–1657.
- Ramesh, K., Alwarsamy, T., and Jayabal, S. (2013). "Investigation of chatter stability in boring tool and tool wear prediction using neural network." *Int. J. Mater. Prod. Technol.*, 46(1), 47.
- Ramirez-Nunez, J. A., Trejo-Hernandez, M., Romero-Troncoso, R. J., Herrera-Ruiz, G., and Osornio-Rios, R. A. (2018). "Smart-sensor for tool-breakage detection in milling process under dry and wet conditions based on infrared thermography." *Int. J. Adv. Manuf. Technol.*, 97(5–8), 1753–1765.
- Rao, S. S. (2010). *Mechanical Vibrations*. (arcia J. Horton, ed.), NJ: Pearson.
- Ravikumar, K. N., Kumar, H., GN, K., and KV, G. (2020). "Fault diagnosis of internal combustion engine gearbox using vibration signals based on signal processing techniques." *J. Qual. Maint. Eng.*, 27(2), 385–412.
- Rivin, E. I. (2000). "Tooling structure: Interface between cutting edge and machine tool." *CIRP Ann. - Manuf. Technol.*, 49(2), 591–634.

Rodríguez, J. J., Kuncheva, L. I., and Alonso, C. J. (2006). "Rotation forest: A New classifier ensemble method." *IEEE Trans. Pattern Anal. Mach. Intell.*, 28(10), 1619–1630.

rong, L. C., Lei, X., xia, Z. D., Qiong, L., Liao, C. R., Xie, L., Zhao, D. X., and Liu, Q. (2013). "Quasi-steady modelling for magneto-rheological fluid mount based on squeeze mode and experimental testing." *Int. J. Veh. Des.*, 63(2/3), 275.

Roy, D., Srivastava, R., Jat, M., and Karaca, M. S. (2022). "A complete overview of analytics techniques: descriptive, predictive, and prescriptive." *Decis. Intell. Anal. Implement. Strateg. Bus. Manag.*, 15–30.

Sajedipour, D., and Behbahani, S. (2010). "with a MR Damper for Chatter Suppression." 802–807.

Saleh, M. K. A., Nejatpour, M., Yagci Acar, H., and Lazoglu, I. (2021). "A new magnetorheological damper for chatter stability of boring tools." *J. Mater. Process. Technol.*, 289(September 2020), 116931.

Salonitis, K., and Kolios, A. (2014). "Reliability assessment of cutting tool life based on surrogate approximation methods." *Int. J. Adv. Manuf. Technol.*, 71(5–8), 1197–1208.

Saravanan, N., and Ramachandran, K. I. (2010). "Incipient gear box fault diagnosis using discrete wavelet transform (DWT) for feature extraction and classification using artificial neural network (ANN)." *Expert Syst. Appl.*, 37(6), 4168–4181.

Schmitt, R., Cai, Y., and Pavim, A. (2012). "Machine Vision System for Inspecting Flank Wear on Cutting Tools." *ACEEE Int J Control Syst. Instrum.*, 03(01), 13.

Seung-Bok, C., and Young-Min, H. (2013). *Magnetorheological Fluid technology: Applications in vehicle systems*. Boca Raton London New York: CRC Press, Taylor & Francis Group, 2013.

Sharma, A., Amarnath, M., and Kankar, P. K. (2017). "Novel ensemble techniques for classification of rolling element bearing faults." *J. Braz. Soc. Mech. Sci. Eng.*, 39(3), 709–724.

Shaw, M. C., Smith, P. A., and Cook, N. H., (1952). "Discussion: 'The Rotary Cutting Tool.'" *Trans. Am. Soc. Mech. Eng.*, 74(6), 1065–1073.

Shihab, S. K., Khan, Z. A., Mohammad, A., and Siddiquee, A. N. (2014). "A review of turning of hard steels used in bearing and automotive applications." *Prod. Manuf. Res.*, 2(1), 24–49.

- Siddhpura, M., and Paurobally, R. (2012). "A review of chatter vibration research in turning." *Int. J. Mach. Tools Manuf.*, 61, 27–47.
- Sims, N. D., Bayly, P. V., and Young, K. A. (2005). "Piezoelectric sensors and actuators for milling tool stability lobes." *J. Sound Vib.*, 281(3–5), 743–762.
- Singh, A., and Amarnath, V. S. and M. (2016). "Fault Diagnosis of Helical Gearbox through Vibration Signals using J48 Decision Tree and Wavelet." *Indian J. Sci. Technol.*, 9(33), 1–8.
- Som, A., Kim, D. H., and Son, H. (2015). "Semiactive Magnetorheological Damper for High Aspect Ratio Boring Process." *IEEEASME Trans. Mechatron.*, 20(5), 2575–2582.
- Song, K. H., Lee, D. Y., Park, K. H., Kim, J. H., and Choi, Y. J. (2020). "Cutting force estimation using feed motor drive current in cutting process monitoring." *J. Korean Soc. Precis. Eng.*, 37(11), 803–812.
- Song, K. H., Park, B. J., and Choi, H. J. (2009). "Effect of Magnetic Nanoparticle Additive on Characteristics of Magnetorheological Fluid." *IEEE Trans. Magn.*, 45(10), 4045–4048.
- Sørby, K. (2017). "Development and Optimization of Vibration-Damped Tool Holders for High Length-to-Diameter Boring Operations." *High Speed Mach.*, 2(1), 51–58.
- Spaggiari, A. (2012). "Properties and applications of magnetorheological fluids." *Frat. Ed Integrita Strutt.*, 23(23), 57–61.
- Stone, B. (2014). *Chatter and machine tools*. Springer.
- Stone, B. J. (1970). "The effect on the chatter behaviour of machine tools of cutters with different helix angles on adjacent teeth." *Proc MTDR*, 169–180.
- Sugumaran, V., Muralidharan, V., and Ramachandran, K. I. (2007). "Feature selection using Decision Tree and classification through Proximal Support Vector Machine for fault diagnostics of roller bearing." *Mech. Syst. Signal Process.*, 21(2), 930–942.
- Talib, M. H. A., and Darus, I. Z. M. (2013). "Self-tuning PID controller with MR damper and hydraulic actuator for suspension system." *Proc. Int. Conf. Comput. Intell. Model. Simul.*, 119–124.
- Taylor, F. W. (1906). *On the art of cutting metals*. American society of mechanical engineers.

Thomas, M., Beauchamp, Y., Youssef, A., and Masounave, J. (1996). "Effect of tool vibrations on surface roughness during lathe dry turning process." *Comput. Ind. Eng.*, 31(3–4), 637–644.

Tiwari, R. (2000). *ROTOR SYSTEMS: Analysis and Identification*. ぎょうせい, CRC Press, Taylor & Francis Group, 2018.

Thusty, J., and Polacek, M. (1963). "The stability of machine tools against self-excited vibrations in machining." *Pittsburgh USA, Proceedings of the ASME International Research in Production Engineering*, 465–474.

Tobias, S., and Fishwick, W. (1958). "Theory of regenerative machine tool chatter." *The engineer*, 205(7), 199–203.

Tunç, L. T., and Budak, E. (2012). "Effect of cutting conditions and tool geometry on process damping in machining." *Int. J. Mach. Tools Manuf.*, 57, 10–19.

Turkes, E., Orak, S., Neseli, S., and Yaldiz, S. (2011). "Linear analysis of chatter vibration and stability for orthogonal cutting in turning." *Int. J. Refract. Met. Hard Mater.*, 29(2), 163–169.

Uehara, K., Ryabov, O., Mori, K., and Kasashima, N. (1996). "An in-process direct monitoring method for milling tool failures using a laser sensor." *CIRP Ann. - Manuf. Technol.*, 45(1), 97–100.

Urbikain, G., Fernández, A., López de Lacalle, L. N., and Gutiérrez, M. E. (2013). "Stability lobes for general turning operations with slender tools in the tangential direction." *Int. J. Mach. Tools Manuf.*, 67, 35–44.

Vanherck, P. (1967). "Increasing milling machine productivity by use of cutters with non-constant cutting edge pitch." *8th MTDR Conf.*, 947–960.

Vnukov, Y., Germashev, A., Logominov, V., and Kryshstal, V. (2017). "Possibilities of using stability lobe diagram for stability prediction of high speed milling of thin-walled details." *Mech. Adv. Technol.*, 1, 41–48.

Wang, F., and Fang, L. (2019). "A Fault Diagnosis Method for Automaton based on Morphological Component Analysis and Ensemble Empirical Mode Decomposition." *Int. J. Eng.*, 32(7).

Wang, J., Ma, Y., Zhang, L., Gao, R. X., and Wu, D. (2018). "Deep learning for smart manufacturing : Methods and applications." *J. Manuf. Syst.*, 48, 144–156.

Wang, Q., Garrity, G. M., Tiedje, J. M., and Cole, J. R. (2007). “Naïve Bayesian classifier for rapid assignment of rRNA sequences into the new bacterial taxonomy.” *Appl. Environ. Microbiol.*, 73(16), 5261–5267.

Wang, S., Nguyen, T., Anderson, W., Ciocanel, C., Elahinia, M., Nguyen, T., Anderson, W., Ciocanel, C., and Elahinia, M. (2010). “Skyhook control of a mixed mode magnetorheological fluid mount.” *Proc. ASME Des. Eng. Tech. Conf.*, 4, 325–330.

Wu, X., Liu, Y., Zhou, X., and Mou, A. (2019). “Automatic identification of tool wear based on convolutional neural network in face milling process.” *Sens. Switz.*, 19(18).

Xiao, M., Karube, S., Soutome, T., and Sato, K. (2002). “Analysis of chatter suppression in vibration cutting.” *Int. J. Mach. Tools Manuf.*, 42(15), 1677–1685.

Xu, Z., Sha, L., Zhang, X., and Ye, H. (2013). “Design, performance test and analysis on magnetorheological damper for earthquake mitigation.” *Struct Control Health Monit.*, 20(06), 956–970.

Yamato, S., Ito, T., Matsuzaki, H., Fujita, J., and Kakinuma, Y. (2020). “Self-acting optimal design of spindle speed variation for regenerative chatter suppression based on novel analysis of internal process energy behavior.” *Int. J. Mach. Tools Manuf.*, 159(PA), 103639.

Yao, Z., Mei, D., and Chen, Z. (2010). “On-line chatter detection and identification based on wavelet and support vector machine.” *J. Mater. Process. Technol.*, 210(5), 713–719.

Yue, J. (2006). “Creating a Stability Lobe Diagram.” *IJME-INTERTECH Conf.*, 18.

Zhang, Y., Wu, M., Liu, K., and Zhang, J. (2021). “Optimization Research of Machining Parameters for Cutting GH4169 Based on Tool Vibration and Surface Roughness under High-Pressure Cooling.” *Materials*, 14(24), 7861.



## APPENDIX

### 1. Panther all-g geared precision lathe

Parameter	Specification
Model	1350/1
Height for centres	177 mm
Dist between centres	540
Spindle bore	42 mm
Spindle diameter	45 mm
Travel of tool slide	130
Tool shank section	16 x 16
No of speeds	8 / 16
Range RPM	45 – 938 / 30 – 1250
No of feeds	65
Longitudinal feed	0.05 to 0.8 mm/rev
Transverse feed	0.03 to 0.48 mm/rev
Main motor	2 HP
Power supply	3 phase

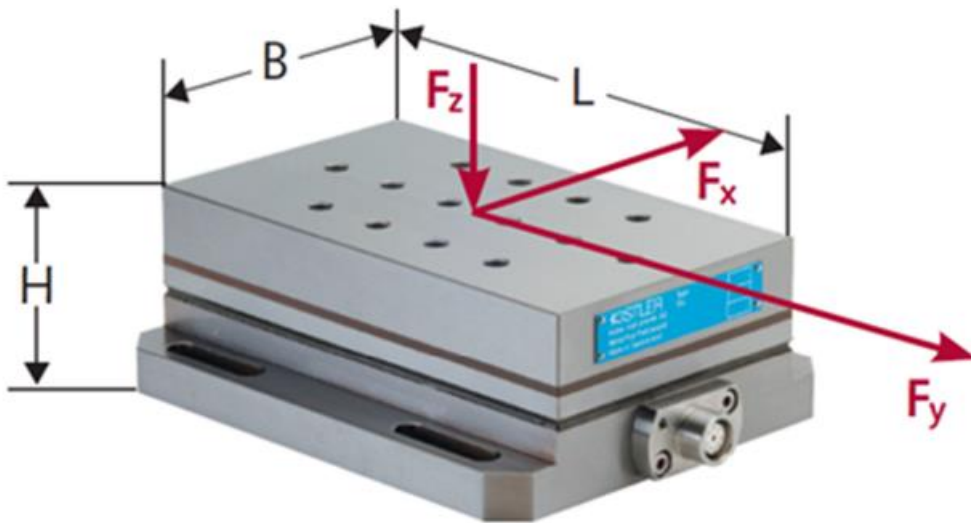
IMAGE



## 2. Cutting tool dynamometer (piezoelectric)

Technical data	Type	9257 B	
Measuring range	$F_x, F_y$	kN	-5...5
	$F_z$	kN	-5...10
Calibrated measuring range	$F_x, F_y$	kN	0...5
	$F_z$	kN	0...10
Sensitivity	$F_x, F_y$	pC/N	~ - 7.5
	$F_z$	pC/N	~ - 3.7
Natural frequency	$F_n(x), F_n(y)$	kHz	~ 2.3
	$F_n(z)$	kHz	~ 3.5
Pretensioning			Vertical
LxWxH		mm	170x100x60
Weight		Kg	7.3

IMAGE






**3. FESEM (Field emission scanning electron Microscope) ( Make: Carl Zeiss-sigma)**

Parameter	Specification
Electron Source	Schottky Thermal Field Emitter
Resolution* at 30 kV (STEM):	1.0 nm
Resolution* at 15 kV :	1.0 nm
Resolution* at 1 kV:	1.6 nm
Resolution* at 30 kV (VP Mode) :	2.0 nm
Maximum Scan Speed :	50 ns/pixel
Accelerating Voltage :	0.02 – 30 kV
Magnification:	10× – 1,000,000×
Probe Current:	3 pA - 20 nA (100 nA (optional))
Image Frame store	32 k × 24 k pixels

**IMAGE**



#### 4. CILAS 1064 Particle size analyser

Parameter	Specification
Particle size range:	0.04 to 500 $\mu\text{m}$
Number of lasers:	2
Laser source:	Fibre and collimated laser diodes
Wavelength :	635 and 830 nm
Power :	3/7 Mw
Beam diameter:	2 and 20 mm
Repeatability	$\pm 0.5 \%$
Reproducibility:	$< 2 \%$
IMAGE	
	

#### 5. Lakeshore:7407- Vibration sample Magnetometer (VSM)

Parameter	Specification
Make and Model:	Lakeshore, USA,
Model	7407
Max. Magnetic field	2.5 T
Dynamic moment range:	$1 \times 10^{-6} \text{emu} - 10^3 \text{emu}$
Vibrating Sample magnetometer feasible measurements <ul style="list-style-type: none"> <li>• M Versus H at Room Temperature.</li> <li>• M Versus T at constant H ( Selected Field) M Versus H at constant Temperature (Low Temperature range 20-300K and High Temperature range 300 -1270K</li> </ul>	

IMAGE



6. Weighing balance

Parameter	Specification
Maximum capacity	1 kg
Accuracy	0.1 g
Power	~230 V , 50 Hz

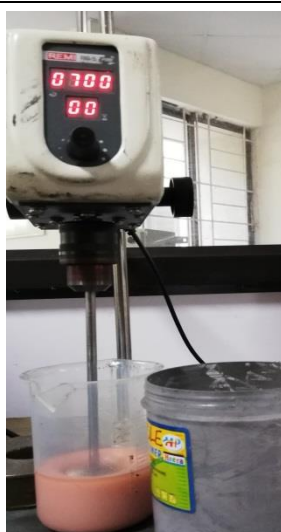
IMAGE



### 7. Mechanical stirrer (Make: Remitek)

Parameter	Specification
Max. Capacity:	5 litres
Speed range:	50-1500 rpm
Power, Voltage, frequency:	10 W, 220-240 V, 50 Hz

IMAGE



### 8. Rheometer MCR 702 (Make: Anton-Paar, Austria)

Parameter	Specification
Minimum torque, rotation:	1nNm
Maximum torque, rotation:	230mNm
Minimum torque, oscillation:	0.5nNm
Maximum angular frequency:	628 rad/s
Normal force:	0.005 to 50 N
Maximum temperature:	160°C to 1000°C
Pressure:	up to 1000bar
Rheometer Software:	RheoCompass,
MRD Cell:	1Tesla
Oil free Motor Power:	0.55 kW
Output (5 bar):	55 l/min max



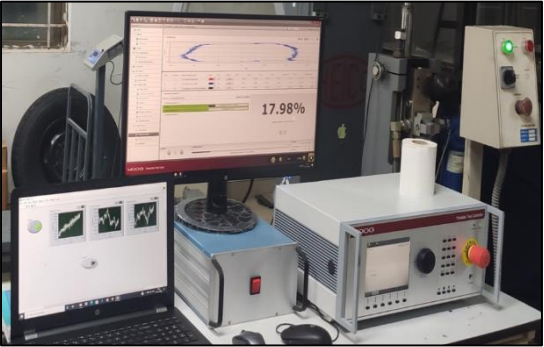

Temperature range:	-10 to 170°C (Peltier Heating/Cooling),
Pressure:	8 bar,
Cooling Tank Volume:	10 L
Weight:	59 kg
Power Supply Magneto Cell	230V HCP 14-12500,12.5,1 mA

IMAGE



### 9. Damper testing machine (DTM)(Make: Heico India)

Parameter	Specification	Image
<b>Actuator</b>		
Capacity	+/- 20 kN	
Stroke:	150 mm (+/- 75 mm) Max.,	
Working pressure:	210 bar Max	
Velocity:	0.8 m/s- 1.2 m/s,	
Servo valve:	63LPM	
Pressure line filter	180 LPM	

Accumulator (2 No.)	0.36 ltr. Capacity	
<b>Displacement sensor</b>		
Range	200 mm	
Full scale output	10 volts	
sampling rate:	2 kHz,	
Operating temperature:	-30 to +75 deg. C	
<b>Load cell</b>		
Load cell: Capacity	+/- 30kN,	
Resolution:	0.001kN,	
Excitation Voltage	10 Volts DC	
Operating temperature	0 to +60 deg. C	
<b>Moog controller</b>		
Auto PID operation, Digital signal processing based closed loop servo controller with 10 kHz.		
Number of control channels	4	
Demand wave generation	Sine, Triangular, Square and ramp	
<b>Hydraulic power pack with radiator</b>		
Flow rate: Operating	64 Litres/min	
Pressure:	210 bar,	
Capacity:	200 litres	
power supply:	440 V	

IMAGE



Damper testing machine

**10. DC power supply**

Parameter	Specification
Output	0-30 V / 5 A
Resolution	10 mV
Current	5 mV
Load regulation	$\leq \pm (0.05 \% + 10 \text{ mV})$
Input supply	230 AC $\pm 10 \%$ / 50-60 Hz
Resistance	$\leq 10 \text{ m Ohms}$
IMAGE	





DC power supply

### 11. Surface roughness tester


Parameter	Specification
Model	Mitutoyo, Talysurf SJ310
Measuring force, Stylus tip radius, Tip angle	4 mN, 5 $\mu\text{m}$ , 90°
Cut off length	0.08, 0.25, 0.8, 2.5, 8 mm
Sampling length	2.5, 8 $\mu\text{m}$
No of sampling length	x1 to x10

IMAGE

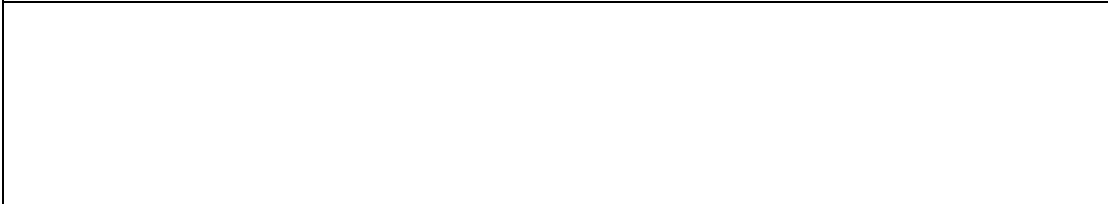




## 12. NI 9234 DAQ

Parameter	Specification
IEPE channels	4-channel sound and vibration input
Resolution	24 bit
Operating range	$\pm 5$ V, 0-20 mA input range
Connectivity	BNC only
Sampling rate	51.2 kS/s
IMAGE	
	

## 13. NI 9403 with DSUB 32 Ch, TTL Digital Input/Output Module

Parameter	Specification
Module type	5V, TTL digital I/O
No. of input output channels	32 - Channel
Speed of operation	7 $\mu$ S
Isolation	60 VDC, CAT I
Operational Temperature	-40 °C to 70 °C
Operating Acceleration	5 g vibration, 50 g shock
IMAGE	
	



NI 9403 with DSUB 32 Ch, TTL Digital Input/Output Module

#### 14. NI C DAQ 9174

Parameter	Specification
Input FIFO size	127 samples per slot
Timing frequency	50 ppm sample rate
Timing resolution	12.5 ns
Resolution (timers and counters)	32 bits
No of slots per module	4

IMAGE



### 15. Triaxial accelerometer

Parameter	Specification
Make and model	PCB PIEZOTRONICS, 356A09
Sensitivity	10 mV/g
Measuring range	$\pm 500$ g pk
Frequency range	2 to 8000 Hz (y or z axis), 2 to 5000 Hz (x)
Resonant frequency	$>50$ kHz
Overload limit	$\pm 5000$ g pk
Excitation voltage	22 to 30 VDC
Constant current excitation	2 to 20 mA
Output impedance	$\leq 200$ Ohm
Output bias	9 to 16 VDC
Size	6.35x6.35x6.35 mm
Mounting	Adhesive

IMAGE



### 16. Impact hammer

Parameter	Specification
Make and model	PCB PIEZOTRONICS, TLD086C03
Sensitivity	2.25 mV/N
Measurement range	$\pm 2000$ N pk
Hammer mass	0.16 kg
Excitation voltage	20-30 V DC

Constant current excitation	2-20m A
Output impedance	<100 m Ohm
Sensing element	Quartz
Electrical connector	BNC Jack

IMAGE



### 17. MRF 132 DG MR fluid

Parameter	Specification
Make	Lord corporation ltd.
Appearance	Dark gray liquid
Viscosity, Calculated as slope 800-1200 sec-1, Pa-s @ 40°C (104°F)	0.112 ± 0.02
Density, g/cm <sup>3</sup> (lb/gal)	2.95-3.15 (24.6-26.3)
Flash Point, °C (°F)	>150 (>302)
Operating Temperature, °C (°F)	-40 to +130 (-40 to +266)



## 18. Software

Name of software	Version	Licensed
MATLAB/SIMULINK (Mathworks)	R2018b to R2022a	NITK
FEMM	4.2	Open-source
ANSYS	2022	Student trial version
LabVIEW (National instruments )	2017	NITK
Signal express (National instruments)	2017	NITK
Origin (OriginLab)	2021	Learning edition (free)
MINITAB	2018	Trial version
WEKA machine learning	3.6.9	Open-source



## LIST OF PUBLICATIONS

### International journals

1. Aralikatti, S. S. and Hemantha Kumar, “Tool Vibration Isolation in Hard Turning Process with Magnetorheological Fluid Damper” *Journal of Manufacturing Processes*, Elsevier, (Scopus and SCIE, IF 5.684, Q1) <https://doi.org/10.1016/j.jmapro.2023.01.044>
2. Aralikatti, S. S., Ravikumar K. N., Kumar, H., Nayaka H. S., and Sugumaran, V. “Comparative Study on Tool Fault Diagnosis Using Vibration Signals and Cutting Force Signals by Machine Learning Technique.” *Structural Durability and Health Monitoring*, Tech Science Press. (Scopus indexed), <https://doi.org/10.32604/sdhm.2020.07595>
3. Aralikatti, S.S., Ravikumar, K.N. and Kumar, H. (2019) “Fault diagnosis of single-point cutting tool using vibration signal by rotation forest algorithm.” *SN Applied. Sciences* 1: 1017. Springer Nature publications. (Scopus indexed and ESCI) (Q2), <https://doi.org/10.1007/s42452-019-1028-9>
4. Aralikatti, S. S., N. P. Puneet, and Hemantha Kumar, “Determining the Optimal Composition of Magnetorheological Fluid for a Short-Stroke Magnetorheological Damper” *Sadhana*, Springer publication, SADH-D 2201052, (Review submitted) (Scopus indexed and SCIE, IF 1.214, Q2 )
5. Aralikatti, S. S. and Hemantha Kumar, “ Real-Time Control of Tool Vibration in Hard Turning using Magneto-rheological damper” *SCIENTIA IRANICA*, SCI-2211-7333, (Under Review) (Scopus indexed and SCI, IF 1.416, Q2)

### International conferences

6. Aralikatti, S. S., Ravikumar K. N., and Hemantha Kumar. “Fault Diagnosis of Single Point Cutting Tool Using Spectrum, Cepstrum and Wavelet Analysis.” *1<sup>st</sup> International Conference Manufacturing, Materials Science and Engineering (ICMMSE 2019)*, August - 2019, CMR Institute of Technology,

Hyderabad, India. **AIP Conference Proceedings (Indexed in Scopus and Web of science)**. <https://doi.org/10.1063/1.5141218>

7. Aralikatti, S. S., and Hemantha Kumar. “Magnetostatic Analysis of Magnetorheological Damper for Tool Vibration Control Application.” *7<sup>th</sup> International Congress on Computational Mechanics and Simulation (ICCMS 2019)*, 11-13 December 2019, IIT Mandi, India

## **Patent**

1. Title: Magnetorheological Fluid Based Tunable Tool Holder in Chatter Vibration Control of a Cutting Tool during Turning Operation. Inventors: Suhas S. Aralikatti and Hemantha Kumar. (Status: Filing in-process, cleared patentability search)



## BIO-DATA

1. Name: Suhas S. Aralikatti
2. Date of Birth: 31/07/1991
3. Nationality: Indian
4. Address: # 07 Renuka Nagar  
Gokul Road, Hubballi - 30
5. Mobile No.: +91 90087 88182
6. Email ID: [amsuhas@gmail.com](mailto:amsuhas@gmail.com)
7. Educational Qualification:



Qualification	Institute	Passing	Score
PhD in Mechanical Engineering	NITK Surathkal, KA, IN	2023	Pass
M.Tech. in Manufacturing Engineering, <i>Supervisor: Dr. M. Amarnath</i>	IITDM Jabalpur, MP, IN	2017	8.10/10
BE in Mechanical Engineering	KLE Technological University, Hubballi, IN	2013	8.02/10

8. Experience:

Graduate Engineer Trainee (GET), '**Operations**' at MSPL PELLETT PLANT, A flagship of BALDOTA GROUP OF COMPANIES, Hospet, KA, IN

*I declare that the above information is true and correct to the best of my knowledge and belief*

(Suhas S. Aralikatti)